Biomaterial Control of Cell Forces to Enable Intercellular Communication During Vasculogenic Assembly

by

Christopher D. Davidson

A dissertation submitted in partial fulfillment
of the requirements for the degree of
Doctor of Philosophy
(Biomedical Engineering)
in the University of Michigan
2022

Doctoral Committee:

Assistant Professor Brendon M. Baker, Chair
Associate Professor Jianping Fu
Professor Andrew J. Putnam
Assistant Professor Mahmut Selman Sakar, EPFL

Christopher D. Davidson

cddavid@umich.edu

ORCID iD: 0000-0003-0504-0215

© Christopher D. Davidson 2022

Dedication

To Claire, none of this would have been possible without you. I can’t thank you enough for your endless, unwavering love and support during this process. You were always there to pick me up in the lows and celebrate with me in the highs. Living life with you is the greatest gift, and I love you more than anything.

To my family, thank you for being my biggest supporters and encouraging me to work hard and pursue what I love.

To my friends, old and new, thank you for always being there and making Ann Arbor feel like home.

Acknowledgements

The contents of this thesis would not have been possible without the tremendous support that I have received from my advisor, lab mates, collaborators, and thesis committee members. First, I would like to thank my advisor, Brendon. Deciding to join the Baker Lab in 2016 was the best choice that I made in graduate school. I have learned so much from you and I wouldn’t be the scientist that I am today without your mentorship and guidance. I’m also proud to be able to call you a great friend, and I’m excited to continue to watch your career grow and succeed.

This work also contains critical contributions from fellow lab mates and close collaborators. I had the unique opportunity to start the Baker Lab alongside William Wang and Daniel Matera, two phenomenal scientists and great friends. I couldn’t have asked for better people to spend these past five and a half years with. Ina Zaimi, Danica Jayco, and Jordan Kamen were all outstanding and diligent undergraduate researchers who were a joy to work with. Sam DePalma, Harrison Hiraki, Bobby Kent, Maggie Jewett, and Raha Kannan, your input towards this work was incredibly impactful and your friendships provided much needed joy and laughter during long days (and nights) in the lab. The Baker Lab is in great hands moving forward! Lastly, Dr. Andrew Putnam, Dr. Selman Sakar, and Dr. Jianping Fu, you were all great mentors and collaborators that added many new exciting dimensions to this thesis project.

Table of Contents

Dedication .... **ii**

Acknowledgements .... **iii**

List of Figures .... **xiii**

List of Movies .... **xxxiii**

Abstract .... **xxxvii**

Chapter 1: Introduction **1**

Chapter 2: Background **5**

- **2.1 Mechanotransduction and the ECM** **5**
    - 2.1.1 ECM structure and composition 5
    - 2.1.2 Mechanosensing at focal adhesions 6
    - 2.1.3 Biomaterial platforms to model the ECM 8
    - 2.1.4 Electrospun fibrous matrices 10
    - 2.1.5 ECM control over traction force and matrix displacements 11
- **2.2 Mechanical Intercellular Communication** **12**
    - 2.2.1 Modes of intercellular communication 12

2.2.2 Examples of mechanical intercellular communication 15

2.3 Engineering Microvascular Networks 16

2.3.1 Vascular tissue engineering 16

2.3.2 Fabrication approaches for engineered microvasculature........................... 17

2.3.3 In vitro vasculogenic assembly.. 18

2.3.4 Mechanical regulation of vasculogenic assembly....................................... 20

Chapter 3: Cell Force-Mediated Matrix Reorganization Underlies Multicellular Network Assembly 22

3.1 Authors.. 22

3.2 Abstract... 22

3.3 Introduction... 23

3.4 Results 26

3.4.1 ECM mechanics regulate EC network formation and matrix reorganization on Matrigel.. 26

3.4.2 Synthetic fibrous DexMA matrices undergo pronounced matrix reorganization during EC network formation 29

3.4.3 Actomyosin contractility is required for EC network formation on fibrous DexMA matrices 32

3.4.4 Physical properties of fibrous ECM influence matrix reorganization and EC network formation... 35

3.4.5 Matrices permissive to physical reorganization and persistent deformations yield EC networks stabilized by VE-cadherin enriched cell-cell junctions.......... 37

3.5 Discussion.. 40

3.6 Materials and Methods... 45

3.6.1 Reagents.. 45

3.6.2 Cell culture.. 45

3.6.3 Network formation on Matrigel.. 45

3.6.4 DexMA synthesis... 46

3.6.5 Fiber matrix fabrication... 47

3.6.6 Mechanical testing... 48

3.6.7 RGD functionalization and seeding on DexMA fibers................. 49

3.6.8 Pharmacologic contractility inhibition.. 49

3.6.9 VE-cadherin disruption.. 50

3.6.10 Bead displacement quantification... 50

3.6.11 Fluorescent staining and microscopy.. 50

3.6.12 Statistics.. 51

3.7 Supplementary Figures.. 52

Chapter 4: Myofibroblast Activation in Synthetic Fibrous Matrices Composed of Dextran Vinyl Sulfone.. 62

4.1 Authors.. 62

4.2 Abstract.. 62

4.3 Introduction.. 63

4.4 Results and Discussion.. 67

4.4.1 DexVS matrix fabrication and mechanical characterization 67

4.4.2 DexVS functionalization to enable user- or cell-defined adhesion 71

4.4.3 Effect of DexVS fibrous matrix stiffness on cell behavior.......................... 73

4.5 Conclusion 78

4.6 Materials and Methods.. 79

4.6.1 Reagents.. 79

4.6.2 Cell culture.. 79

4.6.3 DexVS synthesis... 79

4.6.4 Fibrous matrix fabrication.. 79

4.6.5 Mechanical testing 81

4.6.6 RGD functionalization and seeding on DexVS matrices............................ 82

4.6.7 Passive adsorption of proteins to DexVS matrices..................................... 82

4.6.8 HepMA synthesis and functionalization.. 82

4.6.9 Myofibroblast induction.. 83

4.6.11 Statistics 84

4.7 Supplementary Figures 85

Chapter 5: Fiber Crimp Confers Matrix Mechanical Nonlinearity, Regulates Endothelial Cell Mechanosensing, and Promotes Microvascular Network Formation............................ 88

5.1 Authors.. 88

5.2 Abstract.. 88

5.3 Introduction.. 89

5.4 Results.. 92

5.4.1 Development and mechanical characterization of crimped DexVS fibrous matrices... 92

5.7.2 Endothelial cell spreading and mechanosensing in crimped DexVS matrices 97

5.7.3 EC migration and network formation on crimped DexVS matrices.......... 100

5.5 Discussion.. 103

5.6 Conclusion 107

5.7 Materials and Methods.. 107

5.7.1 Reagents.. 107

5.7.2 Cell culture... 108

5.7.3 DexVS synthesis.. 108

5.7.4 Fibrous matrix fabrication.. 108

5.7.5 Peptide functionalization and seeding of DexVS fibers 109

5.7.6 Mechanical characterization 110

5.7.7 Fluorescent staining and microscopy 110

5.7.8 Time-lapse microscopy and migration analysis 111

5.7.9 Statistics 112

5.8 Supplementary Figures 112

Chapter 6: Mechanical Intercellular Communication via Cell Force Transmission During Vascular Network Formation 113

6.1 Authors 113

6.2 Abstract 113

6.3 Introduction 114

6.4 Results 117

6.4.1 Cell-generated matrix deformations and tension support enhanced cell spreading and multicellular cluster formation 117

6.4.2 Micropatterning single ECs reveals matrix stiffness influences cell spreading, FA formation, and matrix deformations 121

6.4.3 Propagation of mechanical signals between neighboring cells promotes directed migration and formation of cell-cell connections 126

6.4.4 Patterning EC lines identifies a critical role for coordinated intracellular Ca^{2+} signaling during MIC 128

6.4.5 Focal adhesion kinase signaling and mechanosensitive ion channels are required for MIC during 3D vascular network formation 132

6.5 Discussion 135

6.6 Materials and Methods.. 141

6.6.1 Reagents.. 141

6.6.2 Cell culture and biological reagents.. 141

6.6.3 Lentivirus production.. 142

6.6.4 DexMA synthesis.. 142

6.6.5 Fiber matrix fabrication 143

6.6.6 Mechanical testing 144

6.6.7 RGD functionalization and seeding on DexMA matrices 145

6.6.8 Fluorescent staining and microscopy.. 145

6.6.9 Cell migration analysis 146

6.6.10 Microwell patterning stamp fabrication.. 147

6.6.11 Cell patterning on DexMA matrices... 147

6.6.12 Timelapse fiber displacement microscopy... 148

6.6.13 Calcium imaging.. 149

6.6.14 3D vascular network formation 149

6.6.15 Statistical Analysis.. 149

6.7 Supplementary Figures 150

Chapter 7: Synthetic Matrix Fibers Support 3D Vascular Network Assembly in Fibrin Hydrogels... 158

7.1 Authors.. 158

7.2 Abstract.. 158

7.3 Introduction.. 159

7.4 Results and Discussion.. 162

7.4.1 Evaluating the role of synthetic matrix fibers on EC network formation in 3D fibrin hydrogels. 162

7.4.2 Non-cell-adhesive DexVS fibers enable EC network assembly and lumenization.. 165

7.4.3 Bulk RNA-sequencing identifies enhanced cell-ECM interactions during vasculogenic assembly in fiber-reinforced hydrogels...................................... 167

7.4.4 Adhesion and matrix displacements 169

7.5 Conclusions.. 171

7.6 Materials and Methods... 172

7.6.1 Reagents.. 172

7.6.2 Cell culture and biological reagents.. 172

7.6.3 Lentivirus production.. 173

7.6.4 Synthesis of dextran vinyl sulfone.. 173

7.6.5 Fiber segment fabrication 174

7.6.6 DexVS fiber functionalization 174

7.6.7 Fibrin hydrogel formation... 175

7.6.8 Fluorescent staining and microscopy.. 175

7.6.9 Matrix deformation quantification 176

7.6.10 Bulk RNA-sequencing and bioinformatics 177

7.6.11 Statistical analysis 177

Chapter 8: Summary and Future Directions 178

8.1 Summary of findings 178

8.2 Limitations and Future Directions 179

8.2.1 Towards a deeper understanding of MIC 179

8.2.2 Host-response to fiber-reinforced prevascularized tissue constructs 180

Appendix A: Matlab Scripts 182

Analysis of Focal Adhesion Morphology 182

Alpha Smooth Muscle Actin Quantification 183

Fiber Crimp Quantification 184

Transition Strain Quantification 185

Cell Spreading Synergy Analysis 186

Cell Patterning Analysis of Matrix Displacements and Cell Morphology 187

Single Cell Displacement Radial Projection 191

Calcium Signaling Analysis 193

Bibliography 199

List of Figures

Figure 2.1: The ECM is the non-cellular component present in all tissues and organs, providing physical scaffolding and crucial biochemical and biomechanical cues that guide cell behavior. Image reproduced from (Xue & Jackson, 2015).. 6

Figure 2.2: Cells sense the mechanical features of their environment at focal adhesions where biophysical cues are transduced to intracellular signals that alter cell behavior. Image reproduced from (Vogel & Sheetz, 2006).. 7

Figure 2.3: Biomaterial platforms can incorporate a variety of important structural and mechanical features of the ECM. Image reproduced from (Davidson et al., 2020d). 10

Figure 2.4: Cells within 3D tissues communicate through direct or indirect approaches that are mediated by both biochemical and biophysical signals. Image reproduced from (Yang et al., 2021). 14

Figure 2.5: Engineered microvessels can be fabricated using either top-down or bottom-up approaches. Image reproduced from (Song et al., 2018). 20

Figure 3.1: ECM mechanics regulate EC network formation and matrix reorganization on Matrigel. (a) Confocal fluorescence maximum projections of phalloidin-stained ECs seeded on wedge-shaped Matrigel substrates ranging in thickness from approximately 0 to 550 µm, after

12h of culture. (b) Resulting network morphology was determined by the area/perimeter ratio of thresholded images at select thicknesses of Matrigel as indicated (**Supplementary Figure 3.1**). Horizontal error bars represent the range of thickness for each analyzed section of the image; n ≥ 3. (c) Young's modulus of Matrigel crosslinked with varying glutaraldehyde concentrations determined by microscale compression testing; n ≥ 8. (d) Fluorescent images of ECs cultured for 12 hours on Matrigel after glutaraldehyde crosslinking at the indicated concentration; actin (cyan), nuclei (yellow). (e) Cell area/perimeter ratio on Matrigel substrates as a function of glutaraldehyde crosslinking; n ≥ 7. Representative time-lapse images of lifeAct-GFP expressing ECs (top row) and embedded fluorescent microspheres (Fl-µS, bottom row) on untreated control (f) and 0.1% glutaraldehyde treated (g) Matrigel substrates. Rainbow overlays depict cell and Fl-µS motion (with final EC structure outlined in white) over the 8 hour time-lapse. Rightmost images in (f) depict cell and Fl-µS images following cell lysis. Untreated control substrates demonstrate high levels of matrix deformation and reorganization in contrast to glutaraldehyde crosslinked Matrigel. In the control case, limited elastic recovery is observed after removal of the formed network. Scale bars: 500 µm. All data presented as mean ± std, * P<0.05...................... 28

Figure 3.2: Synthetic fibrous DexMA matrices undergo pronounced matrix reorganization during EC network formation. (a) Schematic of microfabricated PDMS multi-well substrate possessing a 4x4 array of wells, each supporting a suspended matrix of non-aligned DexMA fibers coupled with RGD to facilitate cell adhesion. (b) Tile-scan confocal image of EC networks after 24 hours of culture on DexMA fiber matrices; rhodamine-labeled fibers (magenta), F-actin (cyan), and nuclei (yellow) (scale bar: 1 mm). (c) Limited elastic recovery of fibers after lysis of CellTracker labeled ECs, demonstrating that physical matrix reorganization is permanent (scale bar: 100 µm). (d) Representative time-lapse images of lifeAct-GFP expressing ECs at 0, 1, 4, and

24h following seeding (scale bar: 100 μm). Cell area/perimeter ratio (e) and total Fl-μS displacement (f) over the 24-hour time-lapse series of network formation; n = 8. 32

Figure 3.3: Actomyosin contractility is required for EC network formation on fibrous DexMA matrices. (a) Confocal fluorescence images of phalloidin-stained ECs and rhodamine labeled fibers after 24 hours, with indicated pharmacologic inhibitor treatment; actin (cyan), nuclei (yellow), fibers (magenta). Scale bar: 100 μm. (b) Cell area/perimeter ratio after 24 hours of culture as a function of pharmacologic inhibitor treatment. (c) Total Fl-μS displacement over the first 12 hours of network formation as a function of pharmacologic inhibitor treatment. All data presented as mean ± std; n ≥ 6; * P<0.05. 34

Figure 3.4: Physical properties of fibrous ECM influence matrix reorganization and EC network formation. EC network formation was assayed on DexMA fibrous matrices with varying stiffness (a-d), fiber density (e-h), and with modulation of inter-fiber crosslinks (welds) (i-l). (a) Young's modulus of DexMA fiber matrices as a function of photoinitiator (LAP) concentration. (e,i) Fiber density prior to cell seeding determined as the percent total area of each substrate containing fibers. (b,f,j) Representative image of initial fiber density prior to cell seeding (far left); confocal fluorescent images of phalloidin-stained ECs (left) and rhodamine labeled fibers (middle) 24 hours after seeding under the indicated matrix perturbation after 24 hours of culture; merged images (right) showing actin (cyan), nuclei (yellow), and fibers (magenta) (scale bar: 100 μm). (c,g,k) EC area/perimeter ratio as a function of ECM perturbation. (d,h,l) Total Fl-μS displacement over the first 12 hours of network formation as a function of ECM perturbation. All data presented as mean ± std; n ≥ 6; * P<0.05. 37

Figure 3.5: Matrices permissive to physical reorganization and persistent deformations yield EC networks stabilized by VE-cadherin enriched cell-cell junctions. (a) Confocal fluorescence maximum projections of phalloidin-stained ECs (cyan), rhodamine labeled fibers (magenta), nuclei (yellow), and VE-cadherin (gray) at 0, 1, 4, and 24 h after cell seeding on control DexMA matrices (top row). Dashed boxes indicate locations of higher magnification images depicting VE-cadherin expression at cell-cell junctions (bottom row). (c) Confocal fluorescence maximum projections of phalloidin-stained ECs (cyan), rhodamine labeled fibers (magenta), nuclei (yellow), and VE-cadherin (gray) of samples 24 h after seeding on control and stiff DexMA matrices, on control matrices cultured for 24h, lysed, crosslinked, and then reseeded for 24 h (Reorg – Stiff), or on control matrices cultured for 24h, lysed, and then reseeded for 24 h (Reorg – Soft) (top row). Dashed boxes indicate locations of higher magnification images depicting VE-cadherin expression at cell-cell junctions 24 h after cell seeding (bottom row). Scale bars: 50 μm. (b,d) Quantification of total VE-cadherin fluorescent intensity normalized to cell density at each timepoint (b) and matrix condition (d). All data presented as mean ± std; n ≥ 16; * P<0.05. 40

Supplementary Figure 3.1: A/P ratio quantification for three possible cellular phenotypes. Area/perimeter ratio was quantified by calculating the total area and perimeter of thresholded fluorescent images of phalloidin-stained ECs via custom Matlab scripts. a) Single cells that are not interconnected have a small total area and large perimeter, leading to a relatively low area/perimeter ratio value (between 0 and 10). b) Interconnected cellular networks have an intermediate total area and perimeter, leading to an intermediate area/perimeter ratio value (between 10 and 30). c) Monolayers have a large total area and small perimeter, leading to a relatively high area/perimeter ratio value (greater than 30). Scale bars: 100 μm. 52

Supplementary Figure 3.2: Mechanical characterization of Matrigel and DexMA fibrous matrices. a) Stress-strain curves of Matrigel crosslinked with variable concentrations of glutaraldehyde. Right plot shows linear region used to quantify Young's modulus for each condition. b) Force response of DexMA fibrous matrices as a function of indentation depth of networks crosslinked with varying concentrations of LAP photoinitiator. 53

Supplementary Figure 3.3: Matrix reorganization during EC network formation on Matrigel. Vector plots depict Fl-μS motion with respective EC structure outlined in white for individual 1 hour increments on a) untreated control substrates demonstrating high levels of matrix deformation and organization in contrast to b) glutaraldehyde crosslinked Matrigel. Scale bars: 500 μm. 54

Supplementary Figure 3.4: Cellular extensions and inter-connections occur throughout network formation. Confocal fluorescent images of ECs and rhodamine-labeled fibers showing cellular extensions and the formation of cell-cell interconnections during (a) the first four hours of network formation and (b) after the first four hours of network formation, during network stabilization. Scale bars: 50 μm. 55

Supplementary Figure 3.5: Fibronectin secretion during EC network formation on fibrous DexMA matrices. Confocal fluorescent images of ECs, rhodamine-labeled fibers (magenta), and fibronectin (grayscale) after 24 hours of culture on control matrices. Fibronectin secretion was noted at network nodes corresponding to locations with a high relative fiber density due to cell-mediated matrix reorganization. Scale bar: 100 μm. 55

Supplementary Figure 3.6: Quantification of Fl-μS displacement using TrackMate. Matrix reorganization was quantified by calculating the sum of the mean squared displacement of Fl-μS (white) embedded in rhodamine-labeled DexMA fibers (magenta) over 12 hours using TrackMate, an ImageJ plugin (Tinevez et al., 2017). Conditions that allow for high levels of matrix reorganization demonstrate large displacements, with rapid Fl-μS movement over the first four hours. Conditions with low matrix reorganization exhibit limited Fl-μS displacement. Scale bars: 100 μm. 56

Supplementary Figure 3.7: Quantification of matrix remodeling via analysis of pores during EC network formation on fibrous DexMA matrices. Quantitative analysis of pores within DexMA fiber matrices over a 24-hour time-lapse series of network formation. a) Average pore size increases and b) total number of pores decreases during the formation of an EC network, supporting the observation that ECs bundle and condense matrix fibrils as they spread and interconnect; n ≥ 8. 57

Supplementary Figure 3.8: Analysis of cell cytoskeletal structure after treatment with pharmacologic inhibitors of actomyosin contractility. High resolution (40x) confocal fluorescence images of phalloidin-stained ECs and rhodamine-labeled fibers after 24 hours of culture with the indicated pharmacologic inhibitor treatment; actin (cyan), fibers (magenta). Dashed boxes indicate locations of higher magnification images depicting variable cytoskeletal structure between different conditions (far right). Scale bars: 10 μm. 58

Supplementary Figure 3.9: Fiber diameter as a function of physical matrix perturbations. Histograms showing the distribution of diameter across a population of DexMA fibers with indicated matrix perturbations: control (black), intermediate fiber density (magenta), high fiber density (cyan), intermediate fiber stiffness (orange), high fiber stiffness (purple), and inter-fiber crosslinking via welding (green). For each condition, diameters of n ≥ 69 fibers were quantified;

fitted curves assume a Gaussian distribution. Overlay of fitted curves show no statistically significant difference in mean diameter across any matrix perturbation as determined by ANOVA (p=0.7673). 59

Supplementary Figure 3.10: VE-cadherin disruption via calcium chelation alters network architecture. a) Representative confocal fluorescent images of phalloidin-stained ECs and rhodamine-labeled fibers with and without EGTA treatment to chelate free calcium ions and disrupt cadherin-rich cell-cell adhesions; actin (cyan), fibers (magenta), and nuclei (yellow). (b) Cell area/perimeter ratio after 24 hours of culture and EGTA treatment. Scale bars: 100 μm. Data presented as mean ± std; n = 6; * P<0.05. 60

Supplementary Figure 3.11: Long-range cellular extensions during network formation. Representative confocal fluorescent images of ECs and rhodamine-labeled fibers depicting long-range interactions between cells positioned approximately 300 microns apart. Scale bars: 100 μm. 60

Figure 4.1: DexVS fibrous matrices with tunable architectural features. (a) Schematic of microfabricated PDMS multi-well substrate possessing a 4 x 4 array of wells, each supporting a suspended matrix of DexVS fibers coupled with RGD to facilitate cell adhesion. Through modulation of the electrospinning fabrication process, networks were fabricated with varying (b) fiber density via fiber collection duration and (c) alignment via controlling the separation distance between two parallel electrodes at the collecting surface. Scale bars: 50 μm. 68

Figure 4.2: Mechanical characterization of single DexVS fibers by AFM three-point bending. (a) Force response as a function of indentation depth of DexVS fibers exposed to variable crosslinking conditions. Respective Young's modulus values for DexVS fibers crosslinked with (b) varying LAP concentration for 20 s, and (c) varying crosslinking time in 1.0 mg ml^{-1} LAP. All data presented as mean ± std; $n \geq 9$; * $p \leq 0.05$. 69

Figure 4.3: Mechanical characterization of suspended DexVS matrices by microindentation with a cylindrical indenter affixed a calibrated cantilever. (a) Force response as a function of indentation depth of DexVS matrices exposed to variable crosslinking conditions. Respective Young's modulus values for DexVS matrices crosslinked with (b) varying LAP concentration for 20 s, and (c) varying crosslinking time in 1.0 mg ml^{-1} LAP. All data presented as mean ± std; $n = 6$; * $p \leq 0.05$. 70

Figure 4.4: Multi-scale and time-dependent mechanical characterization of DexVS matrices. (a) Matrix Young's modulus as a function of single fiber Young's modulus at variable crosslinking conditions. (b) Chemical schematic of crosslinked DexVS and DexMA. Arrows indicate ester bonds susceptible to hydrolysis. (c) Bulk Young's modulus of DexVS and DexMA matrices as a function of incubation time in basal medium for up to two weeks. All data presented as mean ± std; $n \geq 6$; * $p \leq 0.05$. 71

Figure 4.5: DexVS functionalization with cell-adhesive peptides and passive adsorption of proteins. Confocal fluorescent images of NHLFs cultured on DexVS matrices functionalized with (a) variable cRGD concentrations and (c) soaked in various matrix proteins; actin (cyan), DexVS fibers (magenta), nuclei (yellow). Average cell spread area and number of adhered cells as a function of (b) cRGD concentration and (d) protein functionalization. Scale bars: 200 µm. All data presented as mean ± std; $n \geq 6$; * $p < 0.05$. 72

Figure 4.6: HepMA functionalization increases binding of cell-secreted fibronectin to DexVS fibers. (a) Confocal fluorescent images of fibronectin (white), DexVS fibers (magenta), and nuclei (yellow). (b) Quantification of fibronectin signal per cell as a function of matrix stiffness and HepMA functionalization. Scale bar: 200 μm. All data presented as mean ± std; $n \geq 104$; * $p < 0.05$. 73

Figure 4.7: Soft, deformable DexVS matrices promote increased cell spreading and focal adhesion formation. (a) Cell outlines of nine representative cells. Scale bar: 200 μm. (b) Confocal fluorescent image of rhodamine-labeled DexVS fibers with cell outline shown in red. Scale bar: 100 μm. (c) Confocal fluorescent image of phalloidin-stained NHLFs (cyan) and vinculin (magenta, top left inset). Scale bar: 100 μm. (d) Quantification of cell spread area ($n \geq 171$) and focal adhesion area per cell ($n \geq 29$). All data presented as mean ± std; * $p < 0.05$. 75

Figure 4.8: Soft, deformable DexVS matrices promote MF induction. (a) Confocal fluorescent image of NHLFs cultured for 7 days on soft and stiff DexVS fibrous matrices; F-actin (cyan), DexVS fibers (magenta), nuclei (blue), α-SMA (yellow). Dashed boxes indicate locations of higher magnification images depicting α-SMA stress fibers. (b) Quantification of cell proliferation by EdU labeling ($n \geq 13$) and α-SMA fluorescent intensity ($n \geq 10$). Scale bars: 25 μm. All data presented as mean ± std; * $p \leq 0.05$. 77

Supplementary Figure 4.1: ^{1}H NMR spectrum (D2O) of vinyl sulfonated dextran. The degree of DexVS functionalization was characterized by ^{1}H NMR, calculated as the ratio of averaged vinyl sulfone proton integral (6.36, 6.47, 6.98 ppm in D2O) and the anomeric proton of the glycopyranosyl ring (4.99 and 5.15 ppm in D2O). Since the signal of the anomeric proton of α-1,3 linkages (5.15 ppm) partially overlaps with other protons, a pre-determined ratio of 4% α-1,3 linkages was assumed and the total anomeric proton integral was calculated solely based on the integral at 4.99 ppm. A vinyl sulfone:dextran repeat unit ratio of 0.66 was determined........ 85

Supplementary Figure 4.2: Properties of DexVS fibrous matrices. (a) Orthogonal x-y, x-z, and y-z maximum intensity projection views from a confocal fluorescence image stack of a suspended 3D DexVS fibrous matrix; rhodamine-labeled DexVS fibers (magenta). Histogram of (b) DexVS fiber diameter and (c) DexVS matrix thickness. Scale bar: 20 µm. 85

Supplementary Figure 4.3: Cell survival on DexVS matrices. (a) Live/dead stain of NHLFs seeded on soft and stiff DexVS matrices and (b) quantification of cell viability (n = 11 fields of view). Scale bar: 200 µm. Data presented as mean ± std; * $p \leq 0.05$. 86

Supplementary Figure 4.4: Saturating concentrations of cRGD required to maximize cell adhesion on DexVS matrices. (a) Confocal fluorescent images of NHLFs cultured on DexVS matrices functionalized with 100 or 500 µM cRGD; actin (cyan), nuclei (yellow). Scale bar: 200 µm. (b) Average cell spread area as a function of cRGD concentration (n = 37). Data presented as mean ± std; * $p < 0.05$. 86

Supplementary Figure 4.5: TGF-β1 is required for MF activation on both soft and stiff DexVS fibrous matrices. (a) Confocal fluorescent images of NHLFs cultured for 7 days on DexVS matrices with or without TGF-β1; nuclei (blue), α-SMA (yellow). Scale bar: 200 µm. (b) Quantification of α-SMA fluorescent intensity and final cell density ($n \geq 10$). Data presented as mean ± std; * $p \leq 0.05$... 87

Figure 5.1: Functionalization of hydrogel fibers with hydrophilic swelling peptide induces crimp in DexVS matrices. (a) Schematic representation of DexVS fibers with controlled adhesive ligand and crimping via functionalization with the cell adhesive peptide cRGD and hydrophilic swelling peptide (HSP, peptide sequence: CGRDGS), respectively. (b) Matrix thickness quantified over time immediately after adding 2.0 mM HSP (n = 6 matrices). (c)

Confocal fluorescent images and orthogonal maximum intensity projections of DexVS matrices functionalized with variable HSP concentrations with representative fiber outlines. Scale bar: 50 µm. Quantification of (d) fiber tortuosity (n = 30 fibers), (e) matrix thickness (n = 14 matrices), and (f) fiber diameter (n = 100 fibers) as a function of HSP concentration. All data presented as mean ± standard deviation; * $p < 0.05$. 93

Figure 5.2: Mechanical characterization of crimped DexVS matrices. Average stress-strain curves with quantification of Young's modulus at low (0.00 – 0.05) and high (0.05 – 0.10) strain and transition strain for DexVS matrices with (a) variable HSP concentrations and no additional crosslinking, (b) variable crosslinking at 0.0 mM HSP, (c) variable crosslinking at 1.0 mM HSP, and (d) variable crosslinking at 2.0 mM HSP (n = 5-6 matrices per group). All data presented as mean ± standard deviation; * $p < 0.05$. # indicates statistical significance ($p < 0.05$) between low and high strain. 96

Figure 5.3: Crimped DexVS fibrous matrices regulate EC morphology and physical matrix remodeling. (a) Cell outlines of nine representative cells as a function of HSP concentration. (b) Confocal fluorescent images and orthogonal maximum intensity projects of ECs in DexVS matrices functionalized with varying HSP concentration. F-actin (cyan), DexVS fibers (magenta), nuclei (yellow). Quantification of (c) cell spread area ($n \geq 74$ cells), (d) cell thickness (n = 24 cells), (e) cell volume (n = 18 fields of view), (f) nuclear area ($n \geq 72$ nuclei), (g) nuclear thickness (n = 50 nuclei), (h) nuclear volume (n = 18 fields of view), (i) average DAPI intensity (n = 24 nuclei) (j) fiber recruitment (n = 24 fields of view), and (k) final matrix thickness (n = 24 fields of view). Scale bars: 50 µm. All data presented as mean ± standard deviation; * $p < 0.05$. 98

Figure 5.4: Crimped DexVS fibrous matrices regulate EC mechanosensing. Confocal fluorescent images of ECs on DexVS matrices functionalized with variable HSP concentrations and stained for (a) vinculin and (d) YAP. F-actin (cyan), nuclei (yellow). Quantification of (b) total focal adhesion area per cell, (c) average area of single focal adhesions ($n \geq 31$ cells), (e) YAP nuclear to cytoplasmic ratio, and (f) nuclear YAP intensity ($n \geq 32$ cells). Scale bars: 50 μm. All data presented as mean ± standard deviation; * $p < 0.05$. 99

Figure 5.5: EC spreading and migration dynamics on crimped DexVS matrices. (a) Average cell spread area over 16 hours after seeding on DexVS matrices functionalized with various HSP concentrations ($n = 6$ fields of view). (b) Migration speed as a function of HSP concentration ($n \geq 197$ cells). (c) Representative time-lapse images of lifeAct-GFP expressing ECs on DexVS matrices functionalized with 0.0 and 2.0 mM HSP. Arrows indicate matrix alignment between interacting cells. F-actin (cyan), DexVS fibers (magenta). Scale bars: 50 μm. All data presented as mean ± standard deviation; * $p < 0.05$.. 101

Figure 5.6: EC network formation on crimped DexVS matrices. (a) Confocal fluorescence images of ECs and fibers after 5 days of culture on low density DexVS matrices functionalized with variable HSP concentrations. F-actin (cyan), DexVS fibers (magenta), nuclei (yellow). Scale bar: 300 μm. Dashed boxes indicate locations of higher magnification images depicting VE-cadherin expression at cell-cell junctions. Scale bar: 50 μm. (b) Cell area/perimeter ratio ($n = 12$ fields of view) and (c) total VE-cadherin fluorescent intensity normalized to cell density ($n = 8$ fields of view) as a function of HSP concentration. Representative confocal fluorescent images and z-plane cross sections of tube-like structures in (d) control and (e) crimped matrix conditions. Scale bar: 10 μm. Dashed boxes indicate locations of higher magnification. Scale bar: 5 μm. All data presented as mean ± standard deviation; * $p < 0.05$. 103

Figure 6.1: Cell-generated tensile forces and resulting matrix deformations correspond to increased cell spreading and the formation of multicellular clusters. (A) Schematic of microfabricated PDMS multi-well substrate containing an array of wells, each supporting an isolated suspended matrix of DexMA fibers functionalized with RGD to facilitate cell adhesion (scale bar, 1 mm). (B) Schematic of hypothesis that matrix fibers enable MIC underlying EC network formation. (C-D) Confocal fluorescent images of phalloidin-stained ECs (cyan), nuclei (yellow), and rhodamine-labeled DexMA fibers (magenta) with respective color-coded maps of contiguous actin clusters at low (50 cells mm^{-2}) and high (250 cells mm^{-2}) seeding density in (C) low stiffness, cell-deformable matrices and (D) high stiffness, non-deformable matrices (scale bar, 200 μm). (E) Quantification of cell spread area and (F) average number of ECs per contiguous actin cluster as a function of seeding density and matrix stiffness (n = 12 fields of view). (G-H) Confocal fluorescent images of phalloidin-stained ECs (cyan), nuclei (yellow), vinculin (green), and VE-cadherin (red) at 2 and 12 hours after seeding in (G) low stiffness and (H) high stiffness matrices (scale bar, 25 μm). (I) Quantification of total vinculin and VE-cadherin fluorescent intensity normalized to cell density as a function of time and matrix stiffness (n = 6 fields of view). All data presented as mean ± SD; asterisk denotes significance with $P < 0.05$. 119

Figure 6.2: Low stiffness, cell-deformable fibrous matrices increase cell migration speed during multicellular cluster formation. (A) Migration speed of ECs over 12 hours following seeding in either low stiffness, cell-deformable matrices or high stiffness, non-deformable matrices (n = 6 fields of view). (B) Quantification of migration speed during the first 2 hours and

(C) remaining 10 hours of culture as a function of matrix stiffness (n = 6 fields of view). (D) Maximum cluster size over 12 hours of culture as a function of matrix stiffness (n = 6 fields of view). (E) Temporally color-coded overlay capturing the motion of nuclei over a 2 hour time course in low and high stiffness matrices. Green arrows represent direction of movement for each individual nuclei with eventual contiguous actin structures demarcated in black (scale bars, 50 μm). All data presented as mean ± SD with superimposed data points; asterisk denotes significance with $P < 0.05$. 121

Figure 6.3: Micropatterning single ECs in individual suspended fibrous matrices reveals cell spreading and FA formation are matrix stiffness-dependent. (A) Schematic depicting microfabrication-based patterning approach to isolate individual ECs at the center of suspended fibrous matrices. Representative confocal fluorescent image of patterned EC (cyan), rhodamine-labeled fibers (magenta), and fluorescent beads embedded in matrix fibers (white) (scale bar, 100 μm). (B) F-actin heat map of patterned ECs with histograms of average patterning error in x- and y-directions (n = 91 cells) (scale bar, 100 μm). (C) Cell outlines of nine representative cells as a function of matrix stiffness (scale bar, 100 μm). (D) Representative immunostained images of FAs in ECs as a function of matrix stiffness; F-actin (green), DexMA fibers (grey), nuclei (blue), and vinculin (orange) (scale bar, 100 μm). (E) Quantification of cell spread area (n = 25 cells), (F) number of FAs per cell (n = 25 cells), and (G) average FA area as a function of matrix stiffness. Data presented as mean ± SD with superimposed data points; asterisk denotes significance with $P < 0.05$. (H) Distribution of individual FA area as a function of matrix stiffness showing a larger population of 3+ μm^2 FAs in low stiffness matrices........................ 123

Figure 6.4: Cell-deformable fibrous matrices support more persistent mechanical signals by promoting fewer, but longer lasting protrusions. (A) Representative confocal fluorescent image of LifeAct-GFP expressing ECs (cyan), rhodamine-labeled DexMA fibers (magenta), and fiber-embedded fluorescent beads (white) (scale bar, 100 μm). (B) Temporally color-coded overlay of EC cell bodies over a 12 hour time course following patterning (scale bar, 100 μm). (C) Size- and color-coded vector plots displaying maximum displacement of each bead over a 12 hour time course (scale bar, 100 μm). (D) Binned average bead displacements for all ECs aligned along their long axis (0°) with color-coded magnitudes ($n > 20$ cells). (E) Cell spread area and (F) fluorescent bead displacement over a 12 hour time course as a function of matrix stiffness ($n > 20$ cells). (G) Net migration distance ($n > 20$ cells), (H) total number of protrusions ($n = 6$ cells), (I) average protrusion lifetime ($n = 6$ cells, $n = 30$ protrusions), and (J) maximum bead displacement as a function of matrix stiffness ($n > 20$ cells). (K) Binned average bead displacements as a function of starting distance from the cell centroid ($n > 20$ cells, $n > 627$ beads). All data presented as mean ± SD with superimposed data points; asterisk denotes significance with $P < 0.05$. 125

Figure 6.5: Force transmission through aligned fibers spanning neighboring cells promotes directed migration and the formation of cell-cell connections. (A) Schematic of cell pair patterning in which two ECs are patterned 200 μm apart on a suspended DexMA fibrous matrix. The fiber well is designed such that the distance between the two cells is equal to the distance between cells and well edges. (B) Representative image of initial matrix fiber morphology in non-aligned and aligned conditions. Temporally color-coded overlays capturing EC morphology and migration over a 12 hour time course after cell attachment as a function of matrix alignment and stiffness (scale bars, 100 μm). (C) Quantification of the percent of interacting and non-interacting cells over a 12 hour time course, with interacting cells defined as cell-cell contact at any point during the 12 hour timelapse. P-values determined by Fisher's exact test. (D)

Representative cell pair interaction between ECs patterned in a non-aligned, low stiffness, cell-deformable matrix (scale bar, 100 μm) and (E) quantification indicating an increase in fiber alignment between the two cells followed by a rapid increase in migration speed prior to cell making direct contact. (F) Quantification of average interaction time (duration during which direct cell-cell contact was maintained). All data presented as mean ± SD with superimposed data points; asterisk denotes significance with $P < 0.05$. 128

Figure 6.6: Micropatterned, multicellular lines support a role for coordinated intracellular Ca^{2+} signaling between neighboring cells during MIC. (A) Schematic of EC line patterning consisting of two parallel lines of cells within each suspended fibrous matrices. (B) Representative confocal fluorescent image of phalloidin-stained ECs (cyan), rhodamine-labeled fibers (magenta), nuclei (yellow), and VE-cadherin (red). Dashed boxes indicate locations of higher magnification images of VE-cadherin immunostaining (right column) (scale bars, 200 μm). (C) F-actin (left column) and nuclei (right column) heat maps of EC lines 12 hours after patterning ($n = 37$ fields of view) (scale bar, 200 μm). (D) Quantification of the percent of nuclei in the original patterned region after 12 hours ($n > 35$ fields of view). (E) Quantification of total VE-cadherin expression at cell-cell junctions normalized to cell density for each matrix condition ($n = 8$ fields of view). (F) Normalized Ca^{2+} intensity over a 10 minute time course. (G) Quantification of total number of Ca^{2+} pulses per cell and (H) distribution of cells by number of Ca^{2+} pulses over a 10 minute time frame ($n > 89$ cells). (I) Representative images of Ca^{2+} signal in ECs within a patterned line with corresponding kymograph and (J) normalized Ca^{2+} intensity displaying a wave of Ca^{2+} fluorescence across the line over time. (K) Quantification of the minimum time between Ca^{2+} pulses as a function of distance between all ECs within patterned lines for low ($n = 160$ cell pairs) and high stiffness ($n = 49$ cell pairs) matrix conditions. Grey lines indicate linear correlations with indicated p-values. All data presented as mean ± SD with superimposed data points; asterisk denotes significance with $P < 0.05$. 131

Figure 6.7: Inhibition of FAK signaling and MSIC activity reduce Ca^{2+} signaling and MIC between ECs. (A-C) Normalized Ca^{2+} intensity over a 10 minute time course of patterned EC lines in low stiffness, cell-deformable matrices treated with (A) PF228 (FAK inhibitor), (B) GSK205 (TRPV4 inhibitor) and (C) GsMTx4 (Piezo1 inhibitor). (D) Quantification of total number of Ca^{2+} pulses per cell and (E) percent of cells with at least one Ca^{2+} pulse over a 10 minute time frame ($n > 84$ cells). (F) Schematic of EC bulk seeding in 2 mm diameter circular suspended fibrous matrices. (G) Confocal fluorescent images of phalloidin-stained ECs (cyan), nuclei (yellow), and rhodamine-labeled fibers (magenta) with respective color-coded maps of contiguous actin clusters as a function of matrix stiffness and presence of inhibitors (scale bars, 200 μm). (H) Quantification of average cell spread area and (I) average cells per contiguous actin cluster ($n > 17$ fields of view). All data presented as mean ± SD with superimposed data points; asterisk denotes significance with $P < 0.05$. 133

Figure 6.8: Matrix stiffness/density, FAK signaling, and TRPV4 activity regulate 3D vascular network formation in fibrin hydrogels. (A) Schematic of 3D vascular network formation assay in fibrin hydrogels. (B) Representative confocal maximum intensity projections (100 μm z-stack) of phalloidin-stained ECs (cyan) and nuclei (yellow) with respective color-coded maps of contiguous actin clusters as a function of fibrinogen concentration and presence of inhibitors (scale bars, 200 μm). (C) Quantification of total vessel length and (D) average number of cells in each 3D contiguous actin clusters ($n = 5$ fields of view). All data presented as mean ± SD with superimposed data points; asterisk denotes significance with $P < 0.05$. 135

Supplementary Figure 6.1: Control over substrate stiffness and fiber density in DexMA fiber networks. (A) Force-indentation response and (B) Young's modulus of DexMA fibrous matrices as a function LAP photoinitiator concentration (n = 7 matrices/group). (C) Representative fluorescent images of DexMA fibers at low, intermediate, and high fiber density (scale bar, 100 μm). 150

Supplementary Figure 6.2: Schematic of endothelial cell micropatterning on suspended DexMA fiber matrices. (A) Isometric and side views of fiber matrix substrate and cell patterning stamp. (B) (1) DexMA fibers are electrospun onto a fiber well substrate, crosslinked, and hydrated. (2) The cell patterning stamp is treated with Pluronic F127 solution to prevent cell adhesion, and a cell suspension is seeded onto the stamp. Cells are allowed to settle for 5 minutes. (3) Excess cells are gently flushed away with 4x PBS rinses. (4) The fiber well substrate is inverted onto the cell patterning stamp and aligned using the raised edges of the patterning stamp under a microscope. (5) The entire assembly is inverted to allow cells to settle onto the suspended DexMA matrices. (6) The patterning stamp is removed and transferred for culture and subsequent imaging. 151

Supplementary Figure 6.3: Endothelial cell protrusion analysis. For each frame of the 12 hour timelapse, protrusions were identified and the total number of protrusions as well as lifetime of each individual protrusion was manually determined for cells in (A) low, (B) intermediate, and (C) high stiffness matrices (scale bars, 50 μm). 152

Supplementary Figure 6.4: Bead displacement vector plots as a function of matrix stiffness. Representative endothelial cells (cell periphery denoted by white outline) and their respective bead displacements over 12-hours of culture displayed as vectors with magnitude coded by vector size and color in (A) low, (B) intermediate, and (C) high stiffness DexMA matrices (scale bars, 100 μm). 153

Supplementary Figure 6.5: Single endothelial cell morphology and force transmission as a function of fiber density. (A) Representative confocal fluorescent image of phalloidin-stained ECs (cyan), rhodamine-labeled DexMA fibers (magenta), and fiber-embedded fluorescent beads (white) (scale bar, 100 μm). (B) Temporally color-coded overlay of EC cell bodies over a 12 hour time course following initial patterning (scale bar, 100 μm). (C) Maximum displacement of each bead coded by vector length and color over the 12 hour time course (scale bar, 100 μm). (D) Binned average bead displacements color-coded by magnitude for all analyzed ECs with respect to their long axis (0°) (n > 20 cells/group). (E) Young's modulus of DexMA fiber matrices as a function of matrix density (n = 6). (F) Quantification of maximum bead displacement and (G) binned average bead displacements as a function of starting distance from the cell centroid for low, intermediate, and high fiber densities. All data presented as mean ± SD with superimposed data points; asterisk denotes significance with P < 0.05... 154

Supplementary Figure 6.6: Representative examples of interacting and non-interacting endothelial cell pairs in low stiffness, non-aligned fibrous matrices. (A) Representative confocal fluorescent images of phalloidin-stained ECs (cyan) and rhodamine-labeled fibers (magenta) with quantification of fiber alignment spanning cells and average migration speed of both ECs as a function of time. Red arrows indicate local regions of fiber alignment between neighboring cells (scale bars, 50 μm). (B) Representative confocal fluorescent images of non-interacting ECs. Red arrows indicate cell protrusions extending in the opposite direction of neighboring cell (scale bar, 50 μm). 155

Supplementary Figure 6.7: Spatiotemporal Ca^{2+} signaling analysis. Quantification of the minimum time between Ca^{2+} pulses as a function of intercellular distance within EC lines patterned in (A) low stiffness matrices, (B) high stiffness matrices, (C) low stiffness matrices treated with 10 μM PF228, (D) low stiffness matrices treatedd with 10 μM GSK205, and (E) low stiffness matrices treated with 5 μm GsMTx4. 156

Supplementary Figure 6.8: Cell force-mediated matrix deformations following treatment with FAK, TRPV4, and Piezo1 inhibitors. Representative maximum intensity projections of calcium-labeled ECs (green) and rhodamine-labeled fibers (magenta) 2 h after cell line patterning as a function of matrix stiffness and presence of inhibitors confirms that inhibition of FAK (PF228), TRPV4 (GSK205), or Piezo1 (GsMTx4) does not diminish cell force-mediated matrix reorganization (scale bars: 100 μm). 156

List of Movies

Supplementary Movie 3.1: EC network formation and matrix reorganization on Matrigel. Representative confocal fluorescence time-lapse movie of EC (cyan) network formation on Matrigel with embedded Fl-µS (white). Scale bar: 250 µm. 61

Supplementary Movie 3.2: EC monolayer formation on glutaraldehyde-crosslinked Matrigel with limited matrix reorganization. Representative confocal fluorescence time-lapse movie of ECs (cyan) on 0.1% glutaraldehyde crosslinked Matrigel with embedded Fl-µS (white). Scale bar: 250 µm. 61

Supplementary Movie 3.3: EC network formation and matrix reorganization on synthetic fibrous DexMA matrices. Representative confocal fluorescence 24-hour time-lapse movie of EC (cyan) network formation on soft (0.01 mg ml^{-1} LAP; 1.5 kPa) synthetic DexMA fiber matrices (magenta). Scale bar: 100 µm... 61

Supplementary Movie 3.4: Matrix recruitment and cell spreading during first four hours of network formation on DexMA matrices. Representative confocal fluorescence time-lapse movie of the first four hours of EC (cyan) network formation on soft (0.01 mg ml^{-1} LAP; 1.5 kPa) synthetic DexMA fiber matrices (magenta). Scale bar: 100 µm. 61

Supplementary Movie 3.5: EC monolayer formation on stiff fibrous DexMA matrices with negligible matrix reorganization. Representative confocal fluorescence 12-hour time-lapse movie of ECs (cyan) on stiff (0.1 mg ml^{-1} LAP; 16.7 kPa) synthetic DexMA fiber matrices (magenta). Scale bar: 100 µm. 61

Supplementary Movie 5.1: Crimping of DexVS fibrous matrices. Representative confocal fluorescence time-lapse movie of DexVS fibers (magenta) crimping upon addition of 2.0 mM HSP. Scale bar: 100 µm. 112

Supplementary Movie 5.2: EC migration on control DexVS fibrous matrices. Representative confocal fluorescence time-lapse movie of EC (cyan) migration on control (0.0 mM HSP) DexVS fibrous matrices (magenta). Scale bar: 200 µm. 112

Supplementary Movie 5.3: EC migration on crimped DexVS fibrous matrices. Representative confocal fluorescence time-lapse movie of EC (cyan) migration on crimped (2.0 mM HSP) DexVS fibrous matrices (magenta). Scale bar: 200 µm. 112

Supplementary Movie 6.1: EC bulk seeding in fibrous DexMA matrices. Representative confocal fluorescence 12-hour timelapse movie of lifeAct-GFP expressing ECs (cyan) and rhodamine-labeled DexMA fibers (magenta) seeded at 250 cells mm^{-2} in low stiffness, cell-deformable and high stiffness, non-deformable matrices (Scale bar: 100 µm). 156

Supplementary Movie 6.2: Single cell patterning in fibrous DexMA matrices with variable matrix stiffness. Representative confocal fluorescence 12-hour timelapse movie of a single lifeAct-GFP expressing EC (cyan), rhodamine-labeled DexMA fibers (magenta), and embedded fluorescent beads (white) patterned in low stiffness, cell-deformable and high stiffness, non-deformable matrices (Scale bar: 100 µm). 156

Supplementary Movie 6.3: Single cell patterning in synthetic fibrous DexMA matrices with variable matrix density. Representative confocal fluorescence 12-hour timelapse movie of a single lifeAct-GFP expressing EC (cyan), rhodamine-labeled DexMA fibers (magenta), and embedded fluorescent beads (white) patterned in low and high density matrices with crosslinking equivalent to the lowest stiffness condition (Scale bar: 100 μm). 157

Supplementary Movie 6.4: Cell pair patterning in non-aligned fibrous DexMA matrices with variable matrix stiffness. Representative confocal fluorescence 12-hour timelapse movie of pairs of lifeAct-GFP expressing ECs (cyan) and rhodamine-labeled DexMA fibers (magenta) patterned in low stiffness, cell-deformable and high stiffness, non-deformable non-aligned matrices (Scale bar: 200 μm). 157

Supplementary Movie 6.5: Cell pair patterning in aligned fibrous DexMA matrices with variable matrix stiffness. Representative confocal fluorescence 12-hour timelapse movie of pairs of lifeAct-GFP expressing ECs (cyan) and rhodamine-labeled DexMA fibers (magenta) patterned in low stiffness, cell-deformable and high stiffness, non-deformable aligned matrices (Scale bar: 200 μm)... 157

Supplementary Movie 6.6: Calcium transients of ECs in fibrous DexMA matrices with variable matrix stiffness. Representative confocal fluorescence 10-minute timelapse movie of calcium signaling (green) in ECs patterned into multicellular lines in low stiffness, cell-deformable and high stiffness, non-deformable matrices (Scale bar: 100 μm). 157

Supplementary Movie 6.7: Calcium transients of ECs in fibrous DexMA matrices in the presence of FAK, TRPV4, and Piezo1 inhibitors. Representative confocal fluorescence 10-minute timelapse movie of calcium signaling (green) in ECs patterned into multicellular lines in low stiffness, cell-deformable matrices with inhibition of FAK (PF228, 10 μM), TRPV4 (GSK205, 10 μM), and Piezo1 (GsMTx4, 5 μM) (Scale bar: 100 μm). 157

Supplementary Movie 6.8: Three-dimensional image stack of EC networks in fibrin hydrogels with variable matrix density, FAK inhibition, and TRPV4 inhibition. Representative confocal fluorescence image stacks (100 μm thick) of phalloidin-stained ECs (cyan) and nuclei (yellow) in 2.5 mg mL^{-1} fibrin, 5.0 mg mL^{-1} fibrin, and 2.5 mg mL^{-1} fibrin with inhibition of FAK (PF228, 10 μM) or TRPV4 (GSK205, 10 μM) (Scale bar: 100 μm). 157

Abstract

The ability of cells to communicate and coordinate their activity is crucial to the development and homeostatic function of all tissues. In addition to the well-established means of biochemically mediated signaling, a more recent body of evidence has indicated that cells can also communicate via cell-generated forces transmitted to neighboring cells through the extracellular matrix (ECM). One setting in which a deeper understanding of mechanical intercellular communication (MIC) would be extremely valuable is in vasculogenesis, or the *de novo* formation of a microvascular network. This dynamic process involves the assembly and organization of individual endothelial progenitor cells into an interconnected network of capillaries, thus requiring cellular communication and coordination over large spatial scales. If fully understood and harnessed, vasculogenic assembly presents a promising approach to vascularizing engineered tissue constructs for regenerative medicine applications. We hypothesize physical properties of the ECM are critical to MIC as the matrix context defines not only the generation of cell forces but also force transmission through the matrix to nearby cells. Thus, the focus of this dissertation is to study cell force propagation and MIC between endothelial cells (ECs) in controllable synthetic ECMs towards the informed design of biomaterials that drive rapid self-assembly of functional microvascular networks.

First, this thesis explores how physical attributes of the ECM regulate the assembly of ECs into interconnected multicellular networks. To mimic the fibrous microenvironments where

neovascularization typically occurs in the body, we developed a novel model of the EC network formation assay utilizing 2.5D matrices of electrospun synthetic dextran methacrylate (DexMA) polymeric fibers. Our results revealed that active cell-mediated matrix deformations and fiber recruitment through actomyosin force generation occurs concurrently with the formation and stabilization of multicellular EC networks.

Next, this thesis describes the development and characterization of a new material system composed of electrospun dextran vinyl sulfone (DexVS) polymeric fibers that possess longer-term mechanical stability in culture as compared to DexMA matrices. These matrices were utilized for two major objectives: 1) investigating the role of matrix mechanics on the activation of fibroblasts into myofibroblasts, a key component of wound healing and the fibrotic progression, and 2) exploring the impact of nonlinear matrix mechanical properties on vasculogenic assembly by imbuing fibers with crimped microstructure.

Lastly, this thesis describes the mechanism of MIC between individual ECs during vasculogenic assembly. By combining electrospun DexMA fiber matrices with a microfabrication-based cell-patterning method, we investigated EC force-mediated matrix displacements and MIC as a function of matrix stiffness and identified the critical cellular machinery required for ECs to sense and respond to mechanical signals emanating from neighboring cells. We then sought to harness these observations in more translatable 3D hydrogel constructs by using a composite approach where fibrin hydrogels were reinforced with electrospun DexVS fiber segments. While traditional approaches to prevascularize 3D hydrogels require long-term cocultures of ECs and support stromal cells, our work demonstrated that mechanical cues from synthetic fibers enable ECs alone to rapidly self-assemble into networks of lumenized capillary-like structures.

Overall, the work presented in this dissertation integrates biomaterials, tissue engineering, and microfabrication approaches to investigate the mechanobiology of how cell forces regulate intercellular communication during vasculogenic assembly. The results presented here are critical to the design of biomaterials that promote robust capillary network assembly for applications in tissue engineering and regenerative medicine.

Chapter 1: Introduction

The overarching goal of this thesis is to design and utilize synthetic fibrous matrices towards investigating the role of mechanical signaling during the self-assembly of multicellular structures. To do so, the following work employs a variety of natural and synthetic fibrous biomaterial platforms with tunable biophysical properties, combines cell and matrix labelling techniques with live confocal microscopy to dynamically assess cell force-mediated matrix deformations over time, and identifies critical matrix properties that mediate mechanical intercellular communication (MIC) and the self-assembly of functional engineered microvascular networks.

Chapter 2 provides broad background information on the extracellular matrix (ECM) and biomaterial approaches to study mechanical interactions between cells and their microenvironment. Additionally, this chapter details how cell-generated forces are propagated through the ECM and evidence for these forces acting as mechanical signals during MIC to guide the behavior of neighboring cells. Lastly, Chapter 2 outlines the current state of vascular tissue engineering approaches, specifically bottom-up techniques that rely on cellular self-assembly of microvascular networks. To advance our knowledge, the remaining chapters focus on utilizing synthetic fibrous matrices to study MIC and engineer prevascularized tissue constructs.

Chapter 3 utilizes both natural and synthetic fibrous materials to better understand how physical attributes of the ECM influence the assembly of EC networks in 2D and 2.5D fibrous materials. This work revealed that active cell-mediated matrix recruitment through actomyosin force generation occurs concurrently with network formation on Matrigel, a reconstituted basement membrane matrix regularly used to promote endothelial cell (EC) networks, and on synthetic matrices composed of electrospun dextran methacrylate (DexMA) fibers. Furthermore, modulating physical attributes of fibrous matrices that impair matrix recruitment consequently inhibited the formation of cellular networks. Overall, this chapter suggests an iterative process in which dynamic cell-induced changes to the physical microenvironment reciprocally modulate cell behavior to guide the formation and stabilization of multicellular vessel-like networks.

Chapter 4 shifts in focus onto the development and characterization of a new material system composed of electrospun dextran vinyl sulfone (DexVS) polymeric fibers that have enhanced stability in mechanical properties over longer culture times compared to the DexMA matrices utilized in Chapter 3. These DexVS fibrous matrices exhibit mechanical tunability at both the single fiber and bulk matrix level as well as user-defined cell adhesion by functionalization with thiolated adhesive peptides or methacrylated heparin to sequester cell-derived ECM proteins. This work utilized DexVS fibrous matrices to investigate the role of matrix mechanics on the activation of fibroblasts into myofibroblasts, a key step of the fibrotic progression. In contrast to previous findings with non-fibrous hydrogel substrates, fibroblasts in soft and deformable matrices exhibited increased spreading, focal adhesion formation, proliferation, and myofibroblast activation as compared to cells on stiffer matrices with equivalent starting architecture.

Chapter 5 focuses on the development of a new and simple method for modifying electrospun DexVS matrices to have control over nonlinear mechanical properties by imbuing crimped microstructure. This work utilized a hydrophilic peptide that could be functionalized to DexVS matrices to trigger swelling of individual hydrogel fibers, resulting in orthogonal control over nonlinear stress-strain responses and matrix stiffness. This work also examined ECM mechanosensing of ECs, finding that fiber crimp promoted enhanced physical matrix remodeling, increased migration speed, and evidence for long-range interactions between neighboring ECs. Additionally, ECs seeded in crimped matrices rapidly assembled into capillary-like networks containing tube-like structures. Overall, this work provides an additional level of mechanical and architectural tunability to synthetic fibrous matrices and implicates a critical role for mechanical nonlinearity in EC mechanosensing and network formation.

Chapter 6 focuses on MIC between ECs, specifically investigating how tissue-relevant matrix properties mediate the transmission of cell-generated forces as well as the cellular machinery required for ECs to sense and respond to mechanical signals. This work utilized electrospun DexMA fibrous matrices in conjunction with a microfabrication-based cell patterning approach to examine MIC between individual ECs. This work identified that cell-force mediated matrix displacements in deformable fibrous matrices underly directional migration of neighboring ECs towards each other prior to the formation of stable cell-cell connections. Additionally, these interactions were mediated by intracellular calcium signaling that was correlated with focal adhesion kinase (FAK) and transient receptor potential vanilloid 4 (TRPV4). Lastly, this work extended these observations to 3D fibrous settings by examining MIC during vascular network assembly in fibrin hydrogels.

Chapter 7 focuses on utilizing a composite approach in which fibrin hydrogels are reinforced with electrospun DexVS fiber segments to enhance MIC in 3D. While traditional approaches to prevascularize 3D hydrogels require long-term cocultures of ECs and support stromal cells, this work demonstrates that mechanical cues from non-adhesive synthetic fibers enable ECs alone to rapidly self-assemble into networks of lumenized capillary-like structures. Furthermore, RNA-sequencing and analysis of 3D cell force-mediated matrix displacements identified that fiber-reinforcement of fibrin hydrogels promote cell-ECM interactions and provide local mechanical cues that enable EC communication and assembly. Overall, this work posits that electrospun fibers can be an inexpensive alternative to sourcing and expanding a secondary supporting cell type alongside patient-specific ECs.

Finally, Chapter 8 provides a summary of the major findings from this thesis work and future directions towards investigating MIC and vasculogenic assembly. Recent advances in molecular sensors and synthetic biomaterials as well as *in vivo* analysis will improve our understanding of the mechanisms behind MIC and our ability to engineer prevascularized tissue constructs for regenerative medicine applications.

Chapter 2: Background

2.1 Mechanotransduction and the ECM

2.1.1 ECM structure and composition

The extracellular matrix (ECM) is broadly defined as the non-cellular components in all tissues and organs (Frantz et al., 2010). While one major role of the ECM is to provide the physical scaffolding for cellular components, it also imbues crucial biochemical and biophysical cues that are required for tissue morphogenesis, vascularization, and wound repair processes. There are two major classes of macromolecules that make up the ECM: 1) fibrous proteins (e.g., collagens, elastins, fibronectins, and laminins) and 2) proteoglycans which fill the majority if the interstitial space within a tissue (Järveläinen et al., 2009; Schaefer, 2010). Collagen is the most abundant fibrous protein and constitutes the main structural element of the ECM, providing tensile strength and regulating cell adhesion and migration (Rozario & DeSimone, 2010). The majority of collagen molecules form a triple-stranded helix that can assemble into supramolecular complexes, such as the micron-scale collagen fibril bundles found within interstitial tissue stroma. Proteoglycans are composed of glycosaminoglycan chains covalently linked to a specific protein core and are extremely hydrophilic, contributing to the hydration of extracellular interstitial space (Järveläinen et al., 2009).

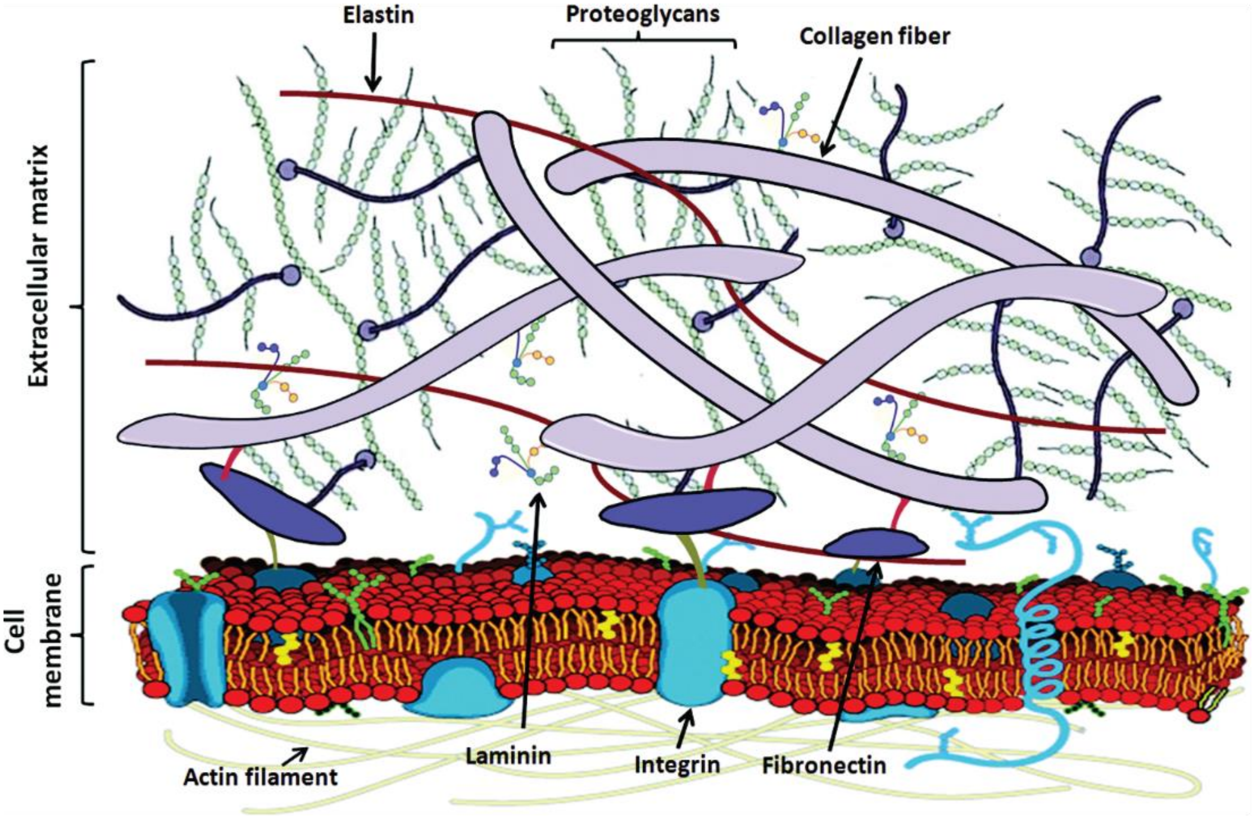
Elastin
Proteoglycans
Collagen fiber
Extracellular matrix
Cell membrane
Actin filament
Laminin
Integrin
Fibronectin

Figure 2.1: The ECM is the non-cellular component present in all tissues and organs, providing physical scaffolding and crucial biochemical and biomechanical cues that guide cell behavior. Image reproduced from (Xue & Jackson, 2015).

2.1.2 Mechanosensing at focal adhesions

The organization and composition of ECM components varies considerably across organ and tissue systems and changes drastically during disease progression, indicating that cells must sense physical aspects of their environment and respond appropriately over time for proper cell function. Indeed, mechanical interactions between cells and their surrounding ECM have been shown to be critical in many single- and multi-cellular processes including cell spreading (Vogel & Sheetz, 2006), cell migration (Charras & Sahai, 2014), and tissue morphogenesis (Lutolf & Hubbell, 2005). While there are many mechanisms by which cells can sense external forces and matrix geometry, one of the most studied mechanisms is sensing through focal adhesions (FAs), the physical link between a cell and its surrounding ECM (Bershadsky et al., 2003; Geiger et al., 2009; Oakes & Gardel, 2014; Parsons et al., 2010). Cells sense matrix rigidity and mechanics by exerting traction forces at FAs. These physical cues are then converted to biochemical signals inside of the cell leading to changes in cytoskeletal reorganization and transcription that regulate basic cell behavior, a process termed mechanotransduction. This information also feeds back to the FA and regulates the amount of traction force that the cell exerts on the ECM (Jansen et al., 2017; Schoen et al., 2013; Vogel & Sheetz, 2006). Mechanotransduction, however, is difficult to study *in vivo* due to the lack of control over ECM properties, leading many to turn towards *in vitro* biomimetic platforms to investigate the role of individual ECM properties on cell behavior (Li et al., 2017).

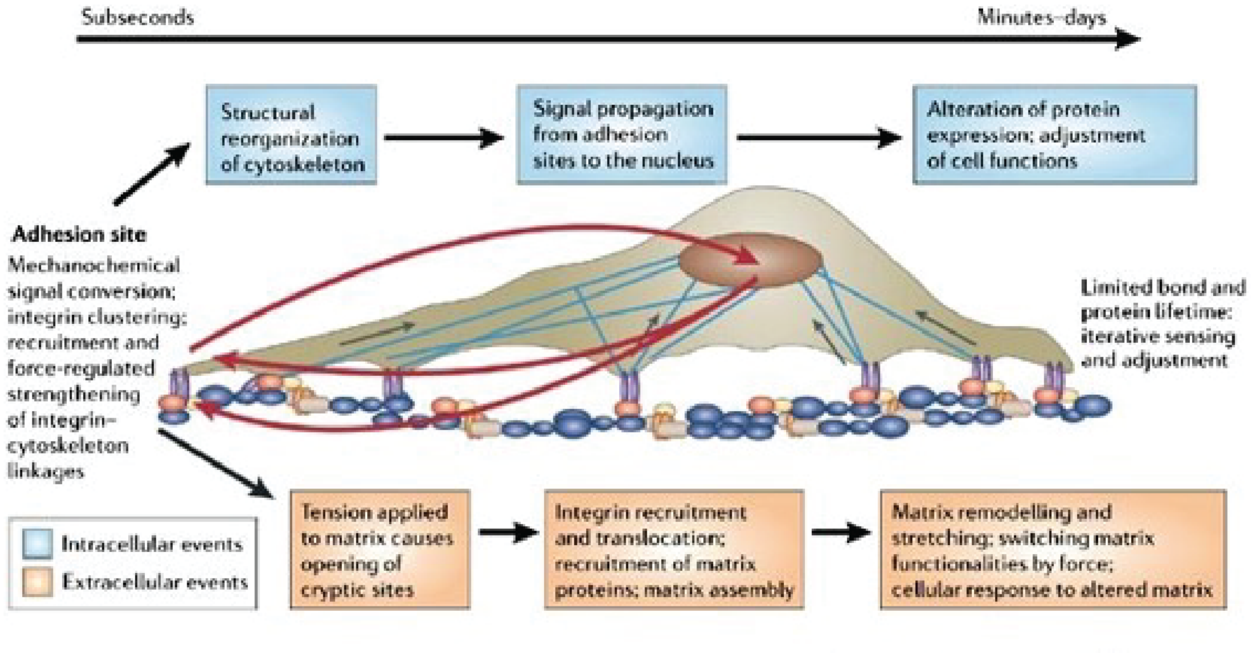
Subseconds
Minutes–days
Structural reorganization of cytoskeleton
Signal propagation from adhesion sites to the nucleus
Alteration of protein expression; adjustment of cell functions
Adhesion site
Mechanochemical signal conversion; integrin clustering; recruitment and force-regulated strengthening of integrin–cytoskeleton linkages
Limited bond and protein lifetime: iterative sensing and adjustment
Tension applied to matrix causes opening of cryptic sites
Integrin recruitment and translocation; recruitment of matrix proteins; matrix assembly
Matrix remodelling and stretching; switching matrix functionalities by force; cellular response to altered matrix
Intracellular events
Extracellular events

Copyright © 2006 Nature Publishing Group
Nature Reviews | Molecular Cell Biology

Figure 2.2: Cells sense the mechanical features of their environment at focal adhesions where biophysical cues are transduced to intracellular signals that alter cell behavior. Image reproduced from (Vogel & Sheetz, 2006).

2.1.3 Biomaterial platforms to model the ECM

The first class of materials employed to study the role of ECM structure in cell behavior were hydrogels based on isolated matrix components such as collagen I, fibrin, or basement membrane (e.g., Matrigel). These natural polymers are suitable for biomedical applications as they are biocompatible, biodegradable, and contain biologically recognizable moieties. Furthermore, they bear structural resemblance to the fiber-rich network of certain native ECM (Levental et al., 2009; Liu et al., 2012). However, these reconstituted gels typically form via noncovalent interactions resulting in poor mechanical properties and nanometer-scale diameter fibrils, whereas *in vivo* interstitia contain assemblies of fibers with micrometer-scale diameters and lengths spanning multiple cell bodies (Wolf et al., 2009). Additionally, gel mechanical properties, fibrous structural features, and biological ligands are typically intertwined, making it difficult to isolate the specific contribution of biophysical vs. biochemical cues on cell behavior (Ghajar et al., 2008; Li et al., 2017).

These limitations have inspired the development of synthetic ECM mimetics that provide controllable and modular design. Specifically, synthetic hydrogels can provide orthogonal control over crosslinking density (bulk stiffness), ligand type and density (cell adhesivity), and crosslinker susceptibility to cleavage (matrix degradability). For example, one common synthetic material used for studies isolating ECM stiffness and adhesion ligand is polyacrylamide (PAA) (Dembo & Wang, 1999; Denisin & Pruitt, 2016; Engler et al., 2006). Due to having limited interactions with proteins, PAA hydrogels can be modified with full-length ECM proteins (e.g., collagen I, fibronectin) or cell-adhesive peptides, thus isolating adhesivity from bulk stiffness. However, PAA hydrogels are only suitable for 2D culture as the catalysts used for polymerization are cytotoxic. One alternative to PAA for 3D culture is poly(ethylene glycol)

(PEG) as it is similarly inert and tunable while able to be polymerized using cytocompatible conditions (Lutolf et al., 2003). Furthermore, PEG-based hydrogels can be crosslinked using matrix metalloproteinase (MMP)-degradable crosslinkers to support cell-mediated degradation of the bulk material. Similar approaches have been taken with polysaccharide-based polymers such as dextran, hyaluronan, gelatin, and alginate, as they provide a high number of active sites for chemical modification resulting in enhanced flexibility in tuning biochemical and biophysical properties (Liang et al., 2017; Matera et al., 2020; Rosales & Anseth, 2016). Furthermore, recent advances in crosslinking strategies have engineered techniques to control the viscoelasticity of hydrogels by introducing non-covalent crosslinks that undergo stress relaxation (Chaudhuri et al., 2015, 2016; Loebel et al., 2019). Despite the multiple levels of control, however, these materials are non-fibrous and mechanically homogeneous, thus failing to mimic the complex physical properties of the *in vivo* cellular microenvironment.

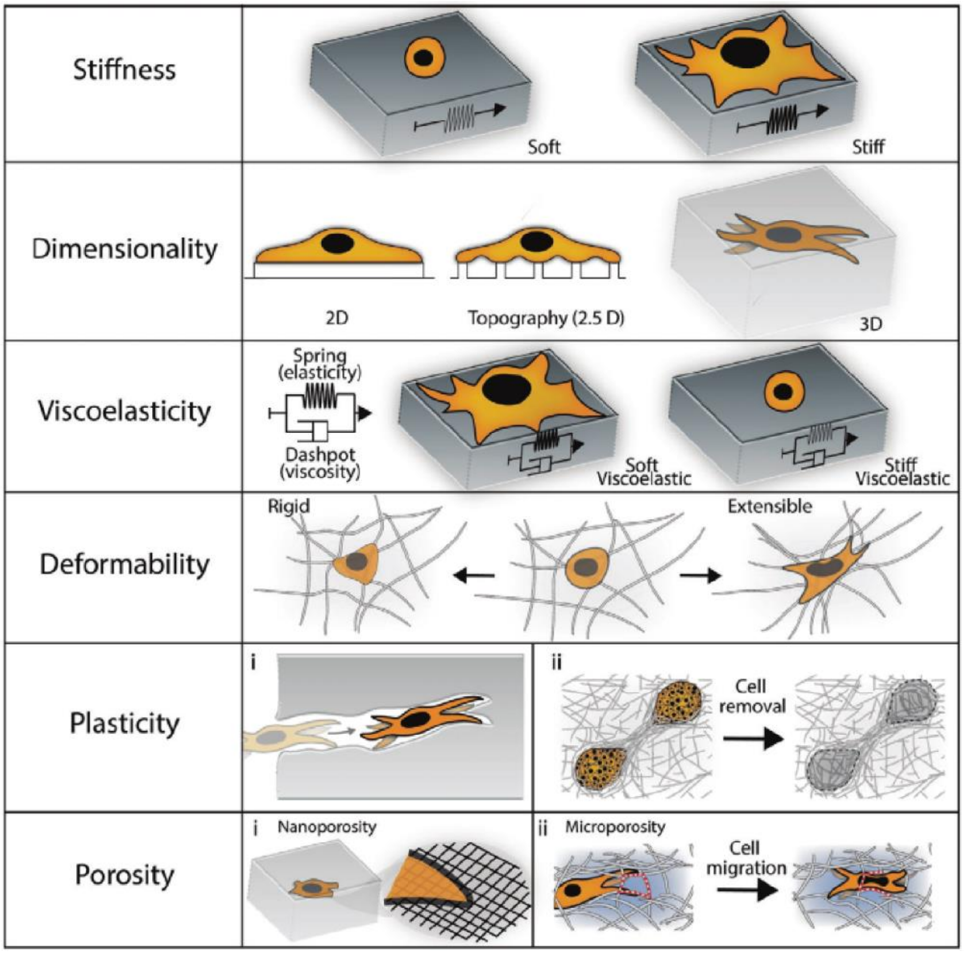
Stiffness
Soft
Stiff
Dimensionality
2D
Topography (2.5 D)
3D
Viscoelasticity
Spring (elasticity)
Dashpot (viscosity)
Soft Viscoelastic
Stiff Viscoelastic
Deformability
Rigid
Extensible
Plasticity
i
ii
Cell removal
Porosity
i Nanoporosity
ii Microporosity
Cell migration

Figure 2.3: Biomaterial platforms can incorporate a variety of important structural and mechanical features of the ECM. Image reproduced from (Davidson et al., 2020d).

2.1.4 Electrospun fibrous matrices

One fabrication technique that has been extensively used to fabricate biomaterials with fibrous microstructure is electrospinning (Mauck et al., 2009). The basic electrospinning setup consists of a polymer solution, a high voltage power supply, and a grounded collecting surface. Briefly, the high voltage source is utilized to charge a polymer solution that is slowly being expelled by a syringe. This causes charge buildup and repulsion amongst the polymer chains within the droplet until these intermolecular forces overcome the surface tension holding the droplet in place. Once this threshold is reached, a fiber jet is ejected and expelled towards the grounded collecting surface. Simultaneous to this process, solvent evaporation result in ultra-fine fibers that accumulate on the surface to develop a fibrous mesh (Reneker & Chun, 1996).

Electrospinning affords high levels of control over architectural features of the fiber matrix by modulating different electrospinning parameters (Baker et al., 2015). For example, mesh density and thickness can be controlled by simply increasing the time of deposition. Additionally, structural anisotropy can be imbued to the fiber mesh via methods to induce fiber alignment. One such method is to spin onto a collecting surface of oppositely charged parallel electrodes with varying separation distance to create an electric field that aligns fibers as they fall to the surface (Wang et al., 2019). Recently, approaches to electrospin hydrogel fibers with tunable mechanics have also been developed. Specifically, much of the work in this thesis is built upon work from Baker et al. that established a technique to electrospin methacrylated dextran (DexMA), a protein-resistant polymer that can be functionalized with cell-adhesive moieties and photocrosslinked after spinning to independently modulate ligand presentation and matrix stiffness (Baker et al., 2015).

2.1.5 ECM control over traction force and matrix displacements

Mechanical forces generated by cells during mechanosensing, and their resultant matrix deformations are greatly influenced by the mechanical properties of the surrounding ECM. These metrics can be quantified experimentally via cellular traction force microscopy (TFM) methods that involve tracking ECM deformations that result from cell-generated forces (Polacheck & Chen, 2016). Briefly, small fluorescent beads are mixed into hydrogel substrates that serve as fiducial markers that can be tracked in space and time with microscopy (Dembo et al., 1996; Legant et al., 2013). Cells are plated on the hydrogel and allowed to spread; the distribution of beads in this stressed state is imaged, cells are then lysed, and beads are imaged again to determine their position in the unstressed state. Computational algorithms can then be utilized to analyze the two images and quantify matrix displacements and the forces required to cause such displacements. Cellular tractions are very small (in the range of piconewtons to micronewtons) thus leading to low levels of deformations on simple elastic materials (such as PAA and PEG) as strain field magnitude decays rapidly from the point of force. For example, ECs cultured on low stiffness PAA gels (500 Pa) generate deformations of only a few microns in magnitude and are only measurable up to approximately 50 µm from the cell (Reinhart-King et al., 2003, 2008).

In contract, force transmission in biological materials is greatly affected by the presence of fibrous networks with a large mesh size and relatively rigid filaments. Specifically, the presence of matrix fibers leads to complex mechanical behavior, namely non-affine deformations, realignment in the stress direction, and resulting strain-stiffening, all of which can enhance the transmission of cell-generated forces (Ma et al., 2013; Ronceray et al., 2016; Wang et al., 2015). For example, fibroblasts cultured on low density collagen hydrogels generate deformations that are measurable up to 1500 µm from the cell (Pakshir et al., 2019). This long-range force transmission has been hypothesized to play an important role in tissue development, normal tissue function, as well as disease progression, but continued understanding of how these forces guide cell behavior is necessary.

2.2 Mechanical Intercellular Communication

2.2.1 Modes of intercellular communication

The ability of cells to communicate and coordinate their activity is crucial to the development and homeostatic function of all tissues (Yang et al., 2021). Despite its importance, however, the precise mechanisms in which cells send and receive signals through biochemical or mechanical stimuli are not completely understood. Intercellular communication can be broadly segregated by direct and indirect forms of signaling (Yang et al., 2021). Direct communication occurs either via exchange of biochemicals or transmission of mechanical stresses through cell-cell contacts. Intercellular communication over larger spatial scales, however, occur via indirect communication, generally mediated through secreted molecules that move by flow or diffusion (Dupont et al., 2018; Grecco et al., 2011; Nguyen et al., 2017; Van Niel et al., 2018). These secreted molecules are either hydrophobic molecules that passively diffuse across the plasma membrane or hydrophilic molecules that are recognized by membrane surface receptors of target cells, ultimately leading to the activation of intracellular signaling pathways that define the cell response. Indirect biochemical signaling can vary in range, with paracrine signaling only affecting neighboring cells near to the signaling cell, and autocrine signaling mediated by endocrine cells that can distribute signaling molecules (i.e., hormones) throughout the body via the circulation system.

In addition to these well-established means of biochemically mediated intercellular signaling, a more recent body of evidence has shown that cells can also communicate via cell-generated forces transmitted to neighboring cells through the ECM (Alisafaei et al., 2021; Sapir & Tzlil, 2017). This type of mechanical intercellular communication (MIC) is unique from biochemical signaling as it is long ranged, possesses strong directionality, and is greatly dependent on the mechanical properties of the ECM spanning the interacting cells. Indeed, these distinctive properties have led many to hypothesize a potential role for MIC during development and tissue morphogenesis as these processes are defined by precise collective motion and spatial coordination of cell orientation (Rozario & DeSimone, 2010). However, the dynamic and reciprocal nature of cells generating and sensing mechanical signals makes MIC difficult to investigate. Additionally, isolating the specific role of mechanical signals from other modes of communication (e.g., chemical, electrical, direct communication) is challenging.

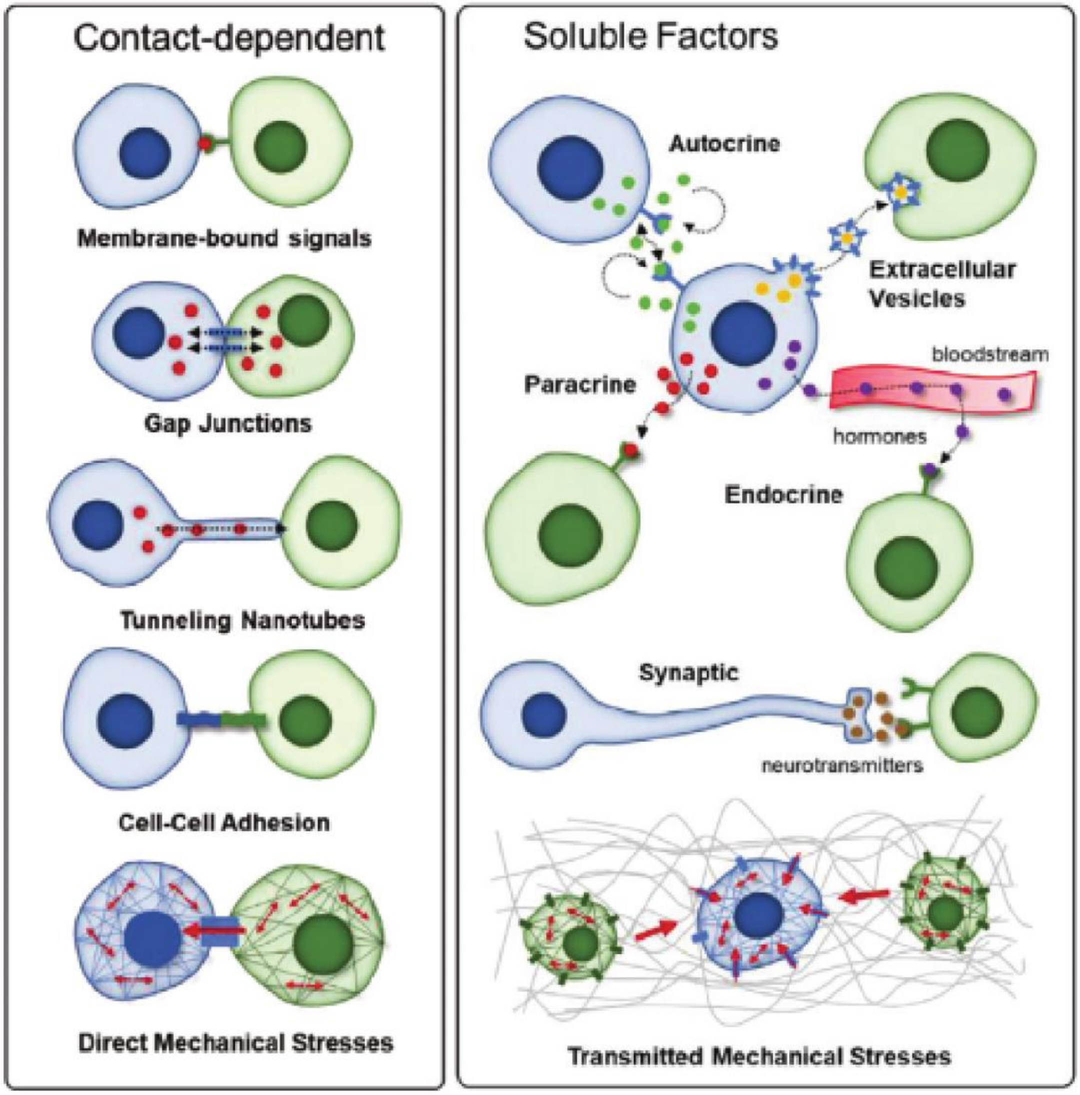
Contact-dependent
Membrane-bound signals
Gap Junctions
Tunneling Nanotubes
Cell-Cell Adhesion
Direct Mechanical Stresses
Soluble Factors
Autocrine
Extracellular Vesicles
Paracrine
bloodstream
hormones
Endocrine
Synaptic
neurotransmitters
Transmitted Mechanical Stresses

Figure 2.4: Cells within 3D tissues communicate through direct or indirect approaches that are mediated by both biochemical and biophysical signals. Image reproduced from (Yang et al., 2021).

2.2.2 Examples of mechanical intercellular communication

Several prior studies suggest that cell force-generated deformations of the ECM mediate communication between neighboring cells to regulate critical cell functions in cell migration and multicellular assembly. MIC has been observed in a variety of settings spanning different cell types, distinct ECM settings, and across scales ranging from tissues (Sawhney & Howard, 2002; Stopak & Harris, 1982), to multicellular clusters (Guo et al., 2012; Shi et al., 2014), to single cells (Natan et al., 2020; Nitsan et al., 2016; Pakshir et al., 2019; Reinhart-King et al., 2008; Winer et al., 2009). One of the first observed instances of MIC was nearly four decades ago, where Stopak and Harris observed that cultured contractile tissue explants embedded within collagen matrices physically reorganized and aligned collagen fibrils, generating tensile regions that directed cell migration between adjacent explants over millimeter length scales (Stopak & Harris, 1982). Similarly, recent studies with mammary epithelial cells cultured in collagen matrices provide evidence that matrix-borne tension can disrupt normal acinar architecture, promote epithelial-mesenchymal transition, and trigger cell escape in the context of metastasis (Shi et al., 2014).

At the single cell level, Reinhart-King et al. showed evidence that endothelial cell (EC) traction forces create local gradients of tension when cultured on low stiffness PAA hydrogels (500 Pa) that influence migration and cell-cell contact between neighboring cells (Reinhart-King et al., 2008). Additionally, more recent work from Pakshir et al. identified evidence for MIC between macrophages and contractile myofibroblasts, a heterotypic cellular interaction that bears significance in pathological healing and fibrosis (Pakshir et al., 2019). When co-cultured on low density collagen matrices (2 mg mL^{-1}), macrophages persistently migrated towards contractile signaling myofibroblasts. Additionally, this work was also able to demonstrate that the strain field generated by the contractile myofibroblast could be replaced with a microneedle to apply a similar magnitude of force and maintain macrophage response, indicating that mechanical signaling is occurring independent of biochemical signals. Beyond regulating cell migration, MIC has also been shown to influence synchronized beating of cardiomyocytes. Work from Nitsan et al. utilized a “mechanical cell” consisting of an oscillatory mechanical probe that mimics the deformations generated by a beating cardiomyocyte on a polyacrylamide hydrogel (Nitsan et al., 2016). Interestingly, cardiomyocytes cultured within 130 microns from the mechanical cell were trained to beat at the same frequency as the mechanical stimulus. This response was maintained for an hour after the stimulation was stopped, implying long-term adaptations within the cell. Furthermore, MIC likely underlies collective motion and spatial coordination of cell orientation during multicellular organization and, if properly harnessed *in vitro*, could be of importance when engineering tissue constructs for regenerative medicine applications.

2.3 Engineering Microvascular Networks

2.3.1 Vascular tissue engineering

The fields of tissue engineering and regenerative medicine are driven by the long-term goal of developing biological constructs that restore, maintain, or improve the function of a tissue or organ (Griffith & Naughton, 2002; Langer & Vacanti, 1993; Vacanti & Langer, 1999). While the past few decades have reported success in relatively thin non-vascularized tissues such as skin or cartilage (Chua et al., 2016; Makris et al., 2015), large and complex tissues require an adequate blood supply throughout the construct (Auger et al., 2013; Griffith et al., 2005; Koike et al., 2004). The rate of host vessel invasion of traditional biomaterials upon transplantation is typically limited to several tenths of a micron per day, leading to necrosis at the center of the construct after implantation (Clark & Clark, 1939; Laschke et al., 2009; Rouwkema et al., 2008). Thus, an engineered graft thicker than the diffusion limit of gases and nutrients (about 150-200 µm) requires a pre-formed vascular network. Additionally, ischemic diseases remain one of the leading causes of mortality and morbidity across the world and present an additional need for prevascularized constructs (Hausenloy & Yellon, 2013). As dense microcapillary networks can supply the demanding oxygen needs of many tissues due to their large surface area, engineered microvascular networks presents the most promising potential to solving this prevascularization problem.

2.3.2 Fabrication approaches for engineered microvasculature

Previous strategies to vascularize 3D engineered biomaterials can generally be categorized as top-down or bottom-up. In top-down approaches, engineered vascular templates are pre-designed and fabricated before cells are introduced and include techniques such as 3D printing bioinks or sacrificial materials (Miller et al., 2012; Norotte et al., 2009; Skardal et al., 2010), laser-mediated ablation (Brown et al., 2017b; Heintz et al., 2016), or layer-by-layer assembly (Morgan et al., 2013; Zhang et al., 2016). For example, the use of sacrificial 3D printing to fabricate perfusable vascular networks was first demonstrated by Miller et al (Miller et al., 2012). In this work, rigid 3D filament networks of carbohydrate glass were printed as a sacrificial template within a hydrogel to generate cylindrical networks that were lined with ECs. More recently, Grigoryan et al. utilized stereolithography, an approach employed to efficiently convert photoactive liquid resins into structured components through localized photopolymerization, to enhance the production speed of 3D hydrogels containing intricate and functional vascular architectures compared to extrusion printing of sacrificial structures (Grigoryan et al., 2019). In these approaches, ECs can be seeded within fabricated hollow spaces where they eventually spread and form a monolayer along the walls of the channel.

Despite exquisite control over network geometry and architecture of top-down approaches, these methods fail to achieve the 5-20 µm diameter of microcapillaries. In contrast, bottom-up methods seek to harness the innate biological mechanisms that drive vessel formation during development and wound healing. In the body, neovascularization occurs via two distinct methods: angiogenesis, the extension of new vessels from a preexisting vessel, or vasculogenesis, the *de novo* formation of new vessels by self-assembly of individual ECs and/or endothelial progenitor cells (Vailhé et al., 2001). Angiogenesis is a multistep process that involves gradients of chemokines that promote tip cell formation, collective migration of multicellular sprouts through the ECM, and subsequent maturation of lumenized microvessels (Potente et al., 2011). One simple approach towards recapitulating angiogenic sprouting *in vitro* is an EC outgrowth assay from microcarrier beads or cell spheroids embedded within 3D hydrogels (Ghajar et al., 2008)g. Additionally, more advanced models have taken advantage of advances in microfluidics to develop tissue-on-a-chip platforms that recapitulate 3D EC sprouting morphogenesis from a stable endothelium of an engineered parent vessel (Nguyen et al., 2013; Trappmann et al., 2017; Wang et al., 2020, 2021a, 2021b).

2.3.3 In vitro vasculogenic assembly

Alternatively, vasculogenesis does not rely on the presence of a parent vessel and can also be recapitulated *in vitro*. Compared to angiogenesis-driven approaches, vasculogenic assembly has increased scalability due to the concurrent formation of vessel-like structures throughout the biomaterial construct as opposed to progressive vascularization via sprouting (Song et al., 2018).

Due to the numerous challenges studying vasculogenesis *in vivo*, *in vitro* network formation assays have greatly facilitated our understanding of the biological regulation of this complex process. The earliest work studying EC network formation consisted of ECs plated on Matrigel, a reconstituted gel containing basement membrane matrix proteins (Kubota, Y., Kleinman, H. K., Marin, G. R., and Lawley, 1988). In this setting, ECs rapidly attach, extend, and form networks of multicellular capillary-like tubules within 24 hours. These studies have been critical in determining vital growth factors, genes, and signaling pathways involved with the self-assembly of EC networks, but the 2D nature of this work yields an incomplete understanding. Thus, many have since developed 3D vasculogenic models in a variety of natural and synthetic ECM settings, such as fibrin, collagen, and PEG, in which ECs associate with neighboring cells to form an interconnected network (Beamish et al., 2019; Chen et al., 2012; Freiman et al., 2016; Koh et al., 2008; Lesman et al., 2011; Rao et al., 2012; Zanotelli et al., 2016). In these 3D settings, the addition of a support stromal cell, such as dermal fibroblasts, mesenchymal stem cells, or pericytes function to guide and stabilize vessel-like networks. The exact mechanism by which stromal cells support vasculogenic assembly is not well understood, but previous work has revealed pivotal importance in secretion of proangiogenic growth factors (DiPietro, 2016; Xiao et al., 2019) and ECM remodeling (i.e., matrix degradation and secretion) (Newman et al., 2011). Interestingly, recent work from Song et al. identified that the presence of stromal cells is only necessary during the first few days of EC morphogenesis, after which they can be ablated without significantly affecting the structural features and functionality of the developed vessel-like networks (Song et al., 2020).

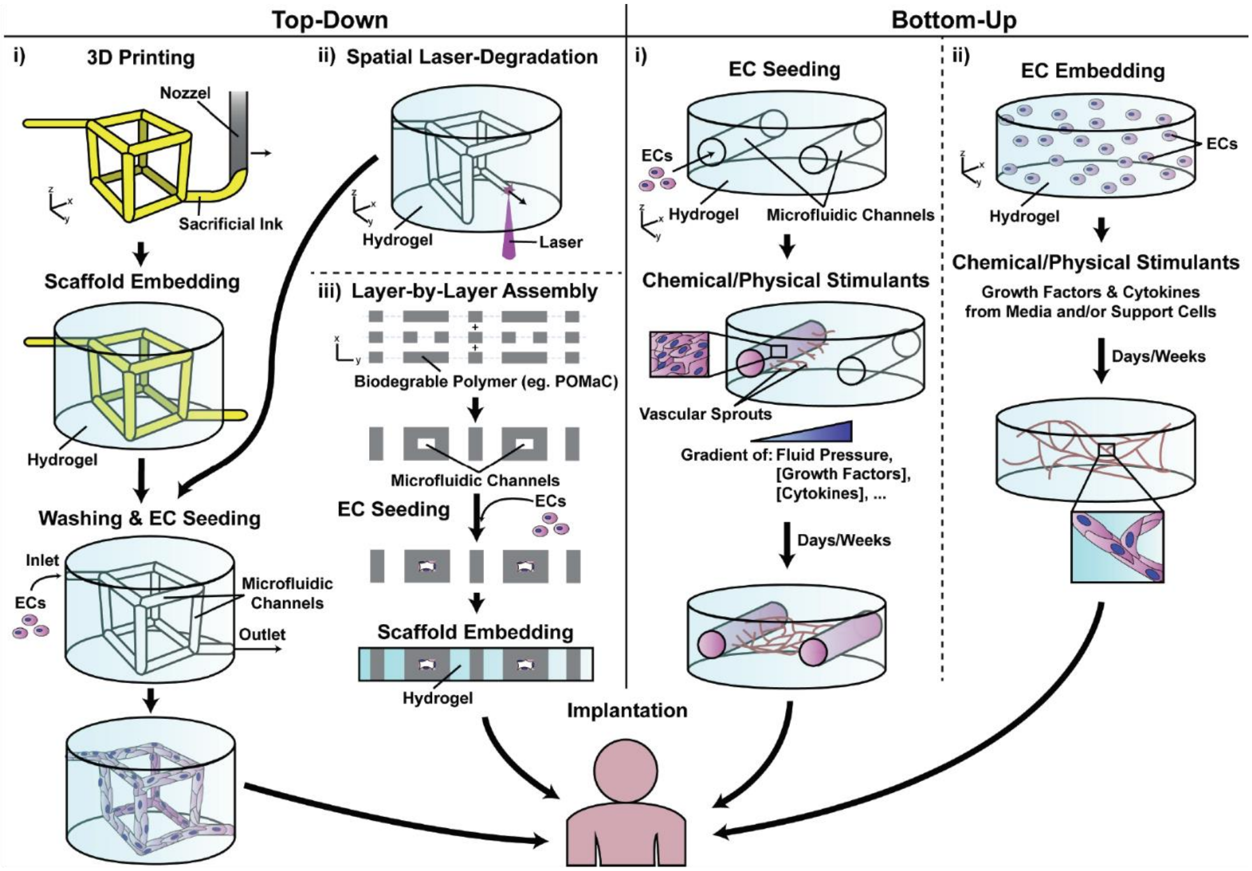
Top-Down
Bottom-Up
i) 3D Printing
Nozzel
Sacrificial Ink
Scaffold Embedding
Hydrogel
Washing & EC Seeding
Inlet
ECs
Microfluidic Channels
Outlet
ii) Spatial Laser-Degradation
Hydrogel
Laser
iii) Layer-by-Layer Assembly
Biodegrable Polymer (eg. POMaC)
Microfluidic Channels
EC Seeding
ECs
Scaffold Embedding
Hydrogel
Implantation
i) EC Seeding
ECs
Hydrogel
Microfluidic Channels
Chemical/Physical Stimulants
Vascular Sprouts
Gradient of: Fluid Pressure, [Growth Factors], [Cytokines], ...
Days/Weeks
ii) EC Embedding
ECs
Hydrogel
Chemical/Physical Stimulants
Growth Factors & Cytokines from Media and/or Support Cells
Days/Weeks

Figure 2.5: Engineered microvessels can be fabricated using either top-down or bottom-up approaches. Image reproduced from (Song et al., 2018).

2.3.4 Mechanical regulation of vasculogenic assembly

While biochemical regulation of vasculogenic assembly has been well studied, far less is known about how physical attributes of the ECM govern the assembly and maturation of engineered microvessels. Previous work implicating matrix mechanical properties in vasculogenesis has identified a role for matrix elastic modulus and generally suggests that the more compliant a material is, the greater its capacity to facilitate EC network formation (Lesman et al., 2016). For example, Vailhé et al. varied fibrin gel concentration and resulting elastic modulus and observed that decreasing fibrin concentration led to an increase in 2D EC network formation (Vailhé et al., 1997). However, given the co-dependence of gel mechanical properties, matrix topography, and ligand density on ECM protein concentration within naturally derived gels, isolating the specific contribution of biophysical vs. biochemical signals proves difficult. One approach to counteract this problem in natural materials is glycation, which increases gel elastic modulus with minimal impact on gel architecture. Using this technique in collagen gels, Mason et al. found that increasing ECM stiffness correlated with the formation of capillary-like structures in 3D, a result opposite of the accepted trend (Mason et al., 2013). Furthermore, studies conducted on PAA gels conversely demonstrated that ECs transition from a monolayer to network-like phenotype with decreasing hydrogel elastic modulus (Califano & Reinhart-King, 2008).

While matrix stiffness is directly regulating cell spreading and migration via mechanotransduction pathways, mechanical properties of the ECM also underly the generation and transmission of cell forces and are likely impacting MIC that could underly vasculogenic assembly. The following thesis chapters focus on designing fibrous biomaterial platforms that support EC network formation (Chapters 3-5), developing techniques to study mechanical communication between ECs in fibrous matrices (Chapter 6), and utilizing this information to design 3D fiber-reinforced hydrogels that optimize MIC to support the self-assembly of ECs into functional prevascularized tissue constructs (Chapter 7). Lastly, Chapter 8 will provide a summary of the main findings of this thesis and future directions of studying MIC and vasculogenic assembly towards improving strategies for regenerative medicine and therapeutic applications.

Chapter 3: Cell Force-Mediated Matrix Reorganization Underlies Multicellular Network Assembly

3.1 Authors

Christopher D. Davidson, William Y. Wang, Ina Zaimi, Danica Kristen P. Jayco, Brendon M. Baker

3.2 Abstract

Vasculogenesis is the *de novo* formation of a vascular network from individual endothelial progenitor cells occurring during embryonic development, organogenesis, and adult neovascularization. Vasculogenesis can be mimicked and studied *in vitro* using network formation assays, in which endothelial cells (ECs) spontaneously form capillary-like structures when seeded in the appropriate microenvironment. While the biochemical regulators of network formation have been well studied using these assays, the role of mechanical and topographical properties of the extracellular matrix (ECM) is less understood. Here, we utilized both natural and synthetic fibrous materials to better understand how physical attributes of the ECM influence the assembly of EC networks. Our results reveal that active cell-mediated matrix recruitment through actomyosin force generation occurs concurrently with network formation on Matrigel, a reconstituted basement membrane matrix regularly used to promote EC networks, and on synthetic matrices composed of electrospun dextran methacrylate (DexMA) fibers. Furthermore,

modulating physical attributes of DexMA matrices that impair matrix recruitment consequently inhibited the formation of cellular networks. These results suggest an iterative process in which dynamic cell-induced changes to the physical microenvironment reciprocally modulate cell behavior to guide the formation and stabilization of multicellular networks.

3.3 Introduction

Vasculogenesis, the *de novo* formation of blood vessels, occurs during embryonic development, organogenesis, and adult neovascularization (Asahara et al., 1997; Matsumoto et al., 2001; Risau & Lemmon, 1988). This dynamic process involves the aggregation and organization of individual endothelial progenitor cells into an interconnected network of capillaries (Drake, 2003). Due to numerous challenges studying vasculogenesis *in vivo*, *in vitro* network formation assays have greatly facilitated our understanding of the biological regulation of this complex process. In typical studies, endothelial cells (ECs) plated on Matrigel (a reconstituted gel containing basement membrane matrix proteins) rapidly attach, extend, and form networks of multicellular capillary-like tubules within 24 hours (Kubota, Y., Kleinman, H. K., Marin, G. R., and Lawley, 1988). These and similar studies performed with two- or three-dimensional collagen and fibrin gels (Davis et al., 2000; Vailhé et al., 1997) have been critical in determining the vital growth factors (Browning et al., 2008), genes (Bell et al., 2001), and signaling pathways (Grove et al., 2002) required for vasculogenesis, but far less is known about how physical attributes of the extracellular matrix (ECM) govern this cell assembly process. A deeper understanding from the perspective of the physical microenvironment would aid in the design of biomaterials that facilitate the rapid formation of vasculature and subsequent host integration following implantation, which are significant outstanding challenges in the field of tissue engineering and regenerative medicine (Auger et al., 2013).

Mechanical interactions between cells and the ECM are critical in many single- and multi-cellular processes including cell spreading (Vogel & Sheetz, 2006), cell migration (Charras & Sahai, 2014), and tissue morphogenesis (Lutolf & Hubbell, 2005). Previous work implicating matrix mechanical properties in vasculogenesis has focused on matrix elastic modulus and generally suggests that the more compliant a material is, the greater its capacity to facilitate EC network formation (Lesman et al., 2016). For example, Vailhé et al varied fibrin gel concentration and resulting elastic modulus, and observed that decreasing fibrin concentrations led to an increase in EC network formation (Vailhé et al., 1997). However, given the co-dependence of gel mechanical properties, matrix topography, and ligand density on ECM protein concentration within naturally derived gels, isolating the specific contribution of biophysical vs. biochemical signals proves difficult. One approach to counteract this problem in natural materials is glycation, which increases gel elastic modulus with minimal impact on gel architecture (Roy et al., 2010). Using this technique in collagen gels, Mason et al found that increasing ECM stiffness correlated with the formation of capillary-like structures, a result opposite to the accepted trend (Mason et al., 2013). Synthetic ECM mimetics typically provide greater control over matrix cues and therefore have provided another key approach to examining the role of matrix mechanical properties on EC network formation. Studies conducted on polyacrylamide (PA) gels, a commonly used elastic hydrogel that enables independent modulation of ECM elastic modulus and ligand density, conversely demonstrated that ECs transition from a monolayer to network-like phenotype with decreasing hydrogel elastic modulus (Califano & Reinhart-King, 2008; Deroanne et al., 2001; Saunders & Hammer, 2010).

One potential source of these conflicting observations is that elastic modulus, although an important metric representing the stress/strain response of an elastically deforming material, may not sufficiently describe the mechanical behavior of all biologic materials. *In vivo* microenvironments that promote vessel formation, such as embryonic mesenchymal tissue during development or fibrin-clots during wound healing, possess complex mechanical behavior due in part to their fibrous composition and viscoelastic properties. Indeed, many of the settings commonly used to promote the formation of EC networks *in vitro* – Matrigel, collagen, and fibrin – also possess fibrous structure at various length scales with complex and hierarchical mechanics not fully encapsulated by an elastic modulus value (Beier et al., 2009; Gelain et al., 2006; Lisi et al., 2012; Nam et al., 2016).

In particular, we recently showed that in fibrous matrices, cellular ECM mechanosensing is affected by dynamic changes in local adhesive ligand availability and matrix topography due to cell-force mediated recruitment of matrix fibers (Baker et al., 2015). Cellular reorganization of the matrix has also been observed *in vivo* (Provenzano et al., 2006), in natural materials such as collagen and fibrin (Ban et al., 2018; Malandrino et al., 2017), and within stress relaxing hydrogels (Lou et al., 2018). Interestingly, matrix reorganization in many of these materials has been shown to be irreversible, implying plastic deformation that permanently alters matrix architecture (Malandrino et al., 2017; Nam et al., 2016). Elastic hydrogels such as PA, however, support limited matrix reorganization (Baker et al., 2015; Legant et al., 2010), and any deformation to the underlying substrate under cell forces is completely reversible (a behavior essential to the use of elastic materials for traction force methodologies) (Dembo & Wang, 1999). As the majority of EC network formation studies in synthetic ECMs have focused on non-fibrous elastic hydrogels, the relationship between matrix reorganization and vasculogenesis has not been explored. Here, we combined experiments in natural and synthetic materials to gain insight into how physical properties of fibrous ECM and cell-mediated matrix reorganization regulate network formation. We established a model of EC network formation in a synthetic fibrous matrix, orthogonally examined the effect of matrix architecture and mechanics on this assembly process, and found that cell-force mediated matrix reorganization and continued force propagation is required for the formation and stabilization of these networks.

3.4 Results

3.4.1 ECM mechanics regulate EC network formation and matrix reorganization on Matrigel

To begin to investigate the role of ECM mechanics on EC network formation we utilized Matrigel, a reconstituted basement membrane matrix known to robustly promote the formation of EC networks (Kubota, Y., Kleinman, H. K., Marin, G. R., and Lawley, 1988). We adopted a technique to fabricate wedge-shaped gels with varying thickness across the substrate (Mullen et al., 2015), thus modulating cell-perceived matrix stiffness via proximity to a rigid underlying boundary condition (Buxboim et al., 2010). Human umbilical vein ECs seeded on these substrates and visualized after 12 hours of culture resulted in varying multicellular morphologies as a function of gel thickness (**Figure 3.1a**). At thicker sections of the gel (> 200 microns), networks formed with long cellular extensions in contrast to thinner sections (< 200 microns) where extensions were shorter and yielded a denser network or a cell monolayer at the thinnest regions examined (< 20 microns). To statistically differentiate these morphological variations, we utilized a previously established metric of the ratio of cellular area to perimeter (A/P ratio) (Califano & Reinhart-King, 2008). This metric numerically distinguishes three possible phenotypes: single, disconnected cells (A/P < 10 μm), an interconnected network (10 μm < A/P < 30 μm), or a cell monolayer (A/P > 30 μm) (**Supplementary Figure 3.1**). In the above experiment, A/P ratio decreased significantly with increasing Matrigel thickness, supporting the morphological transition from monolayer to network phenotype (**Figure 3.1b**).

To provide further evidence that matrix mechanical properties mediate this assembly process, Matrigel substrates of uniform thickness (approximately 450 μm) were crosslinked with glutaraldehyde (Semler et al., 2000). Controlled exposure to varying concentrations of glutaraldehyde increased Young's modulus from 401 to 1126 Pa (**Figure 3.1c**, **Supplementary Figure 3.2**) and led to a graded cellular response ranging from successful network formation in untreated controls (E = 401 Pa), a heterogeneous mixture of networks with large areas containing monolayers at low concentrations of glutaraldehyde (E = 595 Pa), to a complete monolayer lacking network morphology at the highest concentration examined (E = 1126 Pa) (**Figure 3.1d,e**). Taken together, these results obtained by two distinct methods are in agreement with the general claim that more compliant materials promote the formation of EC networks *in vitro* (Califano & Reinhart-King, 2008; Deroanne et al., 2001; Saunders & Hammer, 2010; Vailhé et al., 1997).

To visualize cell-mediated deformations of the underlying matrix, control or glutaraldehyde-crosslinked Matrigel substrates with embedded fluorescent microspheres (Fl-μS) were imaged by time-lapse microscopy immediately after seeding with ECs. In control substrates, cells appeared to exert traction forces to actively deform and recruit the ECM concurrent with cellular reorganization and network assembly, resulting in dense regions of matrix directly beneath ECs that mirrored closely the overall pattern of assembled networks (**Figure 3.1f**, **Supplementary Figure 3.3a**, **Supplementary Movie 3.1**). Furthermore, these cell-mediated deformations to the matrix were permanent, as limited elastic recovery was noted following removal of EC networks by lysis (**Figure 3.1f**). Interestingly, we observed distinct Fl-μS dynamics in crosslinked Matrigel substrates that led to monolayer formation (E = 1126 Pa). Although non-negligible motion was observed, Fl-μS displacement paths were short, randomly directed, and did not condense, implying limited ECM recruitment during the formation of a cellular monolayer (**Figure 3.1g**, **Supplementary Figure 3.3b**, **Supplementary Movie 3.2**). These studies suggest an important role for matrix reorganization in EC network formation, and may in part explain why compliant, deformable matrix settings tend to be pro-vasculogenic.

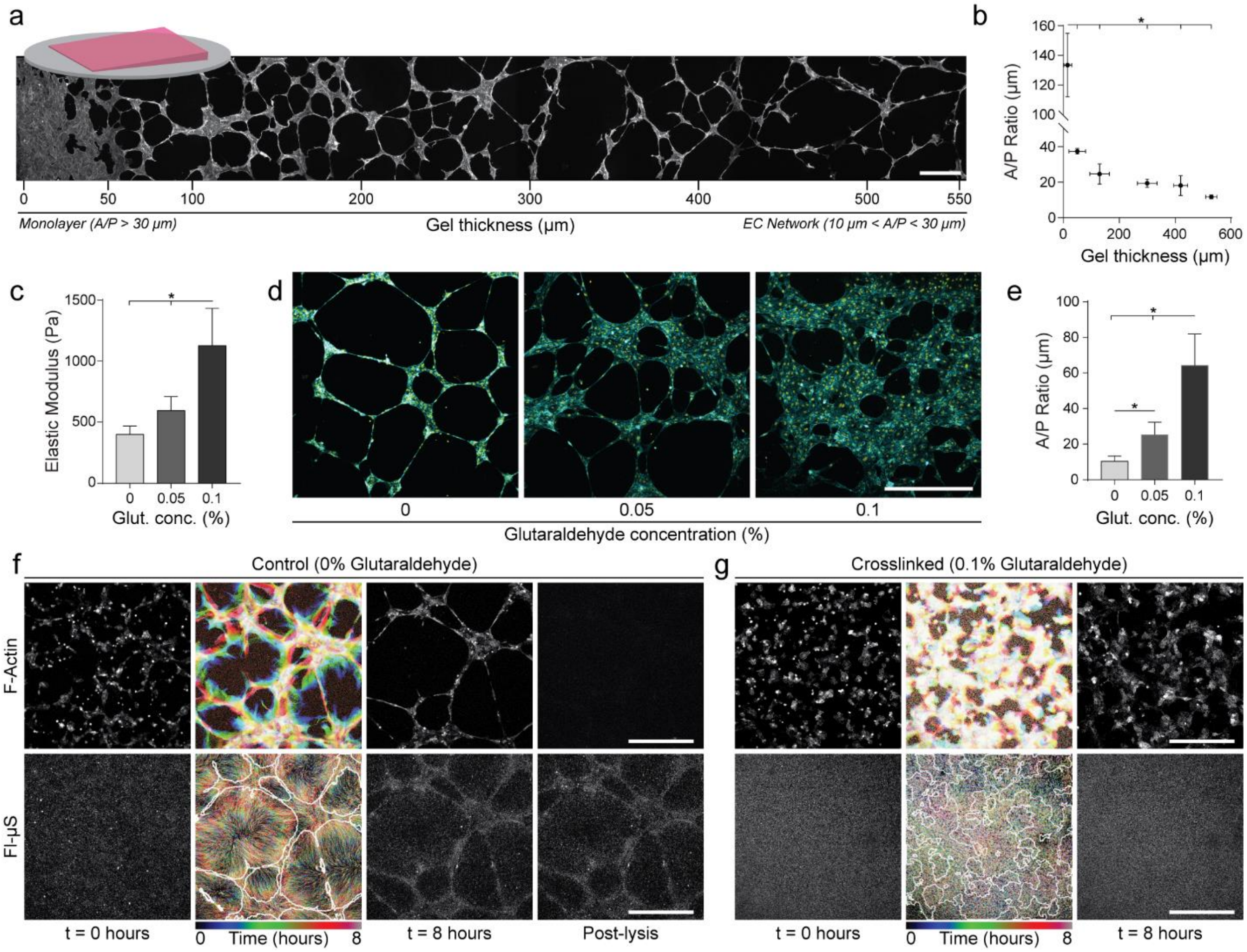

Figure 3.1: ECM mechanics regulate EC network formation and matrix reorganization on Matrigel. (a) Confocal fluorescence maximum projections of phalloidin-stained ECs seeded on wedge-shaped Matrigel substrates ranging in thickness from approximately 0 to 550 μm, after 12h of culture. (b) Resulting network morphology was determined by the area/perimeter ratio of

thresholded images at select thicknesses of Matrigel as indicated (**Supplementary Figure 3.1**). Horizontal error bars represent the range of thickness for each analyzed section of the image; n ≥ 3. (c) Young's modulus of Matrigel crosslinked with varying glutaraldehyde concentrations determined by microscale compression testing; n ≥ 8. (d) Fluorescent images of ECs cultured for 12 hours on Matrigel after glutaraldehyde crosslinking at the indicated concentration; actin (cyan), nuclei (yellow). (e) Cell area/perimeter ratio on Matrigel substrates as a function of glutaraldehyde crosslinking; n ≥ 7. Representative time-lapse images of lifeAct-GFP expressing ECs (top row) and embedded fluorescent microspheres (Fl-μS, bottom row) on untreated control (f) and 0.1% glutaraldehyde treated (g) Matrigel substrates. Rainbow overlays depict cell and Fl-μS motion (with final EC structure outlined in white) over the 8 hour time-lapse. Rightmost images in (f) depict cell and Fl-μS images following cell lysis. Untreated control substrates demonstrate high levels of matrix deformation and reorganization in contrast to glutaraldehyde crosslinked Matrigel. In the control case, limited elastic recovery is observed after removal of the formed network. Scale bars: 500 μm. All data presented as mean ± std, * $P<0.05$.

3.4.2 Synthetic fibrous DexMA matrices undergo pronounced matrix reorganization during EC network formation

While Matrigel has served as an important setting for studying various biological processes including vasculogenesis, eliminating the influence of its numerous biochemical components and orthogonally modulating the biophysical properties of this material proves challenging. In the experiments above, we modulated crosslinking and quantified differences in substrate elastic modulus from bulk compression testing, however glutaraldehyde crosslinking alters biochemical and mechanical properties beyond solely the elastic modulus of the gel. Furthermore, although Matrigel possesses a fibrous ultrastructure (with fibers on the range of 70 nm in diameter (Abrams et al., 2000)), tuning mechanical and topographical features significant to EC network formation is not currently achievable with this material. Given these challenges and a putative role for fibrous structure in vasculogenesis, we adopted a previously developed synthetic fibrous ECM mimetic composed of electrospun dextran methacrylate (DexMA) fibers possessing well-defined and tunable mechanical and biochemical properties (Baker et al., 2015).

DexMA fibrous matrices were suspended over an array of microfabricated wells such that cells in well-regions are not influenced by a rigid underlying support, but instead sense the mechanical properties defined by fibrous architecture, the stiffness of individual fibers, and proximity to rigid boundary conditions of the well edge (**Figure 3.2b**). Fiber matrices with low bulk stiffness (E = 1.5 kPa) were functionalized with the adhesive peptide CCRGDS (RGD) via Michael-type addition with unreacted methacrylates, and seeded with ECs which rapidly adhered, reorganized ECM fibers, and assembled into networks within 24 hours (**Figure 3.2b,d**, **Supplementary Movie 3.3**). During the first four hours, we noted marked matrix reorganization through recruitment of fibers beneath individual ECs and lateral bundling of fibers between adhered cells, accompanied by cell spreading and the formation of cell-cell contacts (**Figure 3.2d**, **Supplementary Movie S4**). Following this initial phase, EC network morphology stabilized over a prolonged period of spatially and temporally heterogeneous deformations and force propagation throughout the matrix and EC network (**Supplementary Movie S3**). Although the majority of cellular connections formed during the first four hours, additional cell extensions leading to inter-cellular connection occurred throughout the 24-hour culture period (**Supplementary Figure 3.4**). Similar to Matrigel, physical matrix reorganization of DexMA matrices proved permanent, as limited recovery of fibers to their initial geometry occurred following cell lysis (**Figure 3.2c**). Furthermore, we note that ECs secrete fibronectin that adheres to DexMA fibers at network nodes where there is high relative fiber density (**Supplementary Figure 3.5**), which could in part explain the permanence of matrix deformations. A/P ratio throughout this dynamic process began low (< 10 μm) while single cells adhered prior to spreading and connecting with other cells, rapidly increased over the first four hours as interconnected network formed, and then settled at an intermediate value (10-30 μm) following stabilization (**Figure 3.2e**). To quantify matrix reorganization over time, Fl-μS were embedded within DexMA fibers and tracked during network formation (Tinevez et al., 2017). The sum of the mean squared displacements between frames for each individual Fl-μS was calculated via custom Matlab script (**Figure 3.2f**, **Supplementary Figure 3.6**). Bead displacement increased rapidly over the first four hours paralleling the dynamics of A/P ratio, but then transitioned to a constant linear increase reflecting continuous matrix deformations and force propagation following EC network stabilization (**Figure 3.2f**, **Supplementary Movie 3.3**). We further quantified matrix remodeling by performing image analysis on the open space, or pores, between DexMA fibers (**Supplementary Figure 3.7**). Through this quantification, we observe that average pore size increases and the total number of pores decreases over time, supporting the observation that ECs bundle and condense matrix fibrils as they spread and interconnect into a multicellular assembly. Overall, these studies established EC network formation in fully synthetic DexMA fibrous matrices that, despite significant distinctions in matrix structure and adhesive ligand, reveal similarities in terms of network morphology and matrix reorganization as studies performed with Matrigel.

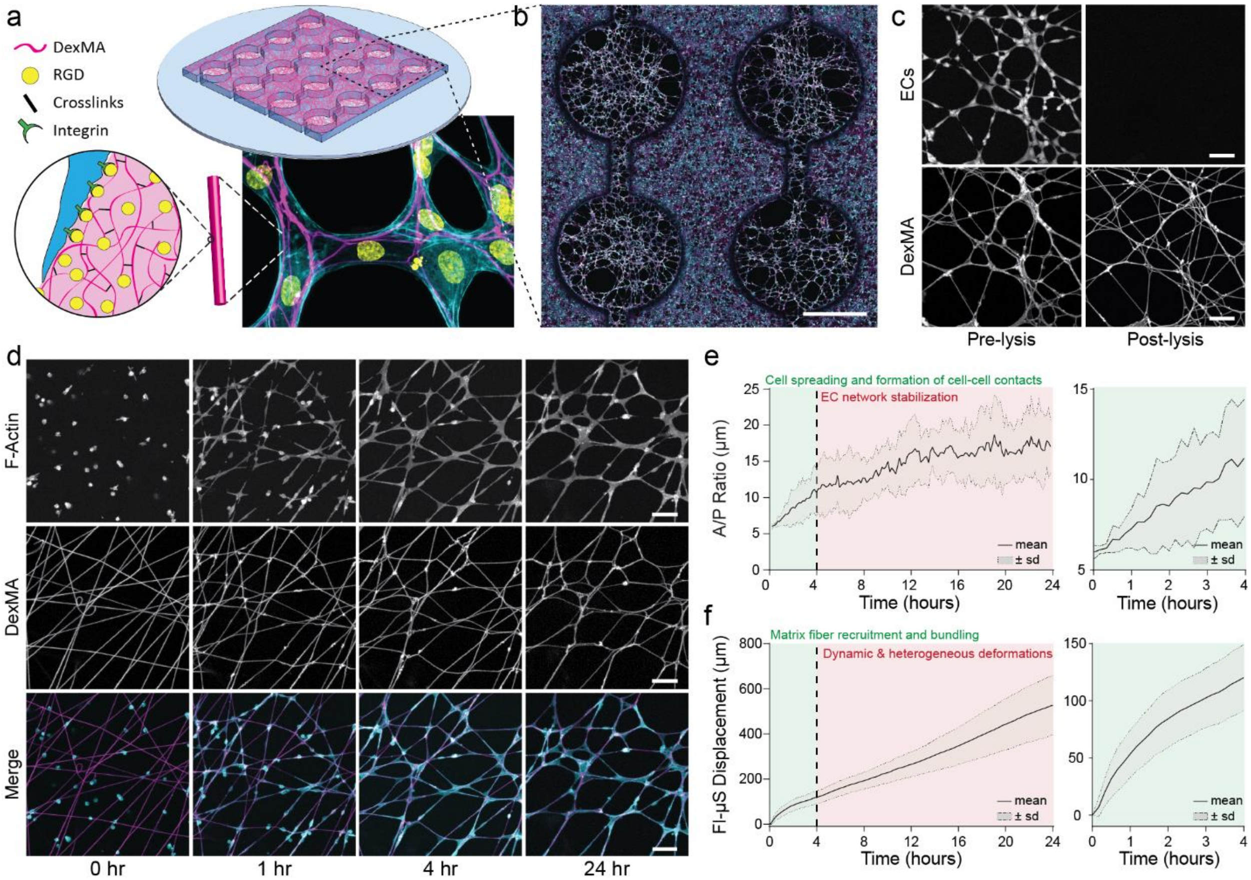

Figure 3.2: Synthetic fibrous DexMA matrices undergo pronounced matrix reorganization during EC network formation. (a) Schematic of microfabricated PDMS multi-well substrate possessing a 4x4 array of wells, each supporting a suspended matrix of non-aligned DexMA fibers coupled with RGD to facilitate cell adhesion. (b) Tile-scan confocal image of EC networks after 24 hours of culture on DexMA fiber matrices; rhodamine-labeled fibers (magenta), F-actin (cyan), and nuclei (yellow) (scale bar: 1 mm). (c) Limited elastic recovery of fibers after lysis of CellTracker labeled ECs, demonstrating that physical matrix reorganization is permanent (scale bar: 100 µm). (d) Representative time-lapse images of lifeAct-GFP expressing ECs at 0, 1, 4, and 24h following seeding (scale bar: 100 µm). Cell area/perimeter ratio (e) and total Fl-µS displacement (f) over the 24-hour time-lapse series of network formation; n = 8.

3.4.3 Actomyosin contractility is required for EC network formation on fibrous DexMA matrices

Given the likelihood that the deformations observed in the above studies are consequences of cell traction forces, we tested a requirement for actomyosin-generated contractile forces in EC network assembly by treatment with pharmacologic inhibitors. Cells dosed with cytochalasin D (actin polymerization inhibitor), blebbistatin (myosin II inhibitor), or

Y-27632 (ROCK inhibitor), EC networks failed to form over 24h (**Figure 3.3a**). Treatment with cytochalasin D completely abrogated cell spreading, resulting in individual cells with a low A/P ratio (**Figure 3.3a,b**). In the presence of blebbistatin and Y-27632, ECs were adhered to the matrix and spread but demonstrated limited interaction with neighboring cells and largely remained as individual cells, resulting in a lower A/P ratio as compared to controls (**Figure 3.3a,b**). Fl-μS displacements were significantly lower for all inhibitors, corresponding to limited reorganization of matrix fibrils (**Figure 3.3a,c**). Additional analysis of cytoskeletal structure via high-resolution confocal microscopy indicates the presence of F-actin stress fibers in control conditions, in contrast to a diffuse or punctate F-actin signal and absence of stress fibers upon treatment with cytochalasin D, blebbistatin, and Y-27632 (**Supplementary Figure 3.8**). These studies demonstrate that actomyosin-generated contractile cell forces are required for matrix reorganization, and associate the absence of matrix reorganization with failure of ECs to form networks.

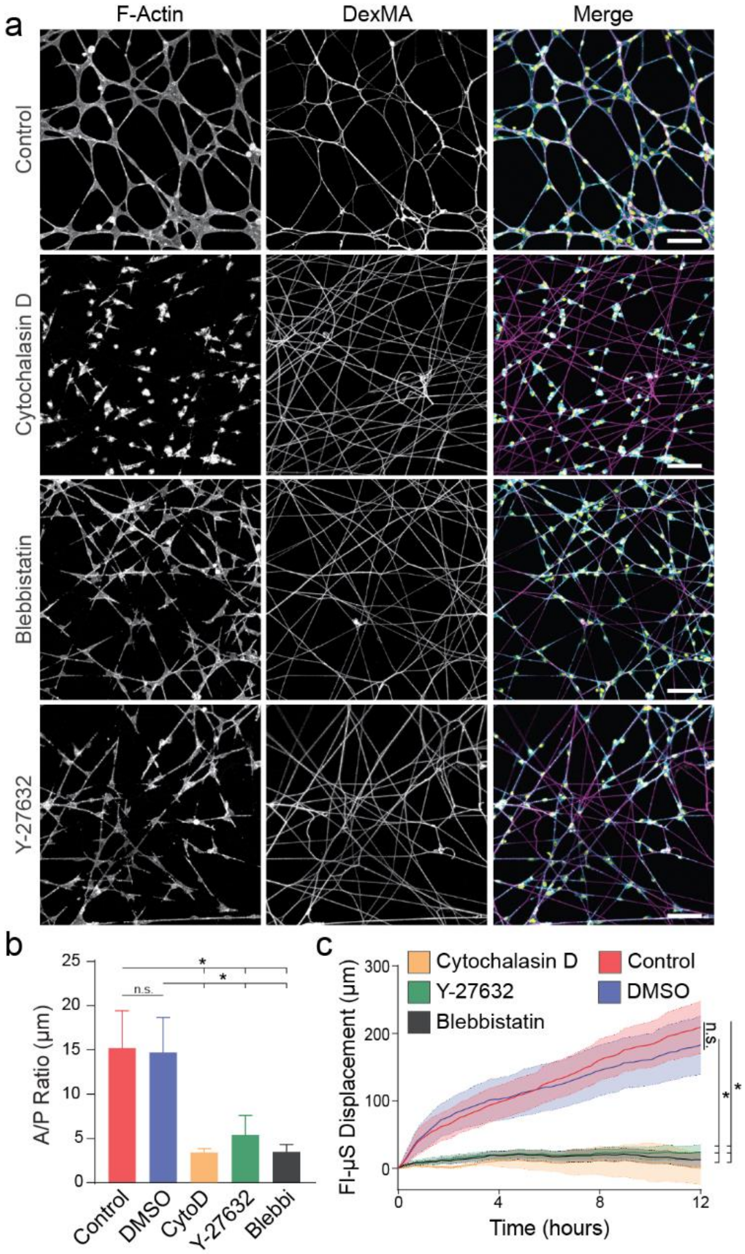

Figure 3.3: Actomyosin contractility is required for EC network formation on fibrous DexMA matrices. (a) Confocal fluorescence images of phalloidin-stained ECs and rhodamine labeled fibers after 24 hours, with indicated pharmacologic inhibitor treatment; actin (cyan), nuclei (yellow), fibers (magenta). Scale bar: 100 µm. (b) Cell area/perimeter ratio after 24 hours of culture as a function of pharmacologic inhibitor treatment. (c) Total Fl-µS displacement over the first 12 hours of network formation as a function of pharmacologic inhibitor treatment. All data presented as mean ± std; n ≥ 6; * P<0.05.

3.4.4 Physical properties of fibrous ECM influence matrix reorganization and EC network formation

The above results suggest a potential requirement for cell-mediated matrix reorganization during EC network formation, so we further hypothesized that matrix mechanics and architecture could regulate this process by impacting the ability of cell forces to reorganize the matrix. Taking advantage of the tunable nature of these synthetic matrices, we orthogonally modulated physical matrix properties relevant to natural tissues and examined matrix reorganization and network formation. First, the stiffness of matrix fibers was modulated by tuning crosslinking via photoinitiator concentration, resulting in increases in the Young's moduli of fiber matrices with no effect on initial fiber density (**Figure 3.4a,b**, **Supplementary Figure 3.2**). In comparison to controls ($E = 1.5$ kPa) where high levels of matrix reorganization corresponded with EC network formation, matrices with increasingly stiffer fibers led to a graded decrease in network formation and a transition towards monolayer formation (**Figure 3.4b**, **Supplementary Movie 3.5**). Increases in A/P ratio as a function of fiber/matrix stiffness corroborated this change in morphology (**Figure 3.4c**). Increasing fiber/matrix stiffness also yielded a graded decrease in matrix reorganization as determined by Fl-μS displacements (**Figure 3.4d**).

We next investigated the effect of matrix fiber density by altering the duration of electrospinning and fiber collection (**Figure 3.4e,f**), while maintaining a constant degree of crosslinking (equivalent to the lowest stiffness concentration). Control matrices with the lowest fiber density examined resulted in formation of EC networks, concurrent with high levels of matrix remodeling (**Figure 3.4f**). Increasing fiber density resulted in a graded response in A/P ratio and Fl-μS displacement similar to the above studies modulating fiber stiffness (**Figure 3.4f-h**), further supporting a strong connection between matrix reorganization and successful network formation.

Lastly, we welded junctions between fibers via exposing substrates to high humidity prior to crosslinking in order to model inter-fiber crosslinking. This perturbation does not alter overall matrix architecture, the elasticity of individual fibers, or the Young’s modulus of the bulk material, but has previously been shown to decrease fiber recruitment by mesenchymal stem cells (Baker et al., 2015). Control conditions with limited inter-fiber welding formed networks concurrent with high levels of matrix reorganization, as in earlier studies (**Figure 3.4j**). However, inter-fiber welding of matrices of the same crosslinking and initial fiber density (**Figure 3.4i,j**) led to a significant increase in A/P ratio and a significant decrease in Fl-μS displacement, indicating a transition to a cellular monolayer and a decrease in matrix remodeling (**Figure 3.4j-l**). While networks still formed in both conditions, there was a clear change in network morphology, as welding led to larger network nodes containing monolayers as compared to the control condition, similar to Matrigel substrates exposed to low concentrations of glutaraldehyde (**Figure 3.1d**). For all matrix perturbations (stiffness, density, and inter-fiber crosslinking) described above, there were no significant differences in fiber diameter (**Supplementary Figure 3.9**).

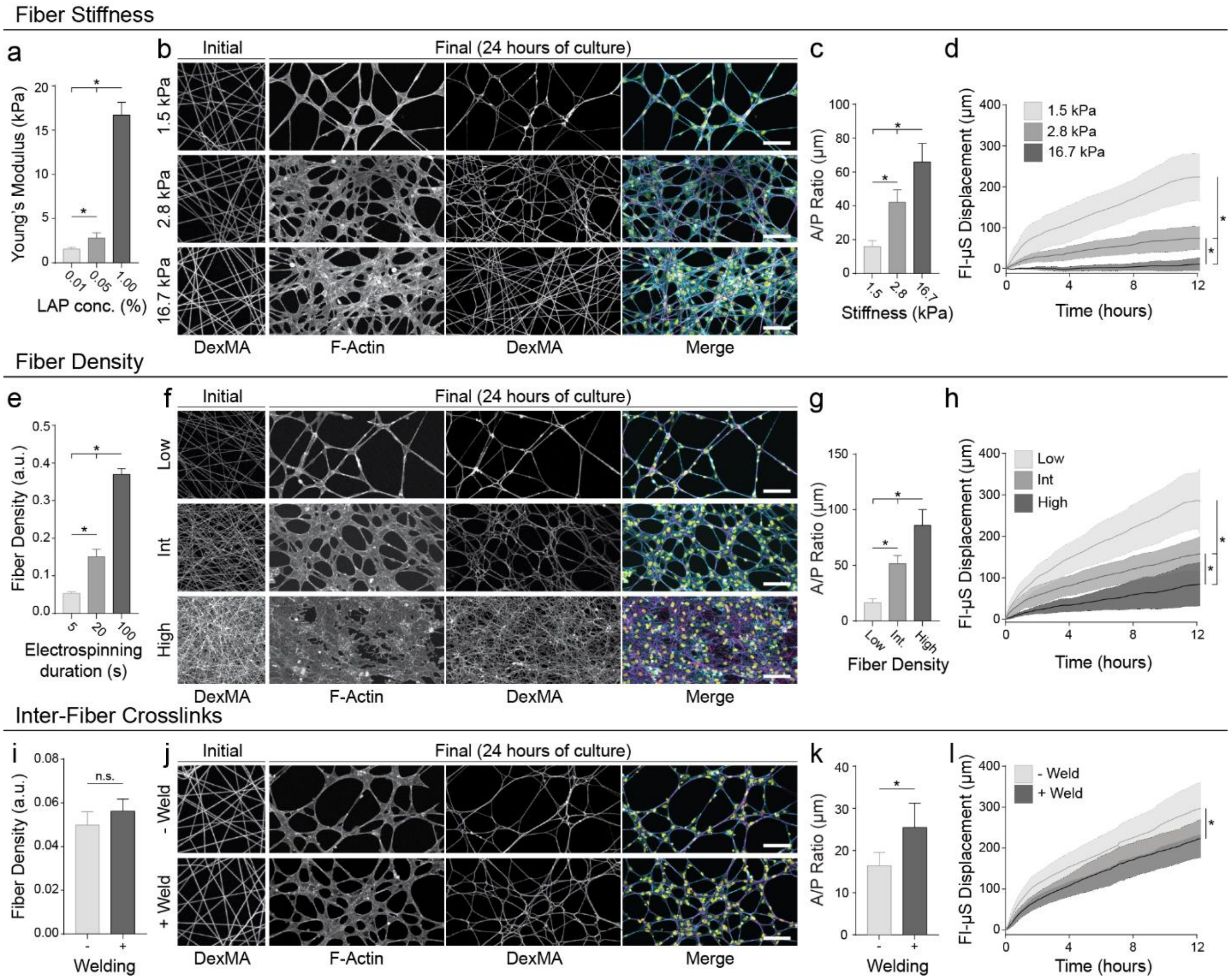

Figure 3.4: Physical properties of fibrous ECM influence matrix reorganization and EC network formation. EC network formation was assayed on DexMA fibrous matrices with varying stiffness (a-d), fiber density (e-h), and with modulation of inter-fiber crosslinks (welds) (i-l). (a) Young's modulus of DexMA fiber matrices as a function of photoinitiator (LAP) concentration. (e,i) Fiber density prior to cell seeding determined as the percent total area of each substrate containing fibers. (b,f,j) Representative image of initial fiber density prior to cell seeding (far left); confocal fluorescent images of phalloidin-stained ECs (left) and rhodamine labeled fibers (middle) 24 hours after seeding under the indicated matrix perturbation after 24 hours of culture; merged images (right) showing actin (cyan), nuclei (yellow), and fibers (magenta) (scale bar: 100 µm). (c,g,k) EC area/perimeter ratio as a function of ECM perturbation. (d,h,l) Total Fl-µS displacement over the first 12 hours of network formation as a function of ECM perturbation. All data presented as mean ± std; n ≥ 6; * $P<0.05$.

3.4.5 Matrices permissive to physical reorganization and persistent deformations yield EC networks stabilized by VE-cadherin enriched cell-cell junctions

These results support a role for cell force-mediated matrix reorganization in EC network formation (primarily over the first 4 hours of culture), but do not address the stabilization of networks and ensuing steady state behavior. A constant A/P ratio with linearly increasing Fl-μS displacements after the initial four hours of culture (**Figure 3.2e,f**) reflect stable cellular connections and network morphology despite continual deformations to the underlying matrix (**Supplementary Movie 3.3**). To investigate stabilization of EC networks, we examined cell-cell adhesion maturity via immunostaining for VE-cadherin, an EC adherens junction molecule critical to blood vessel maturation and stability. Fluorescent intensity of VE-cadherin (normalized to cell density) significantly increased over time on control matrices (**Figure 3.5a,b**). In contrast, cell-cell adhesions in stiff matrices that underwent limited reorganization possessed significantly lower VE-cadherin levels despite successful spreading and formation of cell-cell contacts (**Figure 3.5c,d**). Furthermore, treatment of formed cell networks on control matrices with ethylene glycol-bis(2-aminoethylether)-*N,N,N',N'*-tetraacetic acid (EGTA), which chelates calcium ions and disrupts cadherin-mediated cell-cell adhesions (Telo' et al., 1998; Volberg et al., 1986), resulted in a loss of intercellular connections and dissociation into single cells (**Supplementary Figure 3.10**).

Both matrix reorganization and force transmission may contribute to the observed maturation of cell-cell adhesions, however the above experiment fails to segregate the two. Matrix reorganization to a condensed architecture with restricted fiber/ligand availability could more rapidly facilitate cell-cell engagement through contact guidance, but alternatively, a mechanically permissive matrix that can be reorganized by cells may also facilitate force transmission between interconnected cells that would strengthen cadherin junctions. To discriminate between topographical and mechanical effects, we created soft and stiff matrices with pre-organized fiber architecture reflecting the final state of control matrices in the above studies. Pre-organized matrices were fabricated by allowing networks to form normally followed by cell lysis, as matrix reorganization is largely permanent (**Figure 3.2c**). Following lysis, pre-organized matrices were either UV crosslinked and reseeded ("reorg – stiff") or immediately reseeded with ECs ("reorg – soft"). Reseeding of reorganized stiff matrices which allow for no further matrix deformations after initial organization resulted in significantly lower VE-cadherin expression as compared to control networks, despite retaining a network-like morphology due to contact guidance of pre-organized fibers (**Figure 3.5c,d**). In contrast, the reorganized soft matrices that allow for continued matrix displacements and force propagation resulted in cell-cell junctions with significantly higher VE-cadherin (**Figure 3.5c,d**). Taken together, these results suggest that matrix deformability and force transmission after initial interconnections form between cells stabilizes EC networks through promoting the maturation of cell-cell adhesions.

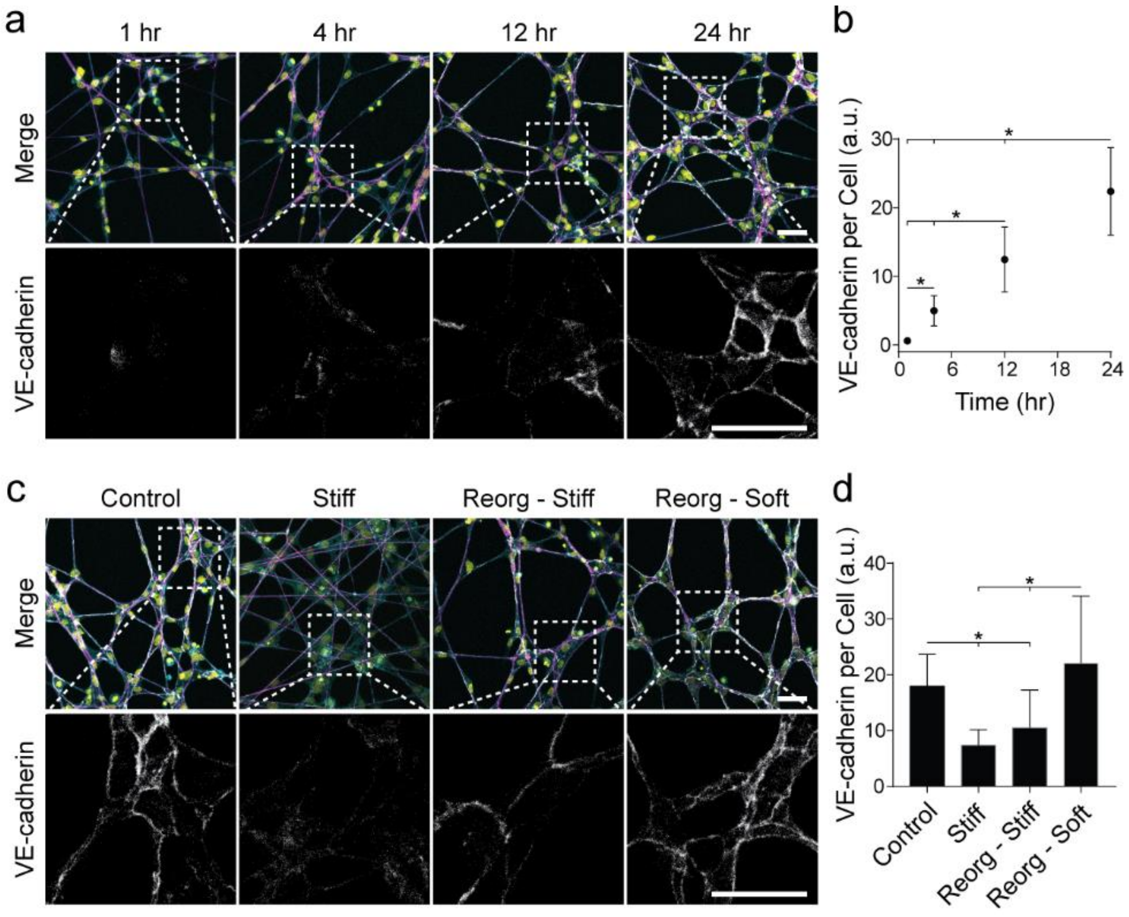
a
1 hr
4 hr
12 hr
24 hr
Merge
VE-cadherin
b
VE-cadherin per Cell (a.u.)
30
20
10
0
*
*
*
0
6
12
18
24
Time (hr)
c
Control
Stiff
Reorg - Stiff
Reorg - Soft
Merge
VE-cadherin
d
VE-cadherin per Cell (a.u.)
40
30
20
10
0
*
*
Control
Stiff
Reorg - Stiff
Reorg - Soft

Figure 3.5: Matrices permissive to physical reorganization and persistent deformations yield EC networks stabilized by VE-cadherin enriched cell-cell junctions. (a) Confocal fluorescence maximum projections of phalloidin-stained ECs (cyan), rhodamine labeled fibers (magenta), nuclei (yellow), and VE-cadherin (gray) at 0, 1, 4, and 24 h after cell seeding on control DexMA matrices (top row). Dashed boxes indicate locations of higher magnification images depicting VE-cadherin expression at cell-cell junctions (bottom row). (c) Confocal fluorescence maximum projections of phalloidin-stained ECs (cyan), rhodamine labeled fibers (magenta), nuclei (yellow), and VE-cadherin (gray) of samples 24 h after seeding on control and stiff DexMA matrices, on control matrices cultured for 24h, lysed, crosslinked, and then reseeded for 24 h (Reorg – Stiff), or on control matrices cultured for 24h, lysed, and then reseeded for 24 h (Reorg – Soft) (top row). Dashed boxes indicate locations of higher magnification images depicting VE-cadherin expression at cell-cell junctions 24 h after cell seeding (bottom row). Scale bars: 50 μm. (b,d) Quantification of total VE-cadherin fluorescent intensity normalized to cell density at each timepoint (b) and matrix condition (d). All data presented as mean ± std; $n \geq 16$; * $P<0.05$.

3.5 Discussion

Mechanical interactions between cells and the ECM have been shown to be crucial in many biological processes, including migration, differentiation, and morphogenesis. Here, we utilized both natural and synthetic matrices to examine how cell interactions with the physical microenvironment mediate the assembly of multicellular networks and found that dynamic force-mediated modulation of matrix structure is critical in this phenomenon. Studies varying the rigid boundary conditions and crosslinking of Matrigel demonstrated that mechanical perturbations to the microenvironment profoundly altered this process. Interestingly, we observed that active matrix recruitment coincided with network formation, resulting in regions of condensed matrix that closely paralleled the patterning of EC networks. Next, we identified matrix conditions that facilitate rapid EC network assembly on synthetic DexMA fibrous matrices affording controllable mechanical and topographical properties. We confirmed a requirement for actyomyosin-generated forces in matrix fibril reorganization and observed a strong association between dynamic changes to matrix structure and successful EC network assembly. Varying physical parameters of these matrices, we further found that perturbations that diminish the ability of cells to physically reorganize the matrix proved inhibitory to network formation. Lastly, we found that deformable matrices that permit active force transmission across an interconnected cell network promoted stabilization of cell-cell junctions as seen by increased VE-cadherin levels. Taken together, these results demonstrate that cell force-mediated reorganization, independent of enzymatic activity, mediates dynamic changes in matrix topography, ligand availability, and mechanical forces that underlie the formation and stabilization of interconnected multicellular networks.

Highly localized reorganization of the matrix through cellular recruitment of matrix fibrils results in actively changing adhesive ligand distribution and density. Our previous work demonstrated that cell-mediated fiber recruitment increased adhesive ligand density proximal to the cell surface, contributing to increases in cell spreading, focal adhesion formation, and associated signaling (Baker et al., 2015). Similar findings have been confirmed in natural fibrous materials, such as type I collagen gels (Xie et al., 2017), and may occur at a smaller length scale in viscoelastic hydrogels (Chaudhuri et al., 2015). Studies performed on 2D elastic hydrogels increasing adhesive ligand concentration while maintaining gel elastic modulus constant revealed increases in cell spreading and cell force generation as measured by traction force microscopy (TFM) (Califano & Reinhart-King, 2010; Engler et al., 2004; Reinhart-King et al., 2003). TFM in fibrous matrices is not yet an established technique due to their composition of discrete fibers (thereby invalidating continuum assumptions), non-linear mechanical behavior, and plastic deformations, thus a direct relationship between cell-generated forces and fibril/ligand organization remains an outstanding challenge. However, given previous studies in a variety of settings connecting ligand availability with focal adhesion maturation (Baker et al., 2015; Xie et al., 2017) and traction force generation (Balaban et al., 2001; Engler et al., 2004; Rape et al., 2011), it is likely that local matrix recruitment in this setting feeds back to increase cell force generation. This suggests the initial phase of EC network assembly involves a cyclic process in which ECs initially adhere and recruit matrix, triggering increased spreading, focal adhesion formation, and force generation, which in turn could further amplify matrix recruitment until an equilibrium is eventually achieved.

Reorganization of the matrix likely also contributes to dynamic and heterogeneous changes in matrix topography and mechanics. In isotropic matrices lacking fibril alignment, cell-generated forces generally lead to radial alignment of fibers around the cell (Baker et al., 2015; Piotrowski-Daspit et al., 2017). However, when cells are in close proximity or sense mechanical resistance from a nearby rigid boundary, cell and force anisotropies rapidly develop (Barocas & Tranquillo, 1997; Stopak & Harris, 1982). In these studies, localized fiber alignment between two cells could contribute to directional extension and formation of cellular interconnections via contact guidance, supporting a role for matrix recruitment and fiber bundling in multicellular assembly. Beyond topography-induced contact guidance, however, the presence of aligned fibers spanning neighboring cells over large distances (up to 300 microns, **Supplementary Figure 3.11**) also suggests the involvement of long-range mechanical force propagation. Heterogeneous force distribution and localized paths of highest tension could induce cell polarization, directional extension, and bundling of matrix fibers. Subsequent alterations to local matrix structure would then reinforce a preferential direction of force transmission along tensile tracks of aligned fibers between neighboring cells. Fibrous matrices in particular have been shown to propagate and focus cell-generated force across large distances (Ma et al., 2013; Ronceray et al., 2016; Sopher et al., 2018a; Wang et al., 2015), and previous studies have implicated cell-cell communication via force transmission through the ECM (Reinhart-King et al., 2008; Sapir &

Tzlil, 2017; Winer et al., 2009). This notion is supported here by experiments on synthetic fibrous matrices where diminished intracellular contractility, and therefore low force generation and transmission, corresponded to the failure of network formation (**Figure 3.3**). Further, increases in fiber stiffness, fiber density, and the addition of inter-fiber crosslinks, perturbations that would dampen force transmission through the ECM, all abrogated network formation (**Figure 3.4**). Taken together, these experiments suggest matrix-regulated mechanical forces enables cells to communicate their position over long distances in order to assemble into networks.

The above provides potential mechanisms influencing cell extension leading to cell-cell contact, but does not address network stabilization after these contacts are formed. Soft matrices permissive to matrix reorganization and network formation yielded cell-cell contacts enriched for VE-cadherin compared to stiff matrices, despite the presence of cell-cell contacts in both conditions. Further, on pre-organized networks, cell-cell contacts and cell networks formed in both soft and stiff conditions, but significantly higher VE-cadherin was noted in pre-organized and deformable matrices (**Figure 3.5**). Previously, Liu et al. used microfabricated force sensors to show that mechanical tugging forces between cells engenders cell-cell adhesion formation and maturation (Liu et al., 2010d) and other work has demonstrated the requirement for actomyosin-generated tensile forces in maturing adherens junctions(Huveneers et al., 2012). Given the appearance of dynamic cell forces throughout the assembled multicellular tissue during stabilization (> 4h, Movie S3), increases in VE-cadherin at cell-cell junctions could similarly be explained by tugging forces between cells at cell-cell junctions and throughout the matrix.

Overall, this study sheds light on the complex relationship between cell-ECM interactions during EC network formation, and highlights an interplay between active and passive mechanical cues from the microenvironment. Active mechanical cues, defined as external stimuli that act directly on a cell (e.g. applied compressive forces, fluid shear), versus passive mechanical cues, defined as physical properties of the environment that cannot directly perturb a cell (e.g. stiffness, viscosity, matrix alignment) (Ricca et al., 2013), have historically been dichotomized. Here, however, passive properties of the matrix (stiffness, density, inter-fiber connections) mediate matrix reorganization to influence active mechanical cues in the form of cell-generated forces propagated through the matrix to neighboring cells. This relationship is reciprocal - active forces can reorganize the matrix, in turn modifying passive matrix properties local to the cell. Importantly, reorganization of the matrix in these studies appeared permanent (**Figure 3.1, Figure 3.2**), implying plastic deformation, a behavior of viscoplastic materials such as Matrigel, collagen, and fibrin (Ban et al., 2018; Nam et al., 2016). Interestingly, these three materials also facilitate network formation *in vivo* and *in vitro*, further supporting a role for matrix remodeling in this process and suggesting that the permanence of these deformations could be essential. Taken together, this information is critical to the design and development of vasculogenic biomaterials. Specifically, when designing synthetic materials to support vasculogenesis, matrix physical properties that support permanent matrix reorganization and long range force transmission should be considered. While elastic modulus influences these processes, physical properties beyond stiffness, such as matrix architecture and plasticity, also require careful consideration. In accord, this study suggests fiber reinforcement of synthetic biomaterials as a means to promote both matrix reorganization and long range cell-cell communication to enable multicellular assembly processes.

3.6 Materials and Methods

3.6.1 Reagents

All reagents were purchased from Sigma Aldrich and used as received, unless otherwise stated.

3.6.2 Cell culture

Human umbilical vein endothelial cells (ECs) were cultured in endothelial growth medium (EGM-2; Lonza, Basel, Switzerland) supplemented with 1% penicillin-streptomycin-fungizone (Gibco, Waltham, MA). Cells were cultured at 37°C and 5% CO_2. ECs were used from passages four to eight in all experiments. For live cell time-lapse imaging, lentiviral transduction of lifeAct-GFP was utilized.

3.6.3 Network formation on Matrigel

Growth factor reduced Matrigel (Corning, Corning, NY) was thawed overnight on ice at 4°C. 100 μL of thawed Matrigel was pipetted onto 25mm glutaraldehyde-functionalized glass coverslips and seeded at 4.5×10^4 cells cm^{-2}. Coverslips were prepared through exposure to oxygen plasma and subsequent 2 hour incubations in 0.1 mg ml^{-1} poly-L-lysine (PLL) and 5% (v/v) glutaraldehyde. Gelation of Matrigel was completed by incubation at 37°C for 30 minutes. For variable thickness Matrigel, 25 mm coverslips were first glutaraldehyde-treated as described above. Separate 18 mm coverslips were silanized with trichloro(1H,1H,2H,2H-perfluorooctyl)silane. A small 600 μm thick rectangle of poly(dimethylsiloxane) (PDMS) (Sylgard 184, Dow-Corning, Midland, MI) was then placed on the edge of the glutaraldehyde-treated coverslip, and the silanized coverslip was placed at an angle on the PDMS wedge. 100 μL of Matrigel was slowly pipetted between the two coverslips, incubated at 37°C for 30 minutes and incubated overnight in PBS. The next day, the silanized coverslip was carefully removed, seeded, and cultured for 12 hours before fixing, staining, and imaging. For studies in which Fl-µS were tracked over time, 0.1% (v/v) blue carboxylate-modified FluoSpheres (1.0 µm diameter, 2% w/v) was added to Matrigel before gelation. For Matrigel crosslinking studies, following gelation, glutaraldehyde solutions of various concentration were pipetted onto the gel and incubated for two minutes and thirty seconds. Samples were then washed twice with 1.0% (w/v) glycine in PBS and incubated for at least 6 hours to neutralize any excess glutaraldehyde in the sample. To quench glutaraldehyde autofluorescence before imaging, substrates were incubated in 1.0% (w/v) sodium borohydride in PBS for 30 minutes at room temperature. To lyse cells on Matrigel, a solution of 20mM ammonium hydroxide (NH_4OH) in 0.05% (v/v) Triton-X in PBS was added to the sample, incubated for 5 minutes, and washed with PBS.

3.6.4 DexMA synthesis

Dextran (MW 86,000 Da, MP Biomedicals, Santa Ana, CA) was methacrylated by reaction with glycidyl methacrylate as previously described (van Dijk-Wotthuis et al., 1995). Briefly, 20 mg of dextran and 2 mg of 4-dimethylaminopyridine was dissolved in 100 mL of anhydrous dimethylsulfoxide (DMSO) under vigorous stirring for 12 h. 24.6 mL of glycidyl methacrylate was then added and the reaction mixture was heated to 45°C for 24 h. The solution was cooled at 4°C for 1 hour and precipitated into 1 L ice-cold 2-isopropanol. The crude product was recovered by centrifugation, redissolved in milli-Q water, and dialyzed against milli-Q water for 3 days. The final product was lyophilized and stored at −20 °C until use. DexMA was characterized by H-NMR. The degree of functionalization was calculated as the ratio of the averaged methacrylate proton integral (6.174 ppm and 5.713 ppm in D2O) and the anomeric proton of the glycopyranosyl ring (5.166 ppm and 4.923 ppm). As the signal of the anomeric proton of α-1,3 linkages (5.166 ppm) partially overlaps with other protons, a pre-determined ratio of 4% α-1,3 linkages was assumed and the total anomeric proton integral was calculated solely on the basis of the integral at 4.923 ppm. A methacrylate/dextran repeat unit ratio of 0.7 was determined.

3.6.5 Fiber matrix fabrication

Suspended DexMA fiber matrices were fabricated through electrospinning and soft lithography as previously described (Baker et al., 2015). DexMA was dissolved at 0.5 g ml^{-1} in a 1:1 mixture of milli-Q water and dimethylformamide with 0.005% Irgacure 2959 photocrosslinker and 0.002% methacrylated rhodamine (Polysciences, Inc., Warrington, PA). For bead tracking studies, 3.0% (v/v) blue carboxylate-modified FluoSpheres (1.0 μm, 2% w/v; Life Technologies, Eugene, OR) was also added. Electrospinning was completed with a set-up consisting of a high-voltage power supply, syringe pump, and a grounded copper collecting surface enclosed within an environmental chamber at 30% relative humidity. Electrospinning was performed at a flow rate of 0.5 ml h^{-1}, voltage of 7.0 kV, and gap distance of 6 cm. Fiber density was varied through modulating electrospinning time and humidity. Samples were primary crosslinked under ultraviolet light to stabilize fibers, hydrated in varying concentrations of lithium phenyl-2,4,6-trimethylbenzoylphosphinate (LAP; Colorado Photopolymer Solutions, Boulder, CO) solution, and then exposed to ultraviolet light (100 mW cm^{-2}) for 20 s for secondary crosslinking. LAP concentration was varied between 0.01 and 1.0 mg ml^{-1} to achieve fibers of varying stiffness. Fibers were collected on PDMS arrays of circular wells (2 mm diameter) functionalized with methacrylates to promote fiber adhesion. Briefly, silicon wafer masters possessing SU-8 photoresist (Microchem, Westborough, MA) were produced by standard photolithography and used to generate PDMS stamps. Following silanization with trichloro(1H,1H,2H,2H-perfluorooctyl)silane, stamps were used to emboss uncured PDMS onto oxygen plasma-treated coverslips. Well arrays were methacrylated with vapor-phase silanization of 3-(trimethoxysilyl)propyl methacrylate (Gelest, Inc., Morrisville, PA) in a vacuum oven at 60°C for at least 6 h. To promote fiber-fiber welding, fiber networks were exposed to a humidified environment for 45 seconds before secondary crosslinking.

3.6.6 Mechanical testing

To determine the Young's modulus of Matrigel substrates assuming a linear elastic material, compression testing with a rigid cylinder was performed on a commercial CellScale Microsquisher (CellScale, Waterloo, Ontario). Cylinders (1 mm diameter, 0.5 mm tall) of SU8 photoresist were microfabricated and affixed to pure tungsten filaments (0.156 mm diameter, 59.6 mm length). Matrigel substrates were generated with a height of 450 µm, and indented to a depth of 150 µm at a strain rate of 0.44% s^{-1}. Young's modulus was then calculated as the slope of the linear region (0.04-0.08 strain) of the engineering stress vs. strain plot to remove the influence of a tow region resulting from surface engagement. Young's moduli of suspended DexMA fiber matrices were measured by microindentation with identical indenters as describe above. Samples were indented to a depth of up to 200 µm at an indentation speed of 2 µm s^{-1}. As previously described (Baker et al., 2015), Young's modulus was approximated assuming the material behaves as an elastic membrane using the following equation:

$$F = \frac{Et\pi\delta^3(r_o^2 - r_i^2)}{2(r_o - r_i)^4(1 - \nu)}$$

where t is the membrane thickness (10 µm, as determined by confocal microscopy), r_o is the membrane radius (1 mm), r_i is the indenter radius (0.5 mm), ν is the Poisson ratio (0.5), F is the indentation force, δ is the indentation depth, and E is Young's modulus.

3.6.7 RGD functionalization and seeding on DexMA fibers

DexMA fibers were functionalized with the cell-adhesive peptide CGRGDS (RGD; Peptides International, Louisville, KY). An RGD concentration of 4 mM was used for all studies. RGD was coupled to available methacrylates via Michael-type addition. Briefly, the peptide was dissolved in milli-Q water containing HEPES (50 mM), phenol red (10 µg ml^{-1}), and 1 M NaOH to adjust the pH to 8.0. 200 µL of this solution was added to each substrate and incubated for 30 minutes at room temperature. Following RGD functionalization, substrates were rinsed 2x with PBS before cell seeding. For network formation studies on DexMA fibers, ECs were trypsinized, resuspended in 1.5% (w/v) methylcellulose supplemented EGM-2 to increase media viscosity, and seeded at 6×10^4 cells cm^{-2}.

3.6.8 Pharmacologic contractility inhibition

Blebbistatin, Y27362, and Cytochalasin D (Santa Cruz Biotechnology, Dallas, TX) were diluted to stock concentrations and stored following the manufacturer's recommendation. Blebbistatin was utilized at 50 µM in DMSO, Y27362 at 30 µM in milli-Q water, and Cytochalasin D at 1 µM in DMSO, and samples were treated with pharmacologics at the point of seeding.

3.6.9 VE-cadherin disruption

EGTA was used to chelate calcium ions, as VE-cadherin engagement at cell-cell adhesions is calcium dependent. Formed EC networks were incubated with 5 mM EGTA at 37°C for 30 minutes and immediately fixed and processed for fluorescent imaging.

3.6.10 Bead displacement quantification

For bead displacement analysis to quantify matrix reorganization, time-lapse imaging on a Zeiss LSM 800 confocal microscope (Zeiss, Oberkochen, Germany) was performed, imaging at minimum every 10 minutes for 12 hours. Images were converted to maximum intensity projections, and single particle tracking was completed with TrackMate, a freely available ImageJ plugin (Tinevez et al., 2017), and custom Matlab scripts. Beads were detected at each time point using a difference of Gaussians (DoG) detector with an estimated particle diameter of 5 μm and threshold of 1.0 with use of a median filter. Single particle tracking was completed using a linear assignment problem tracker with a linking max distance and gap-closing max distance of 50 μm and gap-closing max frame gap of 5 frames. Tracks were filtered to only contain particles detected throughout the entire time-lapse, and total displacement for each particle was calculated via custom Matlab scripts.

3.6.11 Fluorescent staining and microscopy

ECs on Matrigel and DexMA fibers were first fixed in 4% paraformaldehyde for 10 min at room temperature. To stabilize the fibers for long term storage, DexMA samples were crosslinked in 2 mL LAP solution (1.0% w/v) and exposed to UV light (100 mW cm^{-2}) for 30 seconds. To stain the actin cytoskeleton and nuclei, cells were permeabilized in PBS solution containing Triton X-100 (5% v/v), sucrose (10% w/v), and magnesium chloride (0.6% w/v), blocked in 1% bovine serum albumin, and stained simultaneously with phalloidin and DAPI. For fibronectin and VE-cadherin immunostaining, samples were fixed and permeabilized (cells were not permeabilized for fibronectin stain) as explained above, blocked for 1 h in 10% fetal bovine serum, and incubated with fibronectin antibody (1:2000, Sigma #F6140) or VE-cadherin (F-8) Alexa-Fluor 488 primary antibody (1:500, Santa Cruz Biotechnology, Dallas, TX) for 1 h at room temperature. Fixed samples and time-lapse microscopy were imaged on a Zeiss LSM 800 laser scanning confocal microscope. Unless otherwise specified, images are presented as maximum intensity projections. Cell area/perimeter and pore analyses were performed using custom Matlab scripts.

3.6.12 Statistics

Statistical significance was determined by one-way analysis of variance (ANOVA) with post-hoc analysis (Tukey test) or Student’s t-test where appropriate, with significance indicated by $p<0.05$. Sample size is indicated within corresponding figure legends and all data are presented as mean ± standard deviation.

3.7 Supplementary Figures

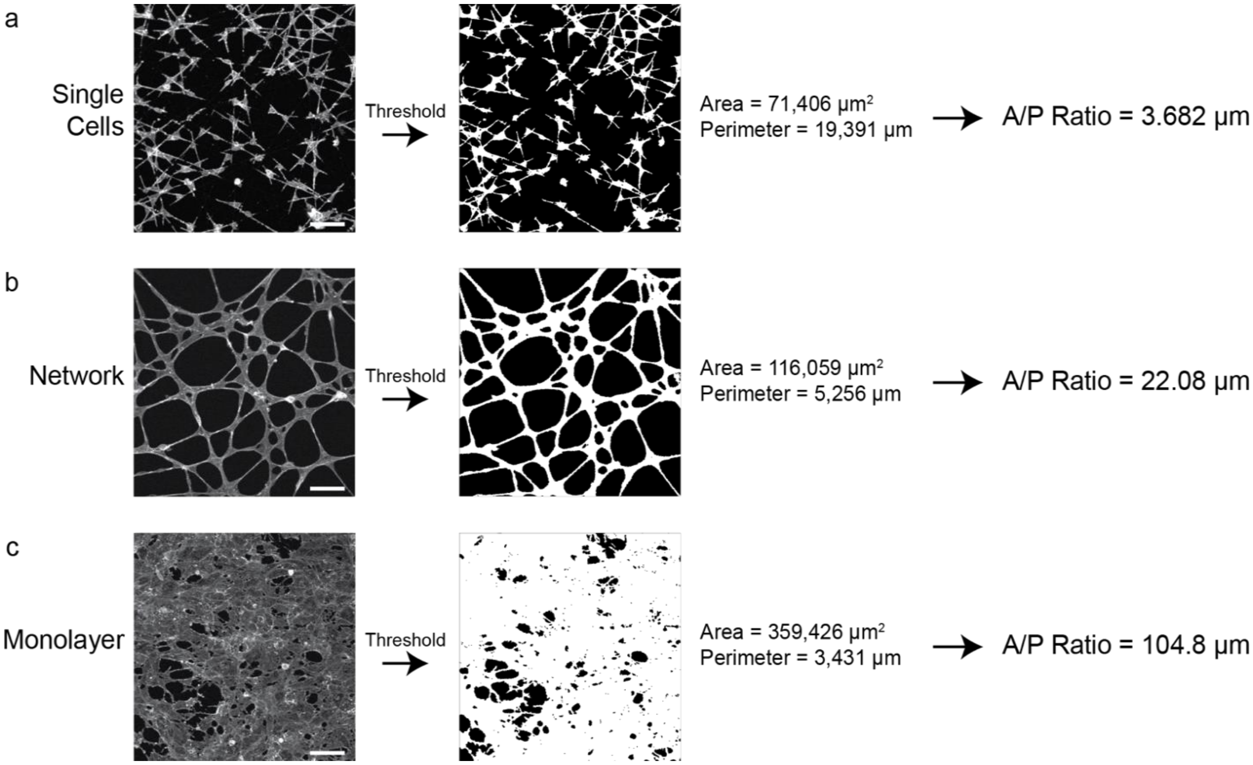
a
Single Cells
Threshold
Area = 71,406 µm²
Perimeter = 19,391 µm
A/P Ratio = 3.682 µm
b
Network
Threshold
Area = 116,059 µm²
Perimeter = 5,256 µm
A/P Ratio = 22.08 µm
c
Monolayer
Threshold
Area = 359,426 µm²
Perimeter = 3,431 µm
A/P Ratio = 104.8 µm

Supplementary Figure 3.1: A/P ratio quantification for three possible cellular phenotypes. Area/perimeter ratio was quantified by calculating the total area and perimeter of thresholded fluorescent images of phalloidin-stained ECs via custom Matlab scripts. a) Single cells that are not interconnected have a small total area and large perimeter, leading to a relatively low area/perimeter ratio value (between 0 and 10). b) Interconnected cellular networks have an intermediate total area and perimeter, leading to an intermediate area/perimeter ratio value (between 10 and 30). c) Monolayers have a large total area and small perimeter, leading to a relatively high area/perimeter ratio value (greater than 30). Scale bars: 100 µm.

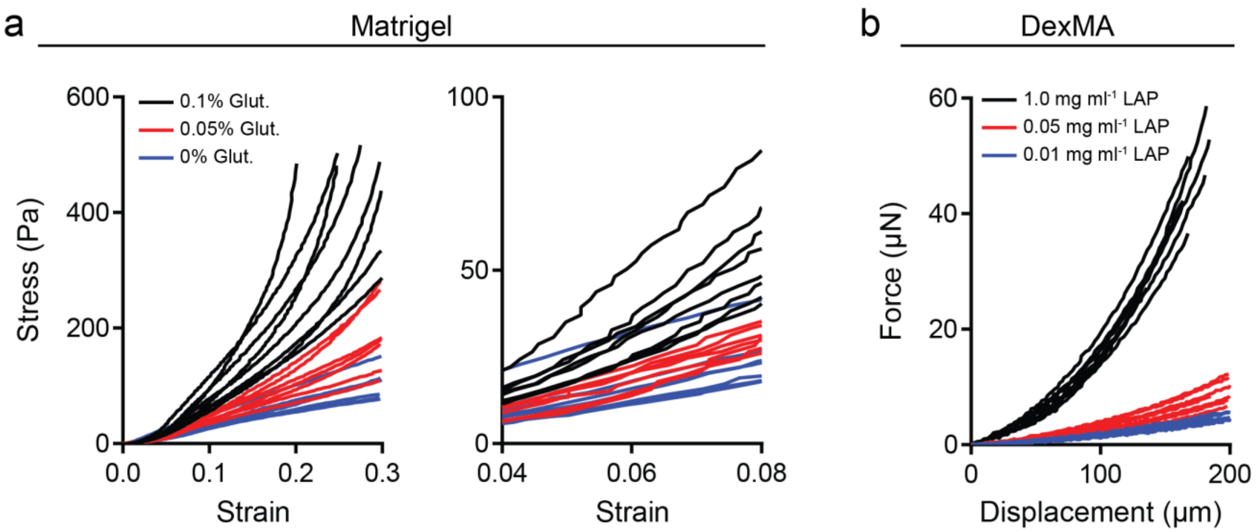

Supplementary Figure 3.2: Mechanical characterization of Matrigel and DexMA fibrous matrices. a) Stress-strain curves of Matrigel crosslinked with variable concentrations of glutaraldehyde. Right plot shows linear region used to quantify Young's modulus for each condition. b) Force response of DexMA fibrous matrices as a function of indentation depth of networks crosslinked with varying concentrations of LAP photoinitiator.

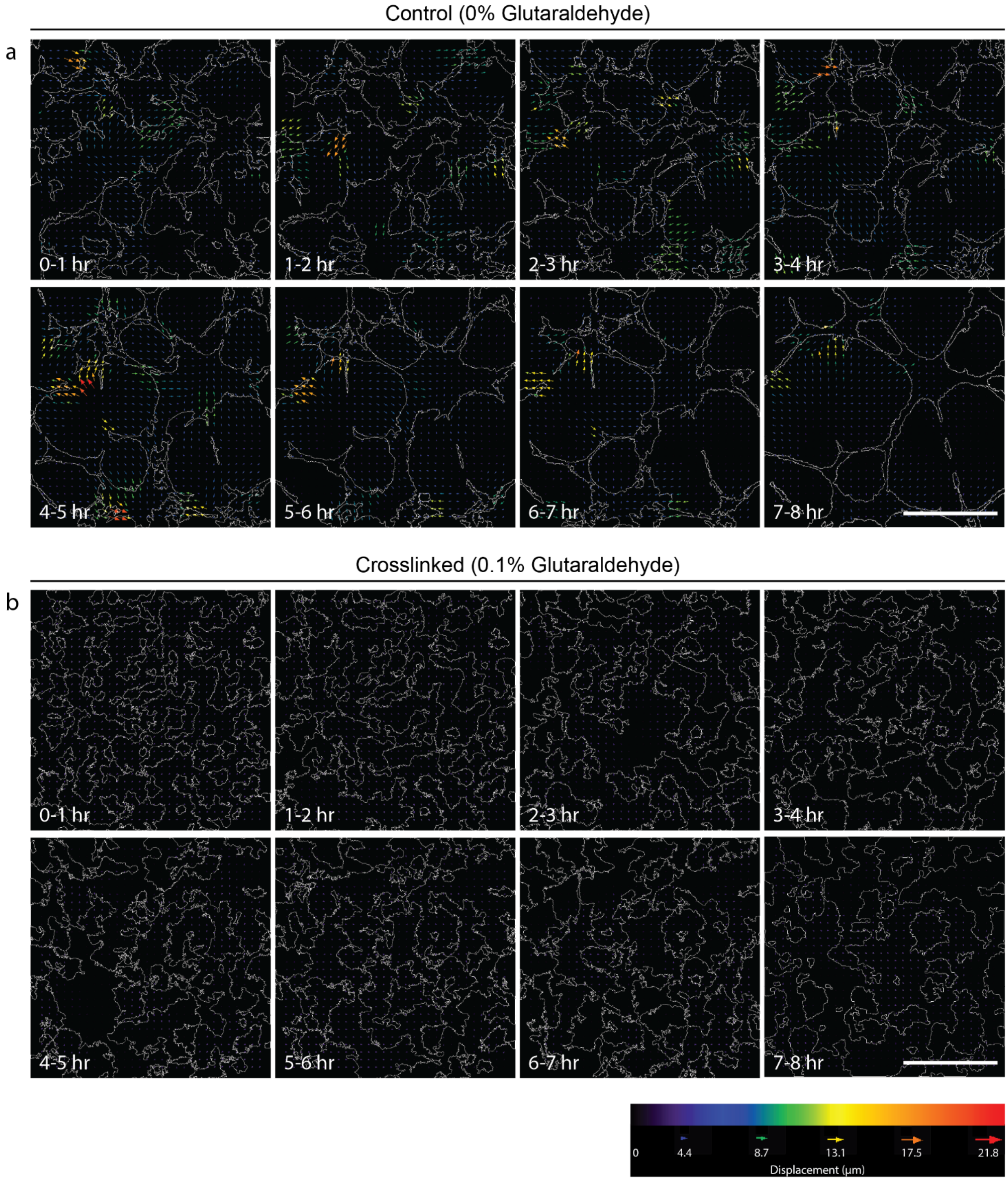
Control (0% Glutaraldehyde)
a
0-1 hr
1-2 hr
2-3 hr
3-4 hr
4-5 hr
5-6 hr
6-7 hr
7-8 hr
Crosslinked (0.1% Glutaraldehyde)
b
0-1 hr
1-2 hr
2-3 hr
3-4 hr
4-5 hr
5-6 hr
6-7 hr
7-8 hr
0
4.4
8.7
13.1
17.5
21.8
Displacement (µm)

Supplementary Figure 3.3: Matrix reorganization during EC network formation on Matrigel. Vector plots depict Fl-μS motion with respective EC structure outlined in white for individual 1 hour increments on a) untreated control substrates demonstrating high levels of matrix deformation and organization in contrast to b) glutaraldehyde crosslinked Matrigel. Scale bars: 500 μm.

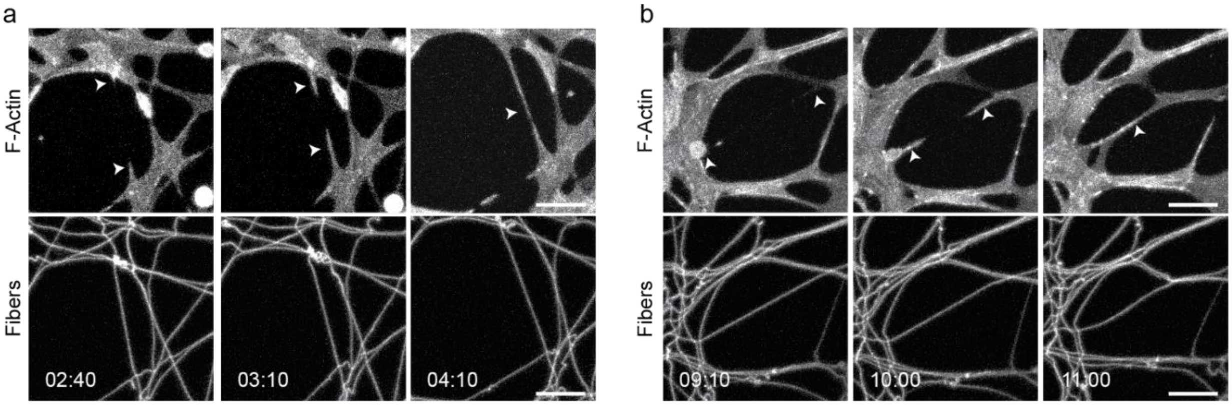
a
b
F-Actin
Fibers
02:40
03:10
04:10
F-Actin
Fibers
09:10
10:00
11:00

Supplementary Figure 3.4: Cellular extensions and inter-connections occur throughout network formation. Confocal fluorescent images of ECs and rhodamine-labeled fibers showing cellular extensions and the formation of cell-cell interconnections during (a) the first four hours of network formation and (b) after the first four hours of network formation, during network stabilization. Scale bars: 50 µm.

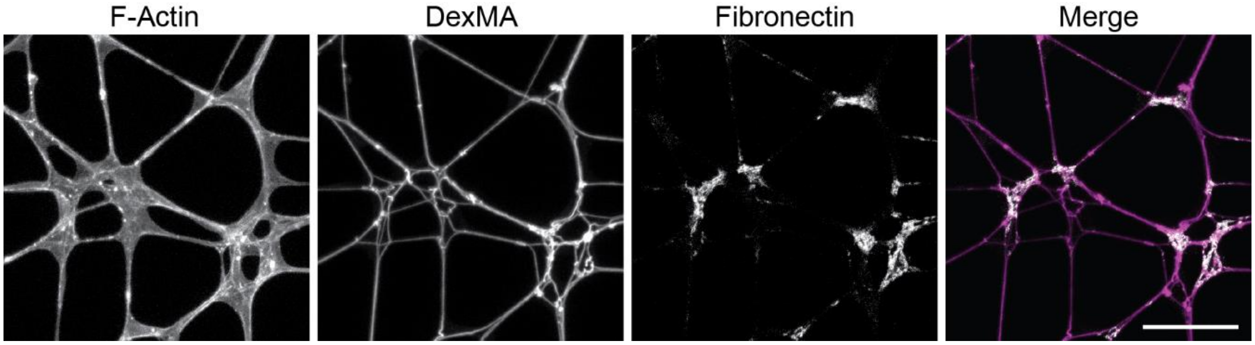
F-Actin
DexMA
Fibronectin
Merge

Supplementary Figure 3.5: Fibronectin secretion during EC network formation on fibrous DexMA matrices. Confocal fluorescent images of ECs, rhodamine-labeled fibers (magenta), and fibronectin (grayscale) after 24 hours of culture on control matrices. Fibronectin secretion was noted at network nodes corresponding to locations with a high relative fiber density due to cell-mediated matrix reorganization. Scale bar: 100 µm.

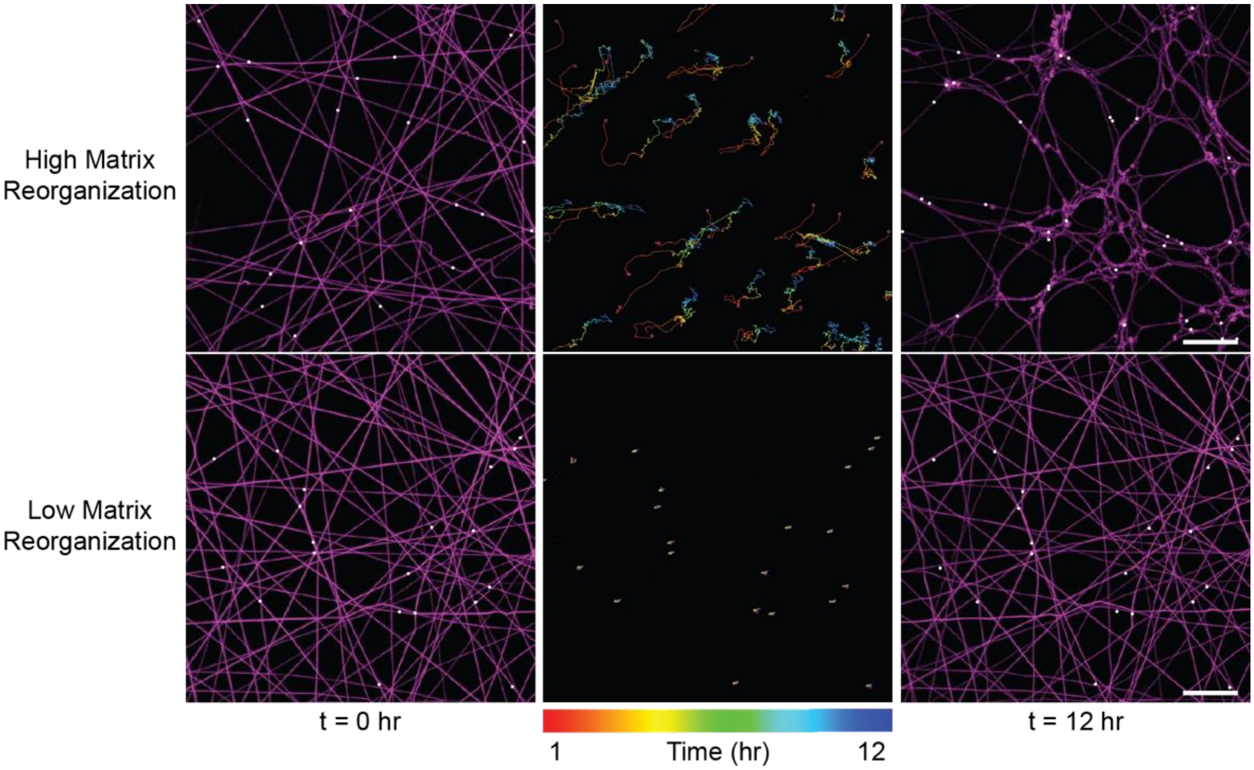
High Matrix Reorganization
Low Matrix Reorganization
t = 0 hr
1
Time (hr)
12
t = 12 hr

Supplementary Figure 3.6: Quantification of Fl-µS displacement using TrackMate. Matrix reorganization was quantified by calculating the sum of the mean squared displacement of Fl-µS (white) embedded in rhodamine-labeled DexMA fibers (magenta) over 12 hours using TrackMate, an ImageJ plugin (Tinevez et al., 2017). Conditions that allow for high levels of matrix reorganization demonstrate large displacements, with rapid Fl-µS movement over the first four hours. Conditions with low matrix reorganization exhibit limited Fl-µS displacement. Scale bars: 100 µm.

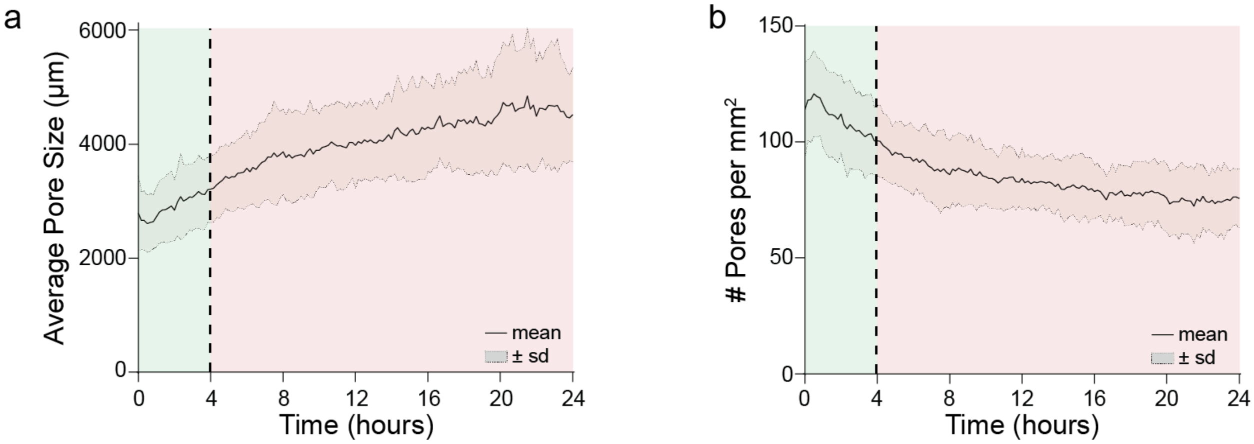

Supplementary Figure 3.7: Quantification of matrix remodeling via analysis of pores during EC network formation on fibrous DexMA matrices. Quantitative analysis of pores within DexMA fiber matrices over a 24-hour time-lapse series of network formation. a) Average pore size increases and b) total number of pores decreases during the formation of an EC network, supporting the observation that ECs bundle and condense matrix fibrils as they spread and interconnect; $n \geq 8$.

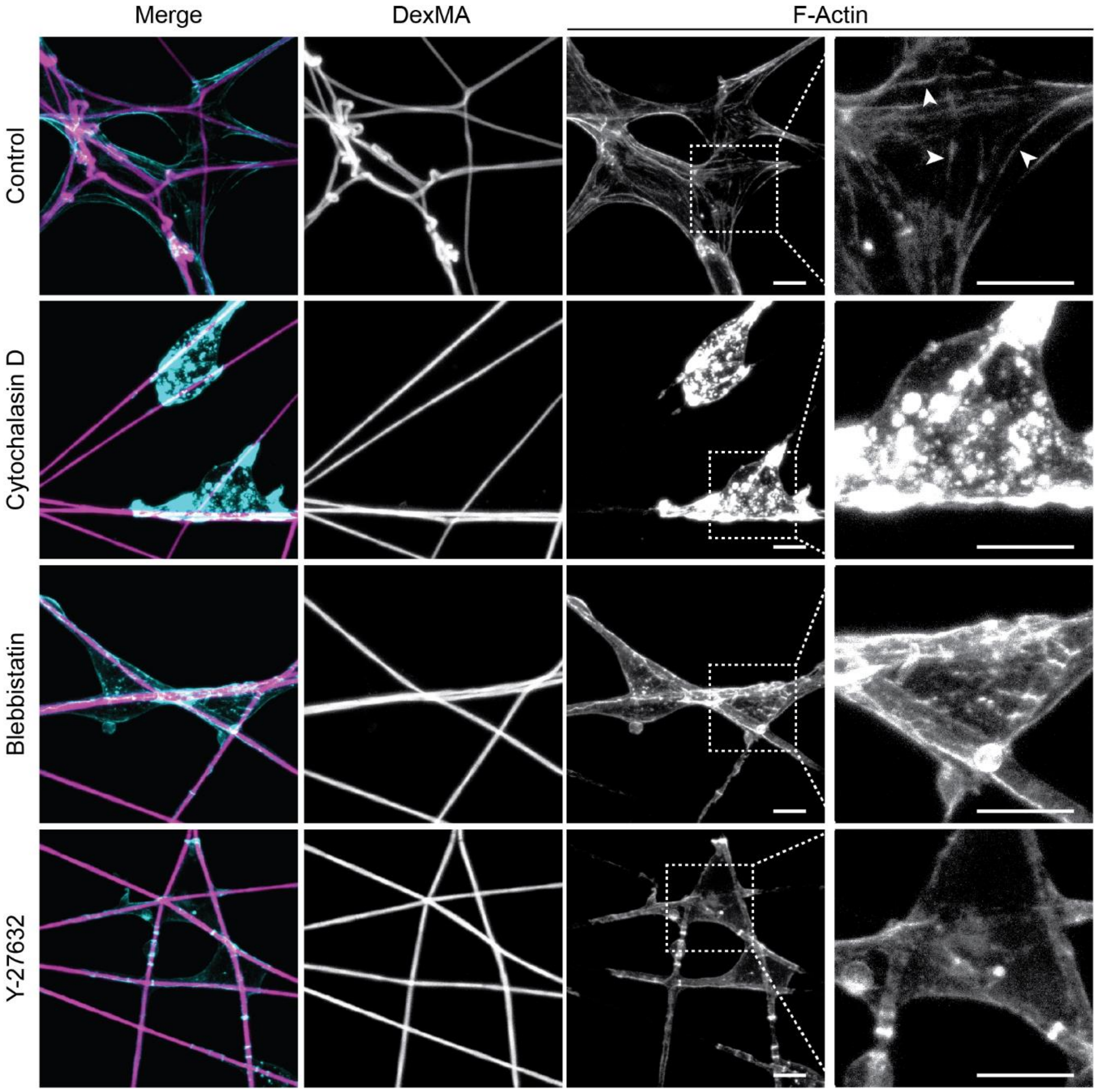
Merge
DexMA
F-Actin
Control
Cytochalasin D
Blebbistatin
Y-27632

Supplementary Figure 3.8: Analysis of cell cytoskeletal structure after treatment with pharmacologic inhibitors of actomyosin contractility. High resolution (40x) confocal fluorescence images of phalloidin-stained ECs and rhodamine-labeled fibers after 24 hours of culture with the indicated pharmacologic inhibitor treatment; actin (cyan), fibers (magenta). Dashed boxes indicate locations of higher magnification images depicting variable cytoskeletal structure between different conditions (far right). Scale bars: 10 μm.

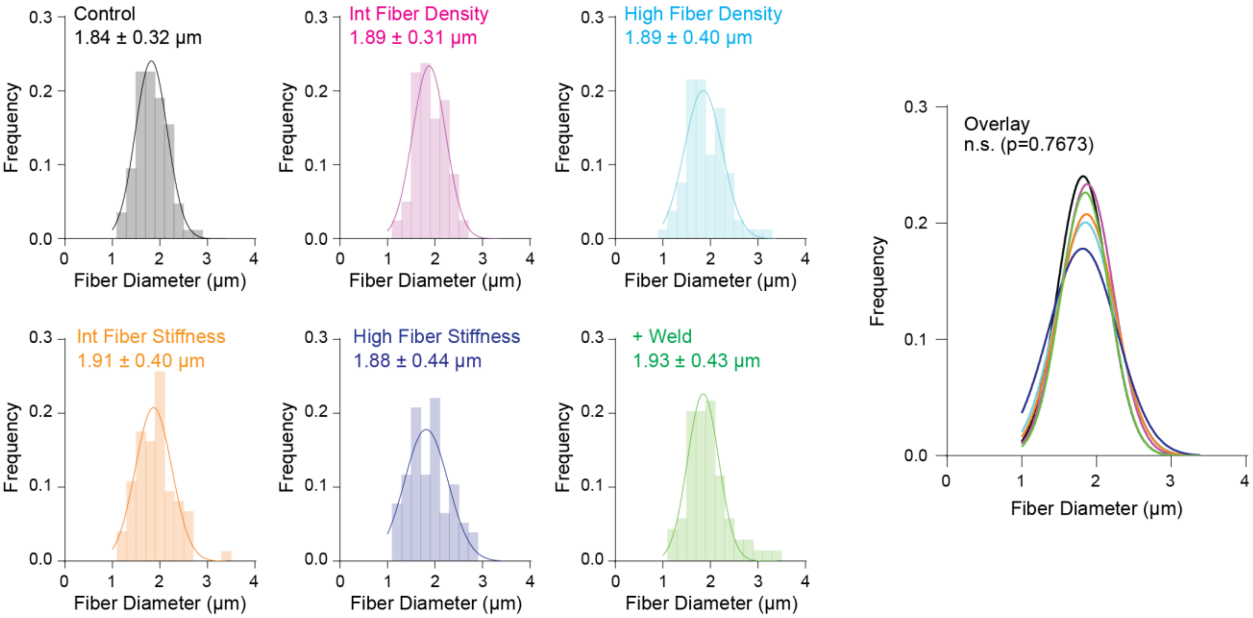

Supplementary Figure 3.9: Fiber diameter as a function of physical matrix perturbations. Histograms showing the distribution of diameter across a population of DexMA fibers with indicated matrix perturbations: control (black), intermediate fiber density (magenta), high fiber density (cyan), intermediate fiber stiffness (orange), high fiber stiffness (purple), and inter-fiber crosslinking via welding (green). For each condition, diameters of $n \geq 69$ fibers were quantified; fitted curves assume a Gaussian distribution. Overlay of fitted curves show no statistically significant difference in mean diameter across any matrix perturbation as determined by ANOVA (p=0.7673).

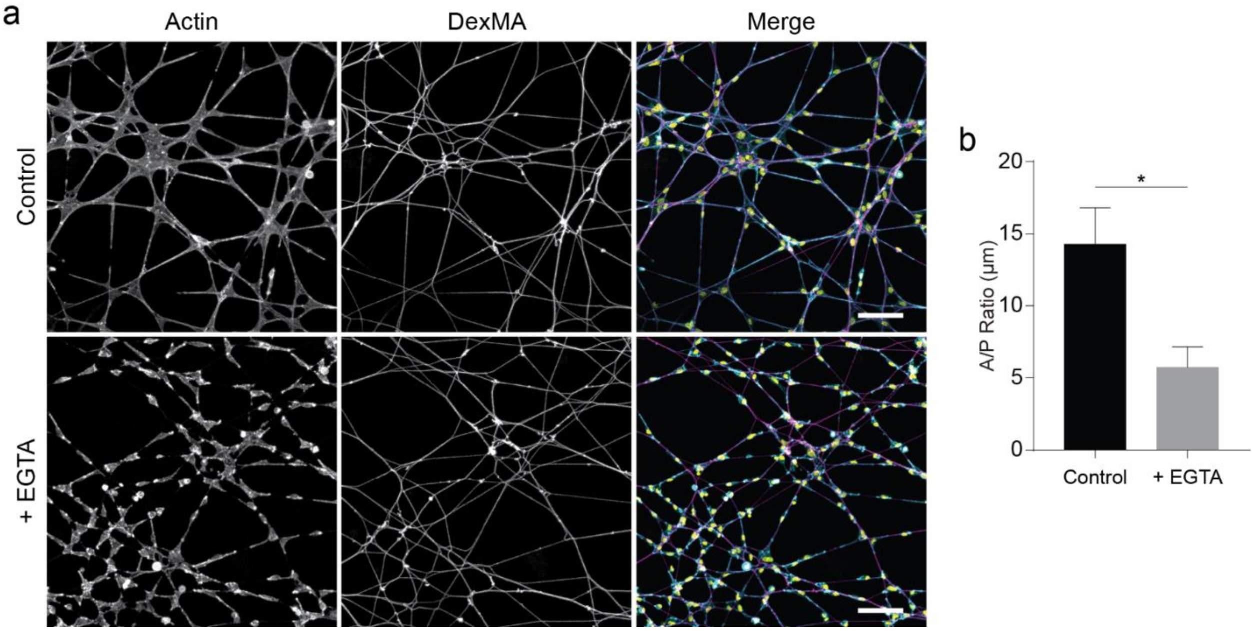
a
Actin
DexMA
Merge
Control
+ EGTA
b
A/P Ratio (µm)
20
15
10
5
0
*
Control
+ EGTA

Supplementary Figure 3.10: VE-cadherin disruption via calcium chelation alters network architecture. a) Representative confocal fluorescent images of phalloidin-stained ECs and rhodamine-labeled fibers with and without EGTA treatment to chelate free calcium ions and disrupt cadherin-rich cell-cell adhesions; actin (cyan), fibers (magenta), and nuclei (yellow). (b) Cell area/perimeter ratio after 24 hours of culture and EGTA treatment. Scale bars: 100 µm. Data presented as mean ± std; n = 6; * P<0.05.

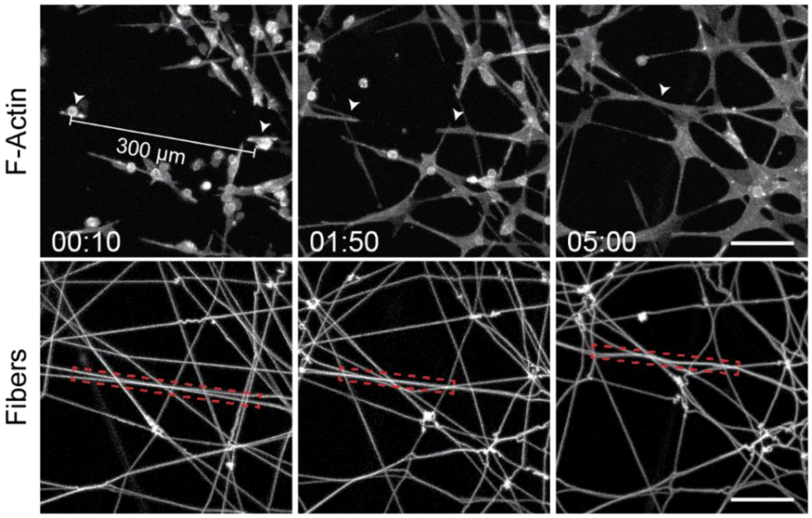
F-Actin
Fibers
300 µm
00:10
01:50
05:00

Supplementary Figure 3.11: Long-range cellular extensions during network formation. Representative confocal fluorescent images of ECs and rhodamine-labeled fibers depicting long-range interactions between cells positioned approximately 300 microns apart. Scale bars: 100 µm.

Supplementary Movie 3.1: EC network formation and matrix reorganization on Matrigel. Representative confocal fluorescence time-lapse movie of EC (cyan) network formation on Matrigel with embedded Fl-µS (white). Scale bar: 250 µm.
https://static-content.springer.com/esm/art%3A10.1038%2Fs41598-018-37044-1/MediaObjects/41598_2018_37044_MOESM1_ESM.avi

Supplementary Movie 3.2: EC monolayer formation on glutaraldehyde-crosslinked Matrigel with limited matrix reorganization. Representative confocal fluorescence time-lapse movie of ECs (cyan) on 0.1% glutaraldehyde crosslinked Matrigel with embedded Fl-µS (white). Scale bar: 250 µm.
https://static-content.springer.com/esm/art%3A10.1038%2Fs41598-018-37044-1/MediaObjects/41598_2018_37044_MOESM2_ESM.avi

Supplementary Movie 3.3: EC network formation and matrix reorganization on synthetic fibrous DexMA matrices. Representative confocal fluorescence 24-hour time-lapse movie of EC (cyan) network formation on soft (0.01 mg ml^{-1} LAP; 1.5 kPa) synthetic DexMA fiber matrices (magenta). Scale bar: 100 µm.
https://static-content.springer.com/esm/art%3A10.1038%2Fs41598-018-37044-1/MediaObjects/41598_2018_37044_MOESM3_ESM.avi

Supplementary Movie 3.4: Matrix recruitment and cell spreading during first four hours of network formation on DexMA matrices. Representative confocal fluorescence time-lapse movie of the first four hours of EC (cyan) network formation on soft (0.01 mg ml^{-1} LAP; 1.5 kPa) synthetic DexMA fiber matrices (magenta). Scale bar: 100 µm.
https://static-content.springer.com/esm/art%3A10.1038%2Fs41598-018-37044-1/MediaObjects/41598_2018_37044_MOESM4_ESM.avi

Supplementary Movie 3.5: EC monolayer formation on stiff fibrous DexMA matrices with negligible matrix reorganization. Representative confocal fluorescence 12-hour time-lapse movie of ECs (cyan) on stiff (0.1 mg ml^{-1} LAP; 16.7 kPa) synthetic DexMA fiber matrices (magenta). Scale bar: 100 µm.
https://static-content.springer.com/esm/art%3A10.1038%2Fs41598-018-37044-1/MediaObjects/41598_2018_37044_MOESM5_ESM.avi

Chapter 4: Myofibroblast Activation in Synthetic Fibrous Matrices Composed of Dextran Vinyl Sulfone

4.1 Authors

Christopher D. Davidson, Danica Kristen P. Jayco, Daniel L. Matera, Samuel J. DePalma, Harrison L. Hiraki, William Y. Wang, Brendon M. Baker

4.2 Abstract

Mechanical interactions between fibroblasts and their surrounding extracellular matrix (ECM) guide fundamental behaviors such as spreading, migration, and proliferation that underlie disease pathogenesis. The challenges of studying ECM mechanics *in vivo* have motivated the development of *in vitro* models of the fibrous ECM in which fibroblasts reside. Natural materials such as collagen hydrogels bear structural and biochemical resemblance to stromal ECM, but mechanistic studies in these settings are often confounded by cell-mediated material degradation and the lack of structural and mechanical tunability. Here, we established a new material system composed of electrospun dextran vinyl sulfone (DexVS) polymeric fibers. These fibrous matrices exhibit mechanical tunability at both the single fiber (80 – 340 MPa) and bulk matrix (0.77 – 11.03 kPa) level, as well as long-term stability in mechanical properties over a two-week period. Cell adhesion to these matrices can be either user-defined by functionalizing synthetic fibers with thiolated adhesive peptides or methacrylated heparin to sequester cell-derived ECM

proteins. We utilized DexVS fibrous matrices to investigate the role of matrix mechanics on the activation of fibroblasts into myofibroblasts, a key step of the fibrotic progression. In contrast to previous findings with non-fibrous hydrogel substrates, we find that fibroblasts in soft and deformable matrices exhibit increased spreading, focal adhesion formation, proliferation, and myofibroblast activation as compared to cells on stiffer matrices with equivalent starting architecture.

4.3 Introduction

Interactions with the extracellular matrix (ECM) guide fundamental cell behaviors including spreading, migration, and proliferation, and thus play an important role in connective tissue homeostasis, repair processes, and pathogenesis (Discher et al., 2005; Vogel & Sheetz, 2006). Due to the diversity in ECM structure and mechanics throughout various tissues, cells are exposed to a wide range of physical cues and must appropriately sense and respond to these signals over time to properly maintain tissue form and function (Ingber, 2003). Cells mechanically engage their physical microenvironment through integrin-based adhesion complexes, or focal adhesions. These mechanoresponsive signaling hubs link the ECM to the actin cytoskeleton, allowing cells to probe and respond to the physical attributes of their surroundings (Bershadsky et al., 2003; Geiger et al., 2009; Gumbiner, 1996). Significant recent work has demonstrated the importance of matrix elastic modulus in regulating focal adhesions and cell behavior (Dupont et al., 2011; Engler et al., 2006; Guilak et al., 2009; Klein et al., 2009), but cells have also been shown to sense a wide range of other physical properties including topography (Kulangara & Leong, 2009), porosity (Zeltinger et al., 2001), and viscoelasticity (Chaudhuri et al., 2015).

It has long been known that abnormal tissue mechanics and consequent altered cellular mechanoresponse is a component of many diseases (Ingber, 2003). However, elucidating the role of mechanics during disease pathogenesis *in vivo* has proven difficult due to the limited ability to experimentally modulate properties of native tissues. Thus, many have turned to *in vitro* models to study how ECM physical properties regulate cell behavior (Li et al., 2017). Natural fibrous biomaterials, such as collagen and fibrin hydrogels, are used extensively due to their structural and biochemical similarity to native connective tissues (Ahmed et al., 2008; Parenteau-Bareil et al., 2010). However, mechanistic studies in these settings are confounded by the rapid production of cell-secreted matrix, impact of cell-mediated ECM proteolysis, and lack of orthogonal control over structural and mechanical characteristics (Li et al., 2017). Furthermore, the limited stability of these hydrogel matrices due to degradation and/or contraction can hinder long term culture (depending on protein density and cell type) (Kniazeva & Putnam, 2009; Nakagawa et al., 1989). Conversely, synthetic hydrogels, such as polyacrylamide or poly(ethylene glycol) (PEG), offer control over matrix elastic modulus, ligand presentation, and degradability, making them ideal for mechanistic studies (Li et al., 2017). However, synthetic hydrogels are nanoporous, mechanically isotropic and homogeneous at the cell-scale. This class of materials lacks the discrete fibrous structure and resulting complex mechanical behavior of native collagen-rich connective tissues.

Electrospinning has been extensively used to fabricate synthetic fibrous scaffolds that mimic the structure of native tissue ECMs (Pham et al., 2006; Sill & von Recum, 2008). A simple and versatile approach, electrospinning can produce scaffolds from a variety of synthetic and natural polymers that facilitate cell attachment and viability (Mauck et al., 2009). By modulating the electrospinning process and solution parameters, electrospun scaffolds have shown high levels of control over matrix topography, such as fiber diameter and pore size. Recent work from our lab has combined the electrospinning technique with photo-crosslinkable polymer chemistry to generate matrices composed of methacrylated dextran (DexMA) fibers with stiffness tuned via light exposure (Baker et al., 2015). While the high degree of control over ECM architectural and mechanical properties has shed insight on how cells interpret the physical properties of fibrous matrices during cell spreading (Baker et al., 2015), migration (Wang et al., 2019), and multicellular assembly (Davidson et al., 2019a), ester hydrolysis mediated degradation of crosslinked DexMA networks has prevented cell studies longer than a few days in this setting.

Fibrosis is one context where an improved understanding of longer-term mechanosensing in fibrous microenvironments would be invaluable. Fibrosis is associated with numerous heart, lung, and vascular diseases, and is implicated in an estimated 45% of all deaths in the developed world (Hinz et al., 2012; Wynn, 2007). The principal cells that drive this disease process are myofibroblasts (MFs), characterized by heightened rates of proliferation and the expression of alpha smooth muscle actin (α-SMA) (Hinz et al., 2001a, 2007, 2012). These cells gradually contribute to organ stiffening, contraction, and eventual failure via excessive ECM synthesis, crosslinking, and application of contractile forces. Profibrotic microenvironmental cues in stromal connective tissues are known to activate cells residing within the tissue or recruited from circulation into MFs (Darby et al., 1990; Gabbiani, 2003; Singer & Clark, 1999). While our understanding of the transition from normal to fibrotic tissue is still incomplete, it is understood that profibrotic soluble signals such as TGF-β1 are potentiated by matrix mechanical cues (Arora et al., 1999; Caliari et al., 2016a; Goffin et al., 2006; Hinz et al., 2001b; Marinkovic et al., 2012). For example, experiments varying the Young's modulus of polyacrylamide, PEG, and hyaluronic acid hydrogel surfaces have demonstrated that substrates with higher stiffness promote fibroblast MF activation (measured via expression levels of α-SMA) as compared to low modulus substrates (Balestrini et al., 2012; Benton et al., 2009; Caliari et al., 2016a; Chia et al., 2012; Goffin et al., 2006). However, as these gel surfaces lack fibrillar structure and possess limited potential for cellular remodeling as observed during fibrosis, there remains a need for fibrous materials that are mechanically well-defined, tunable, and stable over long-term culture to provide insight into the dynamics of ECM mechanics throughout this critical disease process.

Here, we aimed to develop a synthetic fibrous matrix resistant to degradation in order to study long-term cellular behavior in the context of MF activation from normal fibroblasts. We synthesized and electrospun photocrosslinkable dextran vinyl sulfone (DexVS) fibrous matrices that are resistant to hydrolytic degradation and therefore mechanically stable over longer-term cell culture. DexVS matrices have controllable architecture through modulation of electrospinning parameters and are mechanically tunable at both the single fiber and matrix levels. Furthermore, the dextran backbone results in protein-resistant fibers that can be functionalized with thiolated peptides or methacrylated heparin via Michael-type addition with free vinyl sulfone groups to allow for cell adhesion and matrix remodeling, respectively. Examining cell behavior on DexVS matrices as a function of matrix stiffness, we find that fibroblasts cultured on soft matrices actively displace and bundle matrix fibers and have larger spread area and focal adhesion area than fibroblasts on stiff, non-deformable matrices. Additionally, contrary to previous studies on 2D elastic hydrogels, we observed higher levels of MF activation when fibroblasts are cultured on soft rather than stiff fibrous matrices in the presence of the pro-fibrotic soluble factor TGF-β1.

4.4 Results and Discussion

4.4.1 DexVS matrix fabrication and mechanical characterization

To model the fibrous microstructure of collagenous stromal tissue where fibrosis begins, we devised a synthetic matrix composed of assemblies of electrospun dextran vinyl sulfone (DexVS) polymeric fibers (**Figure 4.1a**). The polysaccharide dextran was chosen as a polymer backbone given its abundance of hydroxyl groups for modification and previous literature indicating amenability to electrospinning (Borteh et al., 2013; Jiang et al., 2004; Ritcharoen et al., 2008). Furthermore, materials composed of crosslinked dextran have been shown to be resistant to protein adsorption, thereby allowing user-defined control over cell-adhesive ligand type and concentration (Sun et al., 2010). We have previously employed dextran functionalized with methacrylates (DexMA) to investigate short term (less than 2 days) cell response in fibrous matrices with controllable biophysical and biochemical properties (Baker et al., 2015). Over longer durations of cell culture, however, deviations in pH due to the metabolic activity of cultured cells promote ester hydrolysis-mediated degradation of these matrices. To engineer matrices that permit long-term cell culture, we employed vinyl sulfones due to their reactivity, stability after functionalization, and resultant crosslinks lacking hydrolytically cleavable ester bonds (Day et al., 2018). Like methacrylates, vinyl sulfones enable modular material design through functionalization and crosslinking via Michael-type addition or photopolymerization in the presence of photoinitiator.

Matrices were fabricated by electrospinning a solution of DexVS and LAP photoinitiator onto PDMS collection substrates such that fibers were suspended over an array of microfabricated wells (Ø = 2 mm) (**Figure 4.1a**). Thus, cells that adhere within suspended matrices above microwell regions sense the physical cues defined by the architecture and mechanical properties of the fibrous matrix and its anchorage at microwell edges, without the influence of a rigid underlying support surface. As demonstrated previously with DexMA (Baker et al., 2015), various architectural features of DexVS matrices can be tuned by modulating fabrication parameters. The density and alignment of fibers within matrices were controlled by modulating electrospinning duration and the distance between parallel collecting electrodes, respectively (**Figure 4.1b,c**). DexVS fiber diameter and overall matrix thickness were measured via confocal microscopy to be approximately 1.02 ± 0.15 µm and 8.68 ± 0.73 µm, respectively (**Supplementary Figure 4.2**).

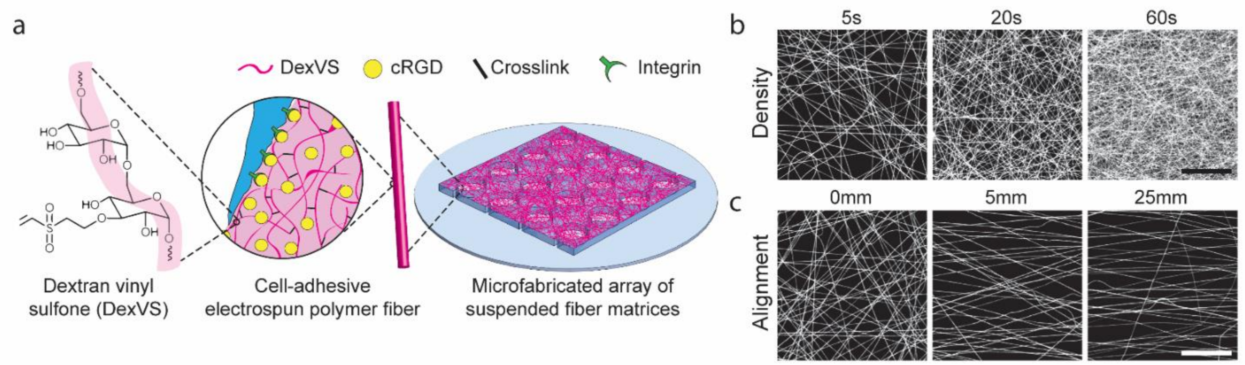
a
DexVS
cRGD
Crosslink
Integrin
HO
HO
OH
HO
OH
O
S
O
Dextran vinyl sulfone (DexVS)
Cell-adhesive electrospun polymer fiber
Microfabricated array of suspended fiber matrices
b
5s
20s
60s
Density
c
0mm
5mm
25mm
Alignment

Figure 4.1: DexVS fibrous matrices with tunable architectural features. (a) Schematic of microfabricated PDMS multi-well substrate possessing a 4 x 4 array of wells, each supporting a suspended matrix of DexVS fibers coupled with RGD to facilitate cell adhesion. Through modulation of the electrospinning fabrication process, networks were fabricated with varying (b) fiber density via fiber collection duration and (c) alignment via controlling the separation distance between two parallel electrodes at the collecting surface. Scale bars: 50 µm.

Beyond architectural features, the stiffness of individual DexVS fibers can be tuned by varying the crosslinking density of the polymer network composing each fiber. Exposure to UV light immediately after electrospinning renders crosslinked fibers water insoluble, allowing a second phase of LAP initiated crosslinking following sample hydration. We hypothesized control over either the duration of UV light exposure or LAP concentration during this second phase of crosslinking could controllably define the stiffness of individual fibers. To directly test this, we determined the Young's moduli of individual fibers via microscale three-point bending tests using AFM (**Figure 4.2a**). Young's modulus of individual fibers was tunable between 80 and 340 MPa and proved more sensitive to LAP concentration than UV exposure time (**Figure 4.2b,c**). These modulus values are within the range of reported values for various fibrous biopolymers such as fibrin or collagen (1-75,000 MPa) (Guthold et al., 2007; Liu et al., 2010b; Yang et al., 2007).

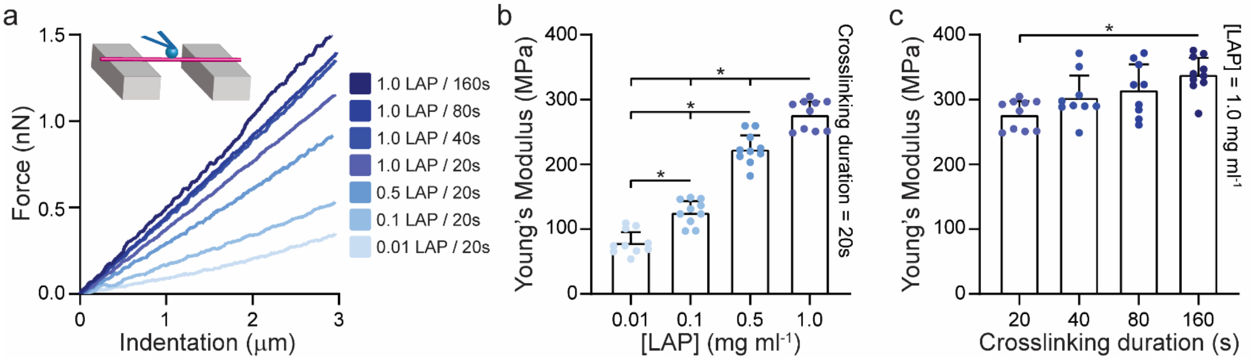

Figure 4.2: Mechanical characterization of single DexVS fibers by AFM three-point bending. (a) Force response as a function of indentation depth of DexVS fibers exposed to variable crosslinking conditions. Respective Young's modulus values for DexVS fibers crosslinked with (b) varying LAP concentration for 20 s, and (c) varying crosslinking time in 1.0 mg ml^{-1} LAP. All data presented as mean ± std; $n \geq 9$; * $p \leq 0.05$.

In addition to mechanically characterizing individual fibers, we also measured stiffness of suspended assemblies of fibers (hereafter referred to as matrix stiffness). We performed microindentation tests of suspended DexVS matrices with a rigid cylindrical indenter to estimate the Young's modulus (**Figure 4.3a**). In agreement with single fiber measurements, increasing both UV exposure time and LAP concentration led to subsequent increases in matrix stiffness. Specifically, we were able to tune the Young's modulus between 0.77 and 11.03 kPa (**Figure 4.3b,c**), allowing for precise control of matrix stiffness over a physiologically relevant range. Additionally, we found that the matrix Young's modulus scales linearly as a function of fiber Young's modulus (**Figure 4.4a**).

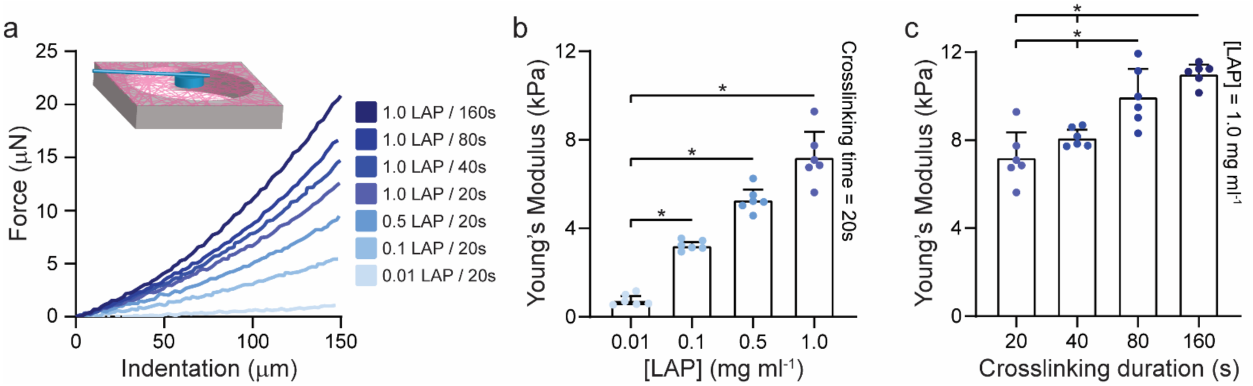

Figure 4.3: Mechanical characterization of suspended DexVS matrices by microindentation with a cylindrical indenter affixed a calibrated cantilever. (a) Force response as a function of indentation depth of DexVS matrices exposed to variable crosslinking conditions. Respective Young's modulus values for DexVS matrices crosslinked with (b) varying LAP concentration for 20 s, and (c) varying crosslinking time in 1.0 mg ml^{-1} LAP. All data presented as mean ± std; n = 6; * $p \leq 0.05$.

To confirm that photocrosslinked DexVS matrices are resistant to ester hydrolysis in conditions relevant to cell culture (**Figure 4.4b**), we performed matrix mechanical testing of substrates incubated in basal media for up to two weeks. No change in Young's modulus was observed over this time period, indicating that DexVS matrices retain mechanical integrity over time in serum-containing media (**Figure 4.4c**). In contrast, DexMA matrices with crosslinks possessing ester bonds (**Figure 4.4b**) revealed evidence of hydrolysis-mediated degradation as marked by gradual reduction in matrix stiffness over time (**Figure 4.4c**). DexMA matrices ultimately exhibited a 62.6% decrease from initial Young's modulus after two weeks in culture conditions.

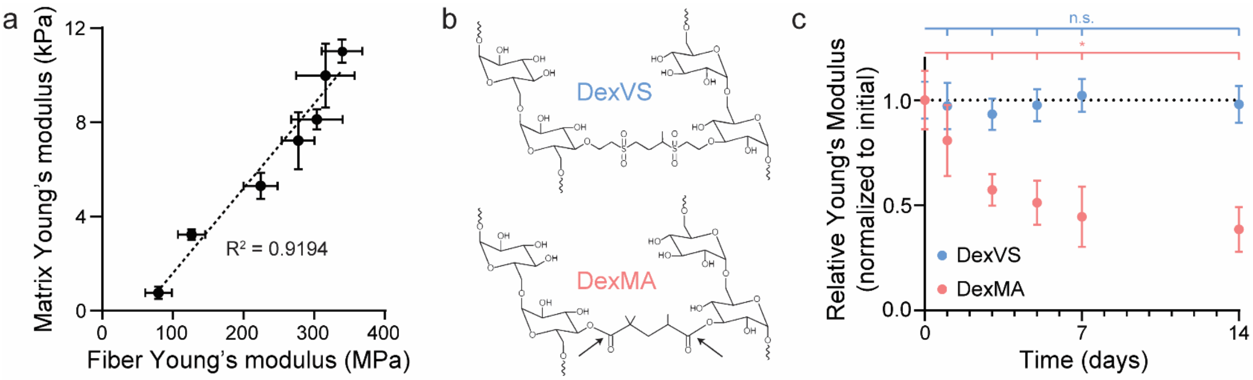

Figure 4.4: Multi-scale and time-dependent mechanical characterization of DexVS matrices. (a) Matrix Young's modulus as a function of single fiber Young's modulus at variable crosslinking conditions. (b) Chemical schematic of crosslinked DexVS and DexMA. Arrows indicate ester bonds susceptible to hydrolysis. (c) Bulk Young's modulus of DexVS and DexMA matrices as a function of incubation time in basal medium for up to two weeks. All data presented as mean ± std; $n \geq 6$; * $p \leq 0.05$.

4.4.2 DexVS functionalization to enable user- or cell-defined adhesion

To study cell behavior on DexVS fibrous matrices, we first functionalized fibers with a cyclized RGD peptide (cRGD) via Michael-type addition to remaining free vinyl sulfones. Fibroblasts were seeded on stiff matrices (E = 11.03 kPa) coupled with cRGD and negligible cell death was noted following overnight culture (**Supplementary Figure 4.3**). Cell attachment and spreading proved highly sensitive to the coupling concentration of cRGD, with limited cell attachment noted in the absence of adhesive ligand functionalization (**Figure 4.5a,b**). As cell attachment and spreading was maximal at 100 µM, this concentration was utilized for all subsequent studies (**Figure 4.5b**, **Supplementary Figure 4.4**). Furthermore, we next aimed to confirm that DexVS matrices do not passively adsorb serum-borne ECM proteins, as this could lead to confounding or uncharacterized effects on cell mechanosensing and behavior. Matrices soaked in collagen, fibronectin, or fetal bovine serum without RGD functionalization demonstrated limited NHLF attachment and lower levels of spreading as compared to fibers functionalized with cRGD (**Figure 4.5c,d**). These results indicate that DexVS does not allow passive adsorption of proteins, but instead requires functionalization of cysteine-terminated ligands to facilitate cell attachment.

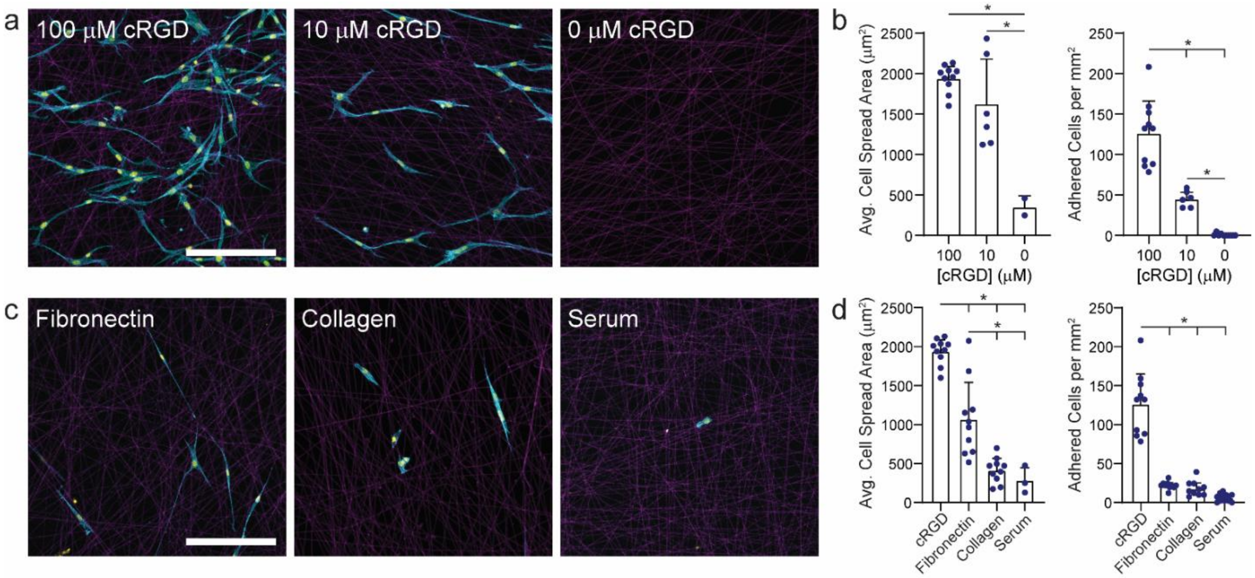

Figure 4.5: DexVS functionalization with cell-adhesive peptides and passive adsorption of proteins. Confocal fluorescent images of NHLFs cultured on DexVS matrices functionalized with (a) variable cRGD concentrations and (c) soaked in various matrix proteins; actin (cyan), DexVS fibers (magenta), nuclei (yellow). Average cell spread area and number of adhered cells as a function of (b) cRGD concentration and (d) protein functionalization. Scale bars: 200 µm. All data presented as mean ± std; n ≥ 6; * $p < 0.05$.

User-defined control over adhesive ligand type and density can be beneficial for mechanistic studies of short-term processes such as cell spreading. However, during longer-term biological processes or in native tissue settings, cell-ECM interactions are bidirectional; cells not only receive physical and biochemical signals from the ECM, but also reciprocally alter encoded signals through modification of the ECM (Bonnans et al., 2014). Heparin sulfate proteoglycans found ubiquitously throughout all tissues bind a plethora of cell secreted ECM proteins and growth factors for subsequent presentation to cells (Bishop et al., 2007; Martino et al., 2013). To imbue protein adsorption-resistant DexVS matrices with the ability to actively bind cell-secreted matrix components, we synthesized heparin methacrylate (HepMA) and functionalized matrices with this structural analog to heparan sulfate. HepMA was covalently conjugated into the polymer network composing DexVS fibers through radical-initiated covalent crosslinks formed between methacrylate and vinyl sulfone groups. To examine the effect of heparin incorporation on cell-secreted ECM sequestration, we seeded NHLFs on cRGD functionalized DexVS matrices with or without HepMA functionalization and stained for fibronectin (**Figure 4.6a**). HepMA functionalization corresponded to significantly more fibronectin bound to synthetic fibers as evident by higher fluorescence intensity than controls (**Figure 4.6b**). No difference in fibronectin staining intensity was noted between soft (E = 0.77 kPa) and stiff (E = 11.03 kPa) HepMA functionalized matrices (**Figure 4.6b**). These results demonstrate an additional means to facilitate cell adhesion to DexVS matrices, where addition of heparin actively sequesters cell-generated ECM components, such as fibronectin, to the cellular microenvironment.

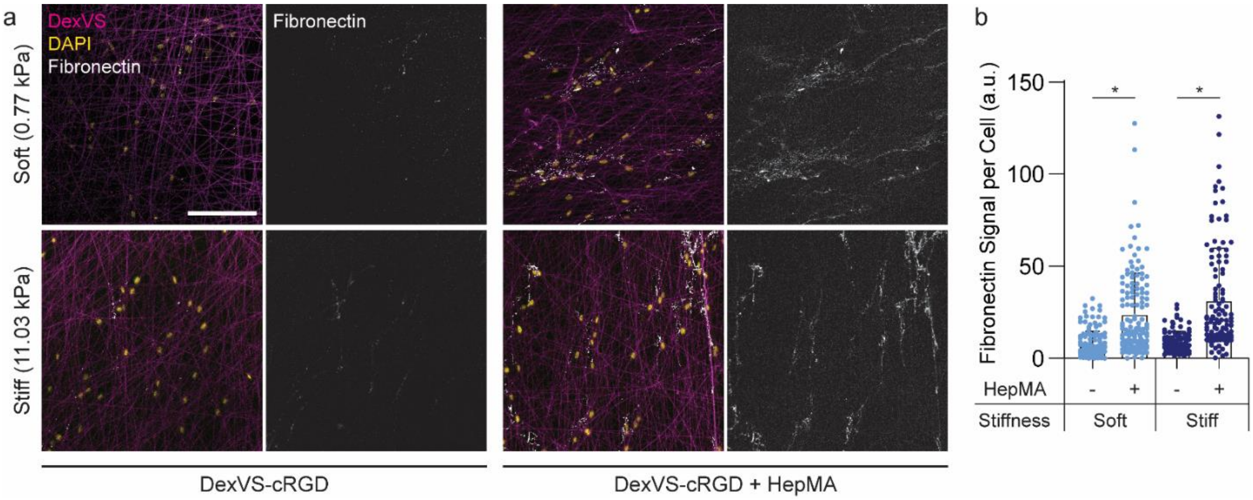

Figure 4.6: HepMA functionalization increases binding of cell-secreted fibronectin to DexVS fibers. (a) Confocal fluorescent images of fibronectin (white), DexVS fibers (magenta), and nuclei (yellow). (b) Quantification of fibronectin signal per cell as a function of matrix stiffness and HepMA functionalization. Scale bar: 200 µm. All data presented as mean ± std; $n \geq 104$; * $p < 0.05$.

4.4.3 Effect of DexVS fibrous matrix stiffness on cell behavior

While cellular mechanosensing of the fibrillar microenvironment plays a critical role in tissue homeostasis and disease progression (Discher et al., 2005; Ingber, 2003; Vogel & Sheetz, 2006), many *in vitro* studies of mechanosensing examine cells plated on flat elastic hydrogel substrates lacking fibrous topography. Recent efforts, however, have sought to compare the cell response to stiffness in fibrous versus elastic hydrogel settings. These studies suggest disparate trends in human mesenchymal stem cell behavior as a function of matrix stiffness in discrete fibrous and continuous hydrogel settings (Baker et al., 2015; Xie et al., 2017). Given these observations, we next aimed to examine shorter-term (< 1 day) mechanosensing behaviors during NHLF adhesion and spreading on DexVS matrices as a function of matrix stiffness.

Previous studies seeding cells on the surface of non-fibrous hydrogel substrates have demonstrated that cell spreading (as measured by steady-state spread area) consistently increases with matrix stiffness (Baker et al., 2015; Engler et al., 2004; Mih et al., 2012). In contrast, we observed a modest decrease in cell spread area with increasing fibrous matrix stiffness (**Figure 4.7a,d**). In soft matrices, traction forces generated by NHLFs deformed the matrix, recruiting fibers directly beneath the cell body (**Figure 4.7b**). Stiff matrices, however, proved too rigid to be deformed by cell forces. We also immunostained for vinculin, a mechanosensitive adhesion protein, to directly examine cell adhesion to the DexVS fibers (**Figure 4.7c**). Previous work from our lab showed that fiber recruitment and densification in DexMA fibrous matrices increases local ligand concentration and correlates with an increase in human mesenchymal stem cell spread area and focal adhesion number (Baker et al., 2015). Here, we observed similar results with NHLFs on DexVS matrices where soft, deformable matrices led to a significant increase in focal adhesion area as compared to stiff, non-deformable matrices (**Figure 4.7d**).

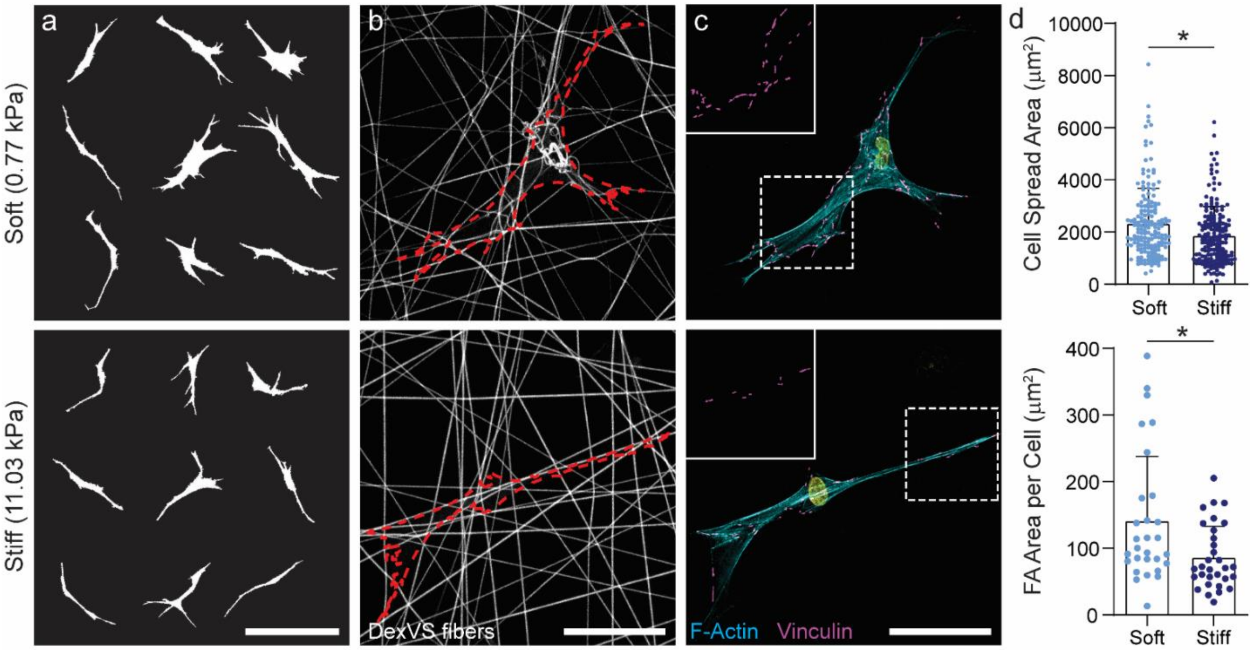
a
b
c
d
Soft (0.77 kPa)
Stiff (11.03 kPa)
DexVS fibers
F-Actin
Vinculin
Cell Spread Area (μm²)
10000
8000
6000
4000
2000
0
*
Soft
Stiff
FA Area per Cell (μm²)
400
300
200
100
0
*
Soft
Stiff

Figure 4.7: Soft, deformable DexVS matrices promote increased cell spreading and focal adhesion formation. (a) Cell outlines of nine representative cells. Scale bar: 200 μm. (b) Confocal fluorescent image of rhodamine-labeled DexVS fibers with cell outline shown in red. Scale bar: 100 μm. (c) Confocal fluorescent image of phalloidin-stained NHLFs (cyan) and vinculin (magenta, top left inset). Scale bar: 100 μm. (d) Quantification of cell spread area ($n \geq 171$) and focal adhesion area per cell ($n \geq 29$). All data presented as mean ± std; * $p < 0.05$.

These results are consistent with previous observations of short term, single cell mechanosensing events on fibrous matrices. However, diseases driven by progressive changes to ECM mechanics typically involve a population or multiple populations of cells that interact bidirectionally with their surroundings over a longer span of time. During fibrosis, for instance, fibroblasts in response to biochemical and biophysical cues differentiate into MFs that excessively synthesize ECM and exert contractile forces to cause tissue contracture, stiffening, and eventual organ failure. To better understand the microenvironmental cues that promote MF activation, many have utilized 2D hydrogel substrates to examine the effect of bulk matrix stiffness. These studies revealed that substrate stiffnesses similar in range to measurements of fibrosed tissue lead to increases in MF activation as measured by expression of alpha smooth muscle actin (α-SMA), a hallmark of the MF phenotype indicative of heightened contractility (Arora et al., 1999; Balestrini et al., 2012; Benton et al., 2009; Caliari et al., 2016a; Chia et al., 2012; Goffin et al., 2006; Hinz et al., 2001b; Liu et al., 2010a; Marinkovic et al., 2012; Wipff et al., 2007). Recently, work by Davidson et al. showed that hepatic stellate cells seeded on hyaluronic acid fibrous matrices expressed higher levels of α-SMA on soft as compared to stiff matrices in the absence of exogenous profibrotic soluble factors, such as TGF-β1 (Davidson et al., 2019c). Additionally, Fiore et al. utilized atomic force microscopy to spatially map stiffness across fibrosing tissue. Interestingly, they found that fibroblastic foci, the region of active fibrogenesis and MF activation, had a low stiffness (E = 1.97 kPa) as compared to mature fibrotic tissue that was much stiffer (E = 8.97 kPa) (Fiore et al., 2018). These results motivated us to utilize our newly developed DexVS fibrous matrix platform to further investigate the role of matrix stiffness on MF activation in the presence of exogenous profibrotic signals.

NHLFs were cultured at high density for up to a week on soft or stiff DexVS matrices with comparable initial architectural features (ie. fiber diameter, density, organization). EdU incorporation over the first 24 hours of culture and immunostaining for α-SMA expression at day 7 were quantified to assess fibroblast proliferation and activation into MFs, respectively, two hallmarks of fibrotic tissues. In the absence of TGF-β1, negligible a-SMA expression was observed after 7 days of culture (**Supplementary Figure 4.5**). However, contrary to previous studies using non-fibrous hydrogel surfaces where stiffer substrates induced higher proliferation and MF activation (Balestrini et al., 2012; Benton et al., 2009; Caliari et al., 2016a; Chia et al., 2012; Goffin et al., 2006), we noted the opposite trend: NHLFs in softer, more deformable fibrous matrices with TGF-β1 supplemented media exhibited increased proliferation and MF activation as compared to cells on stiffer matrices with comparable initial architecture (**Figure**

4.8a,b). Along with reorganization of DexVS fibers leading to an increase in tortuosity of the matrix, fibroblasts in soft matrices exhibited α-SMA-enriched stress fibers (**Figure 4.8a**). Conversely, cells in stiff matrices contained largely cytosolic α-SMA signal and little to no change in matrix structure was noted (**Figure 4.8a**). These data along with previous observations (Davidson et al., 2019c; Fiore et al., 2018) interestingly suggest that softer fibrous matrices are permissive to MF activation, while stiffer matrices mechanically similar to fibrosed tissues are not. Indeed, this could in part be explained by densification of matrix fibers seen on soft matrices (**Figure 4.7b**, **Figure 4.8a**), as recent data from our lab has shown that high local fiber densities in 3D promote Yes-associated protein (YAP) activity (Matera et al., 2019), a transcriptional co-activator required for MF activation (Liu et al., 2015a). On the contrary, current dogma posits a minimum prerequisite matrix stiffness for MF activation, providing a reinforcement mechanism to this progressive and often irreversible process. These conflicting observations motivate a higher spatiotemporal resolution examination of the matrix and constituent cells during fibrosis, including characterization of matrix porosity, ligand type and density in addition to mechanical stiffness.

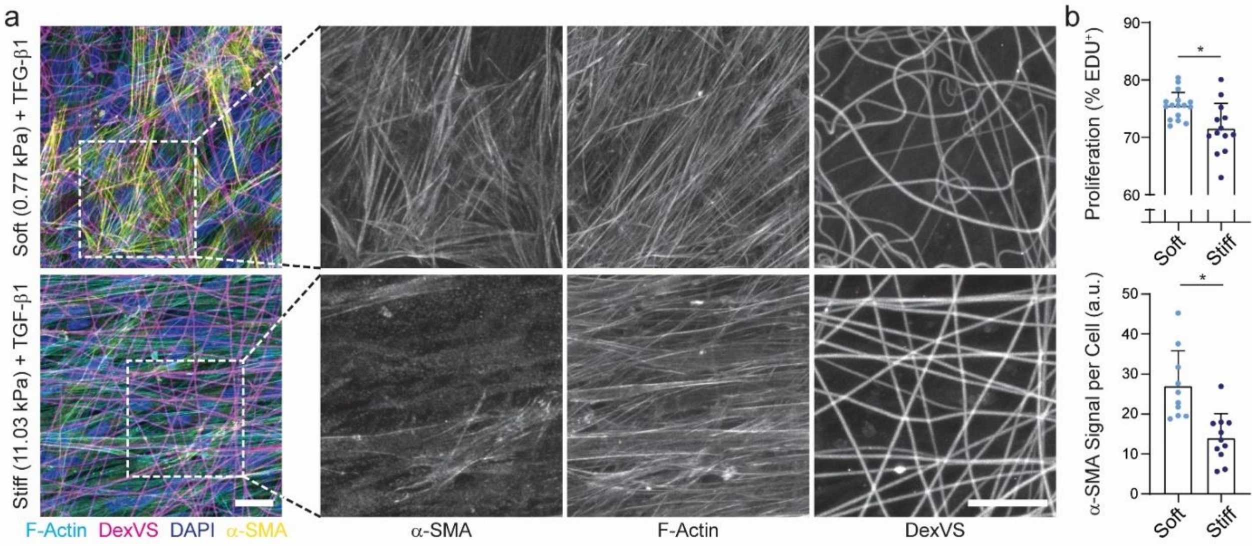
a
Soft (0.77 kPa) + TFG-β1
Stiff (11.03 kPa) + TGF-β1
F-Actin DexVS DAPI α-SMA
α-SMA
F-Actin
DexVS
b
Proliferation (% EDU⁺)
90
80
70
60
*
Soft
Stiff
α-SMA Signal per Cell (a.u.)
50
40
30
20
10
0
*
Soft
Stiff

Figure 4.8: Soft, deformable DexVS matrices promote MF induction. (a) Confocal fluorescent image of NHLFs cultured for 7 days on soft and stiff DexVS fibrous matrices; F-actin (cyan), DexVS fibers (magenta), nuclei (blue), α-SMA (yellow). Dashed boxes indicate locations of higher magnification images depicting α-SMA stress fibers. (b) Quantification of cell proliferation by EdU labeling ($n \geq 13$) and α-SMA fluorescent intensity ($n \geq 10$). Scale bars: 25 μm. All data presented as mean ± std; * $p \leq 0.05$.

4.5 Conclusion

In this work, we developed a synthetic biomaterial system of electrospun DexVS with tunable mechanics in order to model the fibrous microstructure and mechanical behavior of stromal tissue spaces where disease processes such as fibrosis originate. This system provides tunable and stable mechanical properties at both the single fiber and bulk matrix scale (**Figure 4.2, Figure 4.3, Figure 4.4**), as well as user-controlled biochemical functionalization with cysteine-terminated cell adhesive peptides (**Figure 4.5**). Alternatively, functionalization with HepMA allows cells to biochemically modify matrices with secreted ECM proteins (**Figure 4.6**). We then used this *in vitro* model of stromal tissue space to investigate MF activation, an important early step in the fibrotic cascade. In contrast to the relationship between matrix stiffness and MF activation established previously on non-fibrous hydrogel substrates, we observed that fibroblasts in soft and deformable fibrous matrices exhibit increased spreading, FA formation, proliferation, and activation into MFs as compared to cells on stiffer matrices with identical initial architecture (**Figure 4.7, Figure 4.8**). This work provides a new user-defined model that recapitulates the fibrous structure of native tissues while enabling cell-mediated physical and biochemical remodeling of the microenvironment. Future efforts to understand the dynamics and reciprocity underlying long-term interactions between cells and matrix will likely be critical to the discovery and development of therapeutics to treat fibrosis.

4.6 Materials and Methods

4.6.1 Reagents

All reagents were purchased from Sigma Aldrich and used as received, unless otherwise stated.

4.6.2 Cell culture

Normal human lung fibroblasts (NHLFs, University of Michigan Central Biorepository, Ann Arbor, MI) were cultured in DMEM containing 1% penicillin/streptomycin, L-glutamine, and 10% fetal bovine serum (basal medium). Cells were cultured at 37°C and 5% CO_2. NHLFs between passages four and ten were used for experiments.

4.6.3 DexVS synthesis

Dextran was reacted with divinyl sulfone following a previously described procedure (Yu & Chau, 2012). Briefly, dextran (5 g) was dissolved in 250 mL of sodium hydroxide (100 mM) solution on a stir plate at 300 rpm before addition of divinyl sulfone (12.5 mL). The reaction proceeded for 3.5 minutes before termination by addition of 2.5 mL hydrochloric acid (12 M). The product was dialyzed against milli-Q water for 3 days and then lyophilized. DexVS was characterized by ^{1}H NMR and a vinyl sulfone/dextran repeat unit ratio of 0.66 was determined (**Supplementary Figure 4.1**).

4.6.4 Fibrous matrix fabrication

DexVS was dissolved at 0.7 g ml^{-1} in a 1:1 mixture of milli-Q water and dimethylformamide with 0.6% (w/v) lithium phenyl-2,4,6-trimethylbenzoylphosphinate (LAP;

Colorado Photopolymer Solutions, Boulder, CO) photoinitiator, 2.5% (v/v) methacrylated rhodamine (25 mM; Polysciences, Inc., Warrington, PA), and 5.0% (v/v) glycidyl methacrylate. Electrospinning was accomplished with a custom set-up consisting of a high-voltage power supply (Gamma High Voltage Research, Ormond Beach, FL), syringe pump (KD Scientific, Holliston, MA), and a grounded copper collecting surface enclosed within an environmental chamber held at room temperature and 35% relative humidity (Terra Universal, Fullerton, CA). Electrospinning of DexVS solution was performed at a flow rate of 0.2 mL h^{-1}, voltage of 7.0 kV, and gap distance of 7 cm. To induce fiber alignment, fibers were electrospun at a voltage of 4.0 kV onto a collecting surface of oppositely charged (-3.0 kV) parallel electrodes with varying separation distance to control alignment. After electrospinning, fibers were stabilized by primary crosslinking under UV light (100 mW cm^{-2}) for 120 s, hydrated in varying concentrations of LAP solution, and then exposed again to UV light (100 mW cm^{-2}) for varying durations. Fibers were collected on poly(dimethylsiloxane) (PDMS; Dow Silicones Corporation, Midland, MI) arrays of circular wells produced by soft lithography as previously described (Baker et al., 2015). Briefly, silicon wafer masters possessing SU-8 photoresist (Microchem, Westborough, MA) were produced by standard photolithography and used to generate PDMS stamps. Following silanization with trichloro(1H,1H,2H,2H-perfluorooctyl)silane, stamps were used to emboss uncured PDMS onto oxygen plasma-treated coverslips. Well arrays were methacrylated with vapor-phase silanization of 3-(trimethoxysilyl)propyl methacrylate in a vacuum oven at 60°C for at least 6 h to promote fiber adhesion to PDMS.

4.6.5 Mechanical testing

To determine the tensile mechanical properties of individual fibers, three-point bending tests were performed using a Nanosurf FlexBio atomic force microscope (AFM; Nanosurf, Liestal, Switzerland). Single fibers were collected onto microfabricated PDMS troughs (200 μm tall × 200 μm wide) by electrospinning for short durations (1 s). Fibers were hydrated and crosslinked to varying degrees by LAP concentration and UV light exposure as above and deformed by an AFM tip (0.032 N m^{-1}) loaded with a 35 μm diameter bead positioned centrally along the fiber's length. Young's modulus was calculated from the resulting load-displacement curves using known equations for a cylindrical rod undergoing three-point bending with fixed boundaries (Kluge et al., 2010; Yang et al., 2007). To determine the Young's modulus of suspended DexVS fibrous matrices, microindentation testing with a rigid cylinder was performed on a commercial CellScale Microsquisher (CellScale, Waterloo, Ontario). Cylinders (1 mm diameter, 0.5 mm tall) of SU-8 photoresist were microfabricated and affixed to pure tungsten filaments (0.156 mm diameter, 59.6 mm length). Samples were indented to a depth of up to 200 μm at an indentation speed of 2 μm s^{-1}. As previously described (Baker et al., 2015), Young's modulus was approximated assuming the material behaves as an elastic membrane using the following equation:

$$F = \frac{Et\pi\delta^3(r_o^2 - r_i^2)}{2(r_o - r_i)^4(1 - \nu)}$$

Where t is the membrane thickness (8.68 μm, as determined by confocal microscopy; **Supplementary Figure 4.2**), r_o is the membrane radius (1 mm), r_i is the indenter radius (0.5 mm), ν is the Poisson ratio (0.5), F is the indentation force, δ is the indentation depth, and E is Young's modulus.

4.6.6 RGD functionalization and seeding on DexVS matrices

DexVS fibers were functionalized with the cell adhesive peptide cyclized [Arg-Gly-Asp-D-Phe-Lys(Cys)] (cRGD; Peptides International, Louisville, KY) via Michael-type addition to available vinyl sulfone groups to facilitate cell attachment. Briefly, the peptide was dissolved at 100 μM (unless otherwise stated) in milli-Q water containing HEPES (50 mM), phenol red (10 μg ml^{-1}), and 1M NaOH to adjust the pH to 8.0. A 400 μL volume of this solution was added to each substrate and incubated for 30 minutes at room temperature. Following cRGD functionalization, substrates were rinsed 2x with PBS before cell seeding. NHLFs were trypsinized, centrifuged and resuspended in basal medium, and seeded at 10^4 cells cm^{-2}.

4.6.7 Passive adsorption of proteins to DexVS matrices

Type I rat tail collagen and human fibronectin (Corning Incorporated, Corning, NY) were each diluted in PBS at 100 μg ml^{-1}. A 400 μL volume of either collagen solution, fibronectin solution, or fetal bovine serum (Atlanta Biologics, Flowery Branch, GA) was added to each substrate and incubated for 30 minutes at room temperature. Following protein adsorption, substrates were rinsed 3x with PBS before cell seeding.

4.6.8 HepMA synthesis and functionalization

Heparin sodium salt was reacted with methacrylic anhydride following previously described procedures (Brown et al., 2017a; Claaßen et al., 2018). Briefly, heparin sodium salt (500 mg) was dissolved in 50 mL PBS under vigorous stirring before addition of methacrylic anhydride (99.3 mL). The reaction was kept under constant stirring at 4°C for 24 hours. NaOH (1 N) was added every hour for the first 6 hours to maintain a solution pH of 8. The product was dialyzed against milli-Q water for 3 days and then lyophilized. Heparin methacrylate (HepMA) was dissolved in LAP solution at 2.5% (w/v). Fibers were simultaneously crosslinked and functionalized in this solution via exposure to UV light (100 mW cm^{-2}).

4.6.9 Myofibroblast induction

NHLFs were seeded and allowed to adhere for 24 hours. Following cell attachment, basal media was supplemented with TGF-β1 (10 ng ml^{-1}) and cultured for an additional 6 days. Media was replaced every 2 days.

4.6.10 Fluorescent staining and microscopy

NHLFs on DexVS fibers were first fixed in 4% paraformaldehyde for 10 min at room temperature. Alternatively, to extract cytoplasmic vinculin, samples were simultaneously fixed and permeabilized in 2% paraformaldehyde in a buffer containing 1,4-piperazinediethanesulfonic acid (PIPES, 0.1 M), ethylene glycol-bis(2-aminoethylether)-N,N,N',N'-tetraacetic acid (EGTA, 1 mM), magnesium sulfate (1 mM), poly(ethylene glycol) (4 % w/v), and triton X-100 (1%) for 10 min at room temperature. To stabilize the fibers for processing and long-term storage, DexVS samples were crosslinked in 2 mL LAP solution (1.0% w/v) and exposed to UV light (100 mW cm^{-2}) for 30 seconds. To stain the actin cytoskeleton and nuclei, cells were permeabilized in PBS solution containing Triton X-100 (5% v/v), sucrose (10% w/v), and magnesium chloride (0.6% w/v), and simultaneously blocked in 1% (w/v) bovine serum albumin and stained with phalloidin and DAPI. For immunostaining, samples were permeabilized, blocked for 1 h in 1% (w/v) bovine serum albumin, and incubated with mouse monoclonal anti-vinculin antibody (1:1000, Sigma #V9264), mouse monoclonal anti-fibronectin antibody (1:2000, Sigma #F6140), or mouse monoclonal anti-α-SMA (1:2000, Sigma #A2547) followed by secondary antibody (1:1000, Life Technologies #A21236) for 1 h each at room temperature with 3x PBS washes in between. For proliferation studies, EdU labelling was performed following the manufacturer's protocol (Click-iT EdU, Life Technologies, Carlsbad, CA). Fixed samples were imaged on a Zeiss LSM 800 laser scanning confocal microscope (Zeiss, Oberkochen, Germany). For cell studies, only cells in the central region of each suspended matrix (2 mm diameter) were imaged. Unless otherwise specified, images are presented as maximum intensity projections. Fluorescent images were processed and quantified via custom Matlab scripts.

4.6.11 Statistics

Statistical significance was determined by one-way analysis of variance (ANOVA) with post-hoc analysis (Tukey test) or Student's t-test where appropriate, with significance indicated by $p < 0.05$. Sample size is indicated within corresponding figure legends and all data are presented as mean ± standard deviation.

4.7 Supplementary Figures

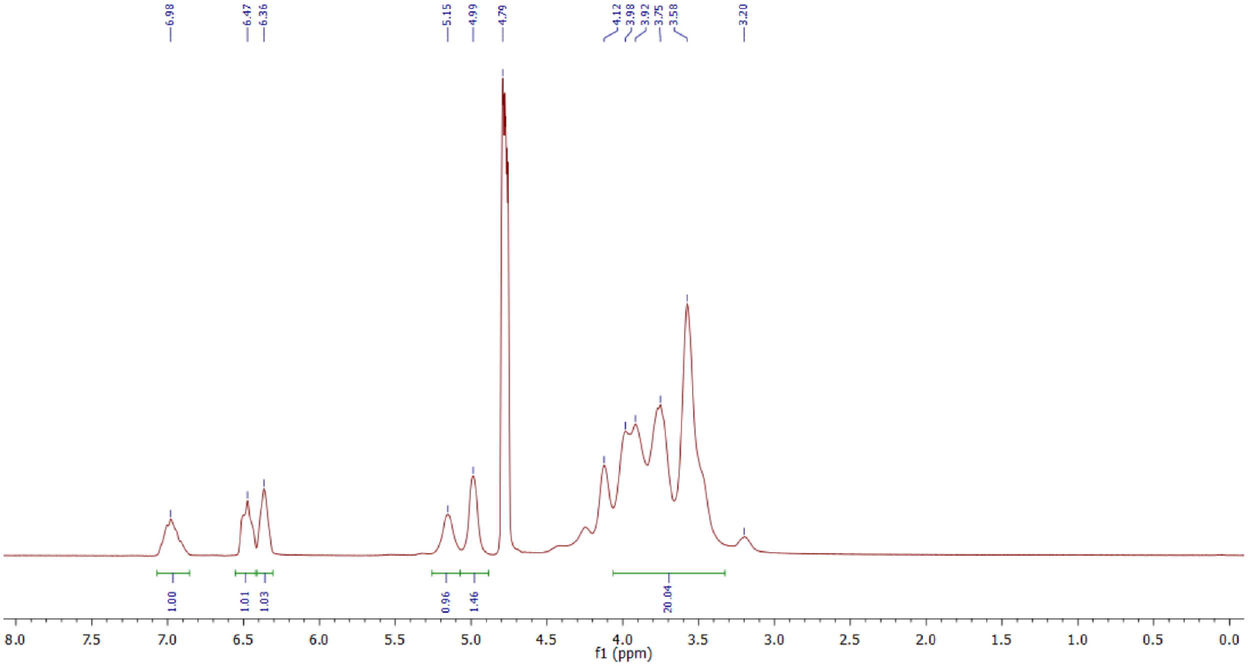

Supplementary Figure 4.1: ^{1}H NMR spectrum (D2O) of vinyl sulfonated dextran. The degree of DexVS functionalization was characterized by ^{1}H NMR, calculated as the ratio of averaged vinyl sulfone proton integral (6.36, 6.47, 6.98 ppm in D2O) and the anomeric proton of the glycopyranosyl ring (4.99 and 5.15 ppm in D2O). Since the signal of the anomeric proton of α-1,3 linkages (5.15 ppm) partially overlaps with other protons, a pre-determined ratio of 4% α-1,3 linkages was assumed and the total anomeric proton integral was calculated solely based on the integral at 4.99 ppm. A vinyl sulfone:dextran repeat unit ratio of 0.66 was determined.

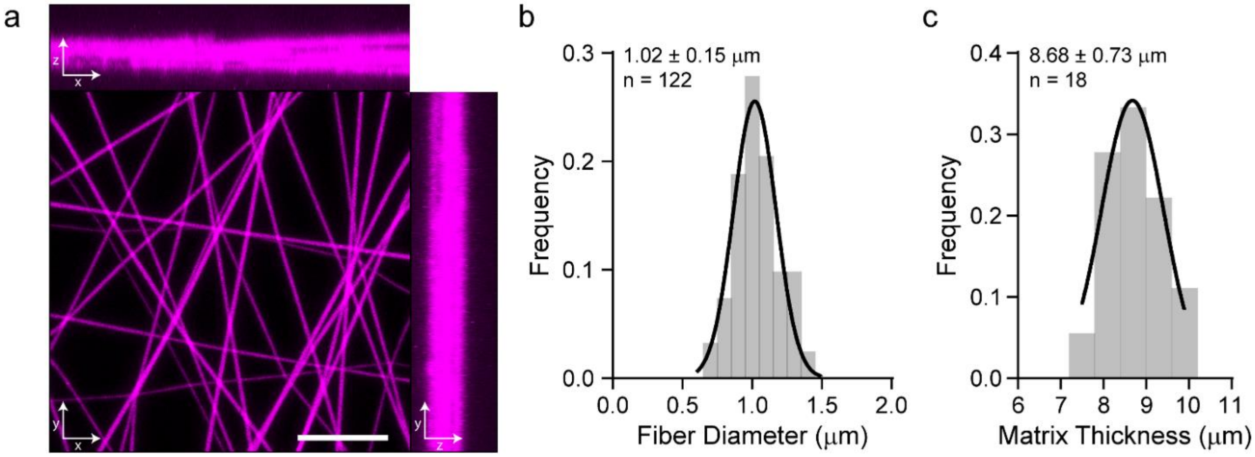

Supplementary Figure 4.2: Properties of DexVS fibrous matrices. (a) Orthogonal x-y, x-z, and y-z maximum intensity projection views from a confocal fluorescence image stack of a suspended 3D DexVS fibrous matrix; rhodamine-labeled DexVS fibers (magenta). Histogram of (b) DexVS fiber diameter and (c) DexVS matrix thickness. Scale bar: 20 μm.

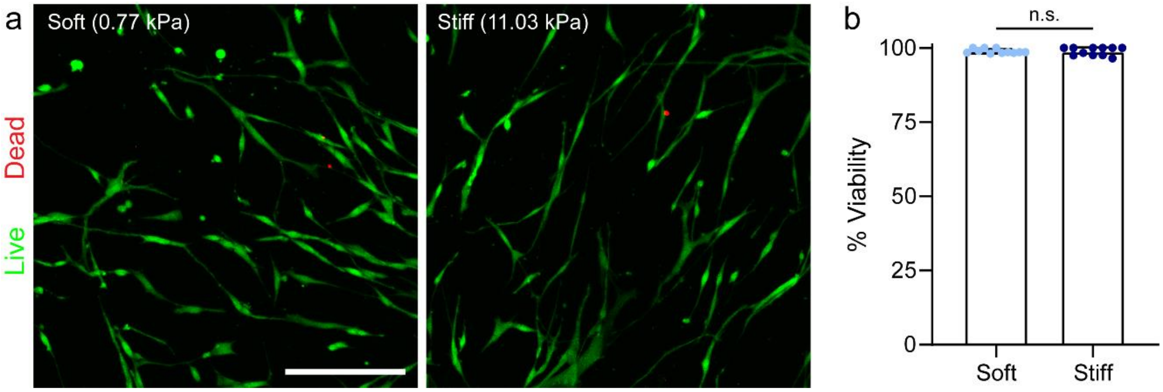
a
Soft (0.77 kPa)
Stiff (11.03 kPa)
Live
Dead
b
n.s.
% Viability
100
75
50
25
0
Soft
Stiff

Supplementary Figure 4.3: Cell survival on DexVS matrices. (a) Live/dead stain of NHLFs seeded on soft and stiff DexVS matrices and (b) quantification of cell viability (n = 11 fields of view). Scale bar: 200 µm. Data presented as mean ± std; * $p \leq 0.05$.

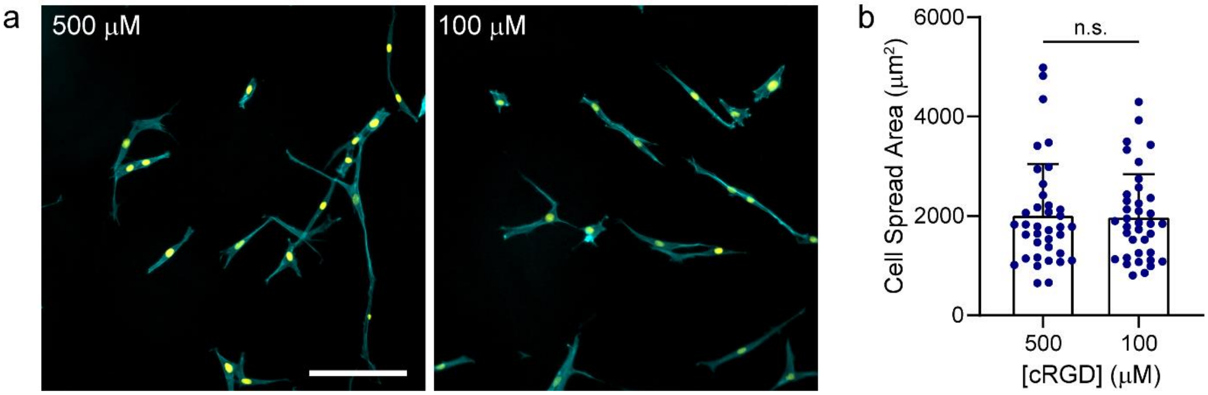
a
500 µM
100 µM
b
n.s.
Cell Spread Area (µm²)
6000
4000
2000
0
500
100
[cRGD] (µM)

Supplementary Figure 4.4: Saturating concentrations of cRGD required to maximize cell adhesion on DexVS matrices. (a) Confocal fluorescent images of NHLFs cultured on DexVS matrices functionalized with 100 or 500 µM cRGD; actin (cyan), nuclei (yellow). Scale bar: 200 µm. (b) Average cell spread area as a function of cRGD concentration (n = 37). Data presented as mean ± std; * $p < 0.05$.

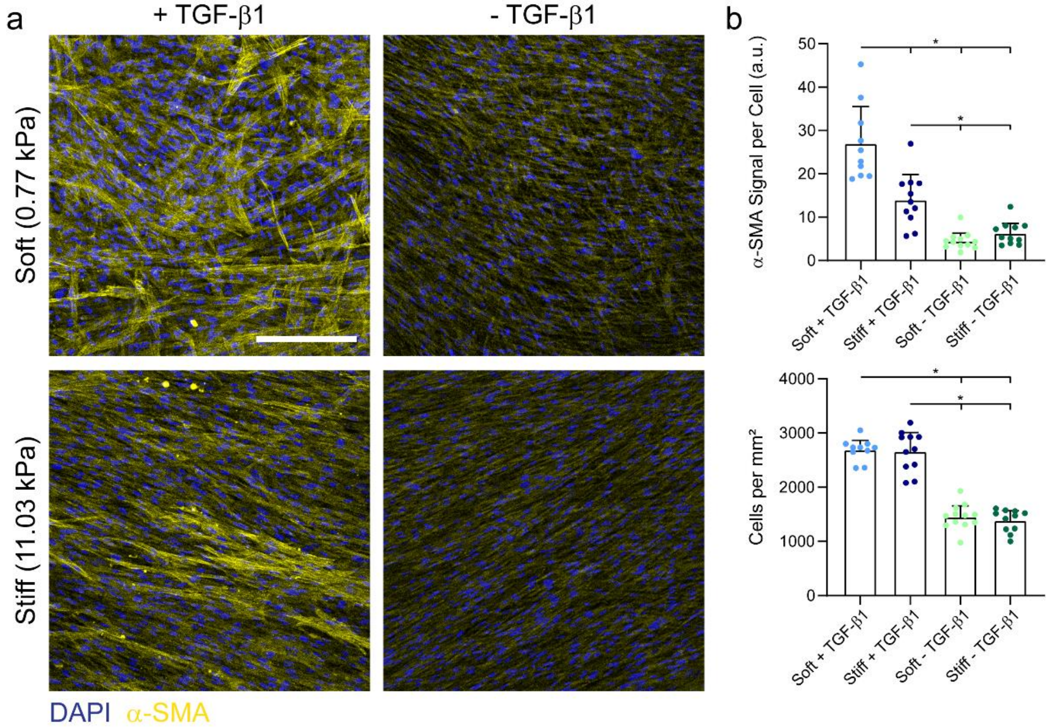

Supplementary Figure 4.5: TGF-β1 is required for MF activation on both soft and stiff DexVS fibrous matrices. (a) Confocal fluorescent images of NHLFs cultured for 7 days on DexVS matrices with or without TGF-β1; nuclei (blue), α-SMA (yellow). Scale bar: 200 µm. (b) Quantification of α-SMA fluorescent intensity and final cell density ($n \geq 10$). Data presented as mean ± std; * $p \leq 0.05$.

Chapter 5: Fiber Crimp Confers Matrix Mechanical Nonlinearity, Regulates Endothelial Cell Mechanosensing, and Promotes Microvascular Network Formation

5.1 Authors

Christopher D. Davidson, Danica Kristen P. Jayco, William Y. Wang, Ariella Shikanov, Brendon M. Baker

5.2 Abstract

Mechanical interactions between cells and their surrounding extracellular matrix (ECM) guide many fundamental cell behaviors. Native connective tissue consists of highly organized, 3D networks of ECM fibers with complex, nonlinear mechanical properties. The most abundant stromal matrix component is fibrillar type I collagen, which often possesses a wavy, crimped morphology that confers strain- and load-dependent nonlinear mechanical behavior. Here, we established a new and simple method for engineering electrospun fibrous matrices composed of dextran vinyl sulfone (DexVS) with controllable crimped structure. A hydrophilic peptide was functionalized to DexVS matrices to trigger swelling of individual hydrogel fibers, resulting in crimped microstructure due to the fixed anchorage of fibers. Mechanical characterization of these matrices under tension confirmed orthogonal control over nonlinear stress-strain responses and matrix stiffness. We next examined ECM mechanosensing of individual endothelial cells (ECs), finding that fiber crimp promoted physical matrix remodeling alongside decreases in cell

spreading, focal adhesion area, and nuclear localization of Yes-associated protein (YAP). These changes corresponded to an increase in migration speed along with evidence for long-range interactions between neighboring cells in crimped matrices. Interestingly, when ECs were seeded at high density in crimped matrices, capillary-like networks rapidly assembled containing tube-like cellular structures wrapped around bundles of synthetic matrix fibers due to increased physical reorganization of matrix fibers. Our work provides an additional level of mechanical and architectural tunability to synthetic fibrous matrices and implicates a critical role for mechanical nonlinearity in EC mechanosensing and network formation.

5.3 Introduction

Native biological tissues are known to exhibit complex, nonlinear mechanical properties (Fung, 1967; Storm et al., 2005). Specifically, connective tissue consists of highly organized, 3D networks of fibrillar extracellular matrix (ECM) proteins that contribute to this mechanical nonlinearity. For example, type I collagen is the most abundant stromal matrix component and exists as fibers or bundles of fibers that often possess a wavy, crimped morphology in a variety of soft tissues including tendons, ligaments, blood vessels, and the intestine (Hiltner et al., 1985). External forces experienced with normal tissue function cause crimped fibers to straighten and gradually bear tensile loads. Thus, crimped fiber microstructure confers strain- and load-dependent nonlinear mechanical behaviors and contributes significantly to the overall compliance, strength, and durability of soft tissues (Diamant et al., 1972; Rigby et al., 1959). Recapitulating this complex mechanical behavior is critical to engineering biomaterials for tissue engineering applications as well as better understanding cell-ECM interactions during normal and abnormal tissue function.

Electrospinning is a technique that has been extensively used to fabricate fibrous scaffolds that mimic the structure and mechanics of native tissue ECMs given its ability to generate polymeric fibers of similar length-scale as native collagen fibrils (Mauck et al., 2009; Pham et al., 2006; Sill & von Recum, 2008). Additional benefits to electrospinning include its low cost, high scalability and speed of scaffold fabrication, as well as versatility in processing a wide variety of synthetic and natural polymers into fibers. By modulating attributes of the polymer solution and electrospinning process parameters, fibrous scaffolds can be fabricated with varied features that reflect the diverse landscapes of native cellular microenvironments. However, most electrospinning processes yield scaffolds containing straight fibers lacking the crimped microstructure of native collagen fibers in soft tissues. To address this limitation and generate electrospun scaffolds composed of tortuous fibers, several methods have recently been developed including electrospinning bi-component polymeric fibers (Lin et al., 2005), air-driven electrospinning (Varesano et al., 2007), magnetic-field-assisted electrospinning (Liu et al., 2010c), plasticizer treatment (Chao et al., 2014; Liu et al., 2015b), or controlled heating above the polymer's glass transition temperature (Chao et al., 2014; Chen et al., 2014; Surrao et al., 2010, 2012b, 2012a; Szczesny et al., 2017). While these methods have successfully generated crimped fibers, resultant scaffolds lack fine control over other physical properties such as the degree of mechanical nonlinearity, matrix stiffness, and fiber density.

Additionally, the cell response to matrices composed of crimped fibers is currently not well understood. As these scaffolds have largely been developed for tendon and ligament tissue engineering applications, the cell response to external loads as a function of fiber crimp has exclusively been explored. Interestingly, these studies have shown that ligament fibroblasts and mesenchymal stem cells cultured in crimped scaffolds exhibit changes in gene expression (Chao et al., 2014; Surrao et al., 2012a) and cell morphology (Szczesny et al., 2017) under static and dynamic loading, suggesting altered mechanosensing as a function of fiber tortuosity. Recent work by our group and others support a key role for cell traction force-induced physical matrix remodeling during mechanosensing of fibrous microenvironments. Physical remodeling through fiber recruitment influences the distribution of adhesive ligand and matrix-borne forces during fundamental cell processes including cell spreading (Baker et al., 2015; Xie et al., 2017), migration (Provenzano et al., 2006; Wang et al., 2019), and assembly of multicellular structures (Davidson et al., 2019a). However, due to the use of stiff synthetic polymeric materials (E = 0.35 – 600 MPa), previous fabrication methods produce matrices of crimped fibers impervious to dynamic remodeling by cell-generated forces (Chao et al., 2014; Chen et al., 2014; Lin et al., 2005; Liu et al., 2015b, 2010c; Surrao et al., 2010, 2012b, 2012a; Szczesny et al., 2017; Varesano et al., 2007). We propose that nonlinear mechanics and the enhanced potential for cell force-mediated remodeling at low force regimes can regulate single cell behavior and ensuing multicellular assembly processes.

Previously, our lab has developed synthetic matrices of electrospun dextran hydrogel fibers with highly tunable architectural, mechanical, and biochemical attributes (Baker et al., 2015; Davidson et al., 2020a). In separate work, we have also demonstrated control over the swelling behavior of dextran-based bulk hydrogels by modulating polymer backbone hydrophobicity via functionalization with hydrophobic methacrylates (Trappmann et al., 2017). Here, we employed a similar strategy to increase hydrophilicity within the neutral polymer network of a polymer fiber in order to confer swelling behavior and crimped microstructure should the fiber be anchored at both ends. The objective of this study was to utilize this approach to examine the role of matrix fiber crimp and mechanical nonlinearity on endothelial cell (EC) behavior.

5.4 Results

5.4.1 Development and mechanical characterization of crimped DexVS fibrous matrices

To develop a synthetic electrospun matrix with controllable crimped microstructure, dextran vinyl sulfone (DexVS) was chosen as a base polymeric material due to its amenability to electrospinning with control over matrix architecture and mechanics (Davidson et al., 2020a). Matrices were fabricated by electrospinning DexVS fibers onto collection substrates such that material was suspended over an array of microfabricated PDMS wells. DexVS fibers were first functionalized with cell-adhesive cyclo[RGDfK(C)] (cRGD) via Michael-type addition to free vinyl sulfones to facilitate cell attachment, ensuring consistent cRGD concentration across all matrix conditions (**Figure 5.1a**). We next coupled CGRDGS, a peptide containing hydrophilic arginine and glycine residues lacking cell-adhesive domains (**Figure 5.1a**). Time-lapse confocal imaging of matrices during functionalization with this hydrophilic swelling peptide (HSP) revealed a rapid increase in fiber tortuosity as well as overall matrix thickness, presumably due to the increase in length of swelled fibers firmly anchored at well edges (**Figure 5.1b**, **Supplementary Movie 5.1**). We noted that matrices achieved a steady-state morphology 45 minutes after the addition of HSP, and so this duration of functionalization was utilized for all subsequent studies.

We additionally demonstrated facile control over the degree of crimping by varying the concentration of HSP coupled to DexVS matrices (**Figure 5.1c**). Control matrices (0.0 mM HSP) possessed straight, taut fibers while increasing HSP concentration led to a stepwise increases in individual fiber tortuosity as well as overall matrix thickness (**Figure 5.1d,e**). This increase in overall matrix thickness also corresponded to enhanced fiber dispersion in the z-direction (**Supplementary Movie 5.2**). As expected, a modest increase in fiber diameter as a function of HSP-mediated swelling was noted (control, unmodified fibers: 0.96 ± 0.10 μm vs. 2.0 mM HSP-functionalized fibers: 1.02 ± 0.13 μm). Although this diameter increase could impact matrix total surface area and the distribution of cell-adhesive cRGD, we anticipate these influences are negligible compared to the influence of matrix structure and mechanical behavior (**Figure 5.1f**).

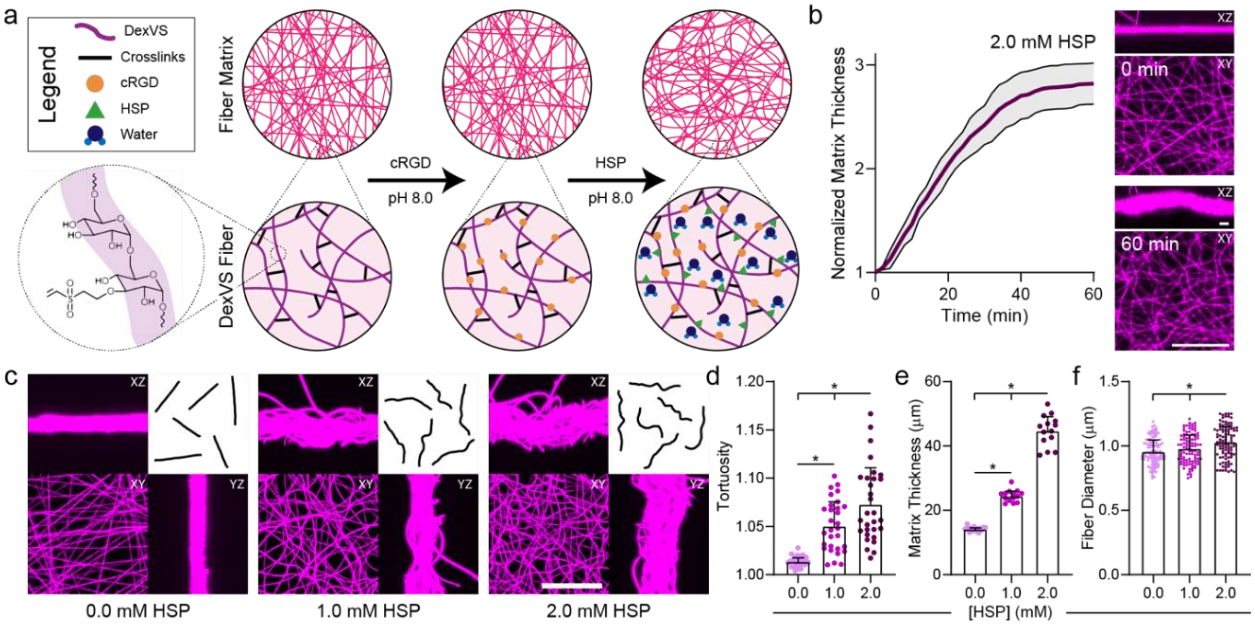

Figure 5.1: Functionalization of hydrogel fibers with hydrophilic swelling peptide induces crimp in DexVS matrices. (a) Schematic representation of DexVS fibers with controlled adhesive ligand and crimping via functionalization with the cell adhesive peptide cRGD and hydrophilic swelling peptide (HSP, peptide sequence: CGRDGS), respectively. (b) Matrix thickness quantified over time immediately after adding 2.0 mM HSP (n = 6 matrices). (c) Confocal fluorescent images and orthogonal maximum intensity projections of DexVS matrices functionalized with variable HSP concentrations with representative fiber outlines. Scale bar: 50 μm. Quantification of (d) fiber tortuosity (n = 30 fibers), (e) matrix thickness (n = 14 matrices), and (f) fiber diameter (n = 100 fibers) as a function of HSP concentration. All data presented as mean ± standard deviation; * $p < 0.05$.

To characterize the influence of fiber crimping on matrix mechanics, the centers of suspended fibrous matrices were indented to capture stress-strain responses under tension.

Similar to observations in native collagenous tissues that possess crimped architecture (Hiltner et al., 1985), engineered crimping of DexVS matrices led to pronounced changes in nonlinearity and a prominent toe region at low levels of strain (**Figure 5.2a**). Non-crimped control matrices (0.0 mM HSP) possessed only a slightly non-linear response, as seen by a modest increase in stiffness from low (E = 812 ± 135 Pa) to high strain (E = 1178 ± 131 Pa) regimes, potentially due to strain-dependent fiber reorientation (Abhilash et al., 2014; Lake et al., 2009; Lynch et al., 2003). With intermediate levels of crimping (1.0 mM HSP), we observed an increase in nonlinearity with a significant decrease in stiffness at low strain (250 ± 88 Pa) compared to control matrices. As crimped fibers would require strain-induced straightening before bearing tensile load, lower stiffness at low strain implies a diminished population of taught, load-bearing fibers. Indeed, higher strains where crimped fibers straightened and began to bear load correlated with a three-fold increase in matrix stiffness (788 ± 164 Pa). At the maximum levels of crimping examined (2.0 mM HSP), the difference between stiffness at low (123 ± 45 Pa) and high (182 ± 81 Pa) strain regimes was marginal. Due to the limited testable strain range imposed by our setup and sample geometry, fibers have likely not fully straightened to bear load even at the maximum testable strain ($\varepsilon = 0.11$). We anticipate that at higher strains ($\varepsilon > 0.15$), we would observe a significant increase in stiffness for this condition. In addition to changes in Young's modulus in different strain regimes, we also noted an increase in transition strain due to a larger toe region with increasing HSP concentration (**Figure 5.2a**).

We next orthogonally varied fiber stiffness at each level of HSP-induced crimp by crosslinking matrices for various durations (20 vs. 160 seconds) in the presence of LAP photoinitiator after cRGD and HSP functionalization. For non-crimped control matrices, photoinitiated crosslinking led to increases in E at both low and high strain regimes (**Figure**

5.2b). With an intermediate degree of crimping, crosslinking did not influence stiffness at low strains ($\varepsilon < 0.05$), but significantly increased E at higher strains (**Figure 5.2c**). At the highest degree of crimping examined, subsequent crosslinking had no measurable effect on E at either low or high strain regimes, again likely due to the lack of engagement with straightened tension-bearing fibers (**Figure 5.2d**). Additionally, transition strain only changed as a function of HSP concentration and not as a function of photoinitiated crosslinking. Together, these results suggest that the crosslinking of single fibers only influences matrix stiffness in strain regimes where fibers are straightened and load bearing.

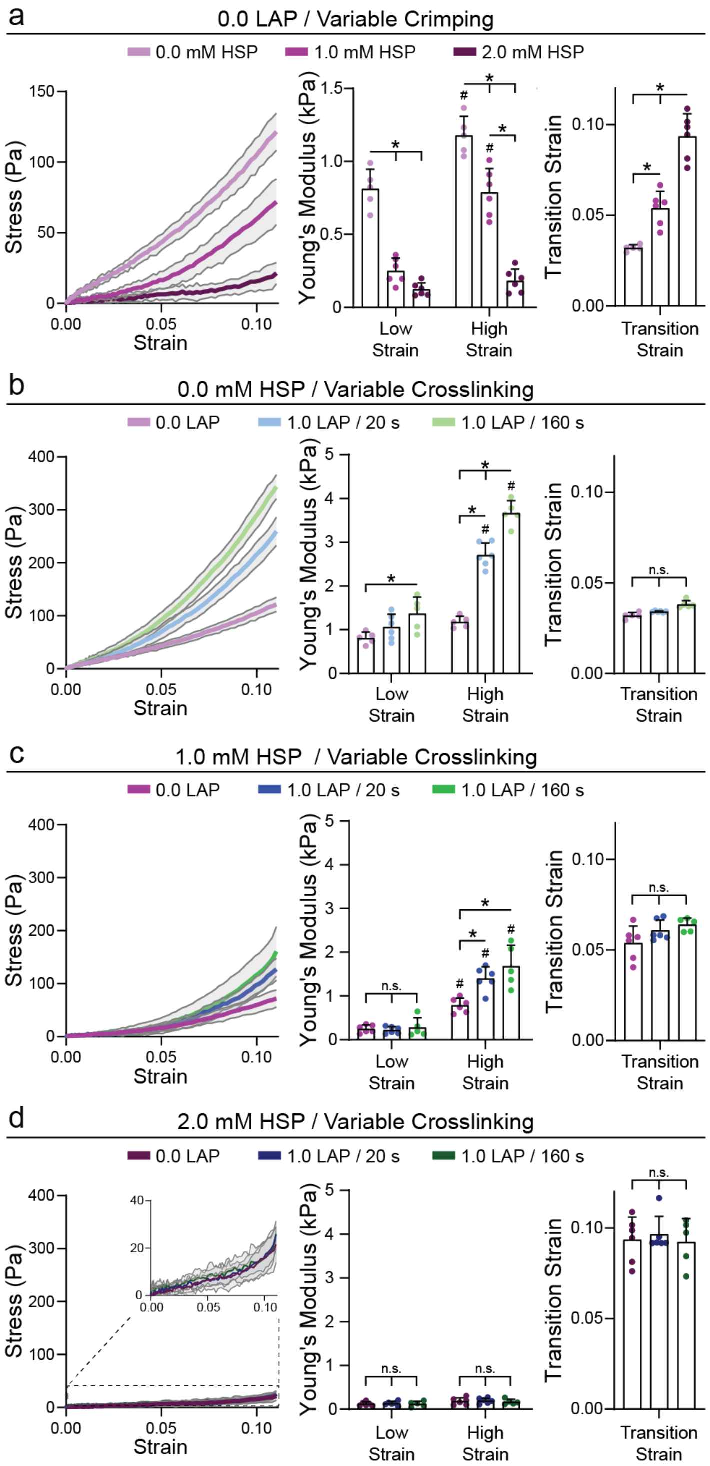

Figure 5.2: Mechanical characterization of crimped DexVS matrices. Average stress-strain curves with quantification of Young's modulus at low (0.00 – 0.05) and high (0.05 – 0.10) strain and transition strain for DexVS matrices with (a) variable HSP concentrations and no additional crosslinking, (b) variable crosslinking at 0.0 mM HSP, (c) variable crosslinking at 1.0 mM HSP, and (d) variable crosslinking at 2.0 mM HSP (n = 5-6 matrices per group). All data presented as mean ± standard deviation; * $p < 0.05$. # indicates statistical significance ($p < 0.05$) between low and high strain.

5.7.2 Endothelial cell spreading and mechanosensing in crimped DexVS matrices

In previous work developing crimped fibrous matrices for tendon and ligament tissue engineering, cell behavior has primarily been studied in response to external static and dynamic tensile loads (Chao et al., 2014; Surrao et al., 2012a; Szczesny et al., 2017). In addition to interpreting external mechanical cues, however, cells continuously sense and respond to passive mechanical cues from the microenvironment including matrix stiffness, topography, and dimensionality (Ricca et al., 2013). Thus, we next aimed to investigate how fiber crimp regulates EC mechanosensing and morphology. As compared to in control matrices, human umbilical vein ECs in crimped matrices exhibited a decrease in projected cell spread area (**Figure 5.3a-c**) and an increase in cell thickness (**Figure 5.3b,d**), potentially due to the enhanced initial thickness and three dimensionality of crimped matrices (**Figure 5.1c**). There was, however, no difference in cell volume between matrix conditions (**Figure 5.3e**). In addition, we also noticed similar changes in nuclear morphology corresponding to differences in overall cell spreading where crimped matrices yielded nuclei with smaller projected area and increased thickness with no change in volume (**Figure 5.3f-h**). Interestingly, however, EC nuclei in crimped matrices had significantly increased DAPI signal intensity suggesting potential changes in chromatin density (**Figure 5.3i**). Lastly, we observed differences in physical reorganization of matrix fibers as a function of crimping. Crimped matrices exhibited increased fiber recruitment beneath the cell surface and additionally maintained increased matrix thickness as compared to control matrices (**Figure 5.3j,k**). Comparing final matrix thickness to initial thickness prior to cell-seeding, though, we noted a 63% decrease in crimped matrices compared to a 34% decrease in the control. In sum, cells in crimped fiber matrices exhibited distinct morphological features and cell-ECM interactions compared to ECs cultured in non-crimped control matrices.

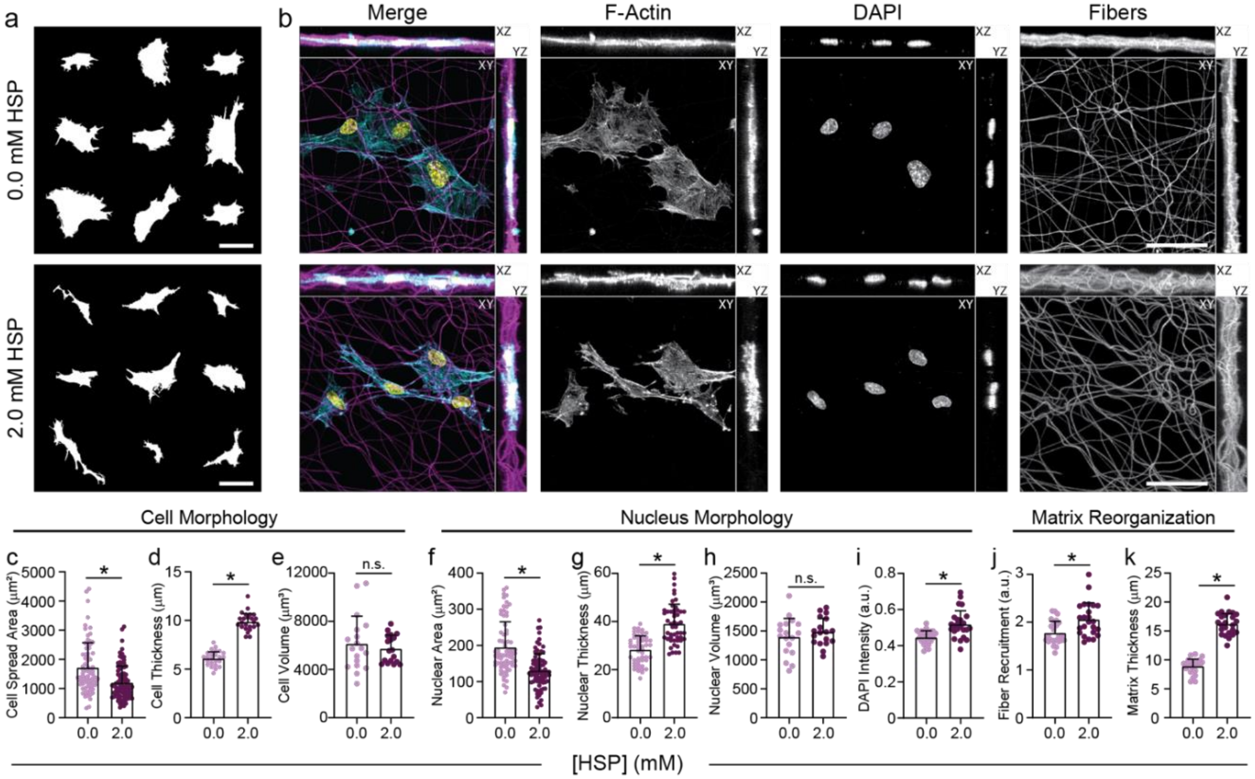
a
b
Merge
F-Actin
DAPI
Fibers
XZ
YZ
XY
0.0 mM HSP
2.0 mM HSP
Cell Morphology
Nucleus Morphology
Matrix Reorganization
c
Cell Spread Area (μm²)
5000
4000
3000
2000
1000
0
*
d
Cell Thickness (μm)
15
10
5
0
*
e
Cell Volume (μm³)
12000
8000
4000
0
n.s.
f
Nuclear Area (μm²)
400
300
200
100
0
*
g
Nuclear Thickness (μm)
60
40
20
0
*
h
Nuclear Volume (μm³)
2500
2000
1500
1000
500
0
n.s.
i
DAPI Intensity (a.u.)
0.8
0.6
0.4
0.2
0
*
j
Fiber Recruitment (a.u.)
3
2
1
0
*
k
Matrix Thickness (μm)
25
20
15
10
5
0
*
0.0
2.0
[HSP] (mM)

Figure 5.3: Crimped DexVS fibrous matrices regulate EC morphology and physical matrix remodeling. (a) Cell outlines of nine representative cells as a function of HSP concentration. (b) Confocal fluorescent images and orthogonal maximum intensity projects of ECs in DexVS matrices functionalized with varying HSP concentration. F-actin (cyan), DexVS fibers (magenta), nuclei (yellow). Quantification of (c) cell spread area (n ≥ 74 cells), (d) cell thickness (n = 24 cells), (e) cell volume (n = 18 fields of view), (f) nuclear area (n ≥ 72 nuclei), (g) nuclear thickness (n = 50 nuclei), (h) nuclear volume (n = 18 fields of view), (i) average DAPI intensity (n = 24 nuclei) (j) fiber recruitment (n = 24 fields of view), and (k) final matrix thickness (n = 24 fields of view). Scale bars: 50 μm. All data presented as mean ± standard deviation; * $p < 0.05$.

Given the noted changes in cell spreading with crimped matrix architecture, we next investigated the mechanosensitive proteins vinculin and Yes-associated protein (YAP). Vinculin is a key force-sensitive adhesion protein and a well-established signaling molecule within focal adhesions (Grashoff et al., 2010; Kanchanawong et al., 2010). In crimped matrices, we noted a decrease in both total focal adhesion area as well as single focal adhesion area as compared to control matrices (**Figure 5.4a-c**). Additionally, YAP is a Hippo pathway transcriptional regulator that functions as a central control point during mechanosensing (Dupont et al., 2011). In line with previous work correlating spreading, cell adhesions, and YAP activity (Caliari et al., 2016b; Nardone et al., 2017), we observed a lower nuclear to cytoplasmic ratio of YAP signal in cells within crimped matrices as compared to controls due to a decrease in YAP localized to the nucleus (**Figure 5.4d-f**).

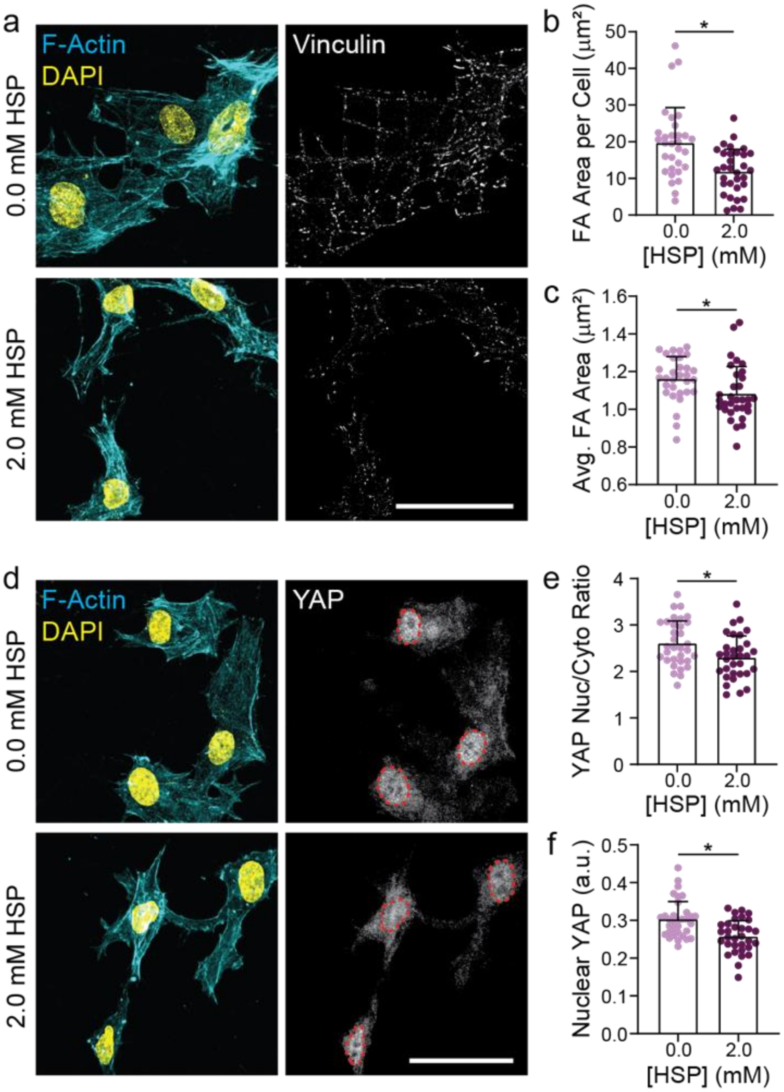

Figure 5.4: Crimped DexVS fibrous matrices regulate EC mechanosensing. Confocal fluorescent images of ECs on DexVS matrices functionalized with variable HSP concentrations and stained for (a) vinculin and (d) YAP. F-actin (cyan), nuclei (yellow). Quantification of (b) total focal adhesion area per cell, (c) average area of single focal adhesions (n ≥ 31 cells), (e) YAP nuclear to cytoplasmic ratio, and (f) nuclear YAP intensity (n ≥ 32 cells). Scale bars: 50 μm. All data presented as mean ± standard deviation; * $p < 0.05$.

5.7.3 EC migration and network formation on crimped DexVS matrices

Examining EC phenotype at fixed timepoints is beneficial in understanding how matrix mechanics regulate cell behavior and mechanosensing. However, we also sought to examine the dynamics of cell-ECM interactions on crimped and control matrices by time-lapse live imaging (**Supplementary Movie 5.3**, **Supplementary Movie 5.4**). Over the first four hours of culture, cells actively recruited matrix fibers without evident spreading or migration. Following this initialization period, cells began to spread and migrate in both matrix conditions (**Figure 5.5a**). Quantifying migration speed from tracked labeled nuclei, we found that ECs migrated 13% faster on crimped matrices compared to control (**Figure 5.5b**). Additionally, in crimped matrices we noted frequent instances of directed protrusion and migration towards neighboring cells positioned multiple cell lengths away, a phenomenon that was not observed in control matrices (**Figure 5.5c**). Physical matrix deformations and local fiber alignment appear to generate lines of tension between cells that promoted directional cell extension, indicative of long-range mechanical communication.

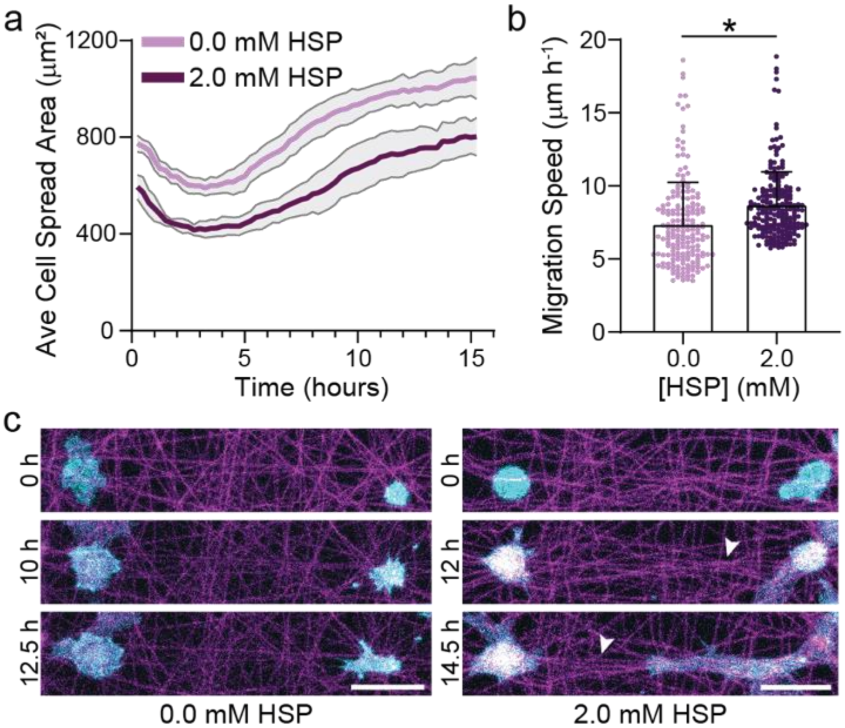

Figure 5.5: EC spreading and migration dynamics on crimped DexVS matrices. (a) Average cell spread area over 16 hours after seeding on DexVS matrices functionalized with various HSP concentrations (n = 6 fields of view). (b) Migration speed as a function of HSP concentration (n ≥ 197 cells). (c) Representative time-lapse images of lifeAct-GFP expressing ECs on DexVS matrices functionalized with 0.0 and 2.0 mM HSP. Arrows indicate matrix alignment between interacting cells. F-actin (cyan), DexVS fibers (magenta). Scale bars: 50 µm. All data presented as mean ± standard deviation; * $p < 0.05$.

Our lab and others have investigated the involvement of long-range mechanical communication in vasculogenesis, the *de novo* formation of microvascular networks (Davidson et al., 2019a; Sapir & Tzlil, 2017). We previously developed a model of EC network formation on suspended matrices of electrospun dextran methacrylate fibers to study *in vitro* vasculogenesis and discovered a critical role for physical matrix remodeling during the assembly of these complex, multicellular, capillary-like structures (Davidson et al., 2019a). As crimped DexVS matrices exhibit low stiffness and increased nonlinearity at low strain regimes (**Figure 5.2**) as well as heightened fiber recruitment by single ECs (**Figure 5.3**), we hypothesized that crimped fibrous microstructure would also encourage EC network formation.

To investigate this, we cultured ECs at high cell density (6 x 10^4 cells cm^{-2}) on control and crimped matrices for 5 days (**Figure 5.6a**). While EC networks formed in both conditions with robust VE-cadherin expression at cell-cell junctions (**Figure 5.6a,c**), networks on crimped matrices exhibited longer extensions between nodes while networks on control matrices had larger nodes with shorter extensions. These observations were supported by a decrease in the ratio of cell area to perimeter in crimped matrices compared to control, a previously used metric to classify network formation (Califano & Reinhart-King, 2008; Davidson et al., 2019a) (**Figure 5.6a,b**). Additionally, high resolution imaging indicated increased fiber bundling and thicker cellular networks in crimped matrices, mirroring results seen earlier with single cells (**Figure 5.6j,k**). Interestingly, ECs in crimped matrices wrapped around bundles of fibers, leading to the formation of tube-like structures; this phenomenon was not observed in control matrices (**Figure 5.6d,e**).

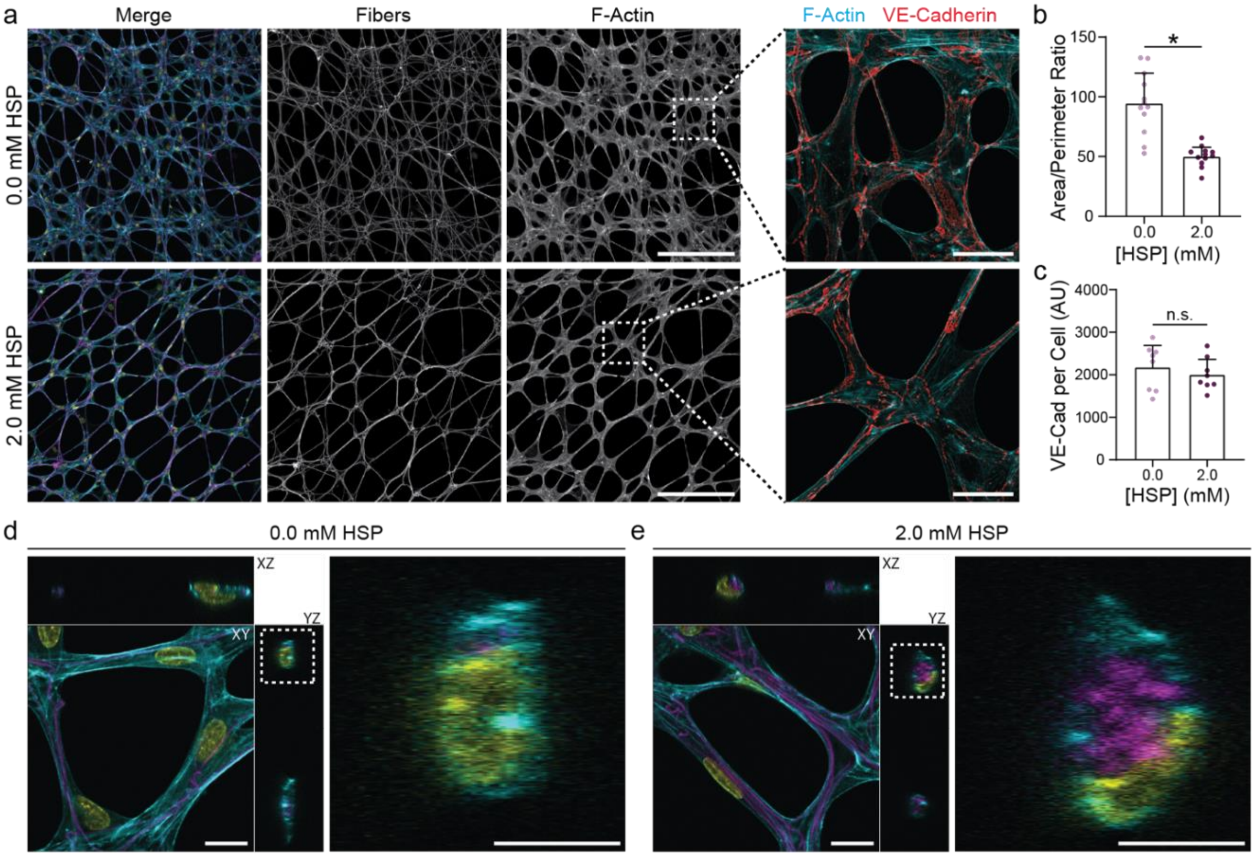
a
Merge
Fibers
F-Actin
F-Actin VE-Cadherin
0.0 mM HSP
2.0 mM HSP
b
Area/Perimeter Ratio
150
100
50
0
*
0.0
2.0
[HSP] (mM)
c
VE-Cad per Cell (AU)
4000
3000
2000
1000
0
n.s.
0.0
2.0
[HSP] (mM)
d
0.0 mM HSP
e
2.0 mM HSP
XZ
XY
YZ

Figure 5.6: EC network formation on crimped DexVS matrices. (a) Confocal fluorescence images of ECs and fibers after 5 days of culture on low density DexVS matrices functionalized with variable HSP concentrations. F-actin (cyan), DexVS fibers (magenta), nuclei (yellow). Scale bar: 300 µm. Dashed boxes indicate locations of higher magnification images depicting VE-cadherin expression at cell-cell junctions. Scale bar: 50 µm. (b) Cell area/perimeter ratio (n = 12 fields of view) and (c) total VE-cadherin fluorescent intensity normalized to cell density (n = 8 fields of view) as a function of HSP concentration. Representative confocal fluorescent images and z-plane cross sections of tube-like structures in (d) control and (e) crimped matrix conditions. Scale bar: 10 µm. Dashed boxes indicate locations of higher magnification. Scale bar: 5 µm. All data presented as mean ± standard deviation; * $p < 0.05$.

5.5 Discussion

Mimicking the architectural and mechanical properties of collagenous tissues is critical to building *in vitro* models for disease modeling applications and scaffolds for tissue repair. Here, we established a new approach to generating crimped electrospun synthetic polymer fibers to mimic the tortuous microstructure of fibrillar collagen in many soft tissues. By functionalizing electrospun DexVS fibrous matrices with HSP, we demonstrated control over the degree of crimping and resulting tensile nonlinearity (**Figure 5.1, Figure 5.2**). Additionally, we utilized photoinitiated radical polymerization of DexVS fibers after functionalization with HSP to orthogonally control stiffness and fiber crimp. Noncrimped fibrous matrices exhibited relatively high Young's moduli values and more linear behavior as compared to crimped fibrous matrices possessing a low stiffness toe region followed by increased stress-strain response beyond the transition strain. Whether this degree of nonlinearity (between 5-15% strain) affects cell behavior, though, likely depends on the forces and strains that cells generate. Previous work from our lab showed cell force-induced strain up to 50% in a similar compliant fibrous matrix (Wang et al., 2019), however further analysis and quantification of cell traction forces and resulting matrix strains during dynamic physical remodeling events remains an outstanding challenge.

Regardless, we observed striking changes in cell morphology and behavior between control and crimped fibrous matrices, where fiber crimp promoted fiber recruitment and increases in cell and nuclear thickness, concurrent with decreases in cell spreading, focal adhesion area, and YAP nuclear localization (**Figure 5.3, Figure 5.4**). These observations contrast previous results in fibrous matrices from our lab and others, where lower matrix stiffness and increased fiber recruitment correlated with increases in cell spreading and adhesion formation (Baker et al., 2015; Davidson et al., 2020a; Xie et al., 2017). We hypothesize that this discrepancy is due to the enhanced three-dimensionality of matrices with crimped fibers (**Figure 5.1, Figure 5.3**). Three-dimensional distribution of cell adhesions has been shown to influence cell shape, polarity, and cytoskeletal organization (Baker & Chen, 2012). Forced apical-basal polarity and unrestricted planar spreading of cells plated in 2D enables distinct cytoskeletal organization compared to cells embedded in 3D ECM, which tend to assume a stellate morphology with limited polarization (Hakkinen et al., 2011). Further, decreases in focal adhesions and YAP nuclear localization have been noted in cells embedded within 3D hydrogels as compared to on flat, 2D surfaces (Caliari et al., 2016b; Doyle & Yamada, 2016; Lee et al., 2019). In addition to the changes in dimensionality, crimped matrices exhibit a lower stress-strain response over large strain regimes which could also contribute to impaired spreading and decreased contractility.

In addition to fixed timepoint analysis, we investigated EC migratory dynamics via time-lapse microscopy. In addition to decreases in cell spreading, adhesion, and nuclear YAP localization, we observed an increase in migration speeds (**Figure 5.5**). This observation is in line with previous reports indicating that larger, more mature adhesions imply slower adhesion turnover and lower migration speeds (Peyton & Putnam, 2005). However, recent work from Mason et al. has linked nuclear YAP/TAZ to limiting adhesion maturation and ultimately increasing migration speeds (Mason et al., 2019). While mechanosensing is likely involved in cell migration, we anticipate other physical cues could contribute to differences in migration speed between crimped and control matrices. Specifically, the same number of fibers distributed throughout a thicker matrix implies a relative increase in porosity, which could facilitate cell migration in 3D (**Supplementary Movie 5.2**). Additionally, the low stiffness at low strains of crimped fibrous matrices enabled prominent fiber recruitment and large matrix deformations (**Figure 5.3**) and the formation of "strap" regions of aligned fibers spanning neighboring cells. These regions of anisotropic topography, adhesive ligand distribution, and stiffness likely directs cell protrusions and subsequent migration (Wang et al., 2018) (**Figure 5.5**). The dynamic reorganization of matrix fibers and cell-to-cell mechanical interactions in crimped matrices may also contribute to the observed increase in migration speeds. Such a result would be supported by computational modeling studies implicating nonlinear mechanics of fibrous ECM structure in the optimization of long-range mechanical communication between cells (Ma et al., 2013; Sopher et al., 2018b; Wang et al., 2015).

Together, the formation of strap regions, long-range mechanical communication, and faster cell migration could all contribute to the enhanced self-assembly of EC networks containing tube-like structures in crimped matrices compared to controls. Increased fiber recruitment with fiber crimp ultimately causes matrix densification and restriction of potential network paths of assembling cells. These restricted paths contain tensile tracks of aligned fibers that facilitate long-range force transmission to support longer cell extensions reflected by the decrease in area to perimeter ratio with fiber crimp. Additionally, densification of matrix fibers beneath extending cells may explain the appearance of tube-like EC structures (**Figure 5.6**). Interestingly, the polarity of tubular structures formed here parallels that of previous work spatially patterning ECs in micromolded collagen gels (Raghavan et al., 2010). In these studies, ECs densified and wrapped around a collagen core to form tubules, yielding structures that anastomosed with host vasculature upon implantation (Baranski et al., 2013). While the presence of synthetic DexVS fibers within these cell structures is a potential limitation, future work could utilize crimped fibers to mediate tubulogenesis followed by triggered degradation of fibers to open lumenal space.

Beyond the potential to engineer vascularized constructs, crimped synthetic fibers may also hold potential for restoring the mechanical function of dense connective fibrous tissues. One outstanding issue with the functionality of fibrous scaffolds for tissue repair is limited cell infiltration due to dense packing of fibers and subcellular pore size. Cell invasion upon implantation, however, is critical for rapid progenitor or repair cell recruitment and as well as vascularization. Our results suggest fiber crimp increases in matrix porosity and cell migration speed. While many methods to increase cell infiltration of fibrous scaffolds have been developed (Baker et al., 2008; Wu & Hong, 2016), crimped fibers could present a new strategy towards resolving this challenge.

5.6 Conclusion

In this work, we developed a new approach to generating crimped structure in electrospun fibrous matrices by functionalizing synthetic DexVS fibers with a hydrophilic swelling peptide. This technique presents an additional level of structural and mechanical control to an already highly tunable biomaterial platform. Due to the ubiquity of fiber crimp in collagenous tissue, this unique microstructure likely has influence on cell and tissue behavior at multiple length scales. We found that matrices possessing crimped fibers led to pronounced changes in mechanical nonlinearity and regulated EC mechanosensing, migration, and network formation. The approach described here could be used in future work to better understand the influence of nonlinear ECM mechanics in healthy and abnormal tissue function and to engineer tissue constructs that more accurately recapitulate the mechanical behavior of native tissues.

5.7 Materials and Methods

5.7.1 Reagents

All reagents were purchased from Sigma Aldrich and used as received, unless otherwise stated.

5.7.2 Cell culture

Human umbilical vein ECs were cultured in endothelial growth medium (EGM-2; Lonza, Basel, Switzerland) supplemented with 1% penicillin-streptomycin-fungizone (Gibco, Waltham, MA). Cells were cultured at 37°C and 5% CO2. ECs were used from passages four to eight in all experiments.

5.7.3 DexVS synthesis

Dextran was reacted with divinyl sulfone following a previously described procedure (Yu & Chau, 2012). Briefly, dextran (5 g) was dissolved in 250 mL of sodium hydroxide (100 mM) solution on a stir plate at 300 rpm before the addition of divinyl sulfone (12.5 mL). The reaction proceeded for 3.5 minutes before termination by addition of 2.5 mL hydrochloric acid (12 M). The product was dialyzed against milli-Q water for 3 days and then lyophilized. DexVS was characterized by ^{1}H NMR and a vinyl sulfone/dextran repeat unit ratio of 0.70 was determined.

5.7.4 Fibrous matrix fabrication

DexVS was dissolved at 0.7 g ml^{-1} in a 1:1 mixture of milli-Q water and dimethylformamide with 1.2% (w/v) lithium phenyl-2,4,6-trimethylbenzoylphosphinate (LAP; Colorado Photopolymer Solutions, Boulder, CO) photoinitiator, 2.5% (v/v) methacrylated rhodamine (25 mM; Polysciences, Inc., Warrington, PA), and 5.0% (v/v) glycidyl methacrylate. Electrospinning of DexVS solution was performed at a flow rate of 0.2 mL h^{-1}, voltage of 7.0 kV, and gap distance of 7 cm. After electrospinning, fibers were stabilized by primary crosslinking under UV light (100 mW cm^{-2}) for 120 s, hydrated in LAP solution (0.01 mg mL^{-1}), and then exposed again to UV light (100 mW cm^{-2}) for 20 s. Fibers were collected on poly(dimethylsiloxane) (PDMS; Dow Silicones Corporation, Midland, MI) arrays of circular wells produced by soft lithography as previously described (Baker et al., 2015). Briefly, silicon wafer masters possessing SU-8 photoresist (Microchem, Westborough, MA) were produced by standard photolithography and used to generate PDMS stamps. Following silanization with trichloro(1H,1H,2H,2H-perfluorooctyl)silane, stamps were used to emboss uncured PDMS onto oxygen plasma-treated coverslips. Well arrays were methacrylated with vapor-phase silanization of 3-(trimethoxysilyl)propyl methacrylate in a vacuum oven at 60°C for at least 6 h to promote fiber adhesion to PDMS.

5.7.5 Peptide functionalization and seeding of DexVS fibers

DexVS fibers were first functionalized with the cell-adhesive peptide cyclo[RGDfK(C)] (cRGD; Peptides International, Louisville, KY; 100 μM) to facilitate cell attachment followed by simultaneous functionalization with the hydrophilic swelling peptide (HSP) CGRDGS (Genscript, Piscataway, NJ) and L-cysteine to induce fiber crimping. Various concentrations of HSP were coupled to control the degree of crimping, and L-cysteine was added to keep the total final peptide concentration consistent at 2 mM for all conditions. All peptides were coupled via Michael-type addition to available vinyl sulfone groups. Peptides were dissolved in milli-Q water containing HEPES (50 mM), phenol red (10 μg mL^{-1}), and 1 M NaOH to adjust the pH to 8.0. A 350 μL volume of solution was added to each substrate. cRGD and HSP/L-cysteine solutions were incubated for 30 and 45 minutes, respectively, at room temperature with 3x PBS rinses in between. Following peptide functionalization, substrates were rinsed 3x with PBS before cell seeding. ECs were trypsinized, centrifuged, and resuspended in 1.5% (w/v) methylcellulose supplemented EGM-2 to increase media viscosity for seeding onto suspended fibrous matrices.

5.7.6 Mechanical characterization

To determine the tensile mechanical properties of suspended DexVS fibrous matrices, microindentation testing with a rigid cylinder was performed on a commercial CellScale Microsquisher (CellScale, Waterloo, Ontario). Cylinders (1 mm diameter, 0.5 mm tall) of SU8 photoresist were microfabricated and affixed to pure tungsten filaments (0.156 mm diameter, 58 mm length). Samples were indented to a depth of 350 μm at an indentation speed of 4 μm s^{-1}. Indenter displacement and force were converted to strain and stress, respectively. Young's modulus was calculated in both low (0.0 – 5.5%) and high (5.5 – 11.0%) strain regimes by linear fits to the stress-strain plot. Transition strain was calculated with a custom Matlab script by finding the transition point between the toe- and linear-regions of the stress-strain data (Lake et al., 2009).

5.7.7 Fluorescent staining and microscopy

ECs on DexVS fibers were first fixed in 4% paraformaldehyde for 10 min at room temperature. Alternatively, to extract cytoplasmic vinculin, samples were simultaneously fixed and permeabilized in 2% paraformaldehyde in a buffer containing 1,4-piperazinediethanesulfonic acid (PIPES, 0.1 M), ethylene glycol-bis(2-aminoethylether)-N,N,N',N'-tetraacetic acid (1 mM), magnesium sulfate (1 mM), poly(ethylene glycol) (4 % w/v), and triton X-100 (1%) for 10 min at room temperature. To stabilize the fibers for sample processing and long-term storage, paraformaldehyde-fixed samples were crosslinked in 2 mL LAP solution (1.0% w/v) and exposed to UV light (100 mW cm^{-2}) for 30 s. To stain the actin cytoskeleton and nuclei, cells were permeabilized in PBS solution containing Triton X-100 (5% v/v), sucrose (10% w/v), and magnesium chloride (0.6% w/v), and simultaneously blocked in 1% (w/v) bovine serum albumin and stained with phalloidin and DAPI. For immunostaining, samples were permeabilized, blocked for 1 h in 1% (w/v) bovine serum albumin, and incubated with mouse monoclonal anti-vinculin antibody (1:1000, Sigma #V9264), mouse monoclonal anti-YAP antibody (1:1000, Santa Cruz #101199), or mouse monoclonal anti-VE-cadherin F-8 (1:1000, Santa Cruz #9989) followed by secondary antibody (1:1000, Life Technologies #A21236) for 1 h each at room temperature with 3x PBS washes in between. Fixed samples were imaged on a Zeiss LSM800 laser scanning confocal microscope (Zeiss, Oberkochen, Germany). Unless otherwise specified, images are presented as maximum intensity projections. Fluorescent images were processed and quantified via custom Matlab scripts. Fiber recruitment was quantified by dividing the average fiber signal intensity beneath the cell body by the average fiber signal intensity outside the cell body.

5.7.8 Time-lapse microscopy and migration analysis

Time-lapse microscopy was performed on a Zeiss LSM800 laser scanning confocal microscope. Migration experiments were imaged immediately after seeding at 15 min frame intervals over 16 hours. To image ECs, lentiviral transduction of lifeAct-GFP was utilized as in our previous work (Wang et al., 2019). Immediately prior to imaging, cell nuclei were labeled with Hoechst 33342 (3 μg mL^{-1}) for 10 min. Following raw image export, average cell spread area was calculated for each timepoint. Additionally, cell nuclei were tracked with a custom Matlab script predicated on the IDL Particle Tracking code (Crocker & Grier, 1996). Migration speed was calculated as total tracked distance over total tracked duration. For migration speed analysis, nuclei were only tracked between 4 and 16 hours after ECs had spread.

5.7.9 Statistics

Statistical significance was determined by one-way analysis of variance (ANOVA) with post-hoc analysis (Tukey test) or Student's t-test where appropriate, with significance indicated by $p < 0.05$. Sample size is indicated within corresponding figure legends and all data are presented as mean ± standard deviation.

5.8 Supplementary Figures

Supplementary Movie 5.1: Crimping of DexVS fibrous matrices. Representative confocal fluorescence time-lapse movie of DexVS fibers (magenta) crimping upon addition of 2.0 mM HSP. Scale bar: 100 µm.

Supplementary Movie 5.2: EC migration on control DexVS fibrous matrices. Representative confocal fluorescence time-lapse movie of EC (cyan) migration on control (0.0 mM HSP) DexVS fibrous matrices (magenta). Scale bar: 200 µm.

Supplementary Movie 5.3: EC migration on crimped DexVS fibrous matrices. Representative confocal fluorescence time-lapse movie of EC (cyan) migration on crimped (2.0 mM HSP) DexVS fibrous matrices (magenta). Scale bar: 200 µm.

Link to all supplementary movies

Chapter 6: Mechanical Intercellular Communication via Cell Force Transmission During Vascular Network Formation

6.1 Authors

Christopher D. Davidson, Samuel J. DePalma, William Y. Wang, Jordan L. Kamen, Danica Kristen P. Jayco, Brendon M. Baker

6.2 Abstract

Intercellular communication is critical to the development and homeostatic function of all tissues. Previous work has shown that cells can communicate mechanically via transmission of cell-generated forces through their surrounding extracellular matrix, but this process is not well understood. Here, we utilized synthetic, electrospun fibrous matrices in conjunction with a microfabrication-based cell patterning approach to examine mechanical intercellular communication (MIC) between endothelial cells (ECs) during the assembly of microvascular networks. We found that cell force-mediated matrix displacements in deformable fibrous matrices underly directional migration of neighboring ECs towards each other prior to the formation of stable cell-cell connections. We also identified a critical role for intracellular calcium signaling mediated by focal adhesion kinase and TRPV4 during MIC that extends to multicellular assembly of vessel-like networks in 3D fibrin hydrogels. The results presented here

are critical to the design of biomaterials that support cellular self-assembly for tissue engineering applications.

6.3 Introduction

The ability of cells to communicate and coordinate their activity is crucial to the development and homeostatic function of all tissues (Yang et al., 2021). Intercellular communication through receptor-ligand engagement at the cell-cell interface or via diffusive soluble factors has been extensively studied (Dejana, 2004; Gumbiner, 1996; Kandler & Katz, 1998; Singer, 1992). In addition to these well-established means of biochemically mediated intercellular signaling, a more recent body of evidence has shown that cells can also communicate via cell-generated forces transmitted to neighboring cells through the extracellular matrix (ECM) (Alisafaei et al., 2021; Sapir & Tzlil, 2017). Cells mechanically engage their surrounding matrix through integrin-based adhesion complexes, or focal adhesions (FAs), which connect the ECM to the cell's actomyosin cytoskeleton (Geiger et al., 2009). These mechanochemical signaling hubs allow cells to continuously sense both passive mechanical and topographical properties of the matrix as well as active external forces applied to the cell (Ricca et al., 2013). Concurrently, cell-generated forces applied to the ECM through FAs result in matrix deformations that may impact surrounding cells. The dynamic and reciprocal nature of generating and sensing mechanical signals, however, makes mechanical intercellular communication (MIC) difficult to investigate.

Several prior studies suggest that cell force-generated deformations of the ECM mediate communication between neighboring cells to regulate critical cell functions in cell migration and multicellular assembly. MIC has been observed in a variety of settings spanning different cell types, distinct ECM settings, and across scales ranging from tissues (Sawhney & Howard, 2002; Stopak & Harris, 1982), to multicellular clusters (Guo et al., 2012; Shi et al., 2014), to single cells (Natan et al., 2020; Nitsan et al., 2016; Pakshir et al., 2019; Reinhart-King et al., 2008; Winer et al., 2009). For example, in seminal work nearly four decades ago, Stopak and Harris observed that cultured contractile tissue explants embedded within collagen matrices physically reorganize and align collagen fibrils, generating tensile regions that direct cell migration between adjacent explants over millimeter length scales (Stopak & Harris, 1982). At the single cell level, Reinhart-King et al. showed evidence that endothelial cell (EC) traction forces create local gradients of tension that influence EC migration and the formation of contacts between neighboring cells on compliant polyacrylamide gels (Reinhart-King et al., 2008). Despite this breadth of evidence, however, we lack an understanding of the cellular machinery required for cells to sense and respond to mechanical signals. Further, how tissue-relevant matrix properties mediate the transmission of cell-generated forces has not been established.

Several computational models suggest that fibrous matrices are optimal for transmitting forces over large distances (i.e., greater than one cell body away) due to their nonlinear elastic behavior and the potential for strain-induced alignment of ECM fibers (Abhilash et al., 2014; Goren et al., 2020; Hall et al., 2016; Humphries et al., 2017; Ma et al., 2013; Notbohm et al., 2015; Ronceray et al., 2016; Rudnicki et al., 2013; Sopher et al., 2018b; Wang et al., 2015). Indeed, collagen and fibrin hydrogels, materials that possess fibrous microstructure and nonlinear mechanics, are the primary settings where long-range mechanical interactions between cells have been previously documented. However, the limited structural and mechanical tunability of these materials limits understanding of how ECM properties regulate MIC (Li et al., 2017). Conversely, tunable, non-fibrous synthetic hydrogels such as polyacrylamide or poly(ethylene glycol) offer a high degree of tunability, but rapidly dissipate forces over short distances (< 25 μm) away from the cell due to their continuum and affine mechanical behavior (Legant et al., 2010; Reinhart-King et al., 2003). Consequently, we lack an understanding of how the distinct topographical and mechanical properties of fibrous ECMs regulate long-range force transmission and resulting MIC between cells.

Our lab has previously developed synthetic matrices of electrospun dextran-based hydrogel fibers with user-defined architecture and mechanical properties (Baker et al., 2015; Davidson et al., 2019b, 2020b, 2020c; Wang et al., 2019). Here, we combined this biomaterial system with a microfabrication-based cell-patterning method to investigate EC force-mediated matrix displacements and MIC as a function of matrix stiffness. Using this approach, we found that soft, deformable fibrous matrices support long-range matrix deformations and MIC between pairs of ECs. Specifically, we observed that force transmission across fibers spanning neighboring cells was required to support directed protrusions, migration, and the formation of cell-cell contact between ECs up to 200 μm apart. We also identified critical roles for intracellular calcium (Ca^{2+}) signaling, focal adhesion kinase (FAK) signaling, and mechanosensitive ion channels during the generation and response to mechanical signals transmitted through the ECM. Lastly, we extended these observations to 3D fibrous settings by examining MIC during vascular network assembly in fibrin hydrogels.

6.4 Results

6.4.1 Cell-generated matrix deformations and tension support enhanced cell spreading and multicellular cluster formation

Vasculogenic assembly is one context where a deeper understanding of long-range mechanical communication could prove invaluable (Risau & Lemmon, 1988). Occurring naturally during embryonic development and adult neovascularization, this process involves assembly of individual ECs into an interconnected network of capillary-like structures and requires cellular communication and coordination over length-scales larger than a cell (Lesman et al., 2016; Van Oers et al., 2014). If better understood, control over this process presents a promising approach to engineer microvasculature to support parenchymal cells, a major challenge in the field of tissue engineering and regenerative medicine (Song et al., 2018). We previously found that cell force-mediated matrix reorganization portends EC network assembly, implicating matrix stiffness in MIC (**Figure 6.1a,b**) (Davidson et al., 2019b). To more closely examine interactions between ECs as a function of fibrous matrix stiffness, matrices of electrospun DexMA fibers were suspended over an array of microfabricated wells (Baker et al., 2015). Prior to cell seeding, the bulk stiffness of matrices was modulated via photocrosslinking and fibers were functionalized with an RGD-containing peptide to facilitate integrin-dependent cell attachment (**Figure 6.1a**).

To test our hypothesis that cell forces and resulting matrix deformations mediate MIC between ECs, we first seeded cells over a range of densities on low stiffness matrices that were deformable (E = 0.724 kPa) or high stiffness matrices that were non-deformable (E = 19.7 kPa) under cellular traction forces (**Supplementary Figure 6.1**). As seeding density roughly corresponds to the average distance between neighboring cells, we hypothesized the effect of

MIC would manifest as cell-density dependent differences in cell spreading on deformable vs. non-deformable matrices. At low seeding densities (50 cells mm^{-2}), isolated cells remained largely unspread independent of matrix stiffness, although a moderately higher spread area was noted in non-deformable matrices (**Figure 6.1c-e**). However, increasing seeding density resulted in more marked increases in cell spread area in deformable matrices as compared to non-deformable matrices, with significant differences noted at 200 and 250 cells mm^{-2}, indicating a synergistic effect between matrix stiffness and seeding density on cell spreading (**Figure 6.1e**). Along with this increase in spread area, larger interconnected multicellular clusters formed on cell-deformable matrices (**Figure 6.1f**). Although this experiment did not control for paracrine effects which likely are operative, these results suggest that the spacing between cells and sensing of cell force-mediated matrix displacements influences cell spreading and the formation of interconnected, multicellular clusters.

We next investigated cell-ECM and cell-cell adhesion during this process by immunostaining for vinculin (a force-sensitive component of FAs) and VE-cadherin (the direct link between ECs at adherens junctions), respectively (**Figure 6.1g,h**). At an early time point when cells are putatively sending and receiving mechanical signals that mediate cell spreading and directional extension (2 h post-seeding), we observed significantly more vinculin-rich FAs in deformable compared to non-deformable matrices, suggesting heightened cell-ECM adhesion and force transmission to the matrix (**Figure 6.1i**). VE-cadherin levels were low independent of matrix stiffness at this time point, likely due to insufficient time for cells to form stable cell-cell junctions (**Figure 6.1i**). At 12 h post-seeding, however, we observed significantly higher VE-cadherin signal in ECs in deformable matrices compared to those in non-deformable matrices (**Figure 6.1i**). Together, these results indicate that cell-deformable fibrous matrices facilitate strong cell-ECM adhesions that presage the formation of robust adherens junctions and further support the involvement of cell-generated forces transmitted between cells through the matrix during intercellular communication.

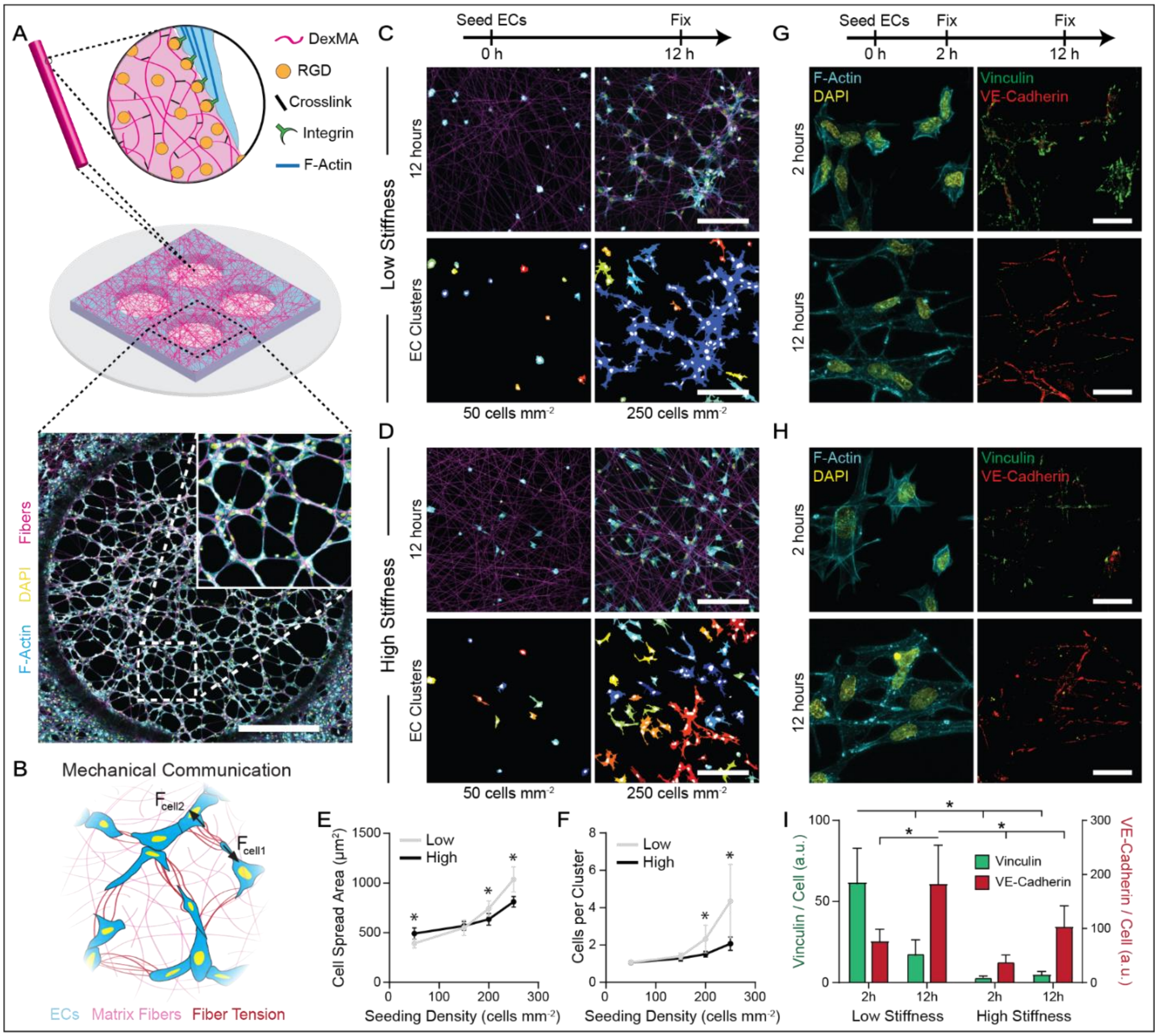

Figure 6.1: Cell-generated tensile forces and resulting matrix deformations correspond to increased cell spreading and the formation of multicellular clusters. (A) Schematic of microfabricated PDMS multi-well substrate containing an array of wells, each supporting an isolated suspended matrix of DexMA fibers functionalized with RGD to facilitate cell adhesion (scale bar, 1 mm). (B) Schematic of hypothesis that matrix fibers enable MIC underlying EC network formation. (C-D) Confocal fluorescent images of phalloidin-stained ECs (cyan), nuclei (yellow), and rhodamine-labeled DexMA fibers (magenta) with respective color-coded maps of contiguous actin clusters at low (50 cells mm^{-2}) and high (250 cells mm^{-2}) seeding density in (C) low stiffness, cell-deformable matrices and (D) high stiffness, non-deformable matrices (scale

bar, 200 μm). (E) Quantification of cell spread area and (F) average number of ECs per contiguous actin cluster as a function of seeding density and matrix stiffness (n = 12 fields of view). (G-H) Confocal fluorescent images of phalloidin-stained ECs (cyan), nuclei (yellow), vinculin (green), and VE-cadherin (red) at 2 and 12 hours after seeding in (G) low stiffness and (H) high stiffness matrices (scale bar, 25 μm). (I) Quantification of total vinculin and VE-cadherin fluorescent intensity normalized to cell density as a function of time and matrix stiffness (n = 6 fields of view). All data presented as mean ± SD; asterisk denotes significance with $P < 0.05$.

The above results suggest low stiffness, cell-deformable fibrous ECM promotes FA formation and generation of mechanical signals that underly cellular communication. To investigate the dynamics of EC assembly into multicellular clusters, timelapse imaging of Hoechst-labeled ECs transduced with a LifeAct-GFP F-actin reporter was conducted over the same 12 h timeframe. As in our previous experiments, ECs actively recruited matrix fibers and formed large multicellular clusters in deformable matrices; this phenomenon was not observed in non-deformable matrices (**Supplementary Movie 6.1**). ECs additionally migrated overall faster in deformable matrices compared to in non-deformable matrices (**Figure 6.2a-c**). Analyzing migration speed over discrete intervals of time, we noted the largest discrepancy in speed (1.5-fold) during the first two hours of culture, compared to a 1.25-fold difference throughout the remainder of timelapse imaging (**Figure 6.2b,c**). Interestingly, enhanced migration speeds over the first two hours coincided with a rapid increase in multicellular cluster size (**Figure 6.2d**). We noted instances of directed extension and migration of neighboring cells towards each other to form multicellular clusters in deformable matrices, while migration in non-deformable matrices appeared uncoordinated or random (**Figure 6.2e**, **Supplementary Movie 6.1**). Together, this data suggests that ECs respond to mechanical signals transmitted through cell-deformable ECM by directionally migrating towards one another at higher speeds to more efficiently form multicellular structures.

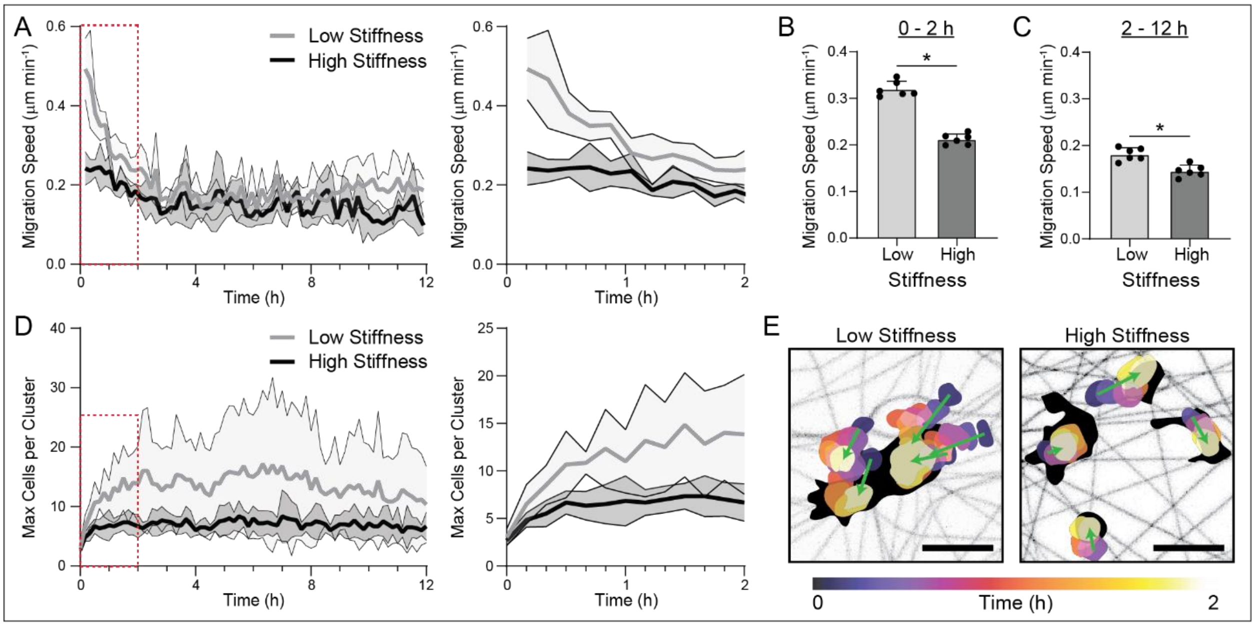

Figure 6.2: Low stiffness, cell-deformable fibrous matrices increase cell migration speed during multicellular cluster formation. (A) Migration speed of ECs over 12 hours following seeding in either low stiffness, cell-deformable matrices or high stiffness, non-deformable matrices (n = 6 fields of view). (B) Quantification of migration speed during the first 2 hours and (C) remaining 10 hours of culture as a function of matrix stiffness (n = 6 fields of view). (D) Maximum cluster size over 12 hours of culture as a function of matrix stiffness (n = 6 fields of view). (E) Temporally color-coded overlay capturing the motion of nuclei over a 2 hour time course in low and high stiffness matrices. Green arrows represent direction of movement for each individual nuclei with eventual contiguous actin structures demarcated in black (scale bars, 50 μm). All data presented as mean ± SD with superimposed data points; asterisk denotes significance with $P < 0.05$.

6.4.2 Micropatterning single ECs reveals matrix stiffness influences cell spreading, FA formation, and matrix deformations

While the previous model provides evidence for MIC in deformable fibrous matrices, the highly dynamic and reciprocal nature of generating, receiving, and responding to mechanical signals within a randomly distributed population of cells is challenging to dissect. Specifically, heterogeneous cell seeding in this setting precludes measuring strain fields of individual ECs, which could provide insight into the generation and transmission of mechanical signals. Thus, we developed a microfabrication-based cell patterning method to precisely pattern individual

ECs at the center of a suspended DexMA fiber matrix with defined properties (**Figure 6.3a**, **Supplementary Figure 6.2**) (Gong & Mills, 2018). Briefly, ECs were isolated using cell-patterning molds containing an array of 30 μm diameter microwells, approximately the size of a suspended EC following trypsin/EDTA treatment. This cell patterning mold was then aligned with an identically spaced fiber matrix array such that single ECs were accurately and consistently patterned at the center of an individual suspended matrix with a 500 µm diameter (**Figure 6.3a,b**).

Single ECs were patterned in low stiffness/cell-deformable (E = 0.724 kPa), intermediate stiffness (E = 3.15 kPa), or high stiffness/non-deformable (E = 19.7 kPa) DexMA matrices, cultured for 12 hours, and analyzed for cell spreading (F-actin) and FAs (vinculin). With increasing matrix stiffness, we observed a slight increase in cell spread area (**Figure 6.3c,e**) in agreement with previous observations at low EC seeding density (**Figure 6.1e**, 50 cells mm^{-2}). Accordingly, we saw a modest increase in the total number of FAs per cell with increasing matrix stiffness (**Figure 6.3d,f**). However, when we analyzed the size of each individual FA, we observed that ECs in soft matrices had significantly higher average FA area despite a lower total number of adhesions (**Figure 6.3g**). This was attributed to a higher proportion of large adhesions (> 3 μm^2) in low stiffness matrices (8.5%) compared to in intermediate (2.5%) and high (2.7%) (**Figure 6.3h**). Interestingly, the difference in adhesion area as a function of stiffness when ECs were isolated as single cells is modest compared to the difference seen with bulk seeding (**Figure 6.1**), suggesting that robust adhesions in low stiffness matrices could be developed as a result of active mechanical signals transmitted by neighboring cells.

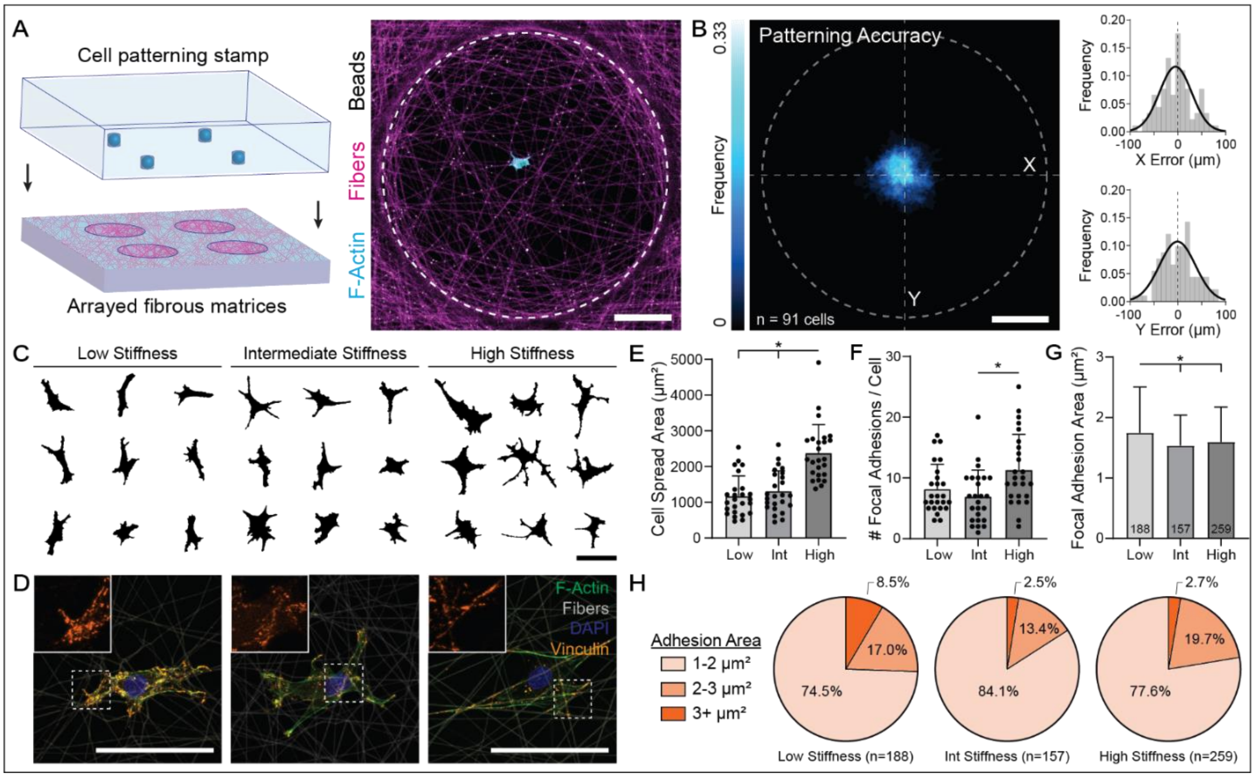

Figure 6.3: Micropatterning single ECs in individual suspended fibrous matrices reveals cell spreading and FA formation are matrix stiffness-dependent. (A) Schematic depicting microfabrication-based patterning approach to isolate individual ECs at the center of suspended fibrous matrices. Representative confocal fluorescent image of patterned EC (cyan), rhodamine-labeled fibers (magenta), and fluorescent beads embedded in matrix fibers (white) (scale bar, 100 µm). (B) F-actin heat map of patterned ECs with histograms of average patterning error in x- and y-directions (n = 91 cells) (scale bar, 100 µm). (C) Cell outlines of nine representative cells as a function of matrix stiffness (scale bar, 100 µm). (D) Representative immunostained images of FAs in ECs as a function of matrix stiffness; F-actin (green), DexMA fibers (grey), nuclei (blue), and vinculin (orange) (scale bar, 100 µm). (E) Quantification of cell spread area (n = 25 cells), (F) number of FAs per cell (n = 25 cells), and (G) average FA area as a function of matrix stiffness. Data presented as mean ± SD with superimposed data points; asterisk denotes significance with $P < 0.05$. (H) Distribution of individual FA area as a function of matrix stiffness showing a larger population of 3+ μm^2 FAs in low stiffness matrices.

While analysis of cell morphology and FAs at fixed timepoints provides useful information, it does not capture the dynamic interplay between cell spreading and ECM deformations. Thus, we next combined our cell/ECM patterning technique with timelapse confocal microscopy (**Supplementary Movie 6.2**). The dynamics of cell spreading and matrix deformations varied with stiffness, specifically in terms of spreading as well as the number and lifetime of protrusions (**Figure 6.4a,b**). In cell-deformable matrices, ECs generally remained unspread for the first four hours of culture during which cells actively recruited matrix fibers beneath the cell body; in contrast, ECs in intermediate stiffness and non-deformable matrices spread immediately (**Figure 6.4e**). In all stiffness conditions, migration was limited and did not significantly vary with matrix stiffness (**Figure 6.4g**). With increasing matrix stiffness, ECs generated more protrusions over the 12-hour timelapse (**Figure 6.4h**, **Supplementary Figure 6.3**), while the average lifetime of each protrusion decreased (**Figure 6.4i**). As cell protrusions and constituent FAs comprise a critical force-generating apparatus of the cell, these data suggest that cell-deformable matrices not only promote increased FA area (**Figure 6.1, Figure 6.3**), but also more directional and longer lasting mechanical signals. In addition, we confirmed expected differences in EC force-mediated matrix deformations (**Figure 6.4c,d,f**). In low stiffness matrices, bead displacements were measurable across the entire suspended matrix (up to 250 μm away from the cell centroid) (**Figure 6.4c,d,l**, **Supplementary Figure 6.4**) and furthermore, temporally correlated with increases in cell spreading (**Figure 6.4e,f**). With increasing matrix stiffness, however, the magnitude and range of displacements diminished, where high stiffness matrices displayed negligible displacements across the entire matrix (**Figure 6.4k,l**).

In addition to stiffness, we also investigated the effect of matrix fiber density by altering the duration of electrospun fiber collection while maintaining a constant degree of crosslinking (equivalent to the lowest stiffness condition above) (**Supplementary Figure 6.1**). Similar to increasing the stiffness of a fixed density of fibers, increasing the density of low stiffness fibers decreased the magnitude and range of displacements, although to a lesser degree (**Supplementary Figure 6.5**, **Supplementary Movie 6.3**). Taken together, this data indicates that low stiffness, low density fibrous matrices support long-range matrix deformations and prime ECs for directed force generation by promoting the formation of larger FAs and fewer but longer-lived protrusions.

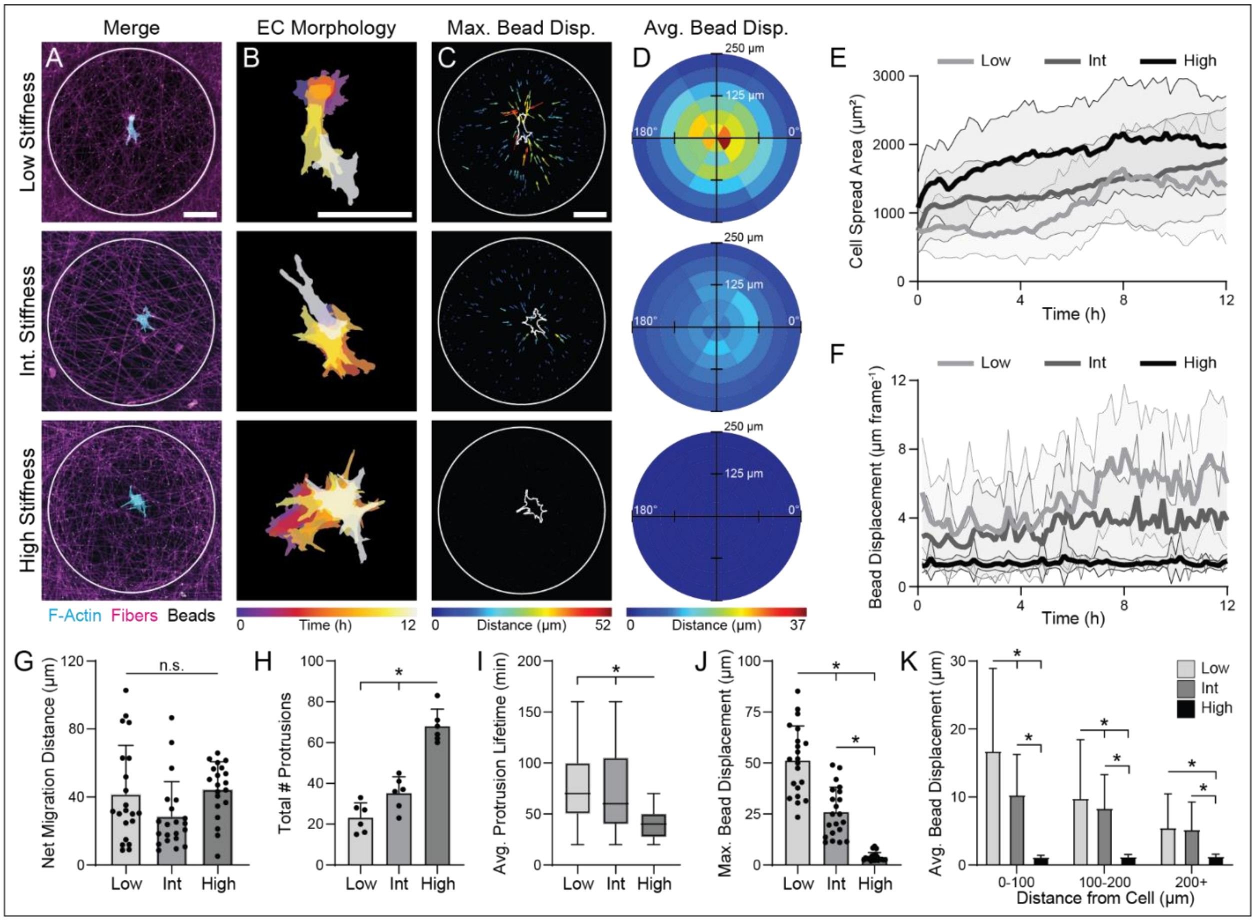

Figure 6.4: Cell-deformable fibrous matrices support more persistent mechanical signals by promoting fewer, but longer lasting protrusions. (A) Representative confocal fluorescent image of LifeAct-GFP expressing ECs (cyan), rhodamine-labeled DexMA fibers (magenta), and fiber-embedded fluorescent beads (white) (scale bar, 100 µm). (B) Temporally color-coded overlay of EC cell bodies over a 12 hour time course following patterning (scale bar, 100 µm). (C) Size- and color-coded vector plots displaying maximum displacement of each bead over a 12 hour time course (scale bar, 100 µm). (D) Binned average bead displacements for all ECs aligned along their long axis (0°) with color-coded magnitudes (n > 20 cells). (E) Cell spread area and (F) fluorescent bead displacement over a 12 hour time course as a function of matrix stiffness (n > 20 cells). (G) Net migration distance (n > 20 cells), (H) total number of protrusions (n = 6 cells), (I) average protrusion lifetime (n = 6 cells, n = 30 protrusions), and (J) maximum bead displacement as a function of matrix stiffness (n > 20 cells). (K) Binned average bead displacements as a function of starting distance from the cell centroid (n > 20 cells, n > 627 beads). All data presented as mean ± SD with superimposed data points; asterisk denotes significance with $P < 0.05$.

6.4.3 Propagation of mechanical signals between neighboring cells promotes directed migration and formation of cell-cell connections

Single cell patterning studies indicate that low stiffness matrices prompt ECs to generate larger, more directional matrix displacements, but the generation of a mechanical signal is only an initial step during MIC. Thus, we next investigated how ECs receive and respond to cell-generated force transmission through fibrous matrices. To do so, we adapted our cell/ECM patterning technique to pattern two cells at a defined distance of 200 μm away from each other (**Figure 6.5a**), as single cell studies demonstrated that ECs in low stiffness matrices generate strain fields that propagate a distance of 200 μm away from the cell (**Figure 6.4**). Rigid boundaries of the microfabricated well were redesigned to ensure even spacing between cell pairs and the fixed boundary at the well edge (**Figure 6.5a**). Combining this approach with timelapse confocal microscopy, we next aimed to determine if and how the stiffness of fibrous matrices regulated cell-cell interactions.

We first patterned cell pairs in cell-deformable and non-deformable DexMA matrices and defined cell-cell interaction as two ECs forming direct cell-cell contact at any time over a 12 h period (**Supplementary Movie 6.4**). In deformable matrices, 46.4% of EC pairs (n = 28) exhibited cell-cell interactions, as compared to 3.9% of EC pairs in high stiffness matrices (n = 26) (**Figure 6.5b,c**). Closer examination of EC pairs in deformable matrices revealed alignment of fibers spanning cell pairs that appeared to mediate directed extension, migration, and resulting cell-cell contact (**Figure 6.5d**). The alignment of fibers appeared to result from cell force-mediated matrix reorganization and preceded directional migration of cell pairs towards one another by approximately 20-30 minutes (**Figure 6.5e**, **Supplementary Figure 6.6**). Aligned fibers spanning cell pairs did not occur in instances where cells did not interact, independent of matrix stiffness, suggesting that cell force-mediated fiber alignment is a prerequisite to mechanical communication (**Supplementary Figure 6.6**).

Two non-mutually exclusive explanations for a requirement of fiber alignment in cell-cell interactions include: 1) aligned fibers promote contact guidance cues, enabling directional migration of cell pairs towards each other, and/or 2) aligned fibers maximize force transmission between cells, in turn promoting directed extension, migration, and interaction. To ascertain the relative importance of these two scenarios, we patterned cell pairs on pre-aligned matrices of either low or high stiffness (**Figure 6.5b**, **Supplementary Movie 6.5**). If contact guidance alone were sufficient for cell-cell interactions, we would expect no effect of matrix stiffness on the percent of interacting cells. However, 76.9% of EC pairs (n = 26) in cell-deformable aligned matrices exhibited cell-cell interactions, in contrast to 33.3% of EC pairs in stiffer, non-deformable aligned matrices (n = 24) (**Figure 6.5b,c**). While interactions occurred in all matrix conditions, we noted that the nature of interaction differed between low and high stiffness matrices regardless of matrix alignment. In deformable matrices, ECs maintained cell-cell contact for significantly longer durations compared to in non-deformable matrices (**Figure 6.5d**). Together, these results indicate that force transmission through aligned fibers spanning neighboring cells maximizes the transmission of intercellular mechanical signals to facilitate direct cell-cell contact.

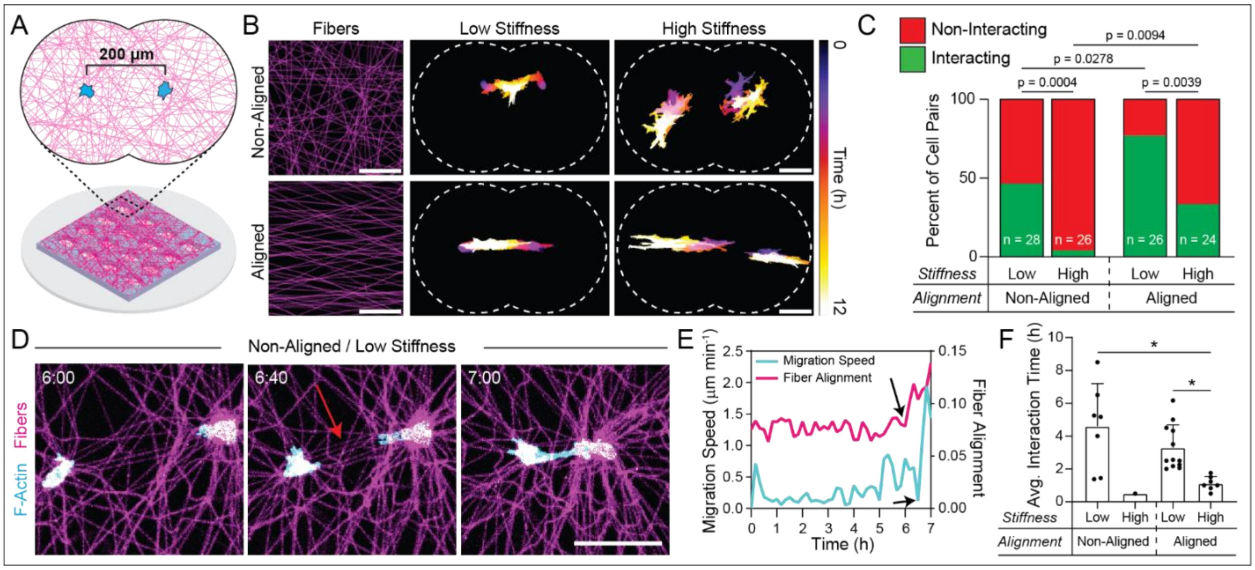

Figure 6.5: Force transmission through aligned fibers spanning neighboring cells promotes directed migration and the formation of cell-cell connections. (A) Schematic of cell pair patterning in which two ECs are patterned 200 µm apart on a suspended DexMA fibrous matrix. The fiber well is designed such that the distance between the two cells is equal to the distance between cells and well edges. (B) Representative image of initial matrix fiber morphology in non-aligned and aligned conditions. Temporally color-coded overlays capturing EC morphology and migration over a 12 hour time course after cell attachment as a function of matrix alignment and stiffness (scale bars, 100 µm). (C) Quantification of the percent of interacting and non-interacting cells over a 12 hour time course, with interacting cells defined as cell-cell contact at any point during the 12 hour timelapse. P-values determined by Fisher's exact test. (D) Representative cell pair interaction between ECs patterned in a non-aligned, low stiffness, cell-deformable matrix (scale bar, 100 µm) and (E) quantification indicating an increase in fiber alignment between the two cells followed by a rapid increase in migration speed prior to cell making direct contact. (F) Quantification of average interaction time (duration during which direct cell-cell contact was maintained). All data presented as mean ± SD with superimposed data points; asterisk denotes significance with $P < 0.05$.

6.4.4 Patterning EC lines identifies a critical role for coordinated intracellular Ca^{2+} signaling during MIC

These insights could enable the formation and stabilization of organized and stable multicellular structures from larger population of cells in larger tissues with translational potential. To explore this possibility, we further modified our cell/ECM patterning technique to pattern lines of equally spaced cells within a 1 mm² square suspended fiber matrix (**Figure 6.6a**).

Cells were patterned approximately 40 μm apart within each line to ensure overlapping cell-generated strain fields in deformable matrices, and two separate lines of cells were placed 500 μm apart to maximize experimental throughput while minimizing potential interactions between lines. Lines of ECs were patterned on cell-deformable and non-deformable matrices to observe how matrix mechanics and MIC regulated the formation and maintenance of organized multicellular structures. ECs patterned in deformable matrices aligned matrix fibers and formed stable structures resembling the original pattern (**Figure 6.6b,c**). ECs patterned in non-deformable matrices, however, appeared to spread and migrate independently, with limited fidelity to their original pattern as quantified by the proportion of nuclei within the original patterned region after 12 hours of culture (**Figure 6.6b-d**). Additionally, VE-cadherin immunostaining to assess the maturation of cell-cell contacts indicated significantly higher VE-cadherin signal in ECs patterned in deformable matrices as compared to non-deformable matrices, in agreement with our previous observations of bulk-seeded matrices (**Figure 6.6b,e**).

Beyond exploring the ability to control patterned multicellular assembly, we also employed this approach to mechanistically explore how ECs communicate with each other during multicellular assembly. Calcium (Ca^{2+}) is critical for many cell functions and in particular, Ca^{2+} cytosolic influx has previously been implicated in mechanosensing due to the presence of stretch activated ion channels in many cell types (Orr et al., 2006). Increases in intracellular Ca^{2+} have been shown to trigger a wide variety of cellular processes, including cytoskeletal reorganization underlying cell polarization, protrusion formation, and migration (Clapham, 2007; Tran et al., 2000). Thus, we hypothesized that intracellular Ca^{2+} signaling could play an important role in the EC response to mechanical signals in fibrous matrices.

To examine EC Ca^{2+} signaling, cells were patterned into lines onto suspended fiber matrices, incubated with a Ca^{2+} sensitive dye, and imaged two hours after patterning to visualize intracellular Ca^{2+} flux during the formation of cell-cell connections (**Supplementary Movie 6.6**). Ca^{2+} activity was significantly higher in ECs in cell-deformable matrices (**Figure 6.6f**), with cells exhibiting more frequent Ca^{2+} signal pulses compared to those in non-deformable matrices (**Figure 6.6g,h**). Additionally, we observed instances of temporally sequenced Ca^{2+} pulses between neighboring cells in deformable matrices, where waves of Ca^{2+} fluxed across the line of assembling ECs (**Figure 6.6i,j**). To assess the spatiotemporal regulation of Ca^{2+} signaling within EC lines, we determined the minimum time between Ca^{2+} pulses between two ECs as a function of their separation distance, hypothesizing that MIC would lead to shorter intervals between Ca^{2+} pulses in neighboring cells. Indeed, this correlation was positive and significant in deformable matrices, in stark contrast to non-deformable matrices (**Figure 6.6k**). Interestingly, neighboring ECs within 200 μm from each other (the same distance that interacting cell pairs were patterned in **Figure 6.5**) displayed coordinated Ca^{2+} signaling as evidenced by a decreased time interval between Ca^{2+} pulses (**Figure 6.6l**). Neighboring ECs that were further than 200 μm apart, however, had longer average time between peaks with greater variation, indicating a decrease in coordinated Ca^{2+} signaling as a function of distance between cells (**Figure 6.6l**). Together, this data indicates that synchronized Ca^{2+} influx underlies MIC between ECs.

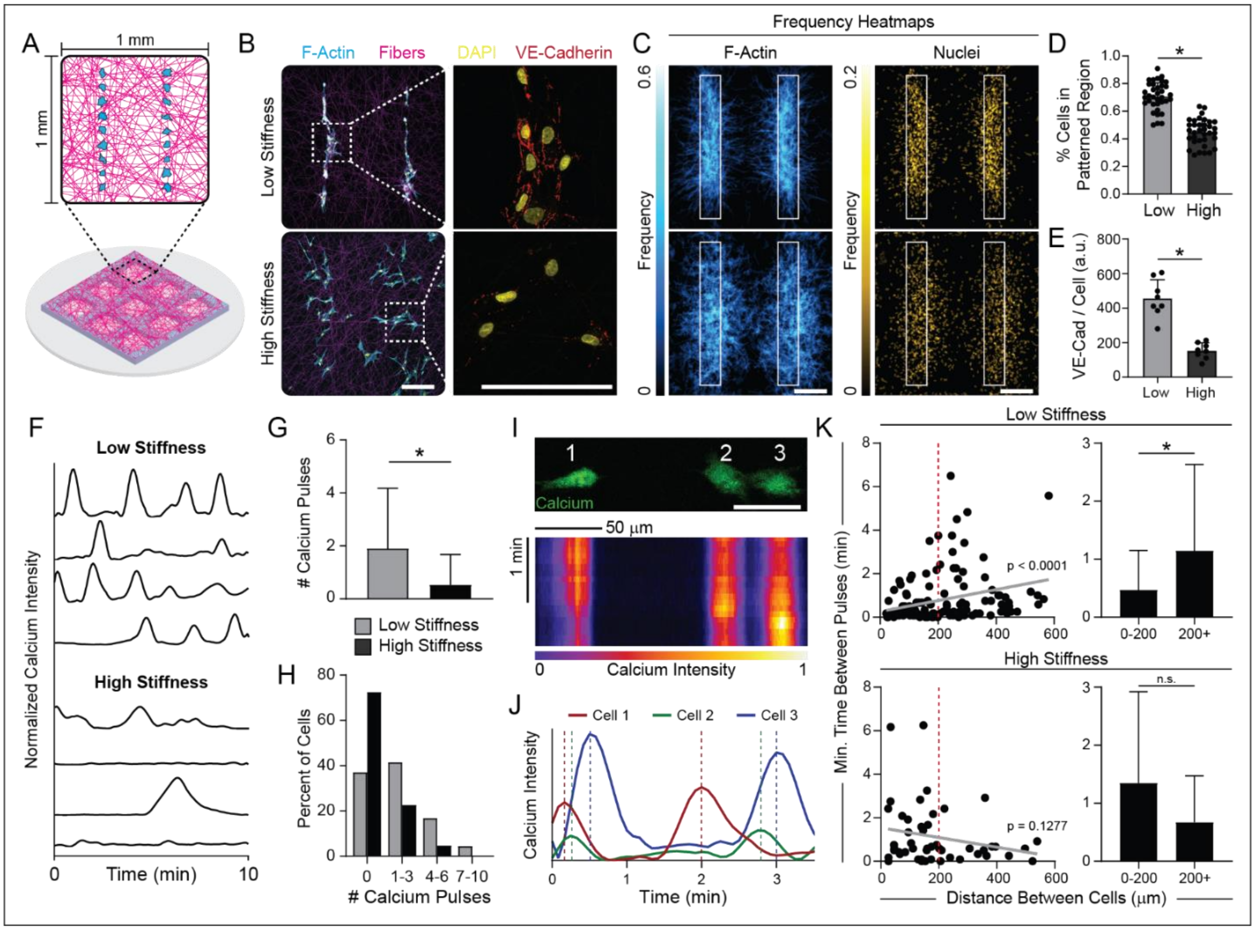

Figure 6.6: Micropatterned, multicellular lines support a role for coordinated intracellular Ca^{2+} signaling between neighboring cells during MIC. (A) Schematic of EC line patterning consisting of two parallel lines of cells within each suspended fibrous matrices. (B) Representative confocal fluorescent image of phalloidin-stained ECs (cyan), rhodamine-labeled fibers (magenta), nuclei (yellow), and VE-cadherin (red). Dashed boxes indicate locations of higher magnification images of VE-cadherin immunostaining (right column) (scale bars, 200 µm). (C) F-actin (left column) and nuclei (right column) heat maps of EC lines 12 hours after patterning (n = 37 fields of view) (scale bar, 200 µm). (D) Quantification of the percent of nuclei in the original patterned region after 12 hours (n > 35 fields of view). (E) Quantification of total VE-cadherin expression at cell-cell junctions normalized to cell density for each matrix condition (n = 8 fields of view). (F) Normalized Ca^{2+} intensity over a 10 minute time course. (G) Quantification of total number of Ca^{2+} pulses per cell and (H) distribution of cells by number of Ca^{2+} pulses over a 10 minute time frame (n > 89 cells). (I) Representative images of Ca^{2+} signal in ECs within a patterned line with corresponding kymograph and (J) normalized Ca^{2+} intensity displaying a wave of Ca^{2+} fluorescence across the line over time. (K) Quantification of the minimum time between Ca^{2+} pulses as a function of distance between all ECs within patterned lines for low (n = 160 cell pairs) and high stiffness (n = 49 cell pairs) matrix conditions. Grey lines indicate linear correlations with indicated p-values. All data presented as mean ± SD with superimposed data points; asterisk denotes significance with $P < 0.05$.

6.4.5 Focal adhesion kinase signaling and mechanosensitive ion channels are required for MIC during 3D vascular network formation

Given the implication of FAs and Ca^{2+} signaling in MIC (**Figure 6.1, Figure 6.3**), we next inhibited focal adhesion kinase (FAK) as well as the mechanosensitive ion channels (MSICs) transient receptor potential vanilloid 4 (TRPV4) and Piezo1 to examine their roles in Ca^{2+} signaling and the formation of multicellular clusters in deformable fibrous matrices. FAK is an essential non-receptor tyrosine kinase that transduces mechanical signals at FAs to intracellular biochemical signals that coordinate cell behavior (Mitra et al., 2005). TRPV4 and Piezo1 are MSICs that open in response to membrane stretch and regulate intracellular Ca^{2+} signaling in ECs (Li et al., 2014; Thodeti et al., 2009). For patterned cell lines in cell-deformable matrices, inhibition of FAK with PF228 (10 μM) (Slack-Davis et al., 2007) led to the largest decrease in intracellular Ca^{2+} signaling, with only 9.5% of all cells exhibiting any Ca^{2+} pulse over a 10 minute time course (**Figure 6.7a,d,e**, **Supplementary Movie 6.7**). Inhibition of TRPV4 with GSK205 (10 μM) (Phan et al., 2009) and Piezo1 with GsMTx-4 (5 μM) (Suchyna et al., 2000) also led to a decrease in Ca^{2+} signaling compared to ECs in deformable matrices, at comparable levels to ECs in non-deformable matrices (**Figure 6.7b-e**, **Supplementary Movie 6.7**). Additionally, inhibition of FAK, TRPV4, or Piezo1 each led to a decrease in spatially coordinated Ca^{2+} signaling and did not diminish cell force-mediated matrix deformations (**Supplementary Figure 6.7, Supplementary Figure 6.8**). After confirming a role for FAK and MSICs in Ca^{2+} signaling, we seeded ECs (250 cells mm^{-2}) in the presence of inhibitors in a 2 mm diameter suspended fiber matrix as in Figure 6.1 (**Figure 6.7f**). Inhibition of FAK, TRPV4, or Piezo1 led to a decrease in average cell spread area as well as the average number of ECs per cluster after 12 hours of culture in deformable matrices, all exhibiting similar behavior to ECs seeded in high stiffness matrices (**Figure 6.7g-i**). These results indicate that FAK signaling and MSIC activity play an important role in regulating MIC between ECs.

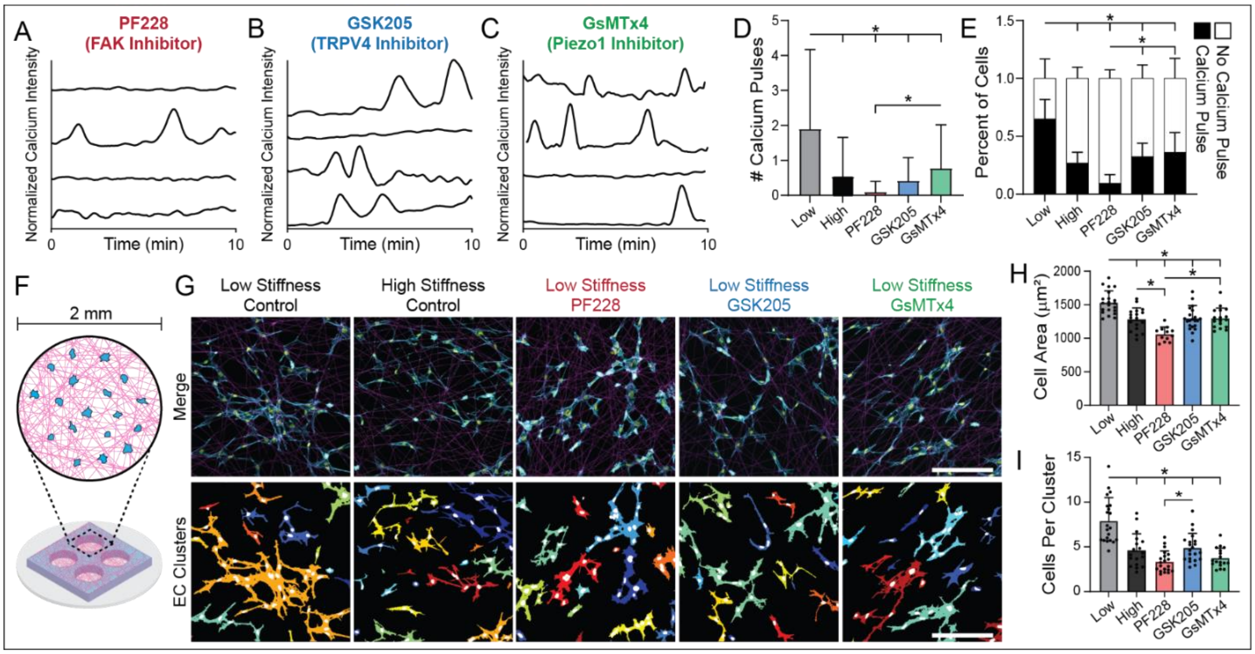

Figure 6.7: Inhibition of FAK signaling and MSIC activity reduce Ca^{2+} signaling and MIC between ECs. (A-C) Normalized Ca^{2+} intensity over a 10 minute time course of patterned EC lines in low stiffness, cell-deformable matrices treated with (A) PF228 (FAK inhibitor), (B) GSK205 (TRPV4 inhibitor) and (C) GsMTx4 (Piezo1 inhibitor). (D) Quantification of total number of Ca^{2+} pulses per cell and (E) percent of cells with at least one Ca^{2+} pulse over a 10 minute time frame (n > 84 cells). (F) Schematic of EC bulk seeding in 2 mm diameter circular suspended fibrous matrices. (G) Confocal fluorescent images of phalloidin-stained ECs (cyan), nuclei (yellow), and rhodamine-labeled fibers (magenta) with respective color-coded maps of contiguous actin clusters as a function of matrix stiffness and presence of inhibitors (scale bars, 200 µm). (H) Quantification of average cell spread area and (I) average cells per contiguous actin cluster (n > 17 fields of view). All data presented as mean ± SD with superimposed data points; asterisk denotes significance with $P < 0.05$.

These 2.5D synthetic fibrous matrices provide a controllable setting that allowed us to investigate how biophysical properties of ECM regulate cell behavior and MIC between ECs. However, controlling MIC *in vitro* to engineer functional microvascular networks for tissue engineering applications requires the control of EC network formation in 3D. Using 2.5D suspended fibrous matrices, we identified that ECs utilize mechanical signaling to communicate their location to neighboring cells and found that this process was dependent on FAK signaling and MSIC activity. Whether these findings hold true in a 3D fibrous settings, however, is unclear as such matrices introduce added complexity from the 3D distribution of adhesions and matrix displacements as well as the dependence of cell spreading and protrusions on matrix degradation.

To test this, we examined MIC during vascular network formation in 3D fibrin hydrogels, a commonly used fibrous biomaterial platform for studying vasculogenic assembly (**Figure 6.8a**) (Morin & Tranquillo, 2013). ECs (4 million cells mL^{-1}) were seeded in both 2.5 and 5.0 mg mL^{-1} fibrin hydrogels to model low and high stiffness/density matrix settings, respectively, and cultured for three days. In 2.5 mg mL^{-1} hydrogels, ECs formed long, interconnected networks suggestive of functional microvasculature. ECs in higher density 5.0 mg mL^{-1} hydrogels, however, displayed reduced network formation with limited cell-cell connectivity (**Figure 6.8b-d**, **Supplementary Movie 6.8**). We additionally inhibited FAK and TRPV4 in 2.5 mg mL^{-1} hydrogels, which also led to a marked decrease in average vessel length and interconnected cluster size compared to control (**Figure 6.8b-d**, **Supplementary Movie 6.8**). These results support our findings in synthetic fibrous matrices and imply a critical role for MIC during 3D vascular network formation mediated by FAK signaling and TRPV4 activity.

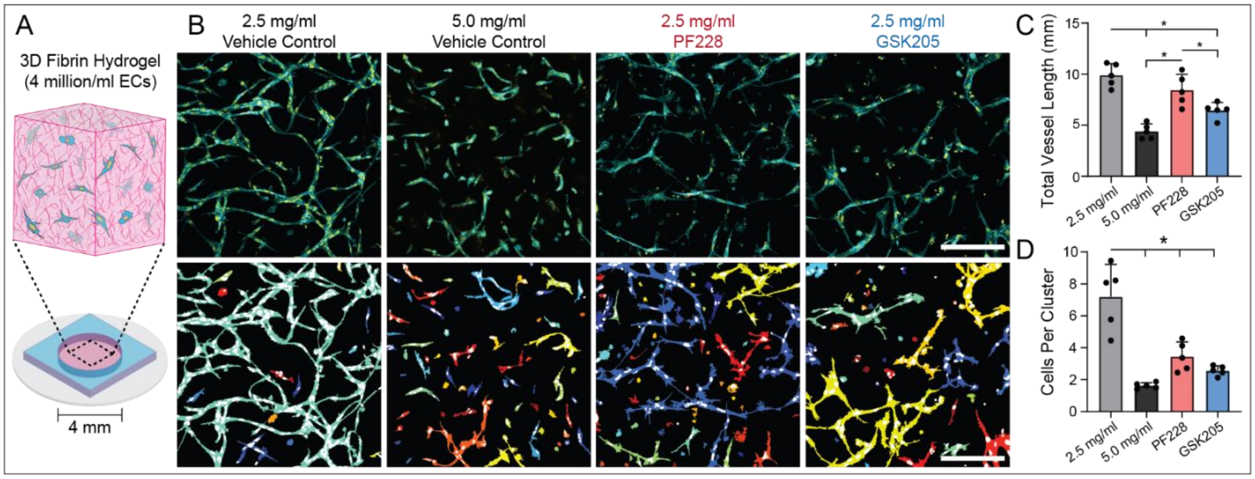

Figure 6.8: Matrix stiffness/density, FAK signaling, and TRPV4 activity regulate 3D vascular network formation in fibrin hydrogels. (A) Schematic of 3D vascular network formation assay in fibrin hydrogels. (B) Representative confocal maximum intensity projections (100 μm z-stack) of phalloidin-stained ECs (cyan) and nuclei (yellow) with respective color-coded maps of contiguous actin clusters as a function of fibrinogen concentration and presence of inhibitors (scale bars, 200 μm). (C) Quantification of total vessel length and (D) average number of cells in each 3D contiguous actin clusters (n = 5 fields of view). All data presented as mean ± SD with superimposed data points; asterisk denotes significance with $P < 0.05$.

6.5 Discussion

MIC involves the generation, transmission, and receipt of cell-generated forces conveyed through the ECM, which we posit to be an important but understudied means of intercellular communication. Here, we utilized synthetic fibrous matrices with tunable mechanics in conjunction with a microfabrication-based cell patterning approach to better understand how physical properties of the matrix modulate MIC between ECs. We first varied cell seeding density (and resulting distance between adhered cells) in low and high stiffness fibrous matrices and found that soft, cell-deformable ECM fibers supported heightened cell-ECM adhesion at early time points that corresponded with enhanced cell spreading, migration, and the eventual formation of multicellular clusters (**Figure 6.1, Figure 6.2**). Cell/ECM patterning experiments with single cells and cell pairs revealed that ECs in cell-deformable matrices favored fewer but longer lasting protrusions, generated longer-range matrix displacements, and enabled directional migration towards neighboring cells to form stable cell-cell connections (**Figure 6.3, Figure 6.4, Figure 6.5, Figure 6.6**). We also utilized this method to explore the cellular machinery responsible for MIC, finding a critical role for intracellular Ca^{2+} signaling mediated by FAK, TRPV4, and Piezo1 during the assembly of multicellular clusters in deformable matrices (**Figure 6.6, Figure 6.7**). Lastly, we tested whether our observations of MIC in synthetic fiber matrices could be extrapolated to translatable settings by examining 3D vascular network formation in fibrin hydrogels. Indeed, while interconnected vascular-like networks formed in 2.5 mg mL^{-1} fibrin hydrogels, impairing MIC by increasing fibrinogen density (5.0 mg mL^{-1}) or FAK/TRPV4 inhibition abrogated the formation of EC networks in 3D fibrous matrices (**Figure 6.8**).

Fibrous matrices have been theorized to promote long-range matrix displacements in a variety of computational models; these studies implicate a role for fiber alignment, strain stiffening, and ECM fiber microbuckling in propagating cell-generated forces (Abhilash et al., 2014; Goren et al., 2020; Hall et al., 2016; Humphries et al., 2017; Ma et al., 2013; Notbohm et al., 2015; Ronceray et al., 2016; Rudnicki et al., 2013; Sopher et al., 2018b; Wang et al., 2015). However, exploring cell-force generation and propagation in fibrous matrices *in vitro* is experimentally challenging due the discrete (non-affine), non-linear, and plastic mechanical behavior of naturally derived fibrous ECMs. Thus, we utilized mechanically tunable synthetic fibrous matrices along with timelapse imaging to quantify matrix deformations and found that low stiffness fibrous matrices support longer-range matrix displacements. Additionally, our analysis of cell morphology and cell-ECM adhesion suggest that deformable fibrous matrices prime cells for enhanced and directed force generation and transmission. In experiments with single ECs patterned in deformable matrices, cells exhibited increased FA size and decreased number of protrusions compared to ECs in stiff, non-deformable matrices, despite encountering the same initial ligand density and matrix topography. This may be explained by differences in mechanical resistance provided by the matrix during cell spreading in each matrix condition. In high stiffness matrices, all matrix fibers can provide sufficient resistance required for FA assembly and associated protrusion formation, allowing cells to isotropically extend in an apparently random fashion. In contrast, ECs in low stiffness matrices rapidly recruit matrix fibers soon after initial adhesion, thus generating tension in fibers as a function of their connection to a local rigid boundary (in this case, the edge of the microfabricated well). This likely results in greater heterogeneity of mechanical resistance, leading to preferential generation of FAs and protrusions along particular fibers that provide greater mechanical resistance resulting in directed extension and force propagation. Future work could combine our cell/ECM patterning approach with intramolecular or polymeric tension sensors to better understand the relationship between FA forces and protrusive activity (Grashoff et al., 2010).

Beyond influencing cell-ECM adhesion, matrix deformations from cell traction forces in low stiffness matrices also led to the formation of structural and mechanical anisotropy via local fiber alignment. When cell pairs were patterned in deformable, randomly oriented fibrous matrices, we observed many instances of fiber alignment between neighboring cells that preceded directional extension, migration, and the formation of cell-cell contact. Several possible explanations exist. Fiber alignment could provide a topographical cue that guides directed migration between cells via contact guidance (Thrivikraman et al., 2021). Additionally, and non-exclusively, aligned fibers spanning cells could maximize the transmission of tensile forces between cells and MIC. Our results suggest active force transmission across aligned fibers enhances MIC, as high stiffness aligned matrices that do not deform under cell forces led to fewer cell-cell interactions compared to softer matrices with the same topography (**Figure 6.5**). In recent work, Pakshir et al. observed that contracting myofibroblasts generate large deformation fields in collagen matrices that provide mechanical signals to macrophages (Pakshir et al., 2019). However, it was also observed that cell force-mediated fiber alignment from myofibroblasts was not required to guide macrophage migration. These conflicting observations may arise from distinct cell types or different ECM settings, as reconstituted collagen hydrogels have relatively short fibrils with nanometer-scale diameters compared to longer electrospun

DexMA fibers with larger diameters used in these studies (Davidson et al., 2019b). Taken together, however, these results confirm that various cell types are able to generate and respond to dynamic mechanical signals in fibrous matrices.

While evidence for MIC has been observed in a variety of settings, the cellular machinery required for cells to send, receive, and respond to mechanical signals has not been established. Here, we identified critical roles for FAK signaling and MSICs in MIC. Inhibition of FAK via PF228 significantly decreased Ca^{2+} signaling and multicellular assembly in matrices permissive to MIC (**Figure 6.7, Figure 6.8**). While FAK inhibition has not been shown to influence FA maturation or traction force magnitudes, it does play an important role in adhesion dynamics and cell motility (Fabry et al., 2011; Plotnikov et al., 2012; Wang et al., 2001). Plotnikov et al. investigated FA traction dynamics in mouse embryonic fibroblasts and found FAK activity was required for traction force fluctuations from FAs (Plotnikov et al., 2012). This could in part explain why FAK inhibition hampered Ca^{2+} fluxes in soft matrices, as dynamic traction forces transmitted through the ECM may be critical to MIC (Pakshir et al., 2019). Furthermore, cells likely sense dynamic mechanical signals from the ECM via membrane stretch resulting in the opening of MSICs. We identified a role for both Piezo1 and TRPV4, two MSICs that are expressed in ECs and are known to be important during the EC response to shear stress (Li et al., 2014; Thodeti et al., 2009). In addition to regulating EC response to shear stress, though, Thodeti et al. showed that TRPV4 mediates EC reorientation under cyclic mechanical stretch (Thodeti et al., 2009). Specifically, uniaxial cyclic strain of flexible substrates seeded with ECs led to cellular realignment perpendicular to the axis of applied strain in a TRPV4 dependent manner. The authors posit that ECs preferentially align perpendicular to the direction of applied strain due to differences in membrane strain, TRPV4 activation, and resulting cytoskeletal activity parallel vs. perpendicular to the direction of stretch. This could also explain alignment of cells and directional protrusions in response to cell-generated forces during MIC, as the side of a cell nearest to a force-generating neighboring cell will experience higher levels of membrane stretch. Direct measurements of membrane tension and ion channel state could provide more information on the molecular mechanisms underlying MIC.

MIC is likely critical to tissue development given the ubiquity of cell-generated forces and dynamic changes to the ECM in the growing embryo. The previous notion that cells divide, migrate, and assemble in a static ECM during embryonic development has been widely discredited (Loganathan et al., 2016; McDole et al., 2018). In contrast, collective motion, spatial coordination, and multi-scale ECM deformations are essential for the morphogenetic transitions required for organogenesis (Kumar et al., 2017; Loganathan et al., 2016; Walma & Yamada, 2020). For example, Zepp et al. recently generated a single-cell RNA-sequencing atlas of the developing mouse lung and identified a critical role for secondary crest myofibroblasts, a highly contractile cell that physically remodels the alveolus and is important for guiding the assembly of alveolar networks (Zepp et al., 2021). Additionally, cell forces have been implicated in the folding of mesenchymal tissue during the formation of 3D structures such as gut villi (Hughes et al., 2018). Furthermore, timelapse recordings of avian embryonic vasculogenesis demonstrate EC self-assembly into an archetypal polygonal network, termed the primary vascular plexus, prior to the onset of circulation (Czirok & Little, 2012; Rupp et al., 2003; Sato et al., 2010). ECM motion and deformations were noted concurrent to primary vascular plexus formation, potentially indicating a role for MIC between single EC progenitors during this key developmental step.

A complete understanding of developmental vasculogenesis would inform the design of biomaterials that facilitate the self-assembly of functional vascular networks *in vitro* for tissue engineering and regenerative medicine applications. Our studies indicate matrices that permit cellular force transmission via far-ranging matrix deformations promote MIC that is required for the assembly and stabilization of microvascular structures. Interestingly, vasculogenic assembly is readily achieved in collagen and fibrin hydrogels – two materials where evidence of MIC has been well-documented (Morin & Tranquillo, 2013; Pakshir et al., 2019; Rao et al., 2012; Winer et al., 2009). These materials, however, hold limited potential for building engineered tissue constructs due to their rapid resorption *in vivo*. Alternatively, synthetic polymeric hydrogels, such as poly(ethylene) glycol, hyaluronic acid, and dextran, offer controllable and modular design better suited for translational applications (Li et al., 2017). However, compared to the aforementioned natural and fibrous materials, building 3D vascular networks has proven more challenging in these biomaterial settings. Based on our studies, one explanation for the challenges of assembling vascular networks in 3D synthetic hydrogels may be the dissipation of cell forces short distances away from the cell (Legant et al., 2010; Reinhart-King et al., 2003). Generally, EC spreading and network formation in these settings requires the addition of a support stromal cell such as dermal fibroblasts, mesenchymal stem cells, or pericytes. The role of these stromal cells has long been considered biochemical in nature via growth factor and matrix secretion or ECM degradation (Ghajar et al., 2008; Newman et al., 2011; Rohringer et al., 2014). However, in addition to biochemical support, these contractile cells may also provide mechanical signals that orchestrate EC network formation. Supporting this notion, recent work from Song et al. found that fibroblasts present during 3D EC network formation in fibrin is only necessary during the first few days of culture, after which they can be selectively ablated without long-term negative effects on formed vascular networks (Song et al., 2020).

Additionally, external mechanical cues applied by actuated or dynamic biomaterials could guide cell extension and migration to form complex multicellular patterns (Uslu et al., 2021). Beyond playing an important role during the bottom-up assembly of multicellular vascular structures, our results indicate a role for MIC and force transmission in stabilization and maturation, evidenced here by enhanced VE-cadherin in EC clusters and patterned lines formed in cell-deformable matrices. This should be considered in top-down approaches to vascular tissue engineering, such as 3D bioprinting of ECs (Daly et al., 2021). While bioprinting techniques continually improve in resolution and complexity and now allow for cell-scale patterning, an understanding of how matrix properties influence maintenance of cell-cell adhesions is critical, and biomaterial design should consider not only cellular assembly, but also long-term maintenance of multicellular structures.

6.6 Materials and Methods

6.6.1 Reagents

All reagents were purchased from Sigma-Aldrich and used as received, unless otherwise stated.

6.6.2 Cell culture and biological reagents

Human umbilical vein endothelial cells (ECs) were cultured in endothelial growth medium (EGM-2; Lonza, Basel, Switzerland) supplemented with 1% penicillin-streptomycin-fungizone (Gibco, Waltham, MA). Cells were cultured at 37°C and 5% CO_2. ECs were used from passages four to eight in all experiments. For live cell time-lapse imaging, lentiviral transduction of LifeAct-GFP was utilized. For inhibition studies, PF-573228 (10 μM), GSK205 (10 μM; Medchem Express, Monmouth Junction, NJ), and GsMTx-4 (5 μM; Abcam, Cambridge, UK) were supplemented in EGM-2 and refreshed every 24 hours.

6.6.3 Lentivirus production

pLenti.PGK.LifeAct-GFP.W was a gift from Rusty Lansford (Addgene plasmid #51010). To generate lentivirus, plasmids were co-transfected with pCMV-VSVG (a gift from Bob Weinberg, Addgene plasmid #8454), pMDLg/pRRE, and pRSV-REV (gifts from Didier Trono, Addgene plasmid #12251 and #12253 (Dull et al., 1998; Stewart et al., 2003)) in 293T cells using the calcium phosphate precipitation method (Kingston et al., 2003). Viral supernatants were collected after 48 h, concentrated with PEG-it^{TM} (System Biosciences, Palo Alto, CA) following the manufacturer's protocol, filtered through a 0.45 μm filter (ThermoFisher Scinetific Nalgene, Waltham, MA), and stored at -80°C. Viral titer was determined by serial dilution and infection of ECs. Titers yielding maximal expression without cell death or detectable impact on cell proliferation or morphology were selected for studies.

6.6.4 DexMA synthesis

Dextran (MW 86,000 Da, MP Biomedicals, Santa Ana, CA) was methacrylated by reaction with glycidyl methacrylate as previously described (van Dijk-Wotthuis et al., 1995). Briefly, 20 mg of dextran and 2 mg of 4-dimethylaminopyridine was dissolved in 100 mL of anhydrous dimethylsulfoxide (DMSO) under vigorous stirring (300 rpm) for 12 h. 24.6 mL of glycidyl methacrylate was then added and the reaction mixture was heated to 45°C for 24 h. The solution was cooled at 4°C for 1 h and precipitated into 1 L ice-cold 2-isopropanol. The crude product was recovered by centrifugation, redissolved in milli-Q water, and dialyzed against milli-Q water for 3 d. The final product was lyophilized and stored at -20°C until use. DexMA was characterized by ^{1}H-NMR. The degree of functionalization was calculated as the ratio of the averaged methacrylate proton integral (6. 174 ppm and 5.713 ppm in D2O) and the anomeric proton of the glycopyranosyl ring (5.166 ppm and 4.923 ppm). As the signal of the anomeric proton of α-1,3 linkages (5.166 ppm) partially overlaps with other protons, a pre-determined ratio of 4% α-1,3 linkages was assumed and the total anomeric proton integral was calculated solely on the basis of the integral at 4.923 ppm. A methacrylate/dextran repeat unit ratio of 0.787 was determined.

6.6.5 Fiber matrix fabrication

Suspended DexMA fiber matrices were fabricated through electrospinning and soft lithography as previously described (Baker et al., 2015). DexMA was dissolved at 0.5 g mL^{-1} in a 1:1 mixture of milli-Q water and dimethylformamide with 1% (w/v) Irgacure 2959 photocrosslinker and 0.625 mM methacrylated rhodamine (Polysciences, Inc., Warrington, PA). For matrix displacement studies, 10% (v/v) blue carboxylate-modified FluoSpheres (1.0 μm diameter, 2% w/v) was also added. Electrospinning was completed with a custom set-up consisting of a high-voltage power supply (Gamma High Voltage Research, Ormond Beach, FL), syringe pump (KD Scientific, Holliston, MA), and a grounded copper collecting surface enclosed within an environmental chamber held at room temperature and 30% relative humidity (Terra Universal, Fullerton, CA). Electrospinning of DexMA solution was performed at a flow rate of 0.45 mL h^{-1}, voltage of 7.0 kV, and gap distance of 6 cm. Fiber density was varied through modulating electrospinning time and relative humidity. To induce fiber alignment, fibers were electrospun at a voltage of 4.0 kV onto a collecting surface of oppositely charged (-3.0 kV) parallel electrodes at a 25 mm separation distance. After electrospinning, fibers were stabilized by primary crosslinking under ultraviolet (UV) light (100 mW cm^{-2}) for 60 s, hydrated in varying concentrations of lithium phenyl-2,4,6-trimethylbenzoylphophinate (LAP; Colorado Photopolymer Solutions, Boulder, CO) photoinitiator solution, and then exposed again to UV light (100 mW cm^{-2}) for 20 s. Low, intermediate, and high stiffness networks were crosslinked in 0.02, 0.075, and 1.0 mg mL^{-1} LAP solutions, respectively. Fibers were collected on various poly(dimethylsiloxane) (PDMS; Dow Silicones Corporation, Midland, MI) arrays of wells produced by soft lithography. Silicon wafer masters possessing SU-8 photoresist (Microchem, Westborough, MA) were first fabricated by standard photolithography. Briefly, a layer of SU-8 2075 (110 μm thick) was spin-coated on a 3-inch silicon wafer and patterned into arrays of various shaped wells spaced evenly within 12 x 12 mm squares. These masters were utilized to make PDMS stamps which were silanized with trichloro(1H,1H,2H,2H-perfluorooctyl)silane and used to emboss uncured PDMS onto oxygen plasma-treated coverslips. Resultant fiber-well substrates were methacrylated by vapor-phase silanization of 3-(trimethoxysilyl)propyl methacrylate in a vacuum oven at 60°C for at least 6 h to promote fiber adhesion to PDMS.

6.6.6 Mechanical testing

To determine the Young’s modulus of suspended DexMA fibrous matrices, microindentation testing with a rigid cylinder was performed on a commercial CellScale Microsquisher (CellScale, Waterloo, Ontario). Briefly, samples were indented to a depth of up to

200 μm at an indentation speed of 2 μm s^{-1}, and Young's modulus was approximated assuming the material behaves as an elastic membrane as previously described (Baker et al., 2015).

6.6.7 RGD functionalization and seeding on DexMA matrices

DexMA fibers were functionalized with the cell adhesive peptide CGRGDS (RGD; Peptides International, Louisville, KY). An RGD concentration of 2 mM was used for all studies. RGD was coupled to available methacrylates via Michael-type addition. Briefly, the peptide was dissolved in milli-Q water containing HEPES (50 mM), phenol red (10 μg mL^{-1}), and 1 M NaOH to adjust the pH to 8.0. 250 μL of this solution was added to each substrate and incubated for 30 min at room temperature. Following RGD functionalization, substrates were rinsed 2x with PBS before cell seeding. For bulk seeding of networks, ECs were trypsinized, resuspended in 1.5% (w/v) methylcellulose supplemented EGM-2 to increase media viscosity, and seeded between 50 and 250 cells mm^{-2}.

6.6.8 Fluorescent staining and microscopy

ECs on DexMA fibers were first fixed in 4% paraformaldehyde for 10 min at room temperature. Alternatively, to extract cytoplasmic vinculin, samples were simultaneously fixed and permeabilized in 2% paraformaldehyde in a microtubule-stabilizing buffer containing 1,4-piperazinediethanesulfonic acid (PIPES, 0.1 M), ethylene glycol-bis(2-aminoethylether)-N,N,N',N'-tetraacetic acid (EGTA, 1 mM), magnesium sulfate (1 mM), poly(ethylene glycol) (4% w/v), and triton X-100 (1% v/v) for 10 min at room temperature. To stabilize the fibers for processing and long-term storage, DexMA samples were crosslinked in 2 mL LAP solution (1 mg mL^{-1}) and exposed to UV light (100 mW cm^{-2}) for 30 s. To stain the actin cytoskeleton and nuclei, cells were permeabilized in PBS solution containing triton X-100 (5% v/v), sucrose (10% w/v), and magnesium chloride (0.6% w/v), and simultaneously blocked in 1% (w/v) bovine serum albumin and stained with phalloidin and DAPI. For immunostaining, samples were blocked for 1 h in 1% (w/v) bovine serum albumin and incubated with mouse monoclonal anti-vinculin antibody (1:1000, Sigma #V9264) or mouse monoclonal anti-VE-cadherin antibody (1:1000, Santa Cruz #sc-9989) followed by secondary antibody (1:1000, Life Technologies #A21236) for 1 h each at room temperature with 3x PBS washes in between. Fixed samples were imaged on a Zeiss LSM800 laser scanning confocal microscope. Unless otherwise specified, images are presented as maximum intensity projections. Fluorescent images were processed and quantified via custom Matlab scripts.

6.6.9 Cell migration analysis

Immediately after seeding, substrates were transferred to a motorized and environmentally controlled stage and imaged using a Zeiss LSM800 laser scanning confocal microscope (Zeiss, Oberkochen, Germany). Prior to imaging, cell nuclei were labeled with Hoechst 33342 (5 μg mL^{-1}) for 10 min. F-Actin, DexMA fibers, and Hoechst-labeled nuclei were imaged at 10 min frame intervals over 12 hours. Following raw image export, images were converted to maximum intensity projections, and cell spreading and cluster formation were quantified using a custom Matlab script. Nuclei tracking was completed with TrackMate, a freely available ImageJ plugin (Tinevez et al., 2017). Nuclei were detected at each time point using a Laplacian of Gaussian (LoG) detector with an estimated particle diameter of 20 μm and threshold of 0.01 with use of a median filter. Single particle tracking was completed using a linear assignment problem tracker with a linking max distance and gap-closing distance of 20 μm and gap-closing max frame gap of 2 frames. Tracks were filtered to only contain nuclei detected through the entire time-lapse, and migration speed for each cell was calculated via custom Matlab scripts.

6.6.10 Microwell patterning stamp fabrication

To pattern single ECs onto suspended matrices of DexMA fibers, we designed a patterning system inspired by a previously developed microwell-based approach (Gong & Mills, 2018). Like the fiber-well substrates, microwell patterning stamps were produced by soft lithography. First, silicon wafer masters were fabricated with two steps of photolithography. First, SU-8 2075 (100-200 μm thick) was spin-coated on a silicon wafer and patterned into 12.05 x 12.05 mm elevated squares. This step allowed for the final patterning stamp to be aligned to the square fiber-well substrate (12 x 12 mm) during patterning. Next, SU-8 2025 (35 μm thick) was spin-coated on top of the previous exposed layer and patterned into arrays of micro-posts (30 μm diameter) centered onto each 12.05 mm square. Non-exposed SU-8 was washed off through the developing process and these masters were utilized to make PDMS microwell patterning stamps as described above.

6.6.11 Cell patterning on DexMA matrices

Microwell patterning stamps were sterilized with 70% ethanol and UVO (Jelight Company Inc., Irvine, CA) for 5 minutes followed by treatment with 0.2% Pluronic F127 to prevent cell adhesion. 500 μL of EC suspension (1 x 10^6 cells mL^{-1}) was seeded on the patterning stamp and the cells were allowed to settle into the microwells for 5 min. The supernatant was subsequently removed and excess, untrapped cells were gently flushed away with 4 rinses of PBS and 1 rinse of EGM-2. The fiber-well substrate containing RGD-functionalized DexMA fiber matrices was carefully inverted on top of the patterning stamp and aligned. This assembly was then inverted to allow single ECs trapped in microwells to settle and adhere to the DexMA fiber matrix for 15 minutes (**Supplementary Figure 6.2**). The final substrate containing patterned ECs on DexMA matrices was then hydrated with EGM-2 supplemented with HEPES (25 mM) to regulate media pH and minimize hydrolysis-mediated fiber degradation during culture.

6.6.12 Timelapse fiber displacement microscopy

Immediately after patterning, substrates were transferred to a motorized and environmentally controlled stage and imaged using a Zeiss LSM800 laser scanning confocal microscope. Images of F-actin, DexMA fibers, and fluorescent beads embedded in fibers were acquired every 10 min for 12 h. Images were converted to maximum intensity projections before analysis. Single particle tracking was completed by first aligning image stacks of fluorescent beads, cropping the images to only track beads within fibers of the suspended matrix, and tracked using TrackMate. Beads were detected at each time point using a Laplacian of Gaussian (LoG) detector with an estimated particle diameter of 5 μm and threshold of 1.0 with use of a median filter. Single particle tracking was completed using a linear assignment problem tracker with a linking max distance and gap-closing max distance of 20 μm and gap-closing max frame gap of 2 frames. Tracks were filtered to only contain particles detected throughout the entire time-lapse and then analyzed using custom Matlab scripts. Additionally, cell morphology, migration, and protrusions were analyzed using custom Matlab scripts.

6.6.13 Calcium imaging

Ca^{2+} handling analysis was performed by incubating cells for 1 h at 37°C with 5 µM Cal520, AM (AAT Bioquest, Sunnyvale, CA) in EGM-2. Cells were then returned to normal EGM-2 and allowed to equilibrate for 30 minutes. Following equilibration, substrates were transferred to a motorized and environmentally controlled stage and imaged using a Zeiss LSM800 laser scanning confocal microscope. Timelapse movies of Ca^{2+} flux were analyzed with custom Matlab scripts (Depalma et al., 2021).

6.6.14 3D vascular network formation

HUVECs were encapsulated (4 million mL^{-1}) in fibrin precursor solutions containing 2.5 mg mL^{-1} or 5.0 mg mL^{-1} fibrinogen from bovine plasma and 1 U mL^{-1} bovine thrombin. This precursor solution was mixed and 20 µL was transferred into a PDMS mold with 4 mm diameter and incubated at 37°C for 20 min. Samples were then hydrated in EGM-2 supplemented with fetal bovine serum (FBS; 5% v/v), vascular endothelial growth factor (VEGF; 50 ng mL^{-1}), and phorbol 12-myristate 13-acetate (PMA; 25 ng mL^{-1}), and media was replaced every 24 hours. Quantification of morphological network properties was performed on 100 µm image stacks. Total vessel length was quantified using AngioTool (Zudaire et al., 2011), and three-dimensional analysis of the number cells per contiguous actin structure was completed using a custom Matlab script.

6.6.15 Statistical Analysis

Statistical significance was determined by one-way or two-way analysis of variance (ANOVA) with post-hoc analysis (Tukey test) or Student’s t-test where appropriate.

Additionally, statistical significance of the proportions of interacting and non-interacting cells was determined by Fisher's exact test. For all studies, significance was indicated by $p < 0.05$. Sample size is indicated within corresponding figure legends and all data are presented as mean ± standard deviation.

6.7 Supplementary Figures

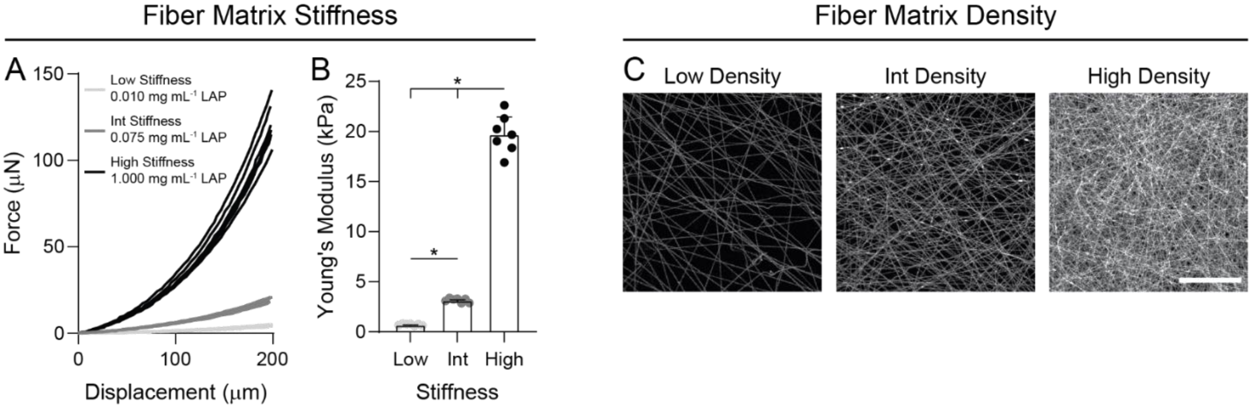

Supplementary Figure 6.1: Control over substrate stiffness and fiber density in DexMA fiber networks. (A) Force-indentation response and (B) Young's modulus of DexMA fibrous matrices as a function LAP photoinitiator concentration (n = 7 matrices/group). (C) Representative fluorescent images of DexMA fibers at low, intermediate, and high fiber density (scale bar, 100 μm).

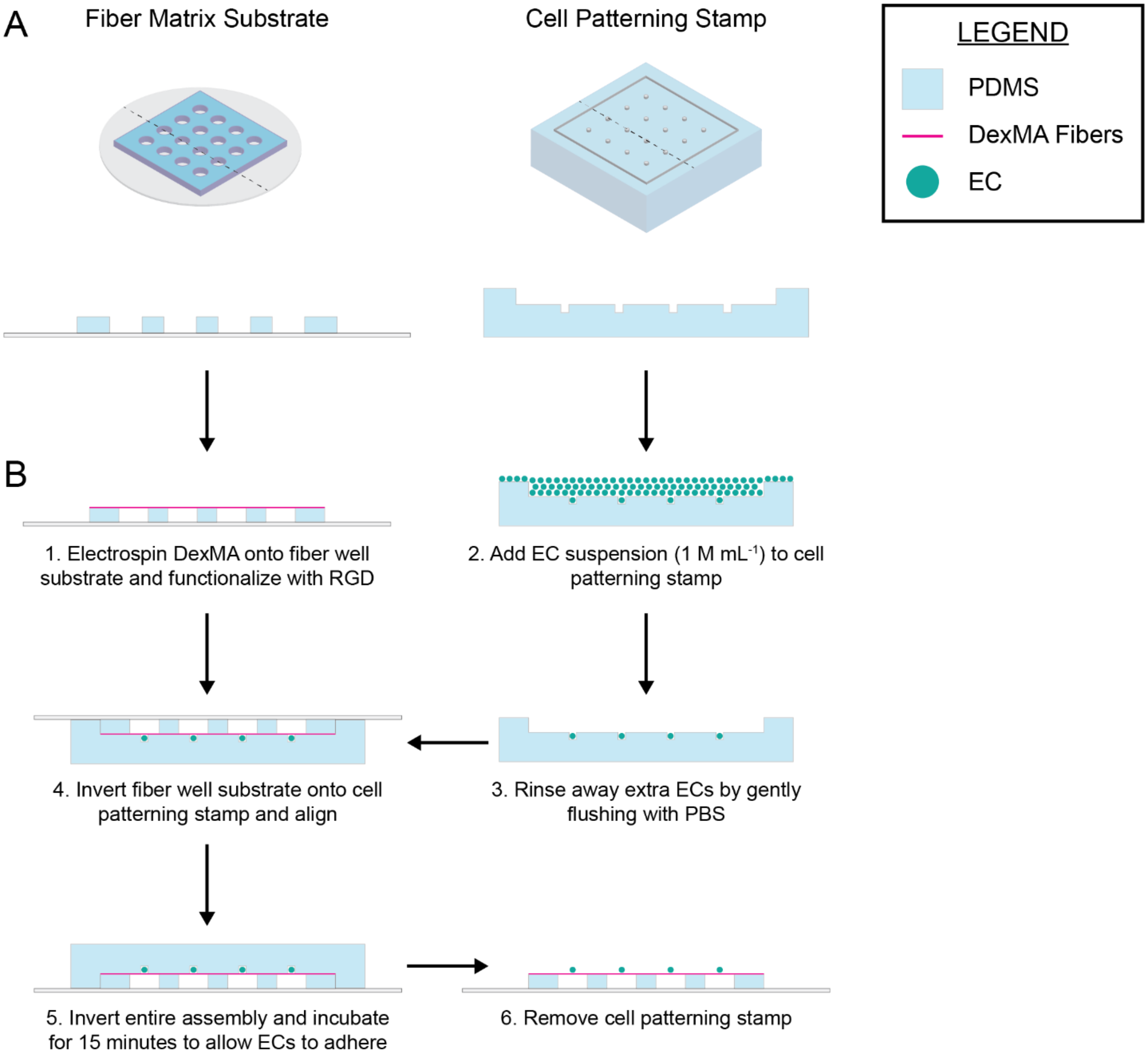
A
Fiber Matrix Substrate
Cell Patterning Stamp
LEGEND
PDMS
DexMA Fibers
EC
B
1. Electrospin DexMA onto fiber well substrate and functionalize with RGD
2. Add EC suspension (1 M mL-1) to cell patterning stamp
3. Rinse away extra ECs by gently flushing with PBS
4. Invert fiber well substrate onto cell patterning stamp and align
5. Invert entire assembly and incubate for 15 minutes to allow ECs to adhere
6. Remove cell patterning stamp

Supplementary Figure 6.2: Schematic of endothelial cell micropatterning on suspended DexMA fiber matrices. (A) Isometric and side views of fiber matrix substrate and cell patterning stamp. (B) (1) DexMA fibers are electrospun onto a fiber well substrate, crosslinked, and hydrated. (2) The cell patterning stamp is treated with Pluronic F127 solution to prevent cell adhesion, and a cell suspension is seeded onto the stamp. Cells are allowed to settle for 5 minutes. (3) Excess cells are gently flushed away with 4x PBS rinses. (4) The fiber well substrate is inverted onto the cell patterning stamp and aligned using the raised edges of the patterning stamp under a microscope. (5) The entire assembly is inverted to allow cells to settle onto the suspended DexMA matrices. (6) The patterning stamp is removed and transferred for culture and subsequent imaging.

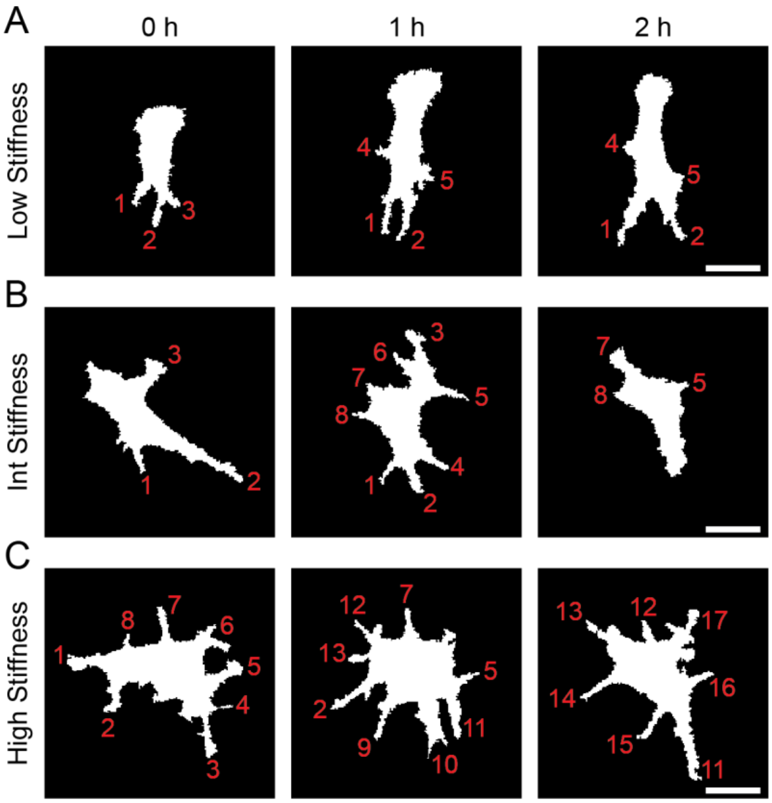
A
0 h
1 h
2 h
Low Stiffness
1
2
3
4
5
1
2
4
5
1
2
B
Int Stiffness
3
1
2
6
3
7
5
8
4
1
2
7
8
5
C
High Stiffness
8
7
6
1
5
4
2
3
12
7
13
5
2
11
9
10
13
12
17
14
16
15
11

Supplementary Figure 6.3: Endothelial cell protrusion analysis. For each frame of the 12 hour timelapse, protrusions were identified and the total number of protrusions as well as lifetime of each individual protrusion was manually determined for cells in (A) low, (B) intermediate, and (C) high stiffness matrices (scale bars, 50 μm).

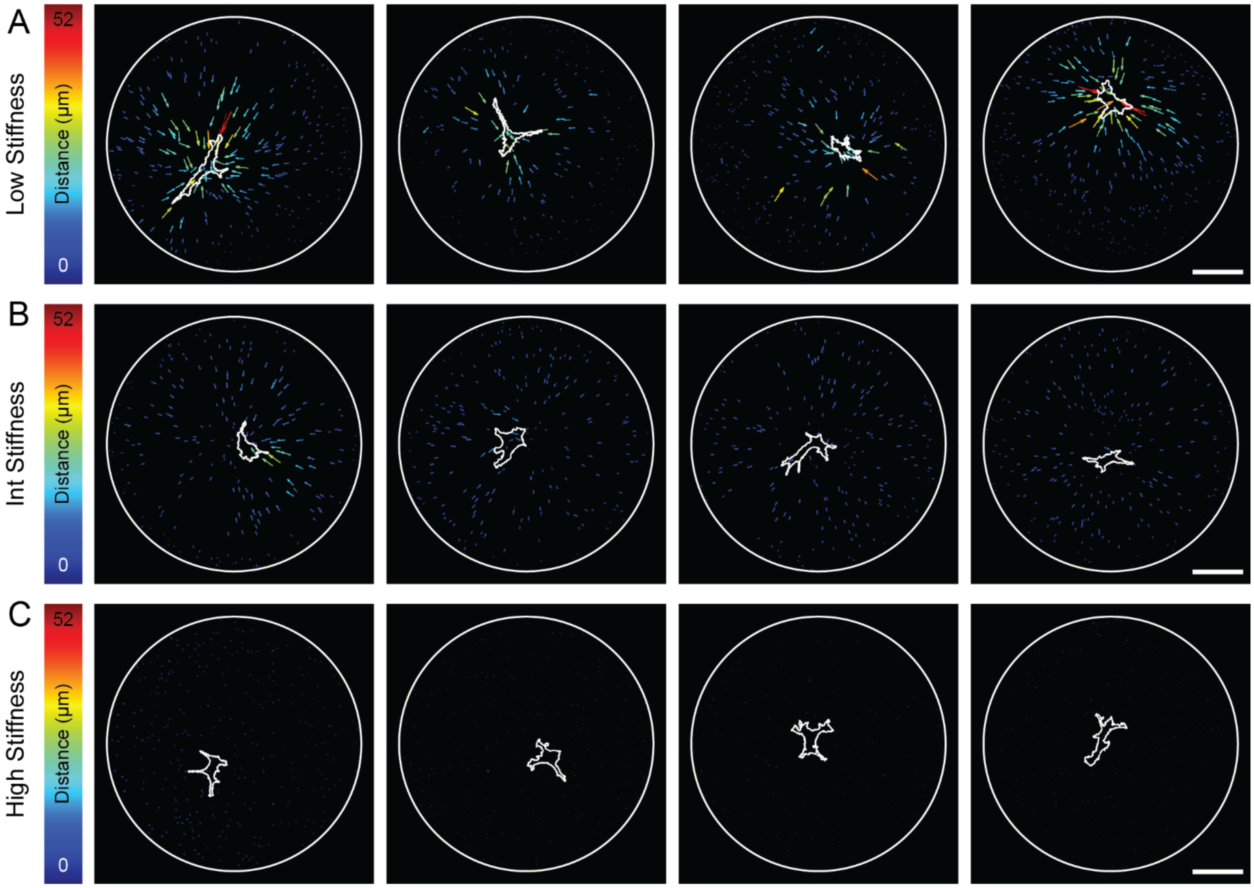
A
B
C
Low Stiffness
Int Stiffness
High Stiffness
52
Distance (μm)
0

Supplementary Figure 6.4: Bead displacement vector plots as a function of matrix stiffness. Representative endothelial cells (cell periphery denoted by white outline) and their respective bead displacements over 12-hours of culture displayed as vectors with magnitude coded by vector size and color in (A) low, (B) intermediate, and (C) high stiffness DexMA matrices (scale bars, 100 μm).

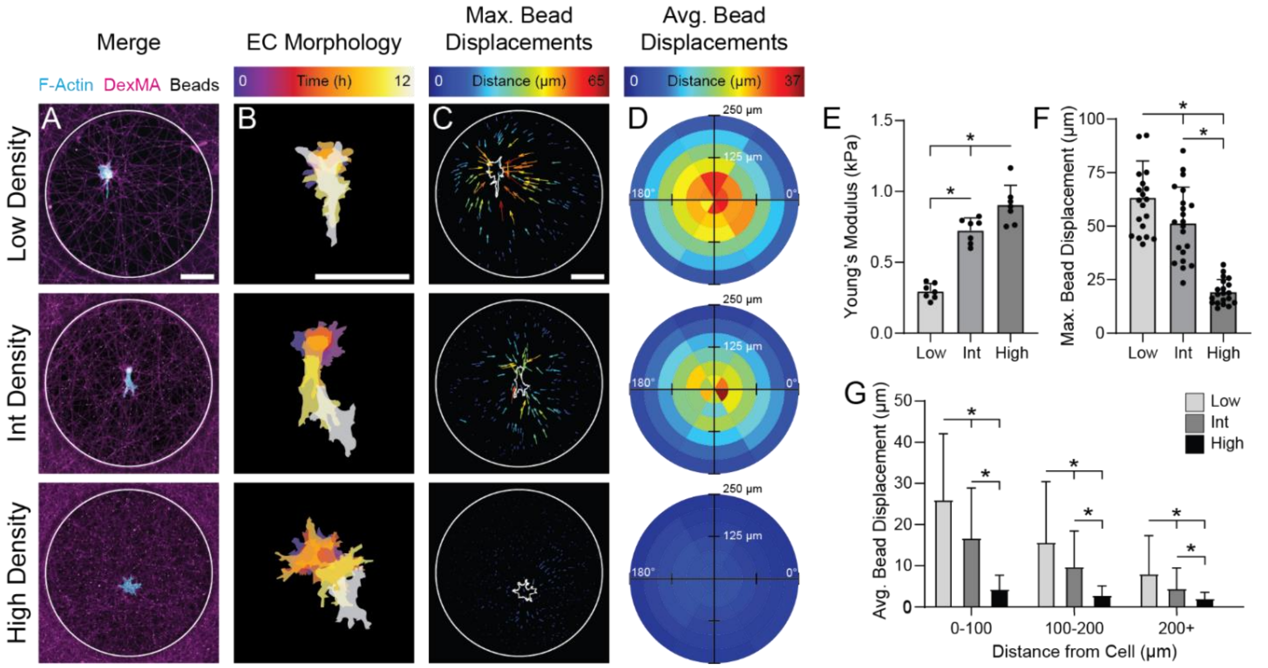

Supplementary Figure 6.5: Single endothelial cell morphology and force transmission as a function of fiber density. (A) Representative confocal fluorescent image of phalloidin-stained ECs (cyan), rhodamine-labeled DexMA fibers (magenta), and fiber-embedded fluorescent beads (white) (scale bar, 100 μm). (B) Temporally color-coded overlay of EC cell bodies over a 12 hour time course following initial patterning (scale bar, 100 μm). (C) Maximum displacement of each bead coded by vector length and color over the 12 hour time course (scale bar, 100 μm). (D) Binned average bead displacements color-coded by magnitude for all analyzed ECs with respect to their long axis (0°) (n > 20 cells/group). (E) Young's modulus of DexMA fiber matrices as a function of matrix density (n = 6). (F) Quantification of maximum bead displacement and (G) binned average bead displacements as a function of starting distance from the cell centroid for low, intermediate, and high fiber densities. All data presented as mean ± SD with superimposed data points; asterisk denotes significance with $P < 0.05$.

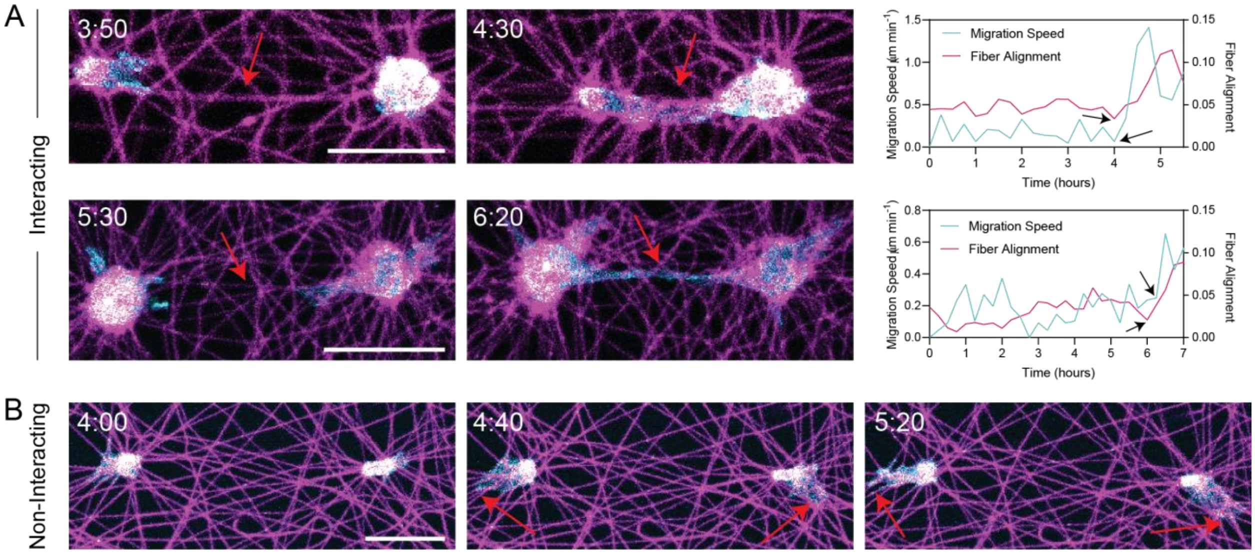
A
Interacting
3:50
4:30
5:30
6:20
Migration Speed (µm min^{-1})
Fiber Alignment
Migration Speed
Fiber Alignment
Time (hours)
B
Non-Interacting
4:00
4:40
5:20

Supplementary Figure 6.6: Representative examples of interacting and non-interacting endothelial cell pairs in low stiffness, non-aligned fibrous matrices. (A) Representative confocal fluorescent images of phalloidin-stained ECs (cyan) and rhodamine-labeled fibers (magenta) with quantification of fiber alignment spanning cells and average migration speed of both ECs as a function of time. Red arrows indicate local regions of fiber alignment between neighboring cells (scale bars, 50 μm). (B) Representative confocal fluorescent images of non-interacting ECs. Red arrows indicate cell protrusions extending in the opposite direction of neighboring cell (scale bar, 50 μm).

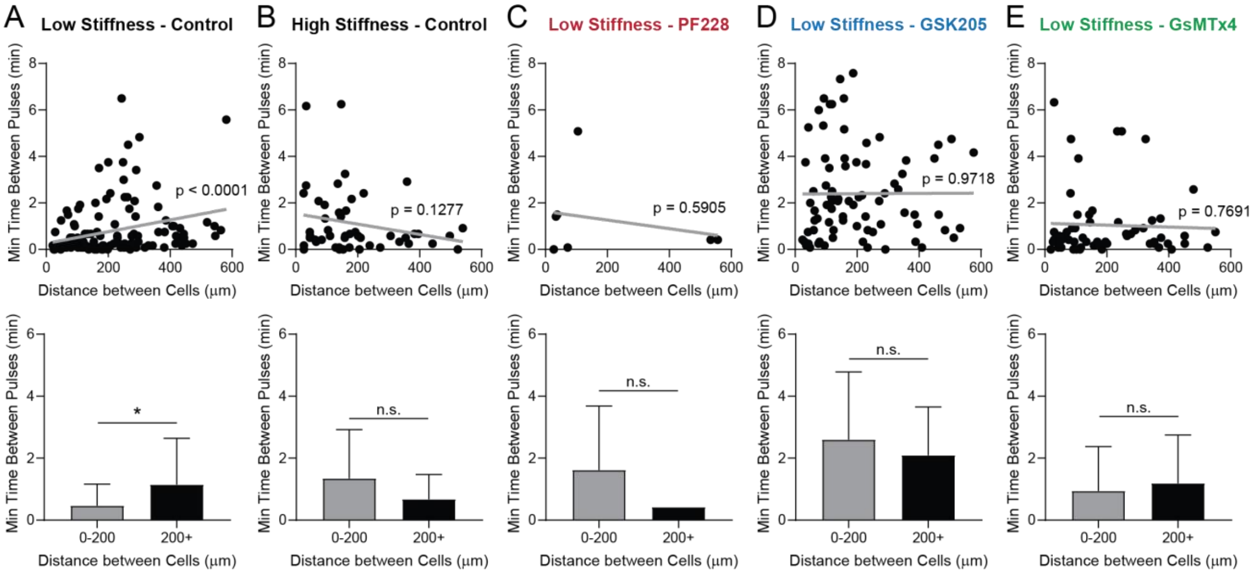

Supplementary Figure 6.7: Spatiotemporal Ca^{2+} signaling analysis. Quantification of the minimum time between Ca^{2+} pulses as a function of intercellular distance within EC lines patterned in (A) low stiffness matrices, (B) high stiffness matrices, (C) low stiffness matrices treated with 10 μM PF228, (D) low stiffness matrices treatedd with 10 μM GSK205, and (E) low stiffness matrices treated with 5 μm GsMTx4.

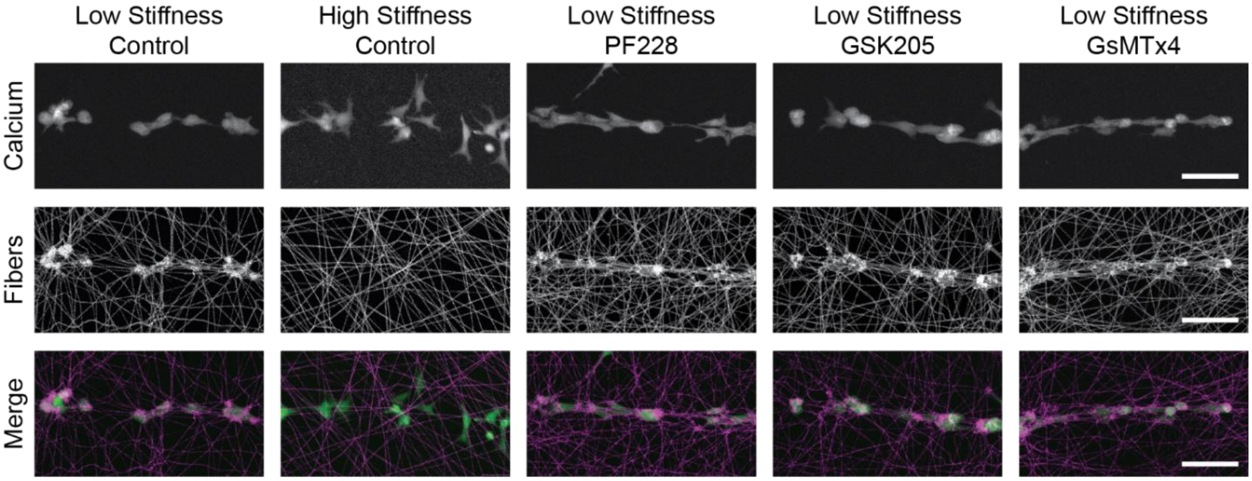

Supplementary Figure 6.8: Cell force-mediated matrix deformations following treatment with FAK, TRPV4, and Piezo1 inhibitors. Representative maximum intensity projections of calcium-labeled ECs (green) and rhodamine-labeled fibers (magenta) 2 h after cell line patterning as a function of matrix stiffness and presence of inhibitors confirms that inhibition of FAK (PF228), TRPV4 (GSK205), or Piezo1 (GsMTx4) does not diminish cell force-mediated matrix reorganization (scale bars: 100 μm).

Supplementary Movie 6.1: EC bulk seeding in fibrous DexMA matrices. Representative confocal fluorescence 12-hour timelapse movie of lifeAct-GFP expressing ECs (cyan) and rhodamine-labeled DexMA fibers (magenta) seeded at 250 cells mm^{-2} in low stiffness, cell-deformable and high stiffness, non-deformable matrices (Scale bar: 100 μm).
https://www.biorxiv.org/content/biorxiv/early/2021/08/18/2021.08.17.456669/DC1/embed/media-1.mp4?download=true

Supplementary Movie 6.2: Single cell patterning in fibrous DexMA matrices with variable matrix stiffness. Representative confocal fluorescence 12-hour timelapse movie of a single lifeAct-GFP expressing EC (cyan), rhodamine-labeled DexMA fibers (magenta), and embedded fluorescent beads (white) patterned in low stiffness, cell-deformable and high stiffness, non-deformable matrices (Scale bar: 100 μm).
https://www.biorxiv.org/content/biorxiv/early/2021/08/18/2021.08.17.456669/DC2/embed/media-2.mp4?download=true

Supplementary Movie 6.3: Single cell patterning in synthetic fibrous DexMA matrices with variable matrix density. Representative confocal fluorescence 12-hour timelapse movie of a single lifeAct-GFP expressing EC (cyan), rhodamine-labeled DexMA fibers (magenta), and embedded fluorescent beads (white) patterned in low and high density matrices with crosslinking equivalent to the lowest stiffness condition (Scale bar: 100 μm).
https://www.biorxiv.org/content/biorxiv/early/2021/08/18/2021.08.17.456669/DC3/embed/media-3.mp4?download=true

Supplementary Movie 6.4: Cell pair patterning in non-aligned fibrous DexMA matrices with variable matrix stiffness. Representative confocal fluorescence 12-hour timelapse movie of pairs of lifeAct-GFP expressing ECs (cyan) and rhodamine-labeled DexMA fibers (magenta) patterned in low stiffness, cell-deformable and high stiffness, non-deformable non-aligned matrices (Scale bar: 200 μm).
https://www.biorxiv.org/content/biorxiv/early/2021/08/18/2021.08.17.456669/DC4/embed/media-4.mp4?download=true

Supplementary Movie 6.5: Cell pair patterning in aligned fibrous DexMA matrices with variable matrix stiffness. Representative confocal fluorescence 12-hour timelapse movie of pairs of lifeAct-GFP expressing ECs (cyan) and rhodamine-labeled DexMA fibers (magenta) patterned in low stiffness, cell-deformable and high stiffness, non-deformable aligned matrices (Scale bar: 200 μm).
https://www.biorxiv.org/content/biorxiv/early/2021/08/18/2021.08.17.456669/DC5/embed/media-5.mp4?download=true

Supplementary Movie 6.6: Calcium transients of ECs in fibrous DexMA matrices with variable matrix stiffness. Representative confocal fluorescence 10-minute timelapse movie of calcium signaling (green) in ECs patterned into multicellular lines in low stiffness, cell-deformable and high stiffness, non-deformable matrices (Scale bar: 100 μm).
https://www.biorxiv.org/content/biorxiv/early/2021/08/18/2021.08.17.456669/DC6/embed/media-6.mp4?download=true

Supplementary Movie 6.7: Calcium transients of ECs in fibrous DexMA matrices in the presence of FAK, TRPV4, and Piezo1 inhibitors. Representative confocal fluorescence 10-minute timelapse movie of calcium signaling (green) in ECs patterned into multicellular lines in low stiffness, cell-deformable matrices with inhibition of FAK (PF228, 10 μM), TRPV4 (GSK205, 10 μM), and Piezo1 (GsMTx4, 5 μM) (Scale bar: 100 μm).
https://www.biorxiv.org/content/biorxiv/early/2021/08/18/2021.08.17.456669/DC7/embed/media-7.mp4?download=true

Supplementary Movie 6.8: Three-dimensional image stack of EC networks in fibrin hydrogels with variable matrix density, FAK inhibition, and TRPV4 inhibition. Representative confocal fluorescence image stacks (100 μm thick) of phalloidin-stained ECs (cyan) and nuclei (yellow) in 2.5 mg mL^{-1} fibrin, 5.0 mg mL^{-1} fibrin, and 2.5 mg mL^{-1} fibrin with inhibition of FAK (PF228, 10 μM) or TRPV4 (GSK205, 10 μM) (Scale bar: 100 μm).
https://www.biorxiv.org/content/biorxiv/early/2021/08/18/2021.08.17.456669/DC8/embed/media-8.mp4?download=true

Chapter 7: Synthetic Matrix Fibers Support 3D Vascular Network Assembly in Fibrin Hydrogels

7.1 Authors

Christopher D. Davidson, Daniel L. Matera, Nicole E. Friend, William Y. Wang, Jordan L. Kamen, Danica Kristen P. Jayco, Harrison L. Hiraki, Andrew J. Putnam, Brendon M. Baker

7.2 Abstract

Vasculogenesis is the *de novo* formation of vascular networks occurring during embryonic development, organogenesis, and adult neovascularization. If properly harnessed *in vitro*, this process presents a promising approach to vascularizing tissue engineered constructs, a significant outstanding challenge in the field of tissue engineering. In 3D hydrogels, the inclusion of stromal cells alongside endothelial cells (ECs) is required to guide and stabilize the self-assembly of vessel-like networks via secretion of proangiogenic factors, matrix remodeling, and generation of mechanical signals. However, long-term culture of stromal cells in engineered constructs could potentially induce undesirable long-term effects in the tissue construct such as tissue contraction, degradation, stiffening, or fibrosis. Here, we find that the inclusion of synthetic electrospun matrix fibers to 3D fibrin hydrogels enhances EC spreading and network assembly in the absence of supporting stromal cells. Specifically, the inclusion of non-cell-adhesive fibers promotes the assembly of lumenized EC networks mimicking microvascular

networks. We utilized RNA-sequencing and 3D matrix displacement analysis to find that matrix fibers enhance cell-matrix interactions and force propagation that underly vasculogenic assembly. This work identifies that electrospun fibers present an inexpensive alternative to sourcing and expanding secondary supporting cell types alongside patient-specific ECs to engineer prevascularized tissue constructs.

7.3 Introduction

Tissue engineering and regenerative medicine are driven by the long-term goal of developing biological constructs that restore, maintain, or improve the function of a tissue or organ (Griffith & Naughton, 2002; Langer & Vacanti, 1993; Vacanti & Langer, 1999). While the past few decades have reported success in relatively thin non-vascularized tissues such as skin or cartilage (Chua et al., 2016; Makris et al., 2015), large and complex tissues require an adequate blood supply throughout the construct (Auger et al., 2013; Griffith et al., 2005; Koike et al., 2004). The rate of host vessel invasion of traditional biomaterials upon transplantation is typically limited to several tenths of a micron per day, leading to necrosis at the center of the construct after implantation (Clark & Clark, 1939; Laschke et al., 2009; Rouwkema et al., 2008). Thus, an engineered graft thicker than the diffusion limit of gases and nutrients (about 150-200 μm) requires a pre-formed vascular network. As dense microcapillary networks supply the demanding oxygen needs of many tissues due to their large surface area, self-assembled microvasculature presents the most promising potential to solving this prevascularization problem.

Previous strategies to vascularize 3D engineered biomaterials can generally be categorized as top-down or bottom-up (Song et al., 2018). In top-down approaches, engineered vasculature is pre-designed and fabricated before cells are introduced. Examples include 3D printing bioinks or sacrificial materials (Miller et al., 2012; Norotte et al., 2009; Skardal et al., 2010), laser-mediated ablation (Brown et al., 2017b; Heintz et al., 2016), or layer-by-layer assembly (Morgan et al., 2013; Zhang et al., 2016). Despite exquisite control over network geometry and architecture, these methods fail to achieve the 5-20 μm diameter of microcapillaries. In contrast, bottom-up methods seek to harness the innate biological mechanisms that drive vessel formation during development and wound healing known as vasculogenesis, where endothelial cells (ECs) self-assemble into multicellular lumenized networks (Song et al., 2018). For example, ECs embedded in an implanted scaffold will assemble into microvessels *in situ*, but the typical >7 days required for this to occur would likely compromise viability of the implanted tissue (Lin et al., 2017; Nör et al., 2001; Schechner et al., 2000). *In vitro* vasculogenic assembly is an alternative where well-formed vessel networks are grown within a tissue construct prior to implantation. For example, self-assembled microvessels have been engineered by co-culturing ECs with support stromal cells (e.g. fibroblasts, smooth muscle cells, mesenchymal stem cells) in a variety of natural and synthetic 3D hydrogels (Beamish et al., 2019; Chen et al., 2012; Freiman et al., 2016; Koh et al., 2008; Lesman et al., 2011; Rao et al., 2012; Zanotelli et al., 2016). While the precise role of the stromal cell is not completely understood, matrix remodeling and the secretion of proangiogenic factors have been implicated in guiding and stabilizing the self-assembly of EC networks (DiPietro, 2016; Newman et al., 2011). However, long-term culture of stromal cells in engineered constructs could potentially induce undesirable effects such as tissue contraction, degradation, stiffening, or fibrosis (Buckley et al., 2001; Lemos & Duffield, 2018; Wynn & Ramalingam, 2012). Further, the high cost of expanding cells is a major challenge in translating cell-based therapies to the clinic. Thus, finding an alternative to co-culturing stromal cells with ECs would be beneficial towards economically engineering prevascularized tissue constructs.

It is well established that mechanical interactions between ECs and their surrounding extracellular matrix (ECM) regulate their ability to assemble into vessel-like structures and that stromal cells provide critical mechanical cues that enable EC morphogenesis (Lesman et al., 2016). Specifically, during 3D vasculogenic assembly, ECs first undergo vacuolization in an integrin-dependent manner followed by assembly of ECs into an interconnected network that requires matrix degradation, migration, and coordination over large length scales (Bayless et al., 2000; Crosby & Zoldan, 2019; Davis & Bayless, 2003; Hanjaya-Putra et al., 2011). Stromal cells are known to actively remodel their surrounding ECM via degradation and deposition of various matrix components. Additionally, stromal cells are highly contractile, therefore actively sending mechanical signals in the form of cell force-mediated matrix deformations. Indeed, previous work from our lab has utilized 2.5D synthetic matrices of electrospun fibers with user-defined architecture and mechanical properties to identify that EC self-assembly is facilitated by cell force-mediated matrix reorganization and mechanical intercellular communication (MIC) (Davidson et al., 2019b, 2021). Thus, we hypothesize that a potential alternative to admixed stromal cells to enable 3D vasculogenic assembly could be the inclusion of synthetic matrix fibers to provide critical mechanical cues to ECs.

In this work, we employed a previously described method from our lab to integrate electrospun dextran vinyl sulfone (DexVS) fibers within a 3D fibrin hydrogel to investigate the role of matrix fiber cues on vasculogenic assembly of ECs (Matera et al., 2019, 2020). Using this fiber-hydrogel composite system, we found that the addition of non-cell-adhesive matrix fibers enhanced EC spreading and promoted the assembly of multicellular networks of lumenized EC structures. Furthermore, we conducted bulk RNA-sequencing and identified that the presence of non-cell-adhesive matrix fibers increased expression of genes associated with cell-matrix adhesion, matrix remodeling, and vasculogenic assembly. Lastly, we confirmed that the inclusion of DexVS matrix fibers enhances cell-matrix adhesion and force-mediated matrix reorganization associated with vasculogenic assembly.

7.4 Results and Discussion

7.4.1 Evaluating the role of synthetic matrix fibers on EC network formation in 3D fibrin hydrogels.

To examine the ability of matrix fibers to enable vasculogenic assembly in the absence of supporting stromal cells, we implemented a recently established composite materials technique that imbues hydrogels with defined fiber segments that we have recently used to model stromal tissue spaces (Matera et al., 2019, 2020). Briefly, DexVS fiber segments were electrospun, photopatterned into defined lengths, collected in solution, and functionalized with the cell adhesive peptide RGD. These cell-adhesive fibers were then incorporated into fibrin hydrogels at varying concentrations to tune the resultant hydrogel fiber density (0.0 – 2.5 vol%), independent of the fibrinogen or thrombin concentrations in the bulk hydrogel (**Figure 7.1a**). Decoupling fiber density with bulk hydrogel properties affords independent tuning of mechanical cues from matrix fibers with bulk ligand density, porosity, and degradability.

Human umbilical vein ECs were first seeded (6 million mL^{-1}) in fibrin hydrogels with varying fibrinogen concentration and DexVS fiber density and cultured for 3 days in EGM-2 supplemented with the proangiogenic factors vascular endothelial growth factor (VEGF; 50 ng mL^{-1}) and phorbol 12-myristate 13-acetate (PMA; 25 ng mL^{-1}). Fibrin was selected as the bulk hydrogel for this model due to its extensive use as a vasculogenic biomaterial system (Morin & Tranquillo, 2013). In the absence of DexVS fibers, ECs exhibited a stepwise decrease in spreading and network length with increasing fibrinogen concentration between 5.0 and 20.0 mg mL^{-1}, and interconnected networks did not form at any matrix density (**Figure 7.1b,c**). Interestingly, the addition of DexVS fibers at 2.5 vol% enhanced EC self-assembly into interconnected structures independent of matrix density (**Figure 7.1b,c**). Furthermore, this increase in EC network assembly was found to increase as a function of fiber density (**Figure 7.1d,e**).

While the assembly of interconnected networks is a critical step during vasculogenic assembly, networks will not prove functional unless the extensions are lumenized and can support flow. In fibrin without DexVS fibers (FD 0.0%), while ECs did not form extensive networks, we identified many instances of vacuole formation and lumenal structures (**Figure 7.1f**). However, in fibrin with cell-adhesive DexVS fibers (FD 2.5% + RGD), despite the formation of extensive cellular networks, we did not identify the formation of luminal structures (**Figure 7.1g**).

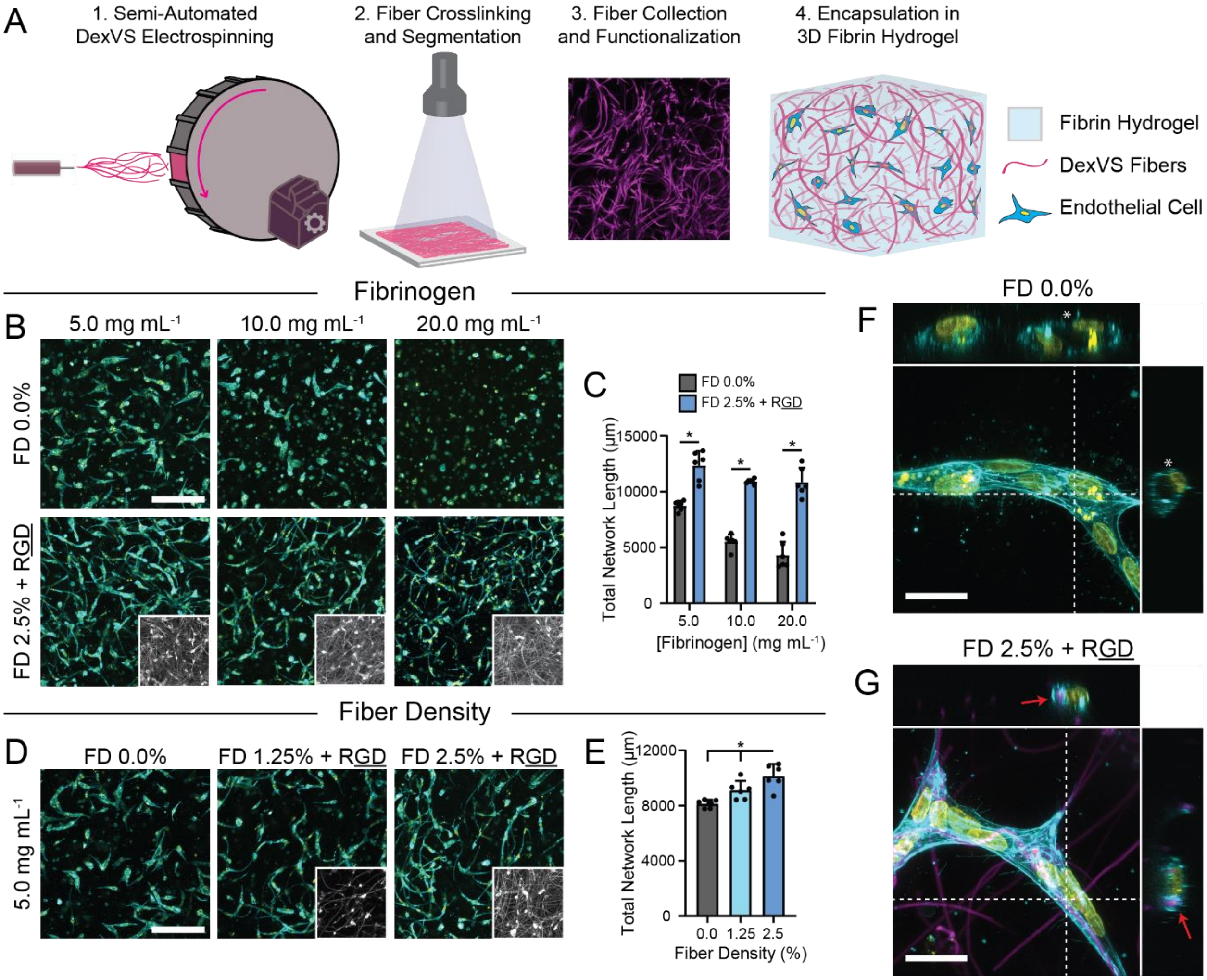

Figure 7.1 Cell-adhesive synthetic DexVS fibers enable EC network assembly in 3D fibrin hydrogels. (A) Fabricated schematic for generating fiber-reinforced fibrin hydrogels. DexVS was electrospun on a cylindrical collection mandrel. Fibers were then UV photo-crosslinked, collected in suspension, and functionalized with peptides to define cell adhesivity. Fibers are then encapsulated within a fibrin hydrogel alongside ECs. (B,D) Confocal fluorescent images of phalloidin-stained ECs (cyan), nuclei (yellow), and rhodamine-labeled DexVS fibers (white) as a function of (B) fibrinogen concentration and (E) fiber density. (C,E) Quantification of total vessel length (n = 6 fields of view). (F,G) Representative confocal maximum intensity projection with orthogonal vies (top and right side) of lumenal structures (indicated with asterisks) in FD 0.0% hydrogels and cell-fiber adhesion (indicated with red arrow) in FD 2.5% + RGD hydrogels. All data presented as mean ± SD with superimposed data points; asterisk denotes significance with $P < 0.05$.

7.4.2 Non-cell-adhesive DexVS fibers enable EC network assembly and lumenization

Given the importance of integrin-mediated adhesion in lumenization pathways, cell contraction, and cell migration, we hypothesized that ligand functionalization of DexVS fibers could play a critical role in guiding EC network assembly (Bayless et al., 2000; Davis & Camarillo, 1995, 1996). Specifically, RGD-functionalized fibers could provide adhesive cues that divert ECs from forming vacuoles that eventually coalesce into luminal structures. To test this hypothesis, we next functionalized DexVS fibers with a chemically equivalent scrambled RGD peptide, CGRDGS, to generate non-cell-adhesive fibers that still provide local mechanical cues to ECs within the bulk fibrin gel, but do not support direct integrin-mediated adhesion.

Interestingly, non-cell-adhesive fibers (FD 2.5% + RDG) enhanced EC spreading and network assembly in fibrin hydrogels compared to both FD 0.0% as well as FD 2.5% + RGD conditions (**Figure 7.2a,b**). Furthermore, high resolution images indicate evidence for the formation of luminal structures along EC extensions in FD 2.5% + RDG hydrogels (**Figure 7.2c**). Despite the inability for ECs to create adhesions on fibers, networks and extensions tracked near to matrix fibers suggesting that ECs sense their presence, likely due to the considerably higher stiffness of fibers (E ~ 100 MPa) (Davidson et al., 2020b) compared to the surrounding fibrin gel (E < 1 kPa). We also compared the dynamics of EC network assembly in FD 2.5% + RDG hydrogels compared to FD 0.0% hydrogels. In fiber-reinforced hydrogels, ECs spread rapidly, forming branched network structures within 24 hours of culture. Following the first day, there was minimal increase in total network length alongside a stepwise increase in average extension length as networks mature. In contrast, ECs exhibit limited spreading or network formation over five days of culture in non-fibrous hydrogels (**Figure 7.3d-f**).

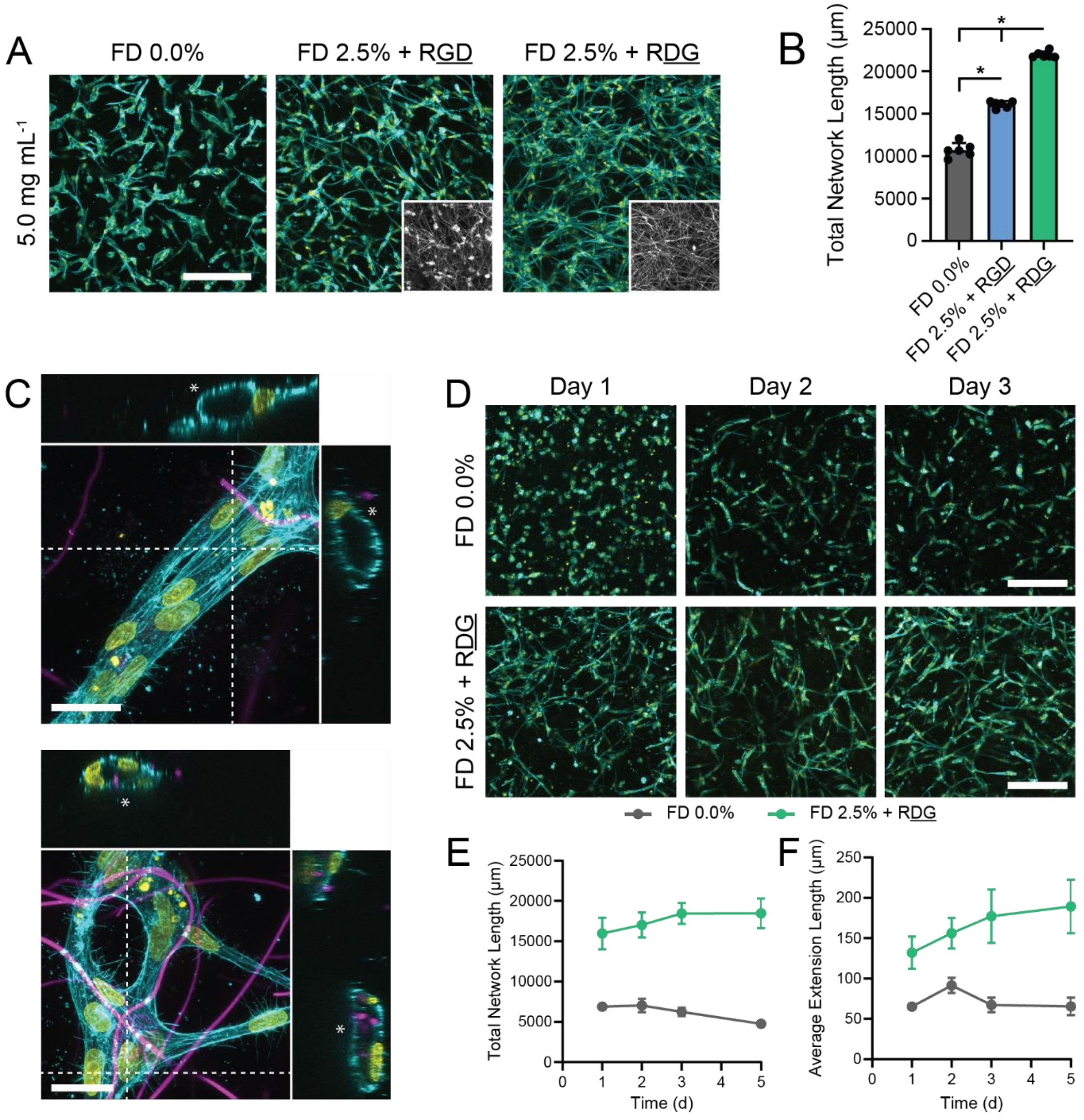

Figure 7.2 Non-cell-adhesive DexVS fibers enable EC network assembly and lumenization. (A) Confocal fluorescent images of phalloidin-stained ECs (cyan), nuclei (yellow), and rhodamine-labeled DexVS fibers (white) and (B) quantification of total network length in 5.0 mg mL^{-1} fibrin hydrogels in the absence of DexVS fibers (FD 0.0%) or with fibers (2.5 vol%) functionalized with either RGD or RDG peptides. (C) Representative confocal maximum intensity projection with orthogonal views (top and right side) of luminal structures (indicated with asterisks) in FD 2.5% + RDG hydrogels after 3 days of culture. (D) Confocal fluorescent images of phalloidin-stained ECs (cyan) and nuclei (yellow) as a function of time in non-fibrous and non-cell-adhesive fibrous fibrin hydrogels with (E) quantification of total network length and (F) average extension length over time. All data presented as mean ± SD with superimposed data points; asterisk denotes significance with $P < 0.05$.

7.4.3 Bulk RNA-sequencing identifies enhanced cell-ECM interactions during vasculogenic assembly in fiber-reinforced hydrogels

RNA sequencing (RNA-seq) was used to analyze global gene expression for ECs during network assembly in fibrin hydrogels without DexVS fibers, with RGD-functionalized fibers, and with RDG-functionalized fibers (**Figure 7.3a**). To assess changes in gene expression during assembly, ECs were cultured in each condition for 1 day (**Figure 7.3b**) upon with nattokinase (a fibrinolytic enzyme) was utilized to digest fibrin hydrogels affording cell isolation. RNA lysates were extracted from each condition and submitted for next generation sequencing.

We first utilized principle component analysis (PCA) to assess the bulk RNA-seq dataset. As expected, all conditions clustered into three groups based on the matrix condition in which they were cultured (**Figure 7.3c**). Interestingly, the two fibrous hydrogel conditions clustered closer to each other along PC1, which captures 78% of the variance seen in expression profiles. We also compared FD0.0% with FD2.5% + RDG hydrogels to identify specific genes that were upregulated in fibrous hydrogel conditions that could be enabling the assembly of EC networks. Several Gene Ontology (GO) terms were significantly modulated in support of our hypothesis that matrix fibers enhance EC activity in the absence of supporting stromal cells, such as cell communication, migration, adhesion, and motility. Interestingly we also saw significant changes in GO terms associated with cell-ECM adhesion, such as actin cytoskeleton organization, integrin-mediated signaling pathways, as well as regulation of focal adhesion assembly. Additionally, GO terms associated with matrix remodeling, like ECM organization, was also identified (**Figure 7.3d**).

Supporting our hypothesis that integrin-mediated adhesion was regulating vasculogenic assembly in fibrin hydrogels, genes encoding for integrins αv, α1, α5, β1, and β3 were all significantly increased at the transcriptomic level (**Figure 7.3e**). Previous work has identified that two integrins, αvβ3 and α5β1, regulate EC vacuolization and lumen formation in 3D fibrin matrices (Bayless et al., 2000), which is in agreement with our observations of enhanced lumen formation in FD2.5% + RDG hydrogels. Furthermore, bulk sequencing data indicated that several genes associated with matrix remodeling were upregulated in FD 2.5% + RDG hydrogels. Specifically, two main families of metalloproteinases that specialize in degrading the ECM, including matrix metalloproteinases (MMPs) and disintegrin and metalloproteinase with thrombospondin motifs (ADAMTS), were identified to be upregulated (MMP1, MMP10, MMP14, ADAMTS1, ADAMTS6, ADAMTS18) (**Figure 7.3e**). Additionally, SERPINE1, which encodes for plasminogen activator inhibitor 1 (PAI-1), was one of the most highly upregulated genes in fibrous hydrogels compared to non-fibrous hydrogels (**Figure 7.3e**). PAI-1 blocks the action of plasminogen activators and resultant fibrinolysis, likely regulating the degradation rate of the fibrin hydrogel during culture (Iwaki et al., 2012). Lastly, we observed that VCL gene expression, which encodes for vinculin, a mechanosensitive focal adhesion (FA) protein, was uniquely upregulated in ECs cultured in FD 2.5% + RDG hydrogels. FAs connect the ECM to the cell’s actomyosin skeleton and generally form at protrusions functioning as adherence points during cell migration (Bershadsky et al., 2003; Geiger et al., 2009). They are critical signaling hubs that regulate mechanical communication between ECs, an important regulator of vasculogenic assembly (Davidson et al., 2021).

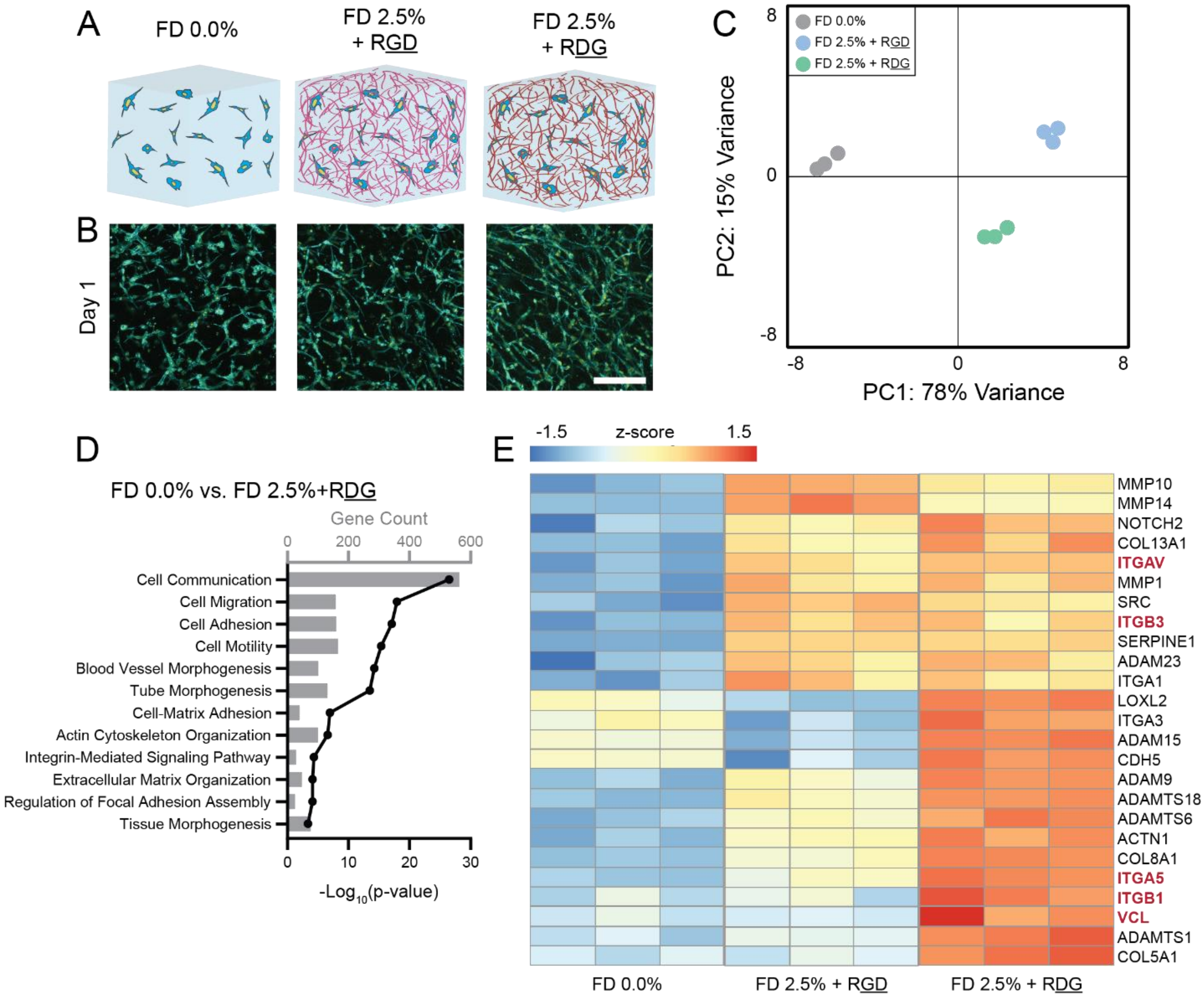

Figure 7.3 Bulk RNA-sequencing analysis of fiber-mediated vasculogenic assembly. (A) Schematic of matrix conditions and (B) representative confocal fluorescent images of phalloidin-stained ECs (cyan) and nuclei (yellow) after one day of culture. (C) Principle component analysis (PCA) clustering of gene signatures for three matrix conditions. (D) Significant Gene Ontology (GO) terms for FD 0.0% vs. FD 2.5% + RDG hydrogel conditions. (E) Curated upregulated genes of interest in FD 0.0%, FD 2.5% + RGD, and FD 2.5% + RDG hydrogel conditions.

7.4.4 Adhesion and matrix displacements

RNA-seq analysis implicated cell-ECM interactions as upregulated in fibrin hydrogels with the inclusion of non-cell-adhesive DexVS fibers in the bulk. To better understand how adhesions are forming during 3D network assembly, we performed immunostaining for vinculin after 1 day of culture while ECs are putatively assembling into interconnected networks. As expected, based on the RNA-seq analysis, FD 2.5% + RDG hydrogels led to the most robust FA formation in ECs (**Figure 7.4a-c**). As ECs cannot directly engage with RDG-functionalized fibers, we next sought to understand the 3D localization of adhesions in hydrogels with RGD and RDG fibers. In FD 2.5% + RGD hydrogels, FAs mainly tracked directly on or near to a fiber, with approximately 37% of total vinculin signal overlapping with fibers. In contrast, FAs in FD 2.5% + RDG hydrogels were not localized to fibers, with approximately 17% of total vinculin signal overlapping with fibers (**Figure 7.4d**).

As vinculin is a force-sensitive protein at FAs and tightly linked to cell forces, we lastly investigated how EC-generated traction forces were being propagated through the ECM as a function of the inclusion of matrix fibers within fibrin hydrogels. To track matrix displacements, fluorescent beads (Ø = 1 µm) were embedded alongside ECs and fibers and samples were imaged live for 15 hours after seeding (**Figure 7.4e**). Average bead displacement was significantly higher in fibrous hydrogels, with the highest level of force propagation in FD 2.5% + RDG hydrogels (**Figure 7.4f**). These results indicate that fibrin hydrogels with non-cell-adhesive fibers enable cell-matrix interactions with fibrin that are reinforced by local mechanical cues from fibers that enhance FA formation and force propagation.

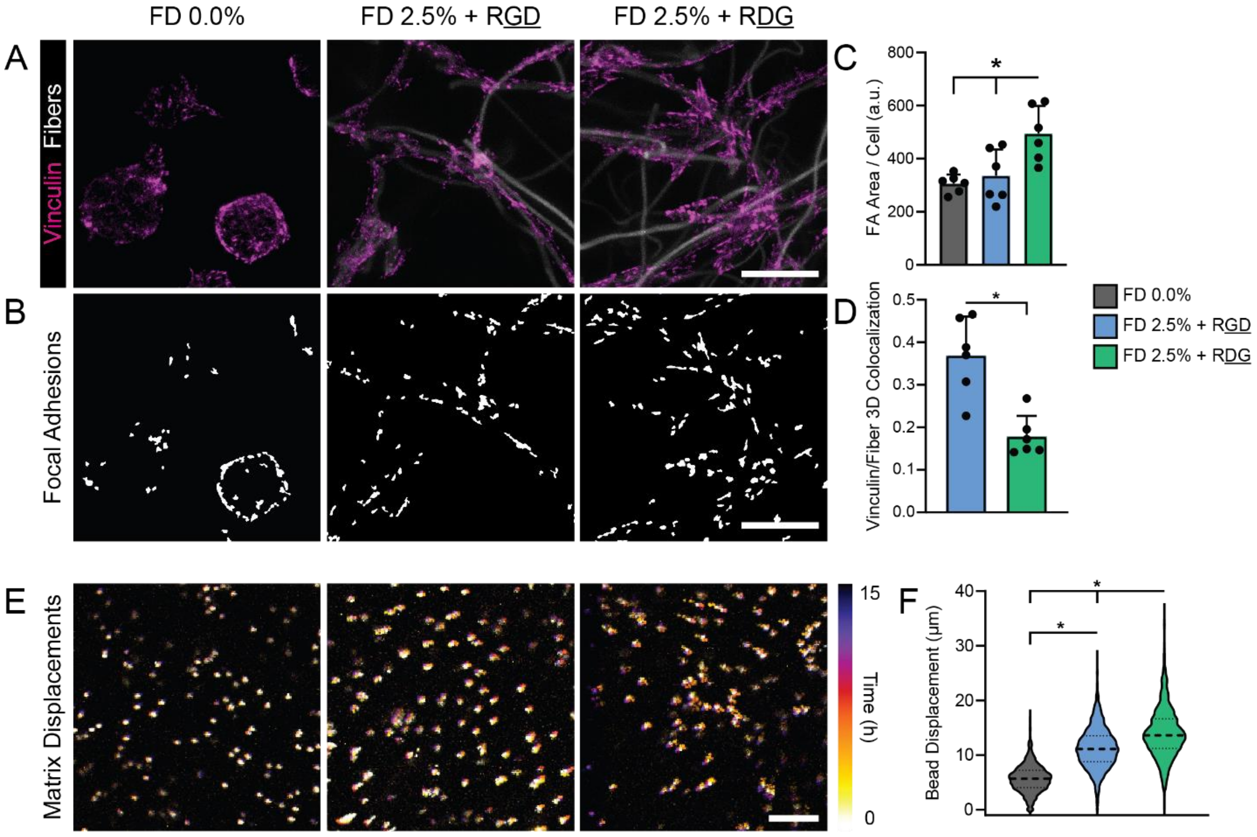

Figure 7.4 Analysis of focal adhesion formation and matrix displacements during 3D EC network assembly. (A,B) Representative immunostained images of (A) vinculin (magenta) and (B) image analysis to identify FAs (white) in ECs as a function of hydrogel conditions. (C) Quantification of total FA area normalized per cell and (D) 3D colocalization of vinculin with DexVS fibers. (E) Temporally color-coded overlays depicting motion of fluorescent beads over a 15 hour timelapse and (F) quantification of average bead displacement distance. All data presented as mean ± SD with superimposed data points; asterisk denotes significance with $P < 0.05$.

7.5 Conclusions

In this work, we utilized a biomaterial system to integrate electrospun DexVS fibers within a 3D fibrin hydrogel to investigate the role of matrix fiber cues on vasculogenic assembly of ECs. The ultimate goal of this work was to identify a potential alternative to admixed stromal cells with ECs to engineer microvascular networks as stromal cells are highly heterogeneous, uncharacterized cells that can potentially introduce undesirable effects, and culture of an additional cell type would drastically increase the cost for future cell-based therapies. Using this fiber-hydrogel composite system, we found that the addition of non-cell-adhesive RDG functionalized DexVS fibers enhanced EC spreading and promoted the assembly of lumenized vessel-like structures. Furthermore, RNA-seq and analysis of cell-matrix adhesion and matrix displacements identified that fibrin hydrogels with RDG-functionalized fibers promote cell-ECM interactions with the bulk fibrin hydrogel while simultaneously providing local mechanical cues that enable EC communication and self-assembly. For future cell-based therapies, electrospun fibers would be an inexpensive alternative to sourcing and expanding a secondary supporting cell type alongside patient-specific ECs.

7.6 Materials and Methods

7.6.1 Reagents

All reagents were purchased from Sigma-Aldrich and used as received, unless otherwise stated.

7.6.2 Cell culture and biological reagents

Human umbilical vein endothelial cells (ECs) were cultured in endothelial growth medium (EGM-2; Lonza, Basel, Switzerland) supplemented with 1% penicillin-streptomycin-fungizone (Gibco, Waltham, MA). Cells were cultured at 37°C and 5% CO_2. ECs were used from passages four to eight in all experiments. For live cell time-lapse imaging, lentiviral transduction of LifeAct-GFP was utilized.

7.6.3 Lentivirus production

pLenti.PGK.LifeAct-GFP.W was a gift from Rusty Lansford (Addgene plasmid #51010). To generate lentivirus, plasmids were co-transfected with pCMV-VSVG (a gift from Bob Weinberg, Addgene plasmid #8454), pMDLg/pRRE, and pRSV-REV (gifts from Didier Trono, Addgene plasmid #12251 and #12253 (Dull et al., 1998; Stewart et al., 2003)) in 293T cells using the calcium phosphate precipitation method (Kingston et al., 2003). Viral supernatants were collected after 48 h, concentrated with PEG-it^{TM} (System Biosciences, Palo Alto, CA) following the manufacturer's protocol, filtered through a 0.45 μm filter (ThermoFisher Scinetific Nalgene, Waltham, MA), and stored at -80°C. Viral titer was determined by serial dilution and infection of ECs. Titers yielding maximal expression without cell death or detectable impact on cell proliferation or morphology were selected for studies.

7.6.4 Synthesis of dextran vinyl sulfone

Dextran was reacted with divinyl sulfone following a previously described procedure (Yu & Chau, 2012). Briefly, dextran (5 g) was dissolved in 250 mL of sodium hydroxide (100 mM) solution on a stir plate at 1500 rpm before addition of divinyl sulfone (12.5 mL; Thermo Fisher Scientific, Hampton, NH). The reaction proceeded for 3.5 min before termination by addition of 2.5 mL hydrochloric acid (12 M). The product was dialyzed against milli-Q water for 3 days and then lyophilized. DexVS was characterized by ^{1}H NMR and a vinyl sulfone/dextran repeat unit ratio of 0.376 was determined.

7.6.5 Fiber segment fabrication

DexVS was dissolved at 0.6 g mL^{-1} in a 1:1 mixture of Milli-Q ultrapure water and dimethylformamide with 0.015% Irgacure 2959 photoinitiator. Methacrylated rhodamine (0.5 mM; Polysciences Inc., Warrington, PA) was incorporated into the electrospinning solution to fluorescently visualize fibers. This polymer solution was used for electrospinning within an environment-controlled glovebox held at 21°C and 30% relative humidity. Electrospinning was performed at a flow rate of 0.3 mL h^{-1}, gap distance of 5 cm, and voltage of -10.0 kV onto a grounded collecting surface attached to a linear actuator. Fiber layers were collected on glass slabs and primary crosslinked under ultraviolet light (100 mW cm^{-2}) and then secondary crosslinked (100 mW cm^{-2}) in a 1 mg mL^{-1} Irgacure 2959 solution. After polymerization, fiber segments were resuspended in a known volume of PBS (typically 3 mL). The total volume of fibers was then calculated via a conservation of volume equation: total resulting solution volume = volume of fibers + volume of PBS. After calculating total fiber volume, solutions were re-centrifuged, supernatant was removed, and fiber pellets were resuspended to create a 1.1 vol% fiber solution, which were then aliquoted and stored at 4°C.

7.6.6 DexVS fiber functionalization

To define cell adhesion to fibers, either the cell-adhesive peptide RGD (CGRGDS, 2.0 mM; Genscript, Pescataway, NJ) or a scrambled RDG peptide (CGRDGS, 2.0 mM) were coupled to vinyl sulfone groups along the DexVS backbone via Michael-type addition chemistry for 15 min, followed by quenching of excess VS groups in a 300 mM cysteine solution for 15 min. To remove free thiols after quenching, fiber solutions were vigorously rinsed via flushing with excess PBS two times before use in cell studies.

7.6.7 Fibrin hydrogel formation

Human umbilical vein ECs were encapsulated (6 million mL^{-1}) in fibrin hydrogels containing 5.0, 10.0, or 20.0 mg mL^{-1} fibrinogen and 1 U mL^{-1} thrombin. Briefly, a fibrinogen precursor solution was prepared by dissolving fibrinogen from bovine plasma in PBS at twice the final concentration. To create fiber-reinforced hydrogels, a defined stock solution (10% v/v) of suspended DexVS fibers in PBS was mixed into this fibrinogen precursor solution. A thrombin precursor solution was simultaneously prepared consisting of ECs at twice the final concentration in EGM-2 with 2 U mL^{-1} bovine thrombin. These two precursor solutions were mixed at a 1:1 ratio and 20 μL was transferred into a PDMS mold with 4 mm diameter and incubated at 37°C for 20 min. Samples were then hydrated in EGM-2 supplemented with fetal bovine serum (FBS; 5% v/v), vascular endothelial growth factor (VEGF; 50 ng mL^{-1}), and phorbol 12-myristate 13-acetate (PMA; 25 ng mL^{-1}), and media was replaced every 24 hours. Quantification of morphological network properties was performed on 100 μm image stacks using Angiotool (Zudaire et al., 2011).

7.6.8 Fluorescent staining and microscopy

Hydrogels were first fixed in 4% paraformaldehyde for 30 min at room temperature. Alternatively, to extract cytoplasmic vinculin, samples were simultaneously fixed and permeabilized in 2% paraformaldehyde in a microtubule-stabilizing buffer containing 1,4-piperazinediethanesulfonic acid (PIPES, 0.1 M), ethylene glycol-bis(2-aminoethylether)-N,N,N',N'-tetraacetic acid (EGTA, 1 mM), magnesium sulfate (1 mM), poly(ethylene glycol) (4% w/v), and triton X-100 (1% v/v) for 30 min at room temperature. To stain the actin cytoskeleton and nuclei, cells were permeabilized in PBS solution containing triton X-100 (5% v/v), sucrose (10% w/v), and magnesium chloride (0.6% w/v) for 1 h. Samples were then simultaneously blocked in 1% (w/v) bovine serum albumin and stained with phalloidin and DAPI for 24 h. For immunostaining, samples were blocked for > 6 h in 1% (w/v) bovine serum albumin and incubated with mouse monoclonal anti-vinculin antibody (1:1000, Sigma #V9264) followed by secondary antibody (1:1000, Life Technologies #A21236) for 6 h each at room temperature with overnight PBS washes between each step. Fixed samples were imaged on a Zeiss LSM800 laser scanning confocal microscope. Unless otherwise specified, images are presented as maximum intensity projections. Fluorescent images were processed and quantified via custom Matlab scripts.

7.6.9 Matrix deformation quantification

Immediately after gelation, fibrin hydrogels were transferred to a motorized and environmentally controlled stage and imaged using a Zeiss LSM800 laser scanning confocal microscope. Images of F-actin, DexVS fibers, and fluorescent beads embedded in the bulk hydrogel were acquired every 30 min for 15 h. Images were converted to maximum intensity projections before analysis. Single particle tracking was completed by first aligning image stacks of fluorescent beads and then tracked using TrackMate, a freely available ImageJ plugin [-]. Beads were detected at each time point using a Laplacian of Gaussian (LoG) detector with an estimated particle diameter of 5 µm and a threshold of 1.0 with use of a median filter. Single particle tracking was completed using a linear assignment problem tracker with a linking max distance and gap-closing max distance of 5 µm and gap-closing max frame gap of 2 frames.

Tracks were filtered to only contain particles detected throughout the entire timelapse and then analyzed using custom Matlab scripts.

7.6.10 Bulk RNA-sequencing and bioinformatics

Samples for bulk RNA-sequencing included human umbilical vein ECs encapsulated in 5.0 mg mL^{-1} fibrin hydrogels with 1) no DexVS fibers, 2) DexVS fibers (2.5 vol%) functionalized with the cell-adhesive peptide RGD, and 3) DexVS fibers (2.5 vol%) functionalized with the scrambled peptide RDG. All conditions were cultured for 18 hours upon which nattokinase (100 fibrinolytic units mL^{-1}) was incorporated into EGM-2 media for 15 minutes to digest the surrounding fibrin hydrogel. ECs were pelleted and RNA isolation was performed via RNeasy mini kit per manufacturer's protocol. Purified RNA samples were submitted to the University of Michigan Sequencing Core for library prep and next generation sequencing. Expression data was analyzed using DESeq2 and custom R scripts.

7.6.11 Statistical analysis

Statistical significance was determined by one-way or two-way analysis of variance (ANOVA) with post-hoc analysis (Tukey test) or Student's t-test where appropriate. For all studies, significance was indicated by $p < 0.05$. Sample size is indicated within corresponding figure legends and all data are presented as mean ± standard deviation.

Chapter 8: Summary and Future Directions

8.1 Summary of findings

Overall, this thesis aimed to design and utilize synthetic fibrous matrices towards investigating the role of mechanical signaling during the self-assembly of multicellular structures. Chapter 2 summarized current biomaterial platforms to model the ECM, evidence for mechanical intercellular communication (MIC), and the current state of microvascular tissue engineering approaches. Specifically, this thesis employed various natural and synthetic fibrous biomaterial platforms that ranged in complexity from 2D Matrigel surfaces, suspended 2.5D synthetic fiber matrices, and fibrous hydrogel composites consisting of synthetic fibers embedded within 3D fibrin hydrogels. These platforms were combined with microfabrication-based approaches, cell and matrix labelling techniques, and confocal microscopy to understand critical matrix properties that mediate MIC and the self-assembly of functional engineered microvascular networks.

Chapter 3 examined how physical attributes of the ECM influence the assembly of EC networks in 2D and 2.5D fibrous materials (Davidson et al., 2019b). Chapters 4-5 worked towards advancing the mechanical tunability of 2.5D electrospun fibrous scaffolds, specifically long-term stability and control over nonlinear mechanical properties (Davidson et al., 2020b, 2020c). Chapter 6 focused on enhancing our understanding of MIC between ECs, specifically investigating how tissue-relevant matrix properties mediate the transmission of cell-generated forces as well as the cellular machinery required for ECs to generate, sense, and respond to mechanical signals (Davidson et al., 2021). Lastly, Chapter 7 looked to harness these observations in more translatable 3D hydrogel constructs by using a composite approach where fibrin hydrogels were reinforced with electrospun DexVS fiber segments. Overall, this improved understanding of how cells communicate via mechanical forces will provide new insights towards the design of morphogenetic biomaterials.

8.2 Limitations and Future Directions

8.2.1 Towards a deeper understanding of MIC

Continuing to advance our understanding of how cells send and receive mechanical signals will require integration of multidisciplinary characterization techniques that probe forces and mechanical strain at the cell-scale. Specifically, advances in Förster resonance energy transfer (FRET)-based molecular tension sensors have enabled the measurement of tensile forces across cytoskeletal proteins and have provided key insights into mechanotransduction (Gates et al., 2019; Ham et al., 2019). The first genetically encoded FRET-based tension sensor was developed to quantify tension across vinculin during focal adhesion assembly and enlargement (Grashoff et al., 2010). Combining this approach with our cell patterning technique and live cell imaging could advance our understanding of the dynamic relationship between FA forces and cell protrusive activity. Furthermore, direct measurements of membrane tension (Stabley et al., 2012) or ion channel state (Agasid et al., 2017) during MIC could provide more information on the molecular mechanisms underlying this phenomenon.

In parallel to enhancing our understanding of intracellular signaling that underlies MIC, we also plan to utilize advances in mechanical manipulation of cells. One major limitation of the cell-patterning approach described in this thesis is that it does not completely isolate mechanical signals from putative chemotactic factors. Recent collaborative work from our lab has developed a robotic manipulation platform that allows for wireless, localized, and programmable deformation within suspended fibrous DexMA or DexVS matrices (Uslu et al., 2021). This technology allows for mechanical activation of cells while simultaneously being able to monitor the cell response and force-mediated changes in network architecture. In addition to being able to isolate mechanical signaling from biochemical signals, this technology would also enable enhanced understanding of how cells respond to different properties of mechanical signals such as the magnitude of force or rate of loading. Overall, the continued development and deployment of such techniques will be essential in further elucidating critical aspects of MIC and employing new strategies to direct cellular assembly.

8.2.2 Host-response to fiber-reinforced prevascularized tissue constructs

Chapter 7 of this thesis describes a new strategy towards engineering microvasculature in 3D biomaterials via the addition synthetic matrix fibers to a 3D monoculture of ECs in fibrin hydrogels. Despite the ability to create vessel-like networks *in vitro*, though, maturation and stability of the formed vasculature and rapid anastomosis to host circulation post-implantation remain significant challenges. Recent work has shown that both vessel maturity (pre-implantation) and contributions from myeloid cells during the host immune response (post-implantation) play critical roles in construct engraftment (Ben-Shaul et al., 2019; Grunewald et al., 2006; Lin et al., 2017; Nahrendorf et al., 2007; Shojaei et al., 2008). Thus, one major future direction for this work is to gain a deeper understanding of microenvironmental regulation of these processes to enable rapid integration of microvascular networks with a host circulatory system upon implantation. Utilizing a subcutaneous implant model in SCID mice would allow us to answer the following critical questions: 1) how does the addition of synthetic matrix fibers to acellular hydrogels regulate host cell invasion (specifically host ECs and myeloid cells) post-implantation, and 2) how does the addition of ECs to fiber-reinforced hydrogels (either seeded immediately before implantation and unassembled or seeded 3 days before implantation to allow for vasculogenic assembly) affect the time to perfusion.

One additional limitation to our current approach is the use of fibrin as the bulk hydrogel. While fibrin has long been used as a matrix for the development of *in vitro* models of microvasculature (Morin & Tranquillo, 2013), major limitations exist, specifically its low mechanical stiffness and rapid resorption with subsequent loss of shape and volume upon implantation. The work in this thesis finds that cell force-mediated MIC between ECs is critical during vasculogenic assembly, and the low stiffness of fibrin enables MIC and as such is likely a major contributor to its vasculogenic potential. Indeed, building 3D vascular networks has proven more challenging in synthetic polymeric hydrogels such as PEG, hyaluronic acid, and dextran, which are more suitable for translational applications, but dissipate cell forces short distances away from the cell. Thus, an immediate next step is incorporating fibrillar features in synthetic hydrogels to enhance MIC and vasculogenic assembly of ECs. Overall, the continued advancement of tunable synthetic hydrogels that enable cellular morphogenesis will enhance our ability to engineer complex tissue constructs for regenerative medicine applications.

Appendix A: Matlab Scripts

Analysis of Focal Adhesion Morphology

```
function [] = faquant2(faFilename, actinFilename, experiment_title, root,
dirOut, dataOut, pathname, imgCount)
%FOCAL ADHESION QUANTIFICATION
%   Detailed explanation goes here

% INPUT FA IMAGE
faScale = [20 255];
faImage = mat2gray(imread(faFilename),faScale);

% MASK FA IMAGE WITH CELL AREA TO REMOVE EXTRACELLULAR NOISE
% cellMask = imthresh(imin(actinFilename));
cellMask = im2bw(imin(actinFilename),0.12);
cellMask = bwmorph(cellMask, 'close');
cellMask = bwareaopen(cellMask, 1000);
cellMask = bwmorph(cellMask, 'spur');
faMaskraw = cellMask .* faImage;



%--------------------------------------------------------------------------
% QUANTIFY ADHESION PROPERTIES

% filter and threshold image using gaussian filter
noiseSize = 5;
backSize = 50;
[faClean, faMask] = gfilt(faMaskraw, noiseSize, backSize);
% filter out adhesions < 1 micron^2
faMask = double(bwareaopen(faMask,40));
% % make all images binary
% faMask = faMask(:,:,2);
% faClean = faClean(:,:,2);
impanel(faMaskraw,faClean,faMask);

% COLLECT AND RECORD DATA ON FILTERED ADHESIONS
[adh, adhCount] = bwlabel(faMask,8);
adhStats =
regionprops(adh,'Area','Eccentricity','Orientation','MajorAxisLength','MinorA
xisLength');
for i=1:adhCount
    rawAdh2D(i,1) = adhStats(i,1).Area;
    rawAdh2D(i,2) = adhStats(i,1).Eccentricity;
    rawAdh2D(i,3) = adhStats(i,1).Orientation;
    rawAdh2D(i,4) = adhStats(i,1).MajorAxisLength;
    rawAdh2D(i,5) = adhStats(i,1).MinorAxisLength;
end

% WRITE RAW ADHESION DATA TO EXCEL SHEET FOR EACH CELL
cd(dirOut);
cd(dataOut);
raw_headers = {'Area', 'Eccentricity', 'Orientation', 'Major Axis Length',
'Minor Axis Length'};
xlsFilename = strcat(experiment_title,num2str(imgCount),'_RAW','.xls');
xlswrite(xlsFilename,raw_headers,1,'A1');
xlswrite(xlsFilename,rawAdh2D,1,'A2');

% CALCULATE ADHESION STATISTICS AND WRITE TO SPREADSHEET
areaMean = mean(rawAdh2D(:,1));
areaStd = std(rawAdh2D(:,1));
eccMean = mean(rawAdh2D(:,2));
eccStd = std(rawAdh2D(:,2));
aspectMean = mean(rawAdh2D(:,3));
aspectStd = std(rawAdh2D(:,3));
angMean = rad2deg(circ_mean(deg2rad(rawAdh2D(:,4))));
angDisp = rad2deg(circ_std(deg2rad(rawAdh2D(:,4))));

cellArea = sum(sum(cellMask));
totalAdhArea = sum(sum(faMask));
xlsOut = {faFilename adhCount areaMean areaStd eccMean eccStd aspectMean
aspectStd angMean angDisp cellArea totalAdhArea};
xlsFilename = strcat(experiment_title,'.xls');
xlsRow = strcat('A',num2str(imgCount+1));
xlswrite(xlsFilename,xlsOut,1,xlsRow);

% IMAGE EXPORTS
cd(pathname);
cd(dirOut);
imwrite(faMask,
strcat(root,num2str(imgCount),'_faMask.tif'),'Compression','none');
imwrite(faClean,
strcat(root,num2str(imgCount),'_faClean.tif'),'Compression','none');
imwrite(cellMask,
strcat(root,num2str(imgCount),'_cellMask.tif'),'Compression','none');
end
```

Alpha Smooth Muscle Actin Quantification

```
function [ actin_signal, asma_signal, nucCount, actinCell, asmaCell,
asmaArea ] = asmaquant(asmaFilename, nucFilename, actinFilename,
threshVal, pathname, dirOut, imgCount)
% ASMA QUANTIFICATION

% INPUT
asmaScale = [6000, 65535];
actinScale = [2515, 35493];
```

```
   asmaImage = mat2gray(imread(asmaFilename),asmaScale);
   actinImage = mat2gray(imread(actinFilename),actinScale);

   % THRESHOLD ACTIN IMAGE AND REMOVE BACKGROUND NOISE
   cell = im2bw(imin(actinFilename),threshVal);
   cell = bwmorph(cell, 'close');
   [objects, totalObjects] = bwlabel(cell, 4);
   stats = regionprops(objects, 'Area', 'PixelIdxList');
   for i = 1:totalObjects
       if stats(i,1).Area < 100 %GET RID OF NOISE THAT IS NOT THE CELL
   NETWORK
           cell(stats(i,1).PixelIdxList) = 0;
       end
   end
   cell = bwmorph(cell, 'spur');

   % CALCULATE aSMA AND ACTIN SIGNAL (MASKED BY CELL AREA)
   cellArea = sum(sum(cell));
   asmaMask = asmaImage .* cell;
   asma_signal = sum(sum(asmaMask));
   actinMask = actinImage .* cell;
   actin_signal = sum(sum(actinMask));

   % GET CELL COUNT BY COUNTING NUMBER OF NUCLEI
   [nucCount] = nuccounter(nucFilename,pathname,dirOut,imgCount);

   % CALCULATE aSMA AND ACTIN SIGNAL PER CELL
   actinCell = actin_signal ./ nucCount;
   asmaCell = asma_signal ./ nucCount;
   asmaArea = asma_signal ./ cellArea;
   end
```

Fiber Crimp Quantification

```
% FIBER TORTUOSITY QUANTIFICATION
[imgName, pathname, filterIndex] = uigetfile('*.*', 'Open Image');
cd(pathname)
img = imread(imgName);
imshow(img);

% while loop until an enter if you want to draw multiple lines

button = 1;
fibCount = 21;
while isempty(button) ~= 1
    imshow(img);
    h = drawfreehand

    % get actual length
    numPoints = length(h.Position);
    sumLength = 0;
    for i=1:numPoints-1;
```

```
        sumLength = sumLength + sqrt((h.Position(i+1,1)-h.Position(i,1))^2 +
(h.Position(i+1,2)-h.Position(i,2))^2);
    end

    % get start to end pt length - as the c row flies distance
    crowLength = sqrt((h.Position(1,1)-h.Position(numPoints,1))^2 +
(h.Position(1,2)-h.Position(numPoints,2))^2);

    % calculate tortuosity
    tortuosity = sumLength/crowLength;

    fibCount = fibCount+1;

    tData(fibCount,1) = sumLength;
    tData(fibCount,2) = crowLength;
    tData(fibCount,3) = tortuosity;

    plot(h.Position(:,1),h.Position(:,2),'bl','LineWidth',20);
    axis([0 1024 0 1024]);
    pbaspect([1,1,1]);
    saveas(gcf,strcat(imgName(1:end-4),'_',num2str(fibCount),'.eps'),'eps');

end
```

Transition Strain Quantification

```
% TRANSITION STRAIN QUANTIFICATION

% input 2 column table with strain and stress
name = swell13stressstrainFINALS2;

% convert table to array and record the number of datapoints
curve = table2array(name);
datapoints = length(curve);

% define low regime as first 25% and high regime as last 25% of data
low_regime = curve((1:round(datapoints/3)),:);
high_regime = curve((2*round(datapoints/3):datapoints),:);

% linear fit to low and high regimes
low_fit = fitlm(low_regime(:,1),low_regime(:,2));
high_fit = fitlm(high_regime(:,1),high_regime(:,2));

% find and display intersection point (transition strain)
low_intercept = low_fit.Coefficients.Estimate(1);
low_slope = low_fit.Coefficients.Estimate(2);
high_intercept = high_fit.Coefficients.Estimate(1);
high_slope = high_fit.Coefficients.Estimate(2);
intersection = (low_intercept-high_intercept)/(high_slope-low_slope);
disp(intersection);
```

Cell Spreading Synergy Analysis

```
function [ clusterNucArray , totalClusters , nucCount , cellPerCluster,
cellArea , aveCellArea, output ] = synergy(cellFilename, nucFilename,
threshVal, pathname, dirOut, imgCount)
%UNTITLED2 Summary of this function goes here
%   Detailed explanation goes here

% INPUT AND THRESHOLD CELL IMAGE
cellImg = imin(cellFilename);
threshCellImg = im2bw(cellImg, threshVal);

% CLEAN IMAGE TO GET RID OF NOISE AND FILL HOLES IN CELL NETWORK
cell = bwmorph(threshCellImg, 'close');
[objects, totalObjects] = bwlabel(cell, 4);
stats = regionprops(objects, 'Area', 'PixelIdxList');
for i = 1:totalObjects
    if stats(i,1).Area < 500 %GET RID OF NOISE THAT IS NOT THE CELL NETWORK
        cell(stats(i,1).PixelIdxList) = 0;
    end
end
cell = bwmorph(cell, 'spur');

% INPUT AND THRESHOLD NUC IMAGE
[nucCountone, aveNucAreaone, nucMask] =
nuccounter(nucFilename,pathname,dirOut,imgCount);

% MAKE ARRAY OF NUC CENTROIDS
minNucArea = 100;
maxNucArea = 1000;
[clusterLabel,totalLabels] = bwlabel(nucMask,4);
allStats = regionprops(clusterLabel,'Area','PixelIdxList','Centroid');
nucCentroids = zeros(size(nucMask));
for i=1:totalLabels
    if allStats(i,1).Area > minNucArea && allStats(i,1).Area < maxNucArea

nucCentroids(round(allStats(i,1).Centroid(2)),round(allStats(i,1).Centroid(1)
)) = 1;
    end
end

% DETERMINE NUMBER NUCLEI IN EACH ACTIN CLUSTER
[objects, totalObjects] = bwlabel(cell, 4);
stats = regionprops(objects,'Area','PixelIdxList');
clusterNucArray = zeros(totalObjects,3);
for i=1:totalObjects
    clusterMask = zeros(size(threshCellImg));
    clusterMask(stats(i,1).PixelIdxList) = 1;
    clusterNuc = nucCentroids .* clusterMask;
    nucCount = sum(sum(clusterNuc));
    if nucCount == 0
        cell(stats(i,1).PixelIdxList) = 0;
    else
        clusterNucArray(i,1) = i;
        clusterNucArray(i,2) = stats(i,1).Area;
        clusterNucArray(i,3) = nucCount;
    end
end

% CALCULATE OUTPUTS
totalClusters = totalObjects - sum(clusterNucArray(:,1)==0);
nucCount = sum(sum(clusterNucArray(:,3)));
cellPerCluster = nucCount ./ totalClusters;
cellArea = sum(sum(cell));
aveCellArea = cellArea ./ nucCount;
output = length(clusterNucArray);

% OUTPUT THRESHOLDED CELL IMAGE
imwrite(cell,strcat(cellFilename(1:end-4),'_threshCellImg.tif'),'TIFF')
end
```

Cell Patterning Analysis of Matrix Displacements and Cell Morphology

```
function [ output_args ] = cptracker2( rootFilename, positionCount, threshVal
)
%CELL PATTERNING QUANTIFICATION
%   this function will input TrackMate file from ImageJ

%--------------------------------------------------------------------------
% INITIALIZE
well_size = 500; %microns
pixel_size = 0.624; %microns per pixel
pixels = 1024; %x/y pixels per image

fibFilename = strcat(rootFilename,positionCount,'_t01c1_ORG.tif');
well_pixel = well_size ./ pixel_size; %well size in pixels
figure, h_im = imshow(fibFilename);
h = imellipse(gca, [100, 100, well_pixel, well_pixel]); wait(h);
wc = getPosition(h); wv = getVertices(h);
well_mask = createMask(h, h_im);
close all;

% IMPORT TRACKMATE FILE FROM IMAGEJ
trackFilename = strcat(rootFilename,positionCount,'_beadstack_Tracks.xml');
[tracks, md] = importTrackMateTracks(trackFilename);
numTrack = length(tracks);
save(strcat(rootFilename,positionCount,'_tracks.mat'),'tracks');

%--------------------------------------------------------------------------
% FIND CELL CENTROID TO DETERMINE BEAD DISTANCES FROM CELL
% IMPUT CELL IMAGE, FILL, AND REMOVE BACKGROUND NOISE
cellFilename = strcat(rootFilename,positionCount,'_t01c2_ORG.tif');
cell = imgopen(cellFilename);
cell_mask = well_mask .* cell;
cell_mask = imbinarize(cell_mask,threshVal);
[clusterLabel, totalLabels] = bwlabel(cell_mask, 4);
allStats = regionprops(clusterLabel, 'Area', 'PixelIdxList');
for i = 1:totalLabels
```

```
    if allStats(i,1).Area < 200 %GET RID OF NOISE
        cell_mask(allStats(i,1).PixelIdxList) = 0;
    end
end
cell_mask = imfill(cell_mask, 'holes');
cell_mask = bwmorph(cell_mask, 'spur');
[objects, totalObjects] = bwlabel(cell_mask, 4);
centroid = cell2mat(struct2cell(regionprops(objects, 'Centroid')));
centroid = centroid .* pixel_size;
save(strcat(rootFilename,positionCount,'_centroid.mat'),'centroid');

% CALCULATE X AND Y DISPLACEMENT BETWEEN INITIAL AND FINAL TIMEPOINT
beadArray = zeros(length(tracks),4);
for i = 1:numTrack
    trackLength = length(tracks{i,1});
    beadArray(i,1) = (tracks{i,1}(1,2));
    beadArray(i,2) = ((pixels.*pixel_size) - tracks{i,1}(1,3));
    beadArray(i,3) = (tracks{i,1}(trackLength,2) - tracks{i,1}(1,2));
    beadArray(i,4) = (tracks{i,1}(1,3) - tracks{i,1}(trackLength,3));
end
save(strcat(rootFilename,positionCount,'_beadArray.mat'),'beadArray');

% QUANTIFICATION OF BEAD DISPLACEMENT (FINAL - INITIAL)
beadStats = zeros(numTrack,2);
for i=1:numTrack
    beadStats(i,1) = sqrt((beadArray(i,1)-centroid(1)).^2 + (beadArray(i,2)-
centroid(2)).^2); %distance from cell
    beadStats(i,2) = sqrt((beadArray(i,3)).^2 + (beadArray(i,4)).^2); %bead
displacement
end
save(strcat(rootFilename,positionCount,'_beadStats.mat'),'beadStats');

% CALCULATE X AND Y COMPONENT OF MAXIMUM DISPLACEMENT
beadArrayMax = zeros(length(tracks),4);
for i = 1:numTrack
    trackLength = length(tracks{i,1});
    beadArrayMax(i,1) = (tracks{i,1}(1,2));
    beadArrayMax(i,2) = ((pixels.*pixel_size) - tracks{i,1}(1,3));
    dispArray = zeros(trackLength,2);
    for j = 1:trackLength-1
        dispLength = sqrt((tracks{i,1}(j+1,2)-tracks{i,1}(1,2)).^2 +
(tracks{i,1}(j+1,3)-tracks{i,1}(1,3)).^2);
        dispArray(j,1) = j+1;
        dispArray(j,2) = dispLength;
    end
    [dispMax,dispIndex] = max(dispArray(:,2));
    beadArrayMax(i,3) = (tracks{i,1}(dispIndex+1,2) - tracks{i,1}(1,2));
    beadArrayMax(i,4) = (tracks{i,1}(1,3) - tracks{i,1}(dispIndex+1,3));
end
save(strcat(rootFilename,positionCount,'_beadArrayMax.mat'),'beadArrayMax');

% QUANTIFICATION OF BEAD DISPLACEMENT (MAX DISPLACEMENT)
beadStatsMax = zeros(numTrack,2);
for i=1:numTrack
    beadStatsMax(i,1) = sqrt((beadArrayMax(i,1)-centroid(1)).^2 +
(beadArrayMax(i,2)-centroid(2)).^2); %distance from cell
```

```
    beadStatsMax(i,2) = sqrt((beadArrayMax(i,3)).^2 +
(beadArrayMax(i,4)).^2); %bead displacement
end
save(strcat(rootFilename,positionCount,'_beadStatsMax.mat'),'beadStatsMax');

% QUANTIFY AVERAGE AND MAX BEAD DISPLACEMENT FOR EACH FRAME
aveDispFrame = zeros(trackLength-1,2);
maxDispFrame = zeros(trackLength-1,2);
for frame=1:trackLength-1
    aveDispFrame(frame,1) = frame+1;
    maxDispFrame(frame,1) = frame+1;
    dispArray = zeros(numTrack,1);
    for bead=1:numTrack
        dispLength = sqrt((tracks{bead,1}(frame+1,2)-
tracks{bead,1}(frame,2)).^2 + (tracks{bead,1}(frame+1,3)-
tracks{bead,1}(frame,3)).^2);
        dispArray(bead,1) = dispLength;
    end
    aveDispFrame(frame,2) = mean(dispArray);
    maxDispFrame(frame,2) = max(dispArray);
end

%--------------------------------------------------------------------------
% QUANTIFY CELL MORPHOLOGY OVER TIME
cellArray = zeros(trackLength,8);
cellOut = 'cell morphology';
mkdir(cellOut);
for timeCount=1:trackLength
    locNum = 0;
    if timeCount <= 9
        locNum = strcat('0',num2str(timeCount));
    else
        locNum = num2str(timeCount);
    end

    cellFilename =
strcat(rootFilename,positionCount,'_t',locNum,'c2_ORG.tif');
    cell = im2bw(double(mat2gray(imread(cellFilename))),threshVal);
    cell = bwareaopen(cell,400);
    cell = imfill(cell, 'holes');
    cell = bwmorph(cell, 'spur');
    cell_mask = cell;

    [cellLabel, totalLabels] = bwlabel(cell_mask, 4);

    while totalLabels > 1
       cellStats = regionprops(cellLabel, 'Area', 'PixelIdxList');
       [maxArea,index] = max(vertcat(cellStats.Area));
       cell_mask = zeros(pixels,pixels);
       cell_mask(cellStats(index,1).PixelIdxList) = 1;
       [cellLabel, totalLabels] = bwlabel(cell_mask,4);
    end

    cellStats = regionprops(cellLabel, 'Area', 'Centroid', 'Eccentricity',
'MajorAxisLength', 'MinorAxisLength', 'Orientation', 'Centroid');
```

```
    cellArray(timeCount,1) = timeCount;
    cellArray(timeCount,2) = cellStats.Centroid(1,1);
    cellArray(timeCount,3) = cellStats.Centroid(1,2);
    cellArray(timeCount,4) = cellStats.Area;
    cellArray(timeCount,5) = cellStats.Eccentricity;
    cellArray(timeCount,6) = cellStats.MajorAxisLength;
    cellArray(timeCount,7) = cellStats.MinorAxisLength;
    cellArray(timeCount,8) = cellStats.Orientation;

    cd(cellOut);
    imwrite(cell_mask,
strcat(rootFilename,positionCount,'_t',locNum,'_threshCellImage.tif'),'Compre
ssion','none');
    cd('..\');
end
save(strcat(rootFilename,positionCount,'_cellArray.mat'),'cellArray');

%---------------------------------------------------------------------------
% OUTPUT BEAD DISPLACEMENT DATA
beadOut = 'bead displacement';
mkdir(beadOut);
cd(beadOut);
headers = {'Distance from Cell' 'Bead Displacement'};

experiment_title = strcat(rootFilename,positionCount,'_finalDisp_beadquant');
xlswrite(strcat(experiment_title,'.xls'),headers,1,'A1');
xlswrite(strcat(experiment_title,'.xls'),beadStats,1,'A2');

experiment_title = strcat(rootFilename,positionCount,'_maxDisp_beadquant');
xlswrite(strcat(experiment_title,'.xls'),headers,1,'A1');
xlswrite(strcat(experiment_title,'.xls'),beadStatsMax,1,'A2');

headers = {'Frame' 'Average Bead Displacement'};
experiment_title =
strcat(rootFilename,positionCount,'_avePerFrame_beadquant');
xlswrite(strcat(experiment_title,'.xls'),headers,1,'A1');
xlswrite(strcat(experiment_title,'.xls'),aveDispFrame,1,'A2');

headers = {'Frame' 'Max Bead Displacement'};
experiment_title =
strcat(rootFilename,positionCount,'_maxPerFrame_beadquant');
xlswrite(strcat(experiment_title,'.xls'),headers,1,'A1');
xlswrite(strcat(experiment_title,'.xls'),maxDispFrame,1,'A2');
cd('..\');


% OUTPUT CELL MORPHOLOGY DATA
cd(cellOut);
headers = {'Time' 'Centroid X Pos' 'Centroid Y Pos' 'Area' 'Eccentricity'
'MajorAxisLength' 'MinorAxisLength' 'Orientation'};
experiment_title = strcat(rootFilename,positionCount,'_cellmorphologyquant');
xlswrite(strcat(experiment_title,'.xls'),headers,1,'A1');
xlswrite(strcat(experiment_title,'.xls'),cellArray,1,'A2');
```

```
% MAKE COLOR-CODED QUIVER PLOT (MAX DISPLACEMENT + MAX CELL AREA OUTLINE)
figure;
title([rootFilename,positionCount]);
set(gcf,'Position',[0,0,pixels,pixels]);
quiverc(beadArrayMax(:,1), beadArrayMax(:,2), beadArrayMax(:,3),
beadArrayMax(:,4));
axis([0, pixels.*pixel_size, 0, pixels.*pixel_size]);
pbaspect([1,1,1]);
[maxArea,maxIndex] = max(cellArray(:,4));
    if maxIndex <= 9
        maxIndex = strcat('0',num2str(maxIndex));
    else
        maxIndex = num2str(maxIndex);
    end
max_cell =
imin(strcat(rootFilename,positionCount,'_t',maxIndex,'_threshCellImage.tif'))
;
outline = bwboundaries(max_cell);
outline{1,1} = outline{1,1} .* pixel_size;
hold on;
outlineSize = size(outline);
number = outlineSize(1,1);
for i=1:number
    outline{i}(:,1) = pixels.*pixel_size - outline{i}(:,1);
    plot(outline{i}(:,2),outline{i}(:,1),'w','LineWidth',3);
end
image = getframe(gcf);
cd('../');
imwrite(image.cdata,
strcat(rootFilename,positionCount,'_beadvector.tif'),'Compression','none');

end
```

Single Cell Displacement Radial Projection

```
% CELL PATTERNING RADIAL PROJECTION
%---------------------------------------------------------------------------
% INITIALIZE
clear;clc;

root = 'cp61_lowdensity-Scene-';
count = 0;

for i = [1,3]
    count = count + 1;
    if i <= 9
        refNum = strcat('0',num2str(i));
    else
        refNum = num2str(i);
    end

    folder = strcat(root,refNum);
    cd(folder);
    load(strcat(root,refNum,'_beadArrayMax.mat'));
    load(strcat(root,refNum,'_beadStatsMax.mat'));
    load(strcat(root,refNum,'_centroid.mat'));
    load(strcat(root,refNum,'_cellArray.mat'));
    cd('../');

    pixels = 1024;
    pixelSize = 0.624;
    beads = length(beadArrayMax);
    beadStats = zeros(beads,3);

    %-------------------------------------------------------------------------
    % QUANTIFY BEAD DISPLACEMENT AND DISTANCE FROM CELL CENTROID
    for i = 1:beads
        if beadStatsMax(i,1) > 250
            beadStatsMax(i,1) = 250;
        end
    end
    beadStats(:,1) = beadStatsMax(:,1);
    beadStats(:,3) = beadStatsMax(:,2);

    %-------------------------------------------------------------------------
    % QUANTIFY CELL LONG AXIS ANGLE AND QUANTIFY RELATIVE BEAD DISPLACEMENT
AND
    % ANGLE
    cellArea = cellArray(:,4);
    maxFrame = find(cellArea == max(cellArea));
    cellAngle = cellArray(maxFrame,8);
    cellAngle = cellAngle(1);

    for i = 1:beads
        a = [centroid(2), pixels.*pixelSize];              % a is arbitrary
point even with cell centroid to define 0 degrees
        b = [centroid(1), centroid(2)];                    % b is cell
centroid
        c = [beadArrayMax(i,1), beadArrayMax(i,2)];        % c is bead
position
        ba = a-b; bc = c-b;
        ba_mag = norm(ba); bc_mag = norm(bc);
        theta = acosd(dot(ba,bc)/(ba_mag*bc_mag));

        if c(1) > b(1)                                      % if bead is
below cell, adjust theta value
            theta = 360 - theta;
        end

        if cellAngle > 0
            if theta < cellAngle
                theta_adjusted = 360 - (cellAngle - theta);
            else
                theta_adjusted = theta - cellAngle;
            end
        else
            thetaNeg = theta - 360;
            if thetaNeg > cellAngle
```

```
                theta_adjusted = thetaNeg - cellAngle;
            else
                theta_adjusted = theta - cellAngle;
            end
        end
        beadStats(i,2) = theta_adjusted;
    end

    n = 7;
    R = linspace(0,250,n);
    A = linspace(0,360,n);
    bin = zeros(beads,2);
    bin(:,1) = discretize(beadStats(:,1),R);
    bin(:,2) = discretize(beadStats(:,2),A);

    displacement = zeros(n,n);
    counter = 0;
    disp = 0;
    for i=1:n
        for j=1:n
            for k=1:beads
                if bin(k,1) == i
                    if bin(k,2) == j
                        counter = counter + 1;
                        disp = disp + beadStats(k,3);
                    end
                end
            end
            displacement(i,j) = disp ./ counter;
            counter = 0;
            disp = 0;
        end
    end
    figure
    colormap('jet');
    [h,c]=polarPcolor(R,A,displacement);
    displacementAll(:,:,count) = displacement;
end
save(strcat(root(1:end-7),'_radialprojData.mat'),'displacementAll');
```

Calcium Signaling Analysis

```
%% ===========================================================================
% WORKSPACE INITIALIZATION

close all;
clear all;

%% ===========================================================================
% DIRECTORY INITIALIZATION

% EXPORT FILES AS AVI BEFORE RUNNING CODE %

% Specify image directory.
% Set of files should be stored in one folder.
% All file names should have the same # of characters.
[filename, pathname, filterIndex] = uigetfile('*.*', 'Open Image');
cd(pathname);
direct=dir;              % Initialize current directory
% create output directery
dirOut = 'calciumQuant';
mkdir(dirOut);

%% Hard coded variables
pixelSize = 0.624;  %micron/pixel
                    % Axiocam 503 Parameters at 10x:
                    % 1x1 = 0.454
                    % 2x2 = 0.908
                    % 3x3 = 1.362
                    % 4x4 = 1.816
                    % 4x4 @ 40x = 0.709

%% ==========================================================================
% Save File Info Initiation
saveFileNameRoot = 'Calcium Imaging_';


% establish excel file for outputs
% cd(dirOut);
% dataOut = 'excel_data';
% mkdir(dataOut);
% cd(dataOut);




%% ==========================================================================

n=1; % Counter for each file in directory, includes non-image files
count=1; % Counter for analyzed images, max(j) = # images in folder


for m=1:length(dir)             % FOR each file in directory @ cd
    cd(pathname)
    if direct(m).bytes < 1000000   % Filter based on filesize
        n=n+1;                  % Skip small files (headers & text)
    else                        % Continue if large enough to be an image
        button = 1;
        raw = VideoReader(direct(m).name); % Read video
        file = raw.Name;
        numFrames = raw.NumberOfFrames;
        frameRate = raw.FrameRate;
        time = raw.Duration;

        saveFileName = strcat(saveFileNameRoot,file(1:end-4),'.xls');
        headers = {'Cell Number','Centroid X','Centroid Y','Num Peaks','Mean
Peak Diff','STD Peak Diff',...
            'Pulse Rate','Pulse PerTime'};
        xlswrite(saveFileName,headers,1,'A1');
        rateInverse = 1/frameRate;
        t = [];
        t = 0:rateInverse:numFrames*rateInverse-rateInverse;

        frameMean = [];
        frames = [];
        for s = 1:numFrames
            video = read(raw,s);
            video = imgaussfilt(video);
            frames(:,:,s) = video(:,:,2); %only care about the green channel
            frameMean(s) = mean2(frames(:,:,s));
        end

        disp(file)
        regionNum = input('How many cells wouold you like to analyze?')

%% Pick cells to measure
% Pick two regions perp to fiber alignment then two parallel.
        centroid = zeros(regionNum,2);
        for rectNum = 1:regionNum
            figure(2);   imshow(frames(:,:,1),[]);     %Display raw frame
with max intensity

            rect = imrect;      % If 5 regions, last region should be area
with no beating for normalization
            imgRect = wait(rect);
            imgRectRound{rectNum} = floor(imgRect);
            rectMat{rectNum} =
zeros(imgRectRound{rectNum}(3),imgRectRound{rectNum}(4),numFrames);
            centroid(rectNum,1:2) =
[imgRect(1)+imgRect(3)/2,imgRect(2)+imgRect(4)/2];

            %Make new matrix containing only chosen area
            for n = 1:numFrames
                for x = 1:imgRectRound{rectNum}(3)
                    for y = 1:imgRectRound{rectNum}(4)

                        rectMat{rectNum}(x,y,n) =
frames((imgRectRound{rectNum}(2)+y),(imgRectRound{rectNum}(1)+x),n);

                    end
                end
            end
        end



        %Find mean intensity in rect in each frame and normalize to
        %nonbeating region (if chosen).
        minVal = zeros(regionNum);
        for k = 1:regionNum % first two regions for perp CV and second two
regions for par CV.
```

```
            for slice = 1:numFrames
                meanIntensity{k}(slice) = mean2(rectMat{k}(:,:,slice));

            end

            minVal(k) = min(meanIntensity{k});
            normInt{k} = meanIntensity{k}./minVal(k);


            time = [0:1/frameRate:numFrames*(1/frameRate)];
            time = time(2:end);

            if length(normInt{k}) ~= numFrames
                normInt{k} = normInt{k}(1:numFrames);
            end

            %Plot time vs. mean intensity
            figure(3)
            plot(time,normInt{k})
            hold on
            title('Calcium Transients')
            xlabel('Time (sec)')
            ylabel('Fluorescence Intensity (A.U.)')
            xlim([0 time(numFrames)])
%             [xPoint,yPoint] = ginput(); %click on peaks and press enter
when done if findPeaks doesn't work well (i.e. data is noisy)

            [pkVals,pkLocs]  = findpeaks(normInt{k},'MinPeakProminence',0.2);
            peaks{k} = pkLocs;

            peakTime{k} = peaks{k}./frameRate; %convert frame to time.

            %Difference between each peak
            numPeaks(k) = length(peaks{k});
            centroidx(k) = centroid(k,1);
            centroidy(k) = centroid(k,2);
            peakDiff{k} = diff(peakTime{k});
            meanPeakDiff(k) = mean(peakDiff{k});  %Mean time between peaks
            stdPeakDiff(k) = std(peakDiff{k});
            pulseRate(k) = 1/meanPeakDiff(k);


            %Filter data via Savitsky-Golay Filtering
            sgFilt{k} = sgolayfilt(normInt{k},7,21);

        end
        centroidx = centroidx'; centroidy = centroidy';
        hold off

%% Plot filter data and save raw data to csv
        rawDataOut = time';
        for plotNum = 1:regionNum
            figure(4)
            plot(t,sgFilt{plotNum})
            hold on
            title(strcat('Filtered Calcium Transients (Num Peaks = 
',num2str(numPeaks(k)),')'))
            xlabel('Time (sec)')
            ylabel('Fluorescence Intensit (A.U.)')
            xlim([0 time(numFrames)])

            [minFiltVal,minFiltValIndex] = min(sgFilt{plotNum}(10:end));
            [maxFiltVal,maxFiltValIndex] = max(sgFilt{plotNum}(10:end));
            filtPkThresh = (maxFiltVal(1) - minFiltVal(1))/4;

            [filtPkVals{plotNum},filtPkLocs]  = 
findpeaks(sgFilt{plotNum},'MinPeakProminence',filtPkThresh);
            peaksFilt{plotNum} = filtPkLocs;
            peakTimeFilt{plotNum} = peaksFilt{plotNum}./frameRate; %convert 
frame to time.

            plot(peakTimeFilt{plotNum},filtPkVals{plotNum},'ko')

            xpoint = []; %clear each time.
            [xPoint,yPoint,button] = ginput(); %click on peaks and press 
enter when done if findPeaks doesn't work well (i.e. data is noisy)

            if button == 1 %left click
                peakTimeFilt{plotNum} = xPoint; %use peaks that were cliked.
                % If new points chosen, outputs need to be updated as well.
                numPeaks(plotNum) = length(xPoint);
                peakDiff{plotNum} = []; % clear old peak diffs
                peakDiff{plotNum} = diff(peakTimeFilt{plotNum});
                meanPeakDiff(plotNum) = mean(peakDiff{plotNum});  %Mean time 
between peaks
                stdPeakDiff(plotNum) = std(peakDiff{plotNum});
                pulseRate(plotNum) = 1/meanPeakDiff(plotNum);
            else
                % if no peaks clicked, use peaks that were found above
            end


            normFiltData{plotNum} = sgFilt{plotNum}/minFiltVal(1);
            rawDataOut(:,plotNum+1) = normFiltData{plotNum}';
        end
        rawDataName = strcat('RawData_',file(1:end-4));
        xlswrite(rawDataName,rawDataOut,1,'A1');
        hold off



%% Output ============================================================

        cellNumVec = [];
        cellNumVec = [1:1:regionNum]';
        numPeaksT = numPeaks';
        meanPeakDiffT = meanPeakDiff';
        stdPeakDiffT = stdPeakDiff';
        pulseRateT = pulseRate';
        pulsePerTime = numPeaksT/time(end);

        %imwrite(pixelPeakNumColor,strcat(filename(1:end-
4),num2str(m),'_numBeatsMap.tif'),'TIFF')
        ALLDATA =
horzcat(cellNumVec,centroidx,centroidy,numPeaksT,meanPeakDiffT,stdPeakDiffT,.
..
            pulseRateT,pulsePerTime);
%          cd(dirOut);
        xlswrite(saveFileName,ALLDATA,1,'A2');

        count = count+1;
    end

    clearvars -except filename pathname filterIndex direct dirOut pixelSize
saveFileNameRoot n count


end
```

Bibliography

Abhilash, A. S., Baker, B. M., Trappmann, B., Chen, C. S., & Shenoy, V. B. (2014). Remodeling of fibrous extracellular matrices by contractile cells: Predictions from discrete fiber network simulations. *Biophysical Journal*, *107*(8), 1829–1840. https://doi.org/10.1016/j.bpj.2014.08.029

Abrams, G. A., Goodman, S. L., Nealey, P. F., Franco, M., & Murphy, C. J. (2000). Nanoscale topography of the basement membrane underlying the corneal epithelium of the rhesus macaque. *Cell and Tissue Research*, *299*(1), 39–46. https://doi.org/10.1007/s004410050004

Agasid, M. T., Comi, T. J., Saavedra, S. S., & Aspinwall, C. A. (2017). Enhanced temporal resolution with ion channel-functionalized sensors using a conductance-based measurement protocol. *Analytical Chemistry*, *89*(2), 1315–1322. https://doi.org/10.1021/acs.analchem.6b04226

Ahmed, T. A. E., Dare, E. V., & Hincke, M. (2008). Fibrin: A versatile scaffold for tissue engineering applications. *Tissue Engineering - Part B: Reviews*, *14*(2), 199–215. https://doi.org/10.1089/ten.teb.2007.0435

Alisafaei, F., Chen, X., Leahy, T., Janmey, P. A., & Shenoy, V. B. (2021). Long-range mechanical signaling in biological systems. *Soft Matter*, *17*(2), 241–253. https://doi.org/10.1039/d0sm01442g

Arora, P. D., Narani, N., & McCulloch, C. A. G. (1999). The compliance of collagen gels regulates transforming growth factor-β induction of α-smooth muscle actin in fibroblasts. *American Journal of Pathology*, *154*(3), 871–882. https://doi.org/10.1016/S0002-9440(10)65334-5

Asahara, T., Murohara, T., Sullivan, A., Silver, M., van der Zee, R., Li, T., Witzenbichler, B., Schatteman, G., & Isner, J. M. (1997). Isolation of Putative Progenitor Endothelial Cells for Angiogenesis. *Science*, *275*(5302), 964–967. https://doi.org/10.1126/science.275.5302.964

Auger, F. A., Gibot, L., & Lacroix, D. (2013). The Pivotal Role of Vascularization in Tissue Engineering. *Annual Review of Biomedical Engineering*, *15*(1), 177–200. https://doi.org/10.1146/annurev-bioeng-071812-152428

Baker, B. M., & Chen, C. S. (2012). Deconstructing the third dimension: how 3D culture microenvironments alter cellular cues. *Journal of Cell Science*, *125*(Pt 13), 3015–3024.

https://doi.org/10.1242/jcs.079509

Baker, B. M., Gee, A. O., Metter, R. B., Nathan, A. S., Marklein, R. A., Burdick, J. A., & Mauck, R. L. (2008). The potential to improve cell infiltration in composite fiber-aligned electrospun scaffolds by the selective removal of sacrificial fibers. *Biomaterials*, *29*(15), 2348–2358. https://doi.org/10.1016/j.biomaterials.2008.01.032

Baker, B. M., Trappmann, B., Wang, W. Y., Sakar, M. S., Kim, I. L., Shenoy, V. B., Burdick, J. A., & Chen, C. S. (2015). Cell-mediated fibre recruitment drives extracellular matrix mechanosensing in engineered fibrillar microenvironments. *Nature Materials*, *14*(12), 1262–1268. https://doi.org/10.1038/nmat4444

Balaban, N. Q., Schwarz, U. S., Riveline, D., Goichberg, P., Tzur, G., Sabanay, I., Mahalu, D., Safran, S., Bershadsky, A., Addadi, L., & Geiger, B. (2001). Force and focal adhesion assembly: a close relationship studied using elastic micropatterened substrates. *Nature Cell Biology*, *3*, 466–472.

Balestrini, J. L., Chaudhry, S., Sarrazy, V., Koehler, A., & Hinz, B. (2012). The mechanical memory of lung myofibroblasts. *Integrative Biology*, *4*(4), 410–421. https://doi.org/10.1039/c2ib00149g

Ban, E., Franklin, J. M., Nam, S., Smith, L. R., Wang, H., Wells, R. G., Chaudhuri, O., Liphardt, J. T., & Shenoy, V. B. (2018). Mechanisms of Plastic Deformation in Collagen Networks Induced by Cellular Forces. *Biophysical Journal*, *114*(2), 450–461. https://doi.org/10.1016/j.bpj.2017.11.3739

Baranski, J. D., Chaturvedi, R. R., Stevens, K. R., Eyckmans, J., Carvalho, B., Solorzano, R. D., Yang, M. T., Miller, J. S., Bhatia, S. N., & Chen, C. S. (2013). Geometric control of vascular networks to enhance engineered tissue integration and function. *Proceedings of the National Academy of Sciences*, *110*(19), 7586–7591. https://doi.org/10.1073/pnas.1217796110

Barocas, V. H., & Tranquillo, R. T. (1997). An anisotropic biphasic theory of tissue-equivalent mechanics: the interplay among cell traction, fibrillar network deformation, fibril alignment, and cell contact guidance. *Journal of Biomechanical Engineering*, *119*(2), 137–145. https://doi.org/10.1115/1.2796072

Bayless, K. J., Salazar, R., & Davis, G. E. (2000). RGD-Dependent Vacuolation and Lumen Formation Observed during Endothelial Cell Morphogenesis in Three-Dimensional Fibrin Matrices Involves the αvβ3 and α5β1 Integrins. *The American Journal of Pathology*, *156*(5), 1673–1683. https://doi.org/10.1016/S0002-9440(10)65038-9

Beamish, J. A., Juliar, B. A., Cleveland, D. S., Busch, M. E., Nimmagadda, L., & Putnam, A. J. (2019). Deciphering the relative roles of matrix metalloproteinase- and plasmin-mediated matrix degradation during capillary morphogenesis using engineered hydrogels. *Journal of Biomedical Materials Research - Part B Applied Biomaterials*. https://doi.org/10.1002/jbm.b.34341

Beier, J. P., Klumpp, D., Rudisile, M., Dersch, R., Wendorff, J. H., Bleiziffer, O., Arkudas, A., Polykandriotis, E., Horch, R. E., & Kneser, U. (2009). Collagen matrices from sponge to nano: New perspectives for tissue engineering of skeletal muscle. *BMC Biotechnology*, *9*, 1–14. https://doi.org/10.1186/1472-6750-9-34

Bell, S. E., Mavila, A., Salazar, R., Bayless, K. J., Kanagala, S., Maxwell, S. A., & Davis, G. E. (2001). Differential gene expression during capillary morphogenesis in 3D collagen matrices: regulated expression of genes involved in basement membrane matrix assembly, cell cycle progression, cellular differentiation and G-protein signaling. *Journal of Cell Science*, *114*(15), 2755–2773. https://doi.org/10.1074/jbc.273.33.20992

Ben-Shaul, S., Landau, S., Merdler, U., & Levenberg, S. (2019). Mature vessel networks in engineered tissue promote graft–host anastomosis and prevent graft thrombosis. *Proceedings of the National Academy of Sciences*, *116*(8), 2955–2960. https://doi.org/10.1073/pnas.1814238116

Benton, J. A., Fairbanks, B. D., & Anseth, K. S. (2009). Characterization of valvular interstitial cell function in three dimensional matrix metalloproteinase degradable PEG hydrogels. *Biomaterials*, *30*(34), 6593–6603. https://doi.org/10.1016/j.biomaterials.2009.08.031

Bershadsky, A. D., Balaban, N. Q., & Geiger, B. (2003). Adhesion-dependent cell mechanosensitivity. *Annual Review of Cell and Developmental Biology*, *19*(1), 677–695. https://doi.org/10.1146/annurev.cellbio.19.111301.153011

Bishop, J. R., Schuksz, M., & Esko, J. D. (2007). Heparan sulphate proteoglycans fine-tune mammalian physiology. *Nature*, *446*(7139), 1030–1037. https://doi.org/10.1038/nature05817

Bonnans, C., Chou, J., & Werb, Z. (2014). Remodelling the extracellular matrix in development and disease. *Nature Reviews Molecular Cell Biology*, *15*(12), 786–801. https://doi.org/10.1038/nrm3904

Borteh, H. M., Gallovic, M. D., Sharma, S., Peine, K. J., Miao, S., Brackman, D. J., Gregg, K., Xu, Y., Guo, X., Guan, J., Bachelder, E. M., & Ainslie, K. M. (2013). Electrospun acetalated dextran scaffolds for temporal release of therapeutics. *Langmuir*, *29*(25), 7957–7965. https://doi.org/10.1021/la400541e

Brown, G. C. J., Lim, K. S., Farrugia, B. L., Hooper, G. J., & Woodfield, T. B. F. (2017a). Covalent incorporation of heparin improves chondrogenesis in photocurable gelatin-methacryloyl hydrogels. *Macromolecular Bioscience*, *17*(12), 1–13. https://doi.org/10.1002/mabi.201700158

Brown, T. E., Marozas, I. A., & Anseth, K. S. (2017b). Amplified Photodegradation of Cell-Laden Hydrogels via an Addition–Fragmentation Chain Transfer Reaction. *Advanced Materials*, *29*(11), 1605001. https://doi.org/10.1002/adma.201605001

Browning, A. C., Dua, H. S., & Amoaku, W. M. (2008). The effects of growth factors on the proliferation and in vitro angiogenesis of human macular inner choroidal endothelial cells.

British Journal of Ophthalmology, *92*(7), 1003–1008. https://doi.org/10.1136/bjo.2007.127670

Buckley, C. D., Pilling, D., Lord, J. M., Akbar, A. N., Scheel-Toellner, D., & Salmon, M. (2001). Fibroblasts regulate the switch from acute resolving to chronic persistent inflammation. *Trends in Immunology*, *22*(4), 199–204. https://doi.org/10.1016/S1471-4906(01)01863-4

Buxboim, A., Rajagopal, K., Brown, A. E. X., & Discher, D. E. (2010). How deeply cells feel: Methods for thin gels. *Journal of Physics Condensed Matter*, *22*, 194116. https://doi.org/10.1088/0953-8984/22/19/194116

Caliari, S. R., Perepelyuk, M., Cosgrove, B. D., Tsai, S. J., Lee, G. Y., Mauck, R. L., Wells, R. G., & Burdick, J. A. (2016a). Stiffening hydrogels for investigating the dynamics of hepatic stellate cell mechanotransduction during myofibroblast activation. *Scientific Reports*, *6*(August 2015), 1–10. https://doi.org/10.1038/srep21387

Caliari, S. R., Vega, S. L., Kwon, M., Soulas, E. M., & Burdick, J. A. (2016b). Dimensionality and spreading influence MSC YAP/TAZ signaling in hydrogel environments. *Biomaterials*, *103*, 314–323. https://doi.org/10.1016/j.biomaterials.2016.06.061

Califano, J. P., & Reinhart-King, C. A. (2008). A Balance of Substrate Mechanics and Matrix Chemistry Regulates Endothelial Cell Network Assembly. *Cellular and Molecular Bioengineering*, *1*(2–3), 122–132. https://doi.org/10.1007/s12195-008-0022-x

Califano, J. P., & Reinhart-King, C. A. (2010). Substrate stiffness and cell area predict cellular traction stresses in single cells and cells in contact. *Cellular and Molecular Bioengineering*, *3*(1), 68–75. https://doi.org/10.1007/s12195-010-0102-6

Chao, P.-H. G., Hsu, H. Y., & Tseng, H. Y. (2014). Electrospun microcrimped fibers with nonlinear mechanical properties enhance ligament fibroblast phenotype. *Biofabrication*, *6*(3). https://doi.org/10.1088/1758-5082/6/3/035008

Charras, G., & Sahai, E. (2014). Physical influences of the extracellular environment on cell migration. *Nature Reviews Molecular Cell Biology*, *15*(12), 813–824. https://doi.org/10.1038/nrm3897

Chaudhuri, O., Gu, L., Darnell, M., Klumpers, D., Bencherif, S. A., Weaver, J. C., Huebsch, N., & Mooney, D. J. (2015). Substrate stress relaxation regulates cell spreading. *Nature Communications*, *6*, 1–7. https://doi.org/10.1038/ncomms7365

Chaudhuri, O., Gu, L., Klumpers, D., Darnell, M., Bencherif, S. A., Weaver, J. C., Huebsch, N., Lee, H. P., Lippens, E., Duda, G. N., & Mooney, D. J. (2016). Hydrogels with tunable stress relaxation regulate stem cell fate and activity. *Nature Materials*, *15*(3), 326–334. https://doi.org/10.1038/nmat4489

Chen, F., Hayami, J. W. S., & Amsden, B. G. (2014). Electrospun poly(L-lactide-co-acryloyl carbonate) fiber scaffolds with a mechanically stable crimp structure for ligament tissue engineering. *Biomacromolecules*, *15*(5), 1593–1601. https://doi.org/10.1021/bm401813j

Chen, Y. C., Lin, R. Z., Qi, H., Yang, Y., Bae, H., Melero-Martin, J. M., & Khademhosseini, A. (2012). Functional human vascular network generated in photocrosslinkable gelatin methacrylate hydrogels. *Advanced Functional Materials*, *22*(10), 2027–2039. https://doi.org/10.1002/adfm.201101662

Chia, H. N., Vigen, M., & Kasko, A. M. (2012). Effect of substrate stiffness on pulmonary fibroblast activation by TGF-β. *Acta Biomaterialia*, *8*(7), 2602–2611. https://doi.org/10.1016/j.actbio.2012.03.027

Chua, A. W. C., Khoo, Y. C., Tan, B. K., Tan, K. C., Foo, C. L., & Chong, S. J. (2016). Skin tissue engineering advances in severe burns: review and therapeutic applications. *Burns & Trauma*, *4*(1), 3. https://doi.org/10.1186/s41038-016-0027-y

Claaßen, C., Southan, A., Grübel, J., Tovar, G. E. M., & Borchers, K. (2018). Interactions of methacryloylated gelatin and heparin modulate physico-chemical properties of hydrogels and release of vascular endothelial growth factor. *Biomedical Materials*, *13*(5). https://doi.org/10.1088/1748-605X/aacdb2

Clapham, D. E. (2007). Calcium Signaling. *Cell*, *131*(6), 1047–1058. https://doi.org/10.1016/j.cell.2007.11.028

Clark, E. R., & Clark, E. L. (1939). Microscopic observations on the growth of blood capillaries in the living mammal. *The American Journal of Anatomy*, *64*(2), 251–301.

Crocker, J. C., & Grier, D. G. (1996). Methods of digital video microscopy for colloidal studies. *Journal of Colloid and Interface Science*, *179*(1), 298–310. https://doi.org/10.1006/jcis.1996.0217

Crosby, C. O., & Zoldan, J. (2019). Mimicking the physical cues of the ECM in angiogenic biomaterials. *Regenerative Biomaterials*, *6*(2), 61–73. https://doi.org/10.1093/rb/rbz003

Czirok, A., & Little, C. D. (2012). Pattern formation during vasculogenesis. *Birth Defects Research Part C - Embryo Today: Reviews*, *96*(2), 153–162. https://doi.org/10.1002/bdrc.21010

Daly, A. C., Prendergast, M. E., Hughes, A. J., & Burdick, J. A. (2021). Bioprinting for the Biologist. *Cell*, *184*(1), 18–32. https://doi.org/10.1016/j.cell.2020.12.002

Darby, I. A., Skalli, O., & Gabbiani, G. (1990). α-Smooth muscle actin is transiently expressed by myofibroblasts during experimental wound healing. *Laboratory Investigation*, *63*(1), 21–29.

Davidson, C. D. C. D., Jayco, D. K. P. D. K. P., Matera, D. L. D. L., DePalma, S. J. S. J., Hiraki, H. L. H. L., Wang, W. Y. W. Y., & Baker, B. M. B. M. (2020a). Myofibroblast activation in synthetic fibrous matrices composed of dextran vinyl sulfone. *Acta Biomaterialia*, *105*, 78–86. https://doi.org/10.1016/j.actbio.2020.01.009

Davidson, C. D. C. D., Wang, W. Y. W. Y., Zaimi, I., Jayco, D. K. P. D. K. P., & Baker, B. M. B. M. (2019a). Cell force-mediated matrix reorganization underlies multicellular network assembly. *Scientific Reports*, *9*(1), 12. https://doi.org/10.1038/s41598-018-37044-1

Davidson, C. D., DePalma, S. J., Wang, W. Y., Kamen, J. L., Jayco, D. K. P., & Baker, B. M. (2021). Mechanical intercellular communication via matrix-borne cell force transmission during vascular network formation. *BioRxiv*, 2021.08.17.456669. https://www.biorxiv.org/content/10.1101/2021.08.17.456669v1%0Ahttps://www.biorxiv.org/content/10.1101/2021.08.17.456669v1.abstract

Davidson, C. D., Jayco, D. K. P., Matera, D. L., DePalma, S. J., Hiraki, H. L., Wang, W. Y., & Baker, B. M. (2020b). Myofibroblast activation in synthetic fibrous matrices composed of dextran vinyl sulfone. *Acta Biomaterialia*. https://doi.org/10.1016/j.actbio.2020.01.009

Davidson, C. D., Jayco, D. K. P., Wang, W. Y., Shikanov, A., & Baker, B. M. (2020c). Fiber crimp confers matrix mechanical nonlinearity, regulates endothelial cell mechanosensing, and promotes microvascular network formation. *Journal of Biomechanical Engineering*, *142*(11). https://doi.org/10.1115/1.4048191

Davidson, C. D., Wang, W. Y., Zaimi, I., Jayco, D. K. P., & Baker, B. M. (2019b). Cell force-mediated matrix reorganization underlies multicellular network assembly. *Scientific Reports*, *9*(1). https://doi.org/10.1038/s41598-018-37044-1

Davidson, M. D., Burdick, J. A., & Wells, R. G. (2020d). Engineered Biomaterial Platforms to Study Fibrosis. *Advanced Healthcare Materials*, *1901682*, 1901682. https://doi.org/10.1002/adhm.201901682

Davidson, M., Song, K., Lee, M. H., Llewellyn, J., Du, Y., Baker, B., Wells, R. G., Burdick, J. A., Lee, H., Llewellyn, J., Du, Y., Baker, B., Wells, R. G., & Burdick, J. A. (2019c). Engineered fibrous networks to investigate the influence of fiber mechanics on myofibroblast differentiation. *ACS Biomaterials Science & Engineering*, *5*(8), 3899–3908. https://doi.org/10.1021/acsbiomaterials.8b01276

Davis, G. E., & Bayless, K. J. (2003). An integrin and Rho GTPase-dependent pinocytic vacuole mechanism controls capillary lumen formation in collagen and fibrin matrices. *Microcirculation*, *10*(1), 27–44. https://doi.org/10.1038/sj.mn.7800175

Davis, G. E., Black, S. M., & Bayless, K. J. (2000). Capillary morphogenesis during human endothelial cell invasion of three-dimensional collagen matrices. *In Vitro Cellular & Developmental Biology - Animal*, *36*(8), 513–519. https://doi.org/10.1290/1071-2690(2000)036<0513:CMDHEC>2.0.CO;2

Davis, G. E., & Camarillo, C. W. (1995). Regulation of endothelial cell morphogenesis by integrins, mechanical forces, and matrix guidance pathways. In *Experimental Cell Research* (Vol. 216, Issue 1, pp. 113–123). Academic Press. https://doi.org/10.1006/excr.1995.1015

Davis, G. E., & Camarillo, C. W. (1996). An α2β1 integrin-dependent pinocytic mechanism involving intracellular vacuole formation and coalescence regulates capillary lumen and tube formation in three-dimensional collagen matrix. *Experimental Cell Research*, *224*(1), 39–51. https://doi.org/10.1006/excr.1996.0109

Day, J. R., David, A., Kim, J., Farkash, E. A., Cascalho, M., Milašinović, N., & Shikanov, A. (2018). The impact of functional groups of poly(ethylene glycol) macromers on the physical properties of photo-polymerized hydrogels and the local inflammatory response in the host. *Acta Biomaterialia*, *67*, 42–52. https://doi.org/10.1016/j.actbio.2017.12.007

Dejana, E. (2004). Endothelial cell-cell junctions: Happy together. In *Nature Reviews Molecular Cell Biology* (Vol. 5, Issue 4, pp. 261–270). Nature Publishing Group. https://doi.org/10.1038/nrm1357

Dembo, M., Oliver, T., Ishihara, A., & Jacobson, K. (1996). Imaging the traction stresses exerted by locomoting cells with the elastic substratum method. *Biophysical Journal*, *70*(4), 2008–2022. https://doi.org/10.1016/S0006-3495(96)79767-9

Dembo, M., & Wang, Y. L. (1999). Stresses at the cell-to-substrate interface during locomotion of fibroblasts. *Biophysical Journal*, *76*(4), 2307–2316. https://doi.org/10.1016/S0006-3495(99)77386-8

Denisin, A. K., & Pruitt, B. L. (2016). Tuning the Range of Polyacrylamide Gel Stiffness for Mechanobiology Applications. *ACS Applied Materials and Interfaces*, *8*(34), 21893–21902. https://doi.org/10.1021/acsami.5b09344

Depalma, S. J., Davidson, C. D., Stis, A. E., Helms, A. S., & Baker, B. M. (2021). Microenvironmental determinants of organized iPSC-cardiomyocyte tissues on synthetic fibrous matrices. *Biomaterials Science*, *9*(1), 93–107. https://doi.org/10.1039/d0bm01247e

Deroanne, C. F., Lapiere, C. M., & Nusgens, B. V. (2001). In vitro tubulogenesis of endothelial cells by relaxation of the coupling extracellular matrix-cytoskeleton. *Cardiovascular Research*, *49*(3), 647–658. https://doi.org/10.1016/S0008-6363(00)00233-9

Diamant, J., Keller, A., Baer, E., Litt, M., & Arridge, R. G. (1972). Collagen; ultrastructure and its relation to mechanical properties as a function of ageing. *Proceedings of the Royal Society of London. Series B. Biological Sciences*, *180*(60), 293–315. https://doi.org/10.1098/rspb.1972.0019

DiPietro, L. A. (2016). Angiogenesis and wound repair: when enough is enough. *Journal of Leukocyte Biology*, *100*(5), 979–984. https://doi.org/10.1189/jlb.4mr0316-102r

Discher, D. E., Janmey, P., & Wang, Y. (2005). Tissue cells feel and respond to the stiffness of their substrate. *Science*, *310*(5751), 1139–1143. https://doi.org/10.1126/science.1116995

Doyle, A. D., & Yamada, K. M. (2016). Mechanosensing via cell-matrix adhesions in 3D microenvironments. In *Experimental Cell Research* (Vol. 343, Issue 1, pp. 60–66). Academic Press Inc. https://doi.org/10.1016/j.yexcr.2015.10.033

Drake, C. J. (2003). Embryonic and adult vasculogenesis. In *Birth Defects Research (Part C)*

(Vol. 69, pp. 73–82). Wiley Subscription Services, Inc., A Wiley Company. https://doi.org/10.1002/bdrc.10003

Dull, T., Zufferey, R., Kelly, M., Mandel, R. J., Nguyen, M., Trono, D., & Naldini, L. (1998). A Third-Generation Lentivirus Vector with a Conditional Packaging System. *Journal of Virology*, *72*(11), 8463–8471. https://doi.org/10.1128/jvi.72.11.8463-8471.1998

Dupont, M., Souriant, S., Lugo-Villarino, G., Maridonneau-Parini, I., & Vérollet, C. (2018). Tunneling nanotubes: Intimate communication between myeloid cells. *Frontiers in Immunology*, *9*(JAN), 1–6. https://doi.org/10.3389/fimmu.2018.00043

Dupont, S., Morsut, L., Aragona, M., Enzo, E., Giulitti, S., Cordenonsi, M., Zanconato, F., Le Digabel, J., Forcato, M., Bicciato, S., Elvassore, N., & Piccolo, S. (2011). Role of YAP/TAZ in mechanotransduction. *Nature*, *474*(7350), 179–184. https://doi.org/10.1038/nature10137

Engler, A., Bacakova, L., Newman, C., Hategan, A., Griffin, M., & Discher, D. (2004). Substrate compliance versus ligand density in cell on gel responses. *Biophysical Journal*, *86*(1), 617–628. https://doi.org/10.1016/S0006-3495(04)74140-5

Engler, A. J., Sen, S., Sweeney, H. L., & Discher, D. E. (2006). Matrix elasticity directs stem cell lineage specification. *Cell*, *126*(4), 677–689. https://doi.org/10.1016/j.cell.2006.06.044

Fabry, B., Klemm, A. H., Kienle, S., Schäffer, T. E., & Goldmann, W. H. (2011). Focal adhesion kinase stabilizes the cytoskeleton. *Biophysical Journal*, *101*(9), 2131–2138. https://doi.org/10.1016/j.bpj.2011.09.043

Fiore, V. F., Hagood, J. S., Barker, T. H., Fiore, V. F., Wong, S. S., Tran, C., Tan, C., Xu, W., Sulchek, T., White, E. S., Hagood, J. S., & Barker, T. H. (2018). αvβ3 Integrin drives fibroblast contraction and strain stiffening of soft provisional matrix during progressive fibrosis. *JCI Insight*, *3*(20). https://doi.org/10.1172/jci.insight.97597

Frantz, C., Stewart, K. M., & Weaver, V. M. (2010). The extracellular matrix at a glance. *Journal of Cell Science*, *123*(24), 4195–4200. https://doi.org/10.1242/jcs.023820

Freiman, A., Shandalov, Y., Rozenfeld, D., Shor, E., Segal, S., Ben-David, D., Meretzki, S., Egozi, D., & Levenberg, S. (2016). Adipose-derived endothelial and mesenchymal stem cells enhance vascular network formation on three-dimensional constructs in vitro. *Stem Cell Research & Therapy*, *7*(5). https://doi.org/10.1186/s13287-015-0251-6

Fung, Y. C. (1967). Elasticity of soft tissues in simple elongation. *The American Journal of Physiology*, *213*(6), 1532–1544. https://doi.org/10.1152/ajplegacy.1967.213.6.1532

Gabbiani, G. (2003). The myofibroblast in wound healing and fibrocontractive diseases. *Journal of Pathology*, *200*(4), 500–503. https://doi.org/10.1002/path.1427

Gates, E. M., LaCroix, A. S., Rothenberg, K. E., & Hoffman, B. D. (2019). Improving Quality, Reproducibility, and Usability of FRET-Based Tension Sensors. *Cytometry Part A*, *95*(2), 201–213. https://doi.org/10.1002/cyto.a.23688

Geiger, B., Spatz, J. P., & Bershadsky, A. D. (2009). Environmental sensing through focal adhesions. *Nature Reviews Molecular Cell Biology*, *10*(1), 21–33. https://doi.org/10.1038/nrm2593

Gelain, F., Bottai, D., Vescovi, A., & Zhang, S. (2006). Designer self-assembling peptide nanofiber scaffolds for adult mouse neural stem cell 3-dimensional cultures. *PLoS One*, *1*(1), e119. https://doi.org/10.1371/journal.pone.0000119

Ghajar, C. M., Chen, X., Harris, J. W., Suresh, V., Hughes, C. C. W., Jeon, N. L., Putnam, A. J., & George, S. C. (2008). The effect of matrix density on the regulation of 3-D capillary morphogenesis. *Biophysical Journal*, *94*(5), 1930–1941. https://doi.org/10.1529/biophysj.107.120774

Goffin, J. M., Pittet, P., Csucs, G., Lussi, J. W., Meister, J. J., & Hinz, B. (2006). Focal adhesion size controls tension-dependent recruitment of α-smooth muscle actin to stress fibers. *Journal of Cell Biology*, *172*(2), 259–268. https://doi.org/10.1083/jcb.200506179

Gong, X., & Mills, K. L. (2018). Large-scale patterning of single cells and cell clusters in hydrogels. *Scientific Reports*, *8*(1), 3849. https://doi.org/10.1038/s41598-018-21989-4

Goren, S., Koren, Y., Xu, X., & Lesman, A. (2020). Elastic Anisotropy Governs the Range of Cell-Induced Displacements. *Biophysical Journal*, *118*(5), 1152–1164. https://doi.org/10.1016/j.bpj.2019.12.033

Grashoff, C., Hoffman, B. D., Brenner, M. D., Zhou, R., Parsons, M., Yang, M. T., McLean, M. A., Sligar, S. G., Chen, C. S., Ha, T., & Schwartz, M. A. (2010). Measuring mechanical tension across vinculin reveals regulation of focal adhesion dynamics. *Nature*, *466*(7303), 263–266. https://doi.org/10.1038/nature09198

Grecco, H. E., Schmick, M., & Bastiaens, P. I. H. (2011). Signaling from the living plasma membrane. *Cell*, *144*(6), 897–909. https://doi.org/10.1016/j.cell.2011.01.029

Griffith, C. K., Miller, C., Sainson, R. C. A., Calvert, J. W., Jeon, N. L., Hughes, C. C. W., & George, S. C. (2005). Diffusion Limits of an *in Vitro* Thick Prevascularized Tissue. *Tissue Engineering*, *11*(1–2), 257–266. https://doi.org/10.1089/ten.2005.11.257

Griffith, L. G., & Naughton, G. (2002). Tissue engineering--current challenges and expanding opportunities. *Science*, *295*(5557), 1009–1014.

Grigoryan, B., Paulsen, S. J., Corbett, D. C., Sazer, D. W., Fortin, C. L., Zaita, A. J., Greenfield, P. T., Calafat, N. J., Gounley, J. P., Ta, A. H., Johansson, F., Randles, A., Rosenkrantz, J. E., Louis-Rosenberg, J. D., Galie, P. A., Stevens, K. R., & Miller, J. S. (2019). Multivascular networks and functional intravascular topologies within biocompatible hydrogels. *Science*, *364*(6439), 458–464. https://doi.org/10.1126/science.aav9750

Grove, A. D., Prabhu, V. V, Young, B. L., Lee, F. C., Kulpa, V., Munson, P. J., & Kohn, E. C.

(2002). Both protein activation and gene expression are involved in early vascular tube formation in vitro. *Clinical Cancer Research*, *8*(9), 3019–3026. http://www.ncbi.nlm.nih.gov/pubmed/12231549

Grunewald, M., Avraham, I., Dor, Y., Bachar-Lustig, E., Itin, A., Yung, S., Chimenti, S., Landsman, L., Abramovitch, R., & Keshet, E. (2006). VEGF-induced adult neovascularization: Recruitment, retention, and role of accessory cells. *Cell*, *124*(1), 175–189. https://doi.org/10.1016/j.cell.2005.10.036

Guilak, F., Cohen, D. M., Estes, B. T., Gimble, J. M., Liedtke, W., & Chen, C. S. (2009). Control of stem cell fate by physical interactions with the extracellular matrix. In *Cell Stem Cell* (Vol. 5, Issue 1, pp. 17–26). Cell Press. https://doi.org/10.1016/j.stem.2009.06.016

Gumbiner, B. M. (1996). Cell adhesion: The molecular basis of tissue architecture and morphogenesis. In *Cell* (Vol. 84, Issue 3, pp. 345–357). Elsevier. https://doi.org/10.1016/S0092-8674(00)81279-9

Guo, C.-L., Ouyang, M., Yu, J.-Y., Maslov, J., Price, A., & Shen, C.-Y. (2012). Long-range mechanical force enables self-assembly of epithelial tubular patterns. *Proceedings of the National Academy of Sciences*, *109*, 5576–5582. https://doi.org/10.1073/pnas.1114781109

Guthold, M., Liu, W., Sparks, E. A., Jawerth, L. M., Peng, L., Falvo, M., Superfine, R., Hantgan, R. R., & Lord, S. T. (2007). A comparison of the mechanical and structural properties of fibrin fibers with other protein fibers. *Cell Biochemistry and Biophysics*, *49*(3), 165–181. https://doi.org/10.1007/s12013-007-9001-4

Hakkinen, K. M., Harunaga, J. S., Doyle, A. D., & Yamada, K. M. (2011). Direct comparisons of the morphology, migration, cell adhesions, and actin cytoskeleton of fibroblasts in four different three-dimensional extracellular matrices. *Tissue Engineering - Part A*, *17*(5–6), 713–724. https://doi.org/10.1089/ten.tea.2010.0273

Hall, M. S., Alisafaei, F., Ban, E., Feng, X., Hui, C., & Shenoy, V. B. (2016). Fibrous nonlinear elasticity enables positive mechanical feedback between cells and ECMs. *Proceedings of the National Academy of Sciences*, *113*(49), 14043–14048. https://doi.org/10.1073/pnas.1613058113

Ham, T. R., Collins, K. L., & Hoffman, B. D. (2019). Molecular tension sensors: moving beyond force. *Current Opinion in Biomedical Engineering*, *12*, 83–94. https://doi.org/10.1016/j.cobme.2019.10.003

Hanjaya-Putra, D., Bose, V., Shen, Y. I., Yee, J., Khetan, S., Fox-Talbot, K., Steenbergen, C., Burdick, J. A., & Gerecht, S. (2011). Controlled activation of morphogenesis to generate a functional human microvasculature in a synthetic matrix. *Blood*, *118*(3), 804–815. https://doi.org/10.1182/blood-2010-12-327338

Hausenloy, D. J., & Yellon, D. M. (2013). Myocardial ischemia-reperfusion injury: A neglected therapeutic target. *Journal of Clinical Investigation*, *123*(1), 92–100. https://doi.org/10.1172/JCI62874

Heintz, K. A., Bregenzer, M. E., Mantle, J. L., Lee, K. H., West, J. L., & Slater, J. H. (2016). Fabrication of 3D Biomimetic Microfluidic Networks in Hydrogels. *Advanced Healthcare Materials*, *5*(17), 2153–2160. https://doi.org/10.1002/adhm.201600351

Hiltner, A., Cassidy, J. J., & Baer, E. (1985). Mechanical properties of biological polymers. *Annual Review of Materials Science*, *15*, 455–482.

Hinz, B., Celetta, G., Tomasek, J. J., Gabbiani, G., & Chaponnier, C. (2001a). Alpha-smooth muscle actin expression upregulates fibroblast contractile activity. *Molecular Biology of the Cell*, *12*(9), 2730–2741. https://doi.org/10.1091/mbc.12.9.2730

Hinz, B., Mastrangelo, D., Iselin, C. E., Chaponnier, C., & Gabbiani, G. (2001b). Mechanical tension controls granulation tissue contractile activity and myofibroblast differentiation. *American Journal of Pathology*, *159*(3), 1009–1020. https://doi.org/10.1016/S0002-9440(10)61776-2

Hinz, B., Phan, S. H., Thannickal, V. J., Galli, A., Bochaton-Piallat, M. L., & Gabbiani, G. (2007). The myofibroblast: One function, multiple origins. *American Journal of Pathology*, *170*(6), 1807–1816. https://doi.org/10.2353/ajpath.2007.070112

Hinz, B., Phan, S. H., Thannickal, V. J., Prunotto, M., Desmoulire, A., Varga, J., De Wever, O., Mareel, M., & Gabbiani, G. (2012). Recent developments in myofibroblast biology: Paradigms for connective tissue remodeling. In *American Journal of Pathology* (Vol. 180, Issue 4, pp. 1340–1355). Elsevier. https://doi.org/10.1016/j.ajpath.2012.02.004

Hughes, A. J., Miyazaki, H., Coyle, M. C., Zhang, J., Laurie, M. T., Chu, D., Vavrušová, Z., Schneider, R. A., Klein, O. D., & Gartner, Z. J. (2018). Engineered Tissue Folding by Mechanical Compaction of the Mesenchyme. *Developmental Cell*, *44*(2), 165-178.e6. https://doi.org/10.1016/j.devcel.2017.12.004

Humphries, D. L., Grogan, J. A., & Gaffney, E. A. (2017). Mechanical Cell–Cell Communication in Fibrous Networks: The Importance of Network Geometry. *Bulletin of Mathematical Biology*. https://doi.org/10.1007/s11538-016-0242-5

Huveneers, S., Oldenburg, J., Spanjaard, E., van der Krogt, G., Grigoriev, I., Akhmanova, A., Rehmann, H., & Rooij, J. De. (2012). Vinculin associates with endothelial VE-cadherin junctions to control force-dependent remodeling. *Journal of Cell*, *196*(5), 641–652. https://doi.org/10.1083/jcb.201108120

Ingber, D. E. (2003). Mechanobiology and diseases of mechanotransduction. *Annals of Medicine*, *35*(8), 564–577. https://doi.org/10.1080/07853890310016333

Iwaki, T., Urano, T., & Umemura, K. (2012). PAI-1, progress in understanding the clinical problem and its aetiology. *British Journal of Haematology*, *157*(3), 291–298. https://doi.org/10.1111/j.1365-2141.2012.09074.x

Jansen, K. A., Atherton, P., & Ballestrem, C. (2017). Mechanotransduction at the cell-matrix interface. In *Seminars in Cell and Developmental Biology* (Vol. 71, pp. 75–83). Academic

Press. https://doi.org/10.1016/j.semcdb.2017.07.027

Järveläinen, H., Sainio, A., Koulu, M., Wight, T. N., & Penttinen, R. (2009). Extracellular matrix molecules: Potential targets in pharmacotherapy. *Pharmacological Reviews*, *61*(2), 198–223. https://doi.org/10.1124/pr.109.001289

Jiang, H., Fang, D., Hsiao, B. S., Chu, B., & Chen, W. (2004). Optimization and characterization of dextran membranes prepared by electrospinning. *Biomacromolecules*, *5*(2), 326–333. https://doi.org/10.1021/bm034345w

Kanchanawong, P., Shtengel, G., Pasapera, A. M., Ramko, E. B., Davidson, M. W., Hess, H. F., & Waterman, C. M. (2010). Nanoscale architecture of integrin-based cell adhesions. *Nature*, *468*(7323), 580–584. https://doi.org/10.1038/nature09621

Kandler, K., & Katz, L. C. (1998). Coordination of neuronal activity in developing visual cortex by gap junction-mediated biochemical communication. *Journal of Neuroscience*, *18*(4), 1419–1427. http://www.ncbi.nlm.nih.gov/entrez/query.fcgi?cmd=Retrieve&db=PubMed&dopt=Citation&list_uids=9454851

Kingston, R. E., Chen, C. A., & Rose, J. K. (2003). Calcium Phosphate Transfection. *Current Protocols in Molecular Biology*, *63*(1), 1–11. https://doi.org/10.1002/0471142727.mb0901s63

Klein, E. A., Yin, L., Kothapalli, D., Castagnino, P., Byfield, F. J., Xu, T., Levental, I., Hawthorne, E., Janmey, P. A., & Assoian, R. K. (2009). Cell-cycle control by physiological matrix elasticity and in vivo tissue stiffening. *Current Biology*, *19*(18), 1511–1518. https://doi.org/10.1016/j.cub.2009.07.069

Kluge, D., Abraham, F., Schmidt, S., Schmidt, H.-W. W., & Fery, A. (2010). Nanomechanical properties of supramolecular self-assembled whiskers determined by AFM force mapping. *Langmuir*, *26*(5), 3020–3023. https://doi.org/10.1021/la904780c

Kniazeva, E., & Putnam, A. J. (2009). Endothelial cell traction and ECM density influence both capillary morphogenesis and maintenance in 3-D. *American Journal of Physiology - Cell Physiology*, *297*(1), 179–187. https://doi.org/10.1152/ajpcell.00018.2009

Koh, W., Stratman, A. N., Sacharidou, A., & Davis, G. E. (2008). In Vitro Three Dimensional Collagen Matrix Models of Endothelial Lumen Formation During Vasculogenesis and Angiogenesis. *Methods in Enzymology*, *443*(08), 83–101. https://doi.org/10.1016/S0076-6879(08)02005-3

Koike, N., Fukumura, D., Gralla, O., Au, P., Schechner, J. S., & Jain, R. K. (2004). Creation of long-lasting blood vessels. *Nature*, *428*(6979), 138–139. https://doi.org/10.1038/428138a

Kubota, Y., Kleinman, H. K., Marin, G. R., and Lawley, T. J. (1988). Role of laminin and basement membrane in the morphological differentiation of human endothelial cells into capillary like structures. *Journal of Cell Biology*, *107*, 1589–1598.

https://doi.org/10.1083/jcb.107.4.1589

Kulangara, K., & Leong, K. W. (2009). Substrate topography shapes cell function. *Soft Matter*, *5*(21), 4072–4076. https://doi.org/10.1039/b910132m

Kumar, A., Placone, J. K., & Engler, A. J. (2017). Understanding the extracellular forces that determine cell fate and maintenance. *Development*, *144*(23), 4261–4270. https://doi.org/10.1242/dev.158469

Lake, S. P., Miller, K. S., Elliott, D. M., & Soslowsky, L. J. (2009). Effect of fiber distribution and realignment on the nonlinear and inhomogeneous mechanical properties of human supraspinatus tendon under longitudinal tensile loading. *Journal of Orthopaedic Research*, *27*(12), 1596–1602. https://doi.org/10.1002/jor.20938

Langer, R., & Vacanti, J. P. (1993). Tissue Engineering. *Science*, *260*(May), 920–926. https://doi.org/10.1126/science.8493529

Laschke, M. W., Vollmar, B., & Menger, M. D. (2009). Inosculation: Connecting the Life-Sustaining Pipelines. *Tissue Engineering Part B*, *15*(4), 455–465. https://doi.org/10.1089/ten.teb.2009.0252

Lee, J. Y., Chang, J. K. J., Dominguez, A. A., Lee, H., Nam, S., Chang, J. K. J., Varma, S., Qi, L. S., West, R. B., & Chaudhuri, O. (2019). YAP-independent mechanotransduction drives breast cancer progression. *Nature Communications*, *10*(1), 1848. https://doi.org/10.1038/s41467-019-09755-0

Legant, W. R., Choi, C. K., Miller, J. S., Shao, L., Gao, L., Betzig, E., & Chen, C. S. (2013). Multidimensional traction force microscopy reveals out-of-plane rotational moments about focal adhesions. *Proceedings of the National Academy of Sciences*, *110*(3), 881–886. https://doi.org/10.1073/pnas.1207997110

Legant, W. R., Miller, J. S., Blakely, B. L., Cohen, D. M., Genin, G. M., & Chen, C. S. (2010). Measurement of mechanical tractions exerted by cells in three-dimensional matrices. *Nature Methods*, *7*(12), 969–971. https://doi.org/10.1038/nmeth.1531

Lemos, D. R., & Duffield, J. S. (2018). Tissue-resident mesenchymal stromal cells: Implications for tissue-specific antifibrotic therapies. *Science Translational Medicine*, *10*(426), 1–10. https://doi.org/10.1126/scitranslmed.aan5174

Lesman, A., Koffler, J., Atlas, R., Blinder, Y. J., Kam, Z., & Levenberg, S. (2011). Engineering vessel-like networks within multicellular fibrin-based constructs. *Biomaterials*, *32*, 7856–7869. https://doi.org/10.1016/j.biomaterials.2011.07.003

Lesman, A., Rosenfeld, D., Landau, S., & Levenberg, S. (2016). Mechanical regulation of vascular network formation in engineered matrices. *Advanced Drug Delivery Reviews*, *96*, 176–182. https://doi.org/10.1016/j.addr.2015.07.005

Levental, K. R., Yu, H., Kass, L., Lakins, J. N., Egeblad, M., Erler, J. T., Fong, S. F. T., Csiszar, K., Giaccia, A., Weninger, W., Yamauchi, M., Gasser, D. L., & Weaver, V. M. (2009). Matrix Crosslinking Forces Tumor Progression by Enhancing Integrin Signaling. *Cell*, *139*(5), 891–906. https://doi.org/10.1016/j.cell.2009.10.027

Li, J., Hou, B., Tumova, S., Muraki, K., Bruns, A., Ludlow, M. J., Sedo, A., Hyman, A. J., McKeown, L., Young, R. S., Yuldasheva, N. Y., Majeed, Y., Wilson, L. A., Rode, B., Bailey, M. A., Kim, H. R., Fu, Z., Carter, D. A. L., Bilton, J., … Beech, D. J. (2014). Piezo1 integration of vascular architecture with physiological force. *Nature*, *515*(7526), 279–282. https://doi.org/10.1038/nature13701

Li, L., Eyckmans, J., & Chen, C. S. (2017). Designer biomaterials for mechanobiology. *Nature Materials*, *16*(12), 1164–1168. https://doi.org/10.1038/nmat5049

Liang, Y., Li, L., Scott, R. A., & Kiick, K. L. (2017). 50th Anniversary Perspective: Polymeric Biomaterials: Diverse Functions Enabled by Advances in Macromolecular Chemistry. *Macromolecules*, *50*(2), 483–502. https://doi.org/10.1021/acs.macromol.6b02389

Lin, R. Z., Lee, C. N., Moreno-Luna, R., Neumeyer, J., Piekarski, B., Zhou, P., Moses, M. A., Sachdev, M., Pu, W. T., Emani, S., & Melero-Martin, J. M. (2017). Host non-inflammatory neutrophils mediate the engraftment of bioengineered vascular networks. *Nature Biomedical Engineering*, *1*(6), 0081. https://doi.org/10.1038/s41551-017-0081

Lin, T., Wang, H., & Wang, X. (2005). Self-crimping bicomponent nanofibers electrospun from polyacrylonitrile and elastomeric polyurethane. *Advanced Materials*, *17*(22), 2699–2703. https://doi.org/10.1002/adma.200500901

Lisi, A., Briganti, E., Ledda, M., Losi, P., Grimaldi, S., Marchese, R., & Soldani, G. (2012). A combined synthetic-fibrin scaffold supports growth and cardiomyogenic commitment of human placental derived stem cells. *PLoS ONE*, *7*(4), e34284. https://doi.org/10.1371/journal.pone.0034284

Liu, F., Lagares, D., Choi, K. M., Stopfer, L., Marinković, A., Vrbanac, V., Probst, C. K., Hiemer, S. E., Sisson, T. H., Horowitz, J. C., Rosas, I. O., Fredenburgh, L. E., Feghali-Bostwick, C., Varelas, X., Tager, A. M., & Tschumperlin, D. J. (2015a). Mechanosignaling through YAP and TAZ drives fibroblast activation and fibrosis. *American Journal of Physiology - Lung Cellular and Molecular Physiology*, *308*(4), 344–357. https://doi.org/10.1152/ajplung.00300.2014

Liu, F., Mih, J. D., Shea, B. S., Kho, A. T., Sharif, A. S., Tager, A. M., & Tschumperlin, D. J. (2010a). Feedback amplification of fibrosis through matrix stiffening and COX-2 suppression. *Journal of Cell Biology*, *190*(4), 693–706. https://doi.org/10.1083/jcb.201004082

Liu, J., Tan, Y., Zhang, H., Zhang, Y., Xu, P., Chen, J., Poh, Y. C., Tang, K., Wang, N., & Huang, B. (2012). Soft fibrin gels promote selection and growth of tumorigenic cells. *Nature Materials*, *11*(8), 734–741. https://doi.org/10.1038/nmat3361

Liu, W., Carlisle, C. R., Sparks, E. A., & Guthold, M. (2010b). The mechanical properties of single fibrin fibers. *Journal of Thrombosis and Haemostasis*, *8*(5), 1030–1036. https://doi.org/10.1111/j.1538-7836.2010.03745.x

Liu, W., Lipner, J., Moran, C. H., Feng, L., Li, X., Thomopoulos, S., & Xia, Y. (2015b). Generation of electrospun nanofibers with controllable degrees of crimping through a simple, plasticizer-based treatment. *Advanced Materials*, *27*(16), 2583–2588. https://doi.org/10.1002/adma.201500329

Liu, Y., Zhang, X., Xia, Y., & Yang, H. (2010c). Magnetic-field-assisted electrospinning of aligned straight and wavy polymeric nanofibers. *Advanced Materials*, *22*(22), 2454–2457. https://doi.org/10.1002/adma.200903870

Liu, Z., Tan, J. L., Cohen, D. M., Yang, M. T., Sniadecki, N. J., Alom, S., Nelson, C. M., & Chen, C. S. (2010d). Mechanical tugging force regulates the size of cell – cell junctions. *Proceedings of the National Academy of Sciences*, *107*(22), 9944–9949. https://doi.org/10.1073/pnas.0914547107/-/DCSupplemental.www.pnas.org/cgi/doi/10.1073/pnas.0914547107

Loebel, C., Mauck, R. L., & Burdick, J. A. (2019). Local nascent protein deposition and remodeling guide mesenchymal stromal cell mechanosensing and fate in three-dimensional hydrogels. *Nature Materials*, *in press*, 1. https://doi.org/10.1038/s41563-019-0307-6

Loganathan, R., Rongish, B. J., Smith, C. M., Filla, M. B., Czirok, A., Bénazéraf, B., & Little, C. D. (2016). Extracellular matrix motion and early morphogenesis. *Development*, *143*(12), 2056–2065. https://doi.org/10.1242/dev.127886

Lou, J., Stowers, R., Nam, S., Xia, Y., & Chaudhuri, O. (2018). Stress relaxing hyaluronic acid-collagen hydrogels promote cell spreading, fiber remodeling, and focal adhesion formation in 3D cell culture. *Biomaterials*, *154*, 213–222. https://doi.org/10.1016/j.biomaterials.2017.11.004

Lutolf, M. P., & Hubbell, J. A. (2005). Synthetic biomaterials as instructive extracellular microenvironments for morphogenesis in tissue engineering. In *Nature Biotechnology* (Vol. 23, Issue 1, pp. 47–55). Nature Publishing Group. https://doi.org/10.1038/nbt1055

Lutolf, M. P., Lauer-Fields, J. L., Schmoekel, H. G., Metters, A. T., Weber, F. E., Fields, G. B., & Hubbell, J. A. (2003). Synthetic matrix metalloproteinase-sensitive hydrogels for the conduction of tissue regeneration: Engineering cell-invasion characteristics. *Proceedings of the National Academy of Sciences of the United States of America*, *100*(9), 5413–5418. https://doi.org/10.1073/pnas.0737381100

Lynch, H. A., Johannessen, W., Wu, J. P., Jawa, A., & Elliott, D. M. (2003). Effect of Fiber Orientation and Strain Rate on the Nonlinear Uniaxial Tensile Material Properties of Tendon. *Journal of Biomechanical Engineering*, *125*(5), 726–731. https://doi.org/10.1115/1.1614819

Ma, X., Schickel, M. E., Stevenson, M. D., Sarang-Sieminski, A. L., Gooch, K. J., Ghadiali, S. N., & Hart, R. T. (2013). Fibers in the extracellular matrix enable long-range stress transmission between cells. *Biophysical Journal*, *104*(7), 1410–1418. https://doi.org/10.1016/j.bpj.2013.02.017

Makris, E. A., Gomoll, A. H., Malizos, K. N., Hu, J. C., & Athanasiou, K. A. (2015). Repair and tissue engineering techniques for articular cartilage. In *Nature Reviews Rheumatology* (Vol. 11, Issue 1, pp. 21–34). Nature Publishing Group. https://doi.org/10.1038/nrrheum.2014.157

Malandrino, A., Mak, M., Trepat, X., & Kamm, R. D. (2017). Non-Elastic Remodeling of the 3D Extracellular Matrix by Cell-Generated Forces. *BioRxiv*, 193458. https://doi.org/10.1101/193458

Marinkovic, A., Mih, J. D., Park, J. A. J.-A., Liu, F., & Tschumperlin, D. J. (2012). Improved throughput traction microscopy reveals pivotal role for matrix stiffness in fibroblast contractility and TGF- responsiveness. *AJP: Lung Cellular and Molecular Physiology*, *303*(3), L169–L180. https://doi.org/10.1152/ajplung.00108.2012

Martino, M. M., Briquez, P. S., Ranga, A., Lutolf, M. P., & Hubbell, J. A. (2013). Heparin-binding domain of fibrin(ogen) binds growth factors and promotes tissue repair when incorporated within a synthetic matrix. *Proceedings of the National Academy of Sciences of the United States of America*, *110*(12), 4563–4568. https://doi.org/10.1073/pnas.1221602110

Mason, B. N., Starchenko, A., Williams, R. M., Bonassar, L. J., & Reinhart-King, C. A. (2013). Tuning three-dimensional collagen matrix stiffness independently of collagen concentration modulates endothelial cell behavior. *Acta Biomaterialia*, *9*(1), 4635–4644. https://doi.org/10.1016/j.actbio.2012.08.007

Mason, D. E., Collins, J. M., Dawahare, J. H., Nguyen, T. D., Lin, Y., Voytik-Harbin, S. L., Zorlutuna, P., Yoder, M. C., & Boerckel, J. D. (2019). YAP and TAZ limit cytoskeletal and focal adhesion maturation to enable persistent cell motility. *Journal of Cell Biology*, *218*(4), 1369–1389. https://doi.org/10.1083/jcb.201806065

Matera, D. L., DiLillo, K. M., Smith, M. R., Davidson, C. D., Parikh, R., Said, M., Wilke, C. A., Lombaert, I. M., Arnold, K. B., Moore, B. B., & Baker, B. M. (2020). Microengineered 3D pulmonary interstitial mimetics highlight a critical role for matrix degradation in myofibroblast differentiation. *Science Advances*, *6*(37), 1–15. https://doi.org/10.1126/sciadv.abb5069

Matera, D. L., Wang, W. Y., Smith, M. R., Shikanov, A., & Baker, B. M. (2019). Fiber density modulates cell spreading in 3D interstitial matrix mimetics. *ACS Biomaterials Science and Engineering*, *5*(6), 2965–2975. https://doi.org/10.1021/acsbiomaterials.9b00141

Matsumoto, K., Yoshitomi, H., Rossant, J., & Zaret, K. S. (2001). Liver organogenesis promoted by endothelial cells prior to vascular function. *Science*, *294*(5542), 559–563. https://doi.org/10.1126/science.1063889

Mauck, R. L., Baker, B. M., Nerurkar, N. L., Burdick, J. A., Li, W.-J. J., Tuan, R. S., & Elliott,

D. M. (2009). Engineering on the straight and narrow: The mechanics of nanofibrous assemblies for fiber-reinforced tissue regeneration. *Tissue Engineering - Part B: Reviews*, *15*(2), 171–193. https://doi.org/10.1089/ten.teb.2008.0652

McDole, K., Guignard, L., Amat, F., Berger, A., Malandain, G., Royer, L. A., Turaga, S. C., Branson, K., & Keller, P. J. (2018). In Toto Imaging and Reconstruction of Post-Implantation Mouse Development at the Single-Cell Level. *Cell*, *175*(3), 859-876.e33. https://doi.org/10.1016/j.cell.2018.09.031

Mih, J. D., Marinkovic, A., Liu, F., Sharif, A. S., & Tschumperlin, D. J. (2012). Matrix stiffness reverses the effect of actomyosin tension on cell proliferation. *Journal of Cell Science*, *125*(24), 5974–5983. https://doi.org/10.1242/jcs.108886

Miller, J. S., Stevens, K. R., Yang, M. T., Baker, B. M., Nguyen, D. H. T., Cohen, D. M., Toro, E., Chen, A. A., Galie, P. A., Yu, X., Chaturvedi, R., Bhatia, S. N., & Chen, C. S. (2012). Rapid casting of patterned vascular networks for perfusable engineered three-dimensional tissues. *Nature Materials*, *11*(9), 768–774. https://doi.org/10.1038/nmat3357

Mitra, S. K., Hanson, D. A., & Schlaepfer, D. D. (2005). Focal adhesion kinase: In command and control of cell motility. *Nature Reviews Molecular Cell Biology*, *6*(1), 56–68. https://doi.org/10.1038/nrm1549

Morgan, J. P., Delnero, P. F., Zheng, Y., Verbridge, S. S., Chen, J., Craven, M., Choi, N. W., Diaz-Santana, A., Kermani, P., Hempstead, B., López, J. A., Corso, T. N., Fischbach, C., & Stroock, A. D. (2013). Formation of microvascular networks in vitro. *Nature Protocols*, *8*(9), 1820–1836. https://doi.org/10.1038/nprot.2013.110

Morin, K. T., & Tranquillo, R. T. (2013). In vitro models of angiogenesis and vasculogenesis in fibrin gel. *Experimental Cell Research*, *319*(16), 2409–2417. https://doi.org/10.1016/J.YEXCR.2013.06.006

Mullen, C. A., Vaughan, T. J., Billiar, K. L., & McNamara, L. M. (2015). The effect of substrate stiffness, thickness, and cross-linking density on osteogenic cell behavior. *Biophysical Journal*, *108*(7), 1604–1612. https://doi.org/10.1016/j.bpj.2015.02.022

Nahrendorf, M., Swirski, F. K., Aikawa, E., Stangenberg, L., Wurdinger, T., Figueiredo, J.-L., Libby, P., Weissleder, R., & Pittet, M. J. (2007). The healing myocardium sequentially mobilizes two monocyte subsets with divergent and complementary functions. *The Journal of Experimental Medicine*, *204*(12), 3037–3047. https://doi.org/10.1084/jem.20070885

Nakagawa, S., Pawelek, P., & Grinnell, F. (1989). Long-term culture of fibroblasts in contracted collagen gels: Effects on cell growth and biosynthetic activity. *Journal of Investigative Dermatology*, *93*(6), 792–798. https://doi.org/10.1111/1523-1747.ep12284425

Nam, S., Lee, J., Brownfield, D. G., & Chaudhuri, O. (2016). Viscoplasticity Enables Mechanical Remodeling of Matrix by Cells. *Biophysical Journal*, *111*(10), 2296–2308. https://doi.org/10.1016/j.bpj.2016.10.002

Nardone, G., Oliver-De La Cruz, J., Vrbsky, J., Martini, C., Pribyl, J., Skládal, P., Pešl, M., Caluori, G., Pagliari, S., Martino, F., Maceckova, Z., Hajduch, M., Sanz-Garcia, A., Pugno, N. M., Stokin, G. B., & Forte, G. (2017). YAP regulates cell mechanics by controlling focal adhesion assembly. *Nature Communications*, *8*(1), 1–13. https://doi.org/10.1038/ncomms15321

Natan, S., Koren, Y., Shelah, O., Goren, S., & Lesman, A. (2020). Long-range mechanical coupling of cells in 3D fibrin gels. *Molecular Biology of the Cell*, *31*(14), 1474–1485. https://doi.org/10.1091/mbc.E20-01-0079

Newman, A. C., Nakatsu, M. N., Chou, W., Gershon, P. D., & Hughes, C. C. W. (2011). The requirement for fibroblasts in angiogenesis: fibroblast-derived matrix proteins are essential for endothelial cell lumen formation. *Molecular Biology of the Cell*, *22*(20), 3791–3800. https://doi.org/10.1091/mbc.E11-05-0393

Nguyen, D.-H. T., Stapleton, S. C., Yang, M. T., Cha, S. S., Choi, C. K., Galie, P. A., & Chen, C. S. (2013). Biomimetic model to reconstitute angiogenic sprouting morphogenesis in vitro. *Proceedings of the National Academy of Sciences*, *110*(17), 6712–6717. https://doi.org/10.1073/pnas.1221526110

Nguyen, T. A., Pang, K. C., & Masters, S. L. (2017). Intercellular communication for innate immunity. *Molecular Immunology*, *86*, 16–22. https://doi.org/10.1016/j.molimm.2016.10.002

Nitsan, I., Drori, S., Lewis, Y. E., Cohen, S., & Tzlil, S. (2016). Mechanical communication in cardiac cell synchronized beating. *Nature Physics*, *12*(January). https://doi.org/10.1038/NPHYS3619

Nör, J. E., Peters, M. C., Christensen, J. B., Sutorik, M. M., Linn, S., Khan, M. K., Addison, C. L., Mooney, D. J., & Polverini, P. J. (2001). Engineering and characterization of functional human microvessels in immunodeficient mice. *Laboratory Investigation*, *81*(4), 453–463. https://doi.org/10.1038/labinvest.3780253

Norotte, C., Marga, F. S., Niklason, L. E., & Forgacs, G. (2009). Scaffold-free vascular tissue engineering using bioprinting. *Biomaterials*, *30*(30), 5910–5917. https://doi.org/10.1016/j.biomaterials.2009.06.034

Notbohm, J., Lesman, A., Rosakis, P., Tirrell, D. A., & Ravichandran, G. (2015). Microbuckling of fibrin provides a mechanism for cell mechanosensing. *Journal of the Royal Society Interface*, *12*(108). https://doi.org/10.1098/rsif.2015.0320

Oakes, P. W., & Gardel, M. L. (2014). Stressing the limits of focal adhesion mechanosensitivity. In *Current Opinion in Cell Biology* (Vol. 30, Issue 1, pp. 68–73). Elsevier Current Trends. https://doi.org/10.1016/j.ceb.2014.06.003

Orr, A. W., Helmke, B. P., Blackman, B. R., & Schwartz, M. A. (2006). Mechanisms of mechanotransduction. *Developmental Cell*, *10*(1), 11–20. https://doi.org/10.1016/j.devcel.2005.12.006

Pakshir, P., Alizadehgiashi, M., Wong, B., Coelho, N. M., Chen, X., Gong, Z., Shenoy, V. B., McCulloch, C., & Hinz, B. (2019). Dynamic fibroblast contractions attract remote macrophages in fibrillar collagen matrix. *Nature Communications*, *10*(1), 1850. https://doi.org/10.1038/s41467-019-09709-6

Parenteau-Bareil, R., Gauvin, R., & Berthod, F. (2010). Collagen-based biomaterials for tissue engineering applications. *Materials, 3*(3), 1863–1887. https://doi.org/10.3390/ma3031863

Parsons, J. T., Horwitz, A. R., & Schwartz, M. A. (2010). Cell adhesion: Integrating cytoskeletal dynamics and cellular tension. In *Nature Reviews Molecular Cell Biology* (Vol. 11, Issue 9, pp. 633–643). Nature Publishing Group. https://doi.org/10.1038/nrm2957

Peyton, S. R., & Putnam, A. J. (2005). Extracellular matrix rigidity governs smooth muscle cell motility in a biphasic fashion. *Journal of Cellular Physiology, 204*(1), 198–209. https://doi.org/10.1002/jcp.20274

Pham, Q. P., Sharma, U., & Mikos, A. G. (2006). Electrospinning of polymeric nanofibers for tissue engineering applications: A review. *Tissue Engineering*, *12*(5), 1197–1211. https://doi.org/10.1089/ten.2006.12.1197

Phan, M. N., Leddy, H. A., Votta, B. J., Kumar, S., Levy, D. S., Lipshutz, D. B., Suk, H. L., Liedtke, W., & Guilak, F. (2009). Functional characterization of TRPV4 as an osmotically sensitive ion channel in porcine articular chondrocytes. *Arthritis and Rheumatism*, *60*(10), 3028–3037. https://doi.org/10.1002/art.24799

Piotrowski-Daspit, A. S., Nerger, B. A., Wolf, A. E., Sundaresan, S., & Nelson, C. M. (2017). Dynamics of Tissue-Induced Alignment of Fibrous Extracellular Matrix. *Biophysical Journal*, *113*(3), 702–713. https://doi.org/10.1016/j.bpj.2017.06.046

Plotnikov, S. V, Pasapera, A. M., Sabass, B., & Waterman, C. M. (2012). Force fluctuations within focal adhesions mediate ECM-rigidity sensing to guide directed cell migration. *Cell*, *151*(7), 1513–1527. https://doi.org/10.1016/j.cell.2012.11.034

Polacheck, W. J., & Chen, C. S. (2016). Measuring cell-generated forces: A guide to the available tools. *Nature Methods, 13*(5), 415–423. https://doi.org/10.1038/nmeth.3834

Potente, M., Gerhardt, H., & Carmeliet, P. (2011). Basic and therapeutic aspects of angiogenesis. *Cell*, *146*(6), 873–887. https://doi.org/10.1016/j.cell.2011.08.039

Provenzano, P. P., Eliceiri, K. W., Campbell, J. M., Inman, D. R., White, J. G., & Keely, P. J. (2006). Collagen reorganization at the tumor-stromal interface facilitates local invasion. *BMC Medicine, 4*, 1–15. https://doi.org/10.1186/1741-7015-4-38

Raghavan, S., Nelson, C. M., Baranski, J. D., Lim, E., & Chen, C. S. (2010). Geometrically Controlled Endothelial Tubulogenesis in Micropatterned Gels. *Tissue Engineering Part A*, *16*(7), 2255–2263. https://doi.org/10.1089/ten.tea.2009.0584

Rao, R. R., Peterson, A. W., Ceccarelli, J., Putnam, A. J., & Stegemann, J. P. (2012). Matrix composition regulates three-dimensional network formation by endothelial cells and mesenchymal stem cells in collagen/fibrin materials. *Angiogenesis*, *15*(2), 253–264. https://doi.org/10.1007/s10456-012-9257-1

Rape, A. D., Guo, W. H., & Wang, Y. L. (2011). The regulation of traction force in relation to cell shape and focal adhesions. *Biomaterials*, *32*(8), 2043–2051. https://doi.org/10.1016/j.biomaterials.2010.11.044

Reinhart-King, C. A., Dembo, M., & Hammer, D. A. (2003). Endothelial Cell Traction Forces on RGD-Derivatized Polyacrylamide Substrata. *Langmuir*, *19*, 1573–1579. https://doi.org/10.1021/LA026142J

Reinhart-King, C. A., Dembo, M., & Hammer, D. A. (2008). Cell-cell mechanical communication through compliant substrates. *Biophysical Journal*, *95*(12), 6044–6051. https://doi.org/10.1529/biophysj.107.127662

Reneker, D. H., & Chun, I. (1996). Nanometre diameter fibres of polymer, produced by electrospinning. *Nanotechnology*, *7*(3), 216–223. https://doi.org/10.1088/0957-4484/7/3/009

Ricca, B. L., Venugopalan, G., & Fletcher, D. A. (2013). To pull or be pulled: parsing the multiple modes of mechanotransduction. *Current Opinion in Cell Biology*, *25*(5), 558–564. https://doi.org/10.1016/J.CEB.2013.06.002

Rigby, B. J., Hirai, N., Spikes, J. D., & Eyring, H. (1959). The mechanical properties of rat tail tendon. *Journal of General Physiology*, *43*(2), 265–283. https://doi.org/10.1085/jgp.43.2.265

Risau, W., & Lemmon, V. (1988). Changes in the vascular extracellular matrix during embryonic vasculogenesis and angiogenesis. *Developmental Biology*, *125*(2), 441–450. https://doi.org/10.1016/0012-1606(88)90225-4

Ritcharoen, W., Thaiying, Y., Saejeng, Y., Jangchud, I., Rangkupan, R., Meechaisue, C., & Supaphol, P. (2008). Electrospun dextran fibrous membranes. *Cellulose*, *15*(3), 435–444. https://doi.org/10.1007/s10570-008-9199-3

Rohringer, S., Hofbauer, P., Schneider, K. H., Husa, A.-M., Feichtinger, G., Peterbauer-Scherb, A., Redl, H., & Holnthoner, W. (2014). Mechanisms of vasculogenesis in 3D fibrin matrices mediated by the interaction of adipose-derived stem cells and endothelial cells. *Angiogenesis*, *17*(4), 921–933. https://doi.org/10.1007/s10456-014-9439-0

Ronceray, P., Broedersz, C. P., & Lenz, M. (2016). Fiber networks amplify active stress. *Proceedings of the National Academy of Sciences*, *113*(11), 2827–2832. https://doi.org/10.1073/pnas.1514208113

Rosales, A. M., & Anseth, K. S. (2016). The design of reversible hydrogels to capture extracellular matrix dynamics. *Nature Reviews Materials*, *1*(2), 1–15. https://doi.org/10.1038/natrevmats.2015.12

Rouwkema, J., Rivron, N. C., & van Blitterswijk, C. A. (2008). Vascularization in tissue engineering. In *Trends in Biotechnology* (Vol. 26, Issue 8, pp. 434–441). Elsevier Current Trends. https://doi.org/10.1016/j.tibtech.2008.04.009

Roy, R., Boskey, A., & Bonassar, L. J. (2010). Processing of type I collagen gels using nonenzymatic glycation. *Journal of Biomedical Materials Research - Part A*, *93*(3), 843–851. https://doi.org/10.1002/jbm.a.32231

Rozario, T., & DeSimone, D. W. (2010). The extracellular matrix in development and morphogenesis: A dynamic view. *Developmental Biology*, *341*(1), 126–140. https://doi.org/10.1016/j.ydbio.2009.10.026

Rudnicki, M. S., Cirka, H. A., Aghvami, M., Sander, E. A., Wen, Q., & Billiar, K. L. (2013). Nonlinear Strain Stiffening Is Not Sufficient to Explain How Far Cells Can Feel on Fibrous Protein Gels. *Biophysical Journal*, *105*(1), 11–20. https://doi.org/10.1016/J.BPJ.2013.05.032

Rupp, P. A., Czirók, A., & Little, C. D. (2003). Novel approaches for the study of vascular assembly and morphogenesis in avian embryos. *Trends in Cardiovascular Medicine*, *13*(7), 283–288. https://doi.org/10.1016/S1050-1738(03)00118-X

Sapir, L., & Tzlil, S. (2017). Talking over the extracellular matrix: How do cells communicate mechanically? In *Seminars in Cell and Developmental Biology* (Vol. 71, pp. 99–105). Elsevier Ltd. https://doi.org/10.1016/j.semcdb.2017.06.010

Sato, Y., Poynter, G., Huss, D., Filla, M. B., Czirok, A., Rongish, B. J., Little, C. D., Fraser, S. E., & Lansford, R. (2010). Dynamic analysis of vascular morphogenesis using transgenic quail embryos. *PLoS ONE*, *5*(9), 1–12. https://doi.org/10.1371/journal.pone.0012674

Saunders, R. L., & Hammer, D. A. (2010). Assembly of Human Umbilical Vein Endothelial Cells on Compliant Hydrogels. *Cellular and Molecular Bioengineering*, *3*(1), 60–67. https://doi.org/10.1007/s12195-010-0112-4

Sawhney, R. K., & Howard, J. (2002). Slow local movements of collagen fibers by fibroblasts drive the rapid global self-organization of collagen gels. *Journal of Cell Biology*, *157*(6), 1083–1091. https://doi.org/10.1083/jcb.200203069

Schaefer, L. (2010). Extracellular matrix molecules: Endogenous danger signals as new drug targets in kidney diseases. *Current Opinion in Pharmacology*, *10*(2), 185–190. https://doi.org/10.1016/j.coph.2009.11.007

Schechner, J. S., Nath, A. K., Zheng, L., Kluger, M. S., Hughes, C. C. W., Sierra-Honigmann, M. R., Lorber, M. I., Tellides, G., Kashgarian, M., Bothwell, A. L. M., & Pober, J. S. (2000). In vivo formation of complex microvessels lined by human endothelial cells in an immunodeficient mouse. *Proceedings of the National Academy of Sciences*, *97*(16), 9191–9196. https://doi.org/10.1073/pnas.150242297

Schoen, I., Pruitt, B. L., & Vogel, V. (2013). The Yin-Yang of Rigidity Sensing: How Forces and Mechanical Properties Regulate the Cellular Response to Materials. *Annual Review of Materials Research*, *43*(1), 589–618. https://doi.org/10.1146/annurev-matsci-062910-100407

Semler, E. J., Ranucci, C. S., & Moghe, P. V. (2000). Mechanochemical manipulation of hepatocyte aggregation can selectively induce or repress liver-specific function. *Biotechnology and Bioengineering*, *69*(4), 359–369. https://doi.org/10.1002/1097-0290(20000820)69:4<359::AID-BIT2>3.0.CO;2-Q

Shi, Q., Ghosh, R. P., Engelke, H., Rycroft, C. H., Cassereau, L., & Sethian, J. A. (2014). Rapid disorganization of mechanically interacting systems of mammary acini. *Proceedings of the National Academy of Sciences*, *111*(2), 658–663. https://doi.org/10.1073/pnas.1311312110/-/DCSupplemental.www.pnas.org/cgi/doi/10.1073/pnas.1311312110

Shojaei, F., Zhong, C., Wu, X., Yu, L., & Ferrara, N. (2008). Role of myeloid cells in tumor angiogenesis and growth. *Trends in Cell Biology*, *18*(8), 372–378. https://doi.org/10.1016/j.tcb.2008.06.003

Sill, T. J., & von Recum, H. A. (2008). Electrospinning: Applications in drug delivery and tissue engineering. In *Biomaterials* (Vol. 29, Issue 13, pp. 1989–2006). Elsevier. https://doi.org/10.1016/j.biomaterials.2008.01.011

Singer, A. J., & Clark, R. A. F. (1999). Cutaneous wound healing. *New England Journal of Medicine*, *341*(0028-4793 (Print)), 738–746.

Singer, S. J. (1992). *Intercellular Communiication Cell-Cell Adhesion*. *C*, 1671–1677.

Skardal, A., Zhang, J., & Prestwich, G. D. (2010). Bioprinting vessel-like constructs using hyaluronan hydrogels crosslinked with tetrahedral polyethylene glycol tetracrylates. *Biomaterials*, *31*(24), 6173–6181. https://doi.org/10.1016/j.biomaterials.2010.04.045

Slack-Davis, J. K., Martin, K. H., Tilghman, R. W., Iwanicki, M., Ung, E. J., Autry, C., Luzzio, M. J., Cooper, B., Kath, J. C., Roberts, W. G., & Parsons, J. T. (2007). Cellular characterization of a novel focal adhesion kinase inhibitor. *Journal of Biological Chemistry*, *282*(20), 14845–14852. https://doi.org/10.1074/jbc.M606695200

Song, H.-H. G., Rumma, R. T., Ozaki, C. K., Edelman, E. R., & Chen, C. S. (2018). Review Vascular Tissue Engineering : Progress, Challenges, and Clinical Promise. *Cell Stem Cell*, *22*(3), 340–354. https://doi.org/10.1016/j.stem.2018.02.009

Song, H. H. G., Lammers, A., Sundaram, S., Rubio, L., Chen, A. X., Li, L., Eyckmans, J., Bhatia, S. N., & Chen, C. S. (2020). Transient Support from Fibroblasts is Sufficient to Drive Functional Vascularization in Engineered Tissues. *Advanced Functional Materials*, *30*(48), 1–13. https://doi.org/10.1002/adfm.202003777

Sopher, R. S., Tokash, H., Natan, S., Sharabi, M., Shelah, O., Tchaicheeyan, O., & Lesman, A. (2018a). Nonlinear elasticity of the ECM fibers facilitates efficient inter-cellular communication. *Biophysical Journal*, *0*(0). https://doi.org/10.1016/j.bpj.2018.07.036

Sopher, R. S., Tokash, H., Natan, S., Sharabi, M., Shelah, O., Tchaicheeyan, O., & Lesman, A. (2018b). Nonlinear Elasticity of the ECM Fibers Facilitates Efficient Intercellular Communication. *Biophysical Journal*, *115*(7), 1357–1370. https://doi.org/10.1016/j.bpj.2018.07.036

Stabley, D. R., Jurchenko, C., Marshall, S. S., & Salaita, K. S. (2012). Visualizing mechanical tension across membrane receptors with a fluorescent sensor. *Nature Methods*, *9*(1), 64–67. https://doi.org/10.1038/nmeth.1747

Stewart, S. A., Dykxhoorn, D. M., Palliser, D., Mizuno, H., Yu, E. Y., An, D. S., Sabatini, D. M., Chen, I. S. Y., Hahn, W. C., Sharp, P. A., Weinberg, R. A., & Novina, C. D. (2003). Lentivirus-delivered stable gene silencing by RNAi in primary cells. *Rna*, *9*(4), 493–501. https://doi.org/10.1261/rna.2192803

Stopak, D., & Harris, A. K. (1982). Connective tissue morphogenesis by fibroblast traction. *Developmental Biology*, *90*(2), 383–398. https://doi.org/10.1016/0012-1606(82)90388-8

Storm, C., Pastore, J. J., MacKintosh, F. C., Lubensky, T. C., & Janmey, P. A. (2005). Nonlinear elasticity in biological gels. *Nature*, *435*(7039), 191–194. https://doi.org/10.1038/nature03521

Suchyna, T. M., Johnson, J. H., Hamer, K., Leykam, J. F., Gage, D. A., Clemo, H. F., Baumgarten, C. M., & Sachs, F. (2000). Identification of a peptide toxin from Grammostola spatulata spider venom that blocks cation-selective stretch-activated channels. *Journal of General Physiology*, *115*(5), 583–598. https://doi.org/10.1085/jgp.115.5.583

Sun, G., Shen, Y. I., Ho, C. C., Kusuma, S., & Gerecht, S. (2010). Functional groups affect physical and biological properties of dextran-based hydrogels. *Journal of Biomedical Materials Research - Part A*, *93*(3), 1080–1090. https://doi.org/10.1002/jbm.a.32604

Surrao, D. C., Fan, J. C. Y., Waldman, S. D., & Amsden, B. G. (2012a). A crimp-like microarchitecture improves tissue production in fibrous ligament scaffolds in response to mechanical stimuli. *Acta Biomaterialia*, *8*(10), 3704–3713. https://doi.org/10.1016/j.actbio.2012.06.016

Surrao, D. C., Hayami, J. W. S., Waldman, S. D., & Amsden, B. G. (2010). Self-crimping, biodegradable, electrospun polymer microfibers. *Biomacromolecules*, *11*(12), 3624–3629. https://doi.org/10.1021/bm101078c

Surrao, D. C., Waldman, S. D., & Amsden, B. G. (2012b). Biomimetic poly(lactide) based fibrous scaffolds for ligament tissue engineering. *Acta Biomaterialia*, *8*(11), 3997–4006. https://doi.org/10.1016/j.actbio.2012.07.012

Szczesny, S. E., Driscoll, T. P., Tseng, H. Y., Liu, P. C., Heo, S. J., Mauck, R. L., & Chao, P. H. G. (2017). Crimped Nanofibrous Biomaterials Mimic Microstructure and Mechanics of Native Tissue and Alter Strain Transfer to Cells. *ACS Biomaterials Science and Engineering*, *3*(11), 2869–2876. https://doi.org/10.1021/acsbiomaterials.6b00646

Telo', P., Breviario, F., Huber, P., Panzeri, C., & Dejana, E. (1998). Identification of a novel cadherin (vascular endothelial cadherin-2) located at intercellular junctions in endothelial cells. *Journal of Biological Chemistry*, *273*(28), 17565–17572. https://doi.org/10.1074/jbc.273.28.17565

Thodeti, C. K., Matthews, B., Ravi, A., Mammoto, A., Ghosh, K., Bracha, A. L., & Ingber, D. E. (2009). TRPV4 channels mediate cyclic strain-induced endothelial cell reorientation through integrin-to-integrin signaling. *Circulation Research*, *104*(9), 1123–1130. https://doi.org/10.1161/CIRCRESAHA.108.192930

Thrivikraman, G., Jagiełło, A., Lai, V. K., Johnson, S. L., Keating, M., Nelson, A., Schultz, B., Wang, C. M., Levine, A. J., Botvinick, E. L., & Tranquillo, R. T. (2021). Cell contact guidance via sensing anisotropy of network mechanical resistance. *Proceedings of the National Academy of Sciences of the United States of America*, *118*(29), 1–11. https://doi.org/10.1073/pnas.2024942118

Tinevez, J. Y., Perry, N., Schindelin, J., Hoopes, G. M., Reynolds, G. D., Laplantine, E., Bednarek, S. Y., Shorte, S. L., & Eliceiri, K. W. (2017). TrackMate: An open and extensible platform for single-particle tracking. *Methods*, *115*, 80–90. https://doi.org/10.1016/j.ymeth.2016.09.016

Tran, Q. K., Ohashi, K., & Watanabe, H. (2000). Calcium signalling in endothelial cells. *Cardiovascular Research*, *48*(1), 13–22. https://doi.org/10.1016/S0008-6363(00)00172-3

Trappmann, B., Baker, B. M., Polacheck, W. J., Choi, C. K., Burdick, J. A., & Chen, C. S. (2017). Matrix degradability controls multicellularity of 3D cell migration. *Nature Communications*, *8*(1), 1–8. https://doi.org/10.1038/s41467-017-00418-6

Uslu, F. E., Davidson, C. D., Mailand, E., Bouklas, N., Baker, B. M., & Sakar, M. S. (2021). Engineered Extracellular Matrices with Integrated Wireless Microactuators to Study Mechanobiology. *Advanced Materials*, *33*(40), 2102641. https://doi.org/10.1002/adma.202102641

Vacanti, J. P., & Langer, R. (1999). Tissue engineering: the design and fabrication of living replacement devices for surgical reconstruction and transplantation. *Lancet*, *354*, 32–34. https://doi.org/10.1016/S0140-6736(99)90247-7

Vailhé, B., Ronot, X., Tracqui, P., Usson, Y., & Tranqui, L. (1997). In vitro angiogenesis is modulated by the mechanical properties of fibrin gels and is related to α(v)β3integrin localization. *In Vitro Cellular and Developmental Biology - Animal*, *33*(10), 763–773. https://doi.org/10.1007/s11626-997-0155-6

Vailhé, B., Vittet, D., & Feige, J. J. (2001). In vitro models of vasculogenesis and angiogenesis. *Laboratory Investigation*, *81*(4), 439–452. https://doi.org/10.1038/labinvest.3780252

van Dijk-Wotthuis, W. N. E., Franssen, O., Talsma, H., van Steenbergen, M. J., Kettenes-van den Bosch, J. J., & Hennink, W. E. (1995). Synthesis, Characterization, and Polymerization of Glycidyl Methacrylate Derivatized Dextran. *Macromolecules*, *28*(18), 6317–6322.

https://doi.org/10.1021/ma00122a044

Van Niel, G., D'Angelo, G., & Raposo, G. (2018). Shedding light on the cell biology of extracellular vesicles. *Nature Reviews Molecular Cell Biology*, *19*(4), 213–228. https://doi.org/10.1038/nrm.2017.125

Van Oers, F. M., Rens, E. G., Lavalley, D. J., Reinhart-King, C. A., & Merks, R. M. H. (2014). Mechanical Cell-Matrix Feedback Explains Pairwise and Collective Endothelial Cell Behavior In Vitro. *PLoS Computational Biology*, *10*(8). https://doi.org/10.1371/journal.pcbi.1003774

Varesano, A., Montarsolo, A., & Tonin, C. (2007). Crimped polymer nanofibres by air-driven electrospinning. *European Polymer Journal*, *43*(7), 2792–2798. https://doi.org/10.1016/j.eurpolymj.2007.04.023

Vogel, V., & Sheetz, M. (2006). Local force and geometry sensing regulate cell functions. In *Nature Reviews Molecular Cell Biology* (Vol. 7, Issue 4, pp. 265–275). Nature Publishing Group. https://doi.org/10.1038/nrm1890

Volberg, T., Geiger, B., Kartenbeck, J., & Franke, W. W. (1986). Changes in membrane-microfilament interaction in intercellular adherens junctions upon removal of extracellular Ca2+ ions. *The Journal of Cell Biology*, *102*(5), 1832–1842. https://doi.org/10.1083/JCB.102.5.1832

Walma, D. A. C., & Yamada, K. M. (2020). The extracellular matrix in development. *Development (Cambridge, England)*, *147*(10). https://doi.org/10.1242/dev.175596

Wang, H., Abhilash, A. S., Chen, C. S., Wells, R. G., & Shenoy, V. B. (2015). Long-range force transmission in fibrous matrices enabled by tension-driven alignment of fibers. *Biophysical Journal*, *107*(11), 2592–2603. https://doi.org/10.1016/j.bpj.2014.09.044

Wang, H. B., Dembo, M., Hanks, S. K., & Wang, Y. L. (2001). Focal adhesion kinase is involved in mechanosensing during fibroblast migration. *Proceedings of the National Academy of Sciences of the United States of America*, *98*(20), 11295–11300. https://doi.org/10.1073/pnas.201201198

Wang, W. Y., Davidson, C. D., Lin, D., & Baker, B. M. (2019). Actomyosin contractility-dependent matrix stretch and recoil induces rapid cell migration. *Nature Communications*, *10*(1). https://doi.org/10.1038/s41467-019-09121-0

Wang, W. Y., Jarman, E. H., Lin, D., & Baker, B. M. (2021a). Dynamic Endothelial Stalk Cell–Matrix Interactions Regulate Angiogenic Sprout Diameter. *Frontiers in Bioengineering and Biotechnology*, *9*(March), 1–12. https://doi.org/10.3389/fbioe.2021.620128

Wang, W. Y., Kent, R. N., Huang, S. A., Jarman, E. H., Shikanov, E. H., Davidson, C. D., Hiraki, H. L., Lin, D., Wall, M. A., Matera, D. L., Shin, J. W., Polacheck, W. J., Shikanov, A., & Baker, B. M. (2021b). Direct comparison of angiogenesis in natural and synthetic biomaterials reveals that matrix porosity regulates endothelial cell invasion speed and sprout diameter. *Acta Biomaterialia*, *135*, 260–273. https://doi.org/10.1016/j.actbio.2021.08.038

Wang, W. Y., Lin, D., Jarman, E. H., Polacheck, W. J., & Baker, B. M. (2020). Functional angiogenesis requires microenvironmental cues balancing endothelial cell migration and proliferation. *Lab on a Chip*, *20*(6), 1153–1166. https://doi.org/10.1039/c9lc01170f

Wang, W. Y., Pearson, A. T., Kutys, M. L., Choi, C. K., Wozniak, M. A., Baker, B. M., & Chen, C. S. (2018). Extracellular matrix alignment dictates the organization of focal adhesions and directs uniaxial cell migration. *APL Bioengineering*, *2*(4), 046107. https://doi.org/10.1063/1.5052239

Winer, J. P., Oake, S., & Janmey, P. A. (2009). Non-linear elasticity of extracellular matrices enables contractile cells to communicate local position and orientation. *PLoS ONE*, *4*(7), e6382. https://doi.org/10.1371/journal.pone.0006382

Wipff, P. J., Rifkin, D. B., Meister, J. J., & Hinz, B. (2007). Myofibroblast contraction activates latent TGF-β1 from the extracellular matrix. *Journal of Cell Biology*, *179*(6), 1311–1323. https://doi.org/10.1083/jcb.200704042

Wolf, K., Alexander, S., Schacht, V., Coussens, L. M., von Andrian, U. H., van Rheenen, J., Deryugina, E., & Friedl, P. (2009). Collagen-based cell migration models in vitro and in vivo. *Seminars in Cell and Developmental Biology*, *20*(8), 931–941. https://doi.org/10.1016/j.semcdb.2009.08.005

Wu, J., & Hong, Y. (2016). Enhancing cell infiltration of electrospun fibrous scaffolds in tissue regeneration. In *Bioactive Materials* (Vol. 1, Issue 1, pp. 56–64). KeAi Communications Co. https://doi.org/10.1016/j.bioactmat.2016.07.001

Wynn, T. A. (2007). Common and unique mechanisms regulate fibrosis in various fibroproliferative diseases. In *Journal of Clinical Investigation* (Vol. 117, Issue 3, pp. 524–529). American Society for Clinical Investigation. https://doi.org/10.1172/JCI31487

Wynn, T. A., & Ramalingam, T. R. (2012). Mechanisms of fibrosis: Therapeutic translation for fibrotic disease. *Nature Medicine*, *18*(7), 1028–1040. https://doi.org/10.1038/nm.2807

Xiao, Y., Liu, C., Chen, Z., Blatchley, M. R., Kim, D., Zhou, J., Xu, M., Gerecht, S., & Fan, R. (2019). Senescent Cells with Augmented Cytokine Production for Microvascular Bioengineering and Tissue Repairs. *Advanced Biosystems*, *3*(8), 1–12. https://doi.org/10.1002/adbi.201900089

Xie, J., Bao, M., Bruekers, M. C., & Huck, W. T. S. (2017). Collagen gels with different fibrillar microarchitectures elicit different cellular responses. *ACS Applied Materials & Interfaces*, *9*, 19630–19637. https://doi.org/10.1021/acsami.7b03883

Xue, M., & Jackson, C. J. (2015). Extracellular Matrix Reorganization During Wound Healing and Its Impact on Abnormal Scarring. *Advances in Wound Care*, *4*(3), 119–136. https://doi.org/10.1089/wound.2013.0485

Yang, B. A., Westerhof, T. M., Sabin, K., Merajver, S. D., & Aguilar, C. A. (2021). Engineered Tools to Study Intercellular Communication. *Advanced Science*, *8*(3), 1–20. https://doi.org/10.1002/advs.202002825

Yang, L., Van Der Werf, K. O., Koopman, B. F. J. M., Subramaniam, V., Bennink, M. L., Dijkstra, P. J., & Feijen, J. (2007). Micromechanical bending of single collagen fibrils using atomic force microscopy. *Journal of Biomedical Materials Research - Part A*, *82*(1), 160–168. https://doi.org/10.1002/jbm.a.31127

Yu, Y., & Chau, Y. (2012). One-step "click" method for generating vinyl sulfone groups on hydroxyl-containing water-soluble polymers. *Biomacromolecules*, *13*(3), 937–942. https://doi.org/10.1021/bm2014476

Zanotelli, M. R., Ardalani, H., Zhang, J., Hou, Z., Nguyen, E. H., Swanson, S., Nguyen, B. K., Bolin, J., Elwell, A., Bischel, L. L., Xie, A. W., Stewart, R., Beebe, D. J., Thomson, J. A., Schwartz, M. P., & Murphy, W. L. (2016). Stable engineered vascular networks from human induced pluripotent stem cell-derived endothelial cells cultured in synthetic hydrogels. *Acta Biomaterialia*, *35*, 32–41. https://doi.org/10.1016/j.actbio.2016.03.001

Zeltinger, J., Sherwood, J. K., Graham, D. A., Müeller, R., & Griffith, L. G. (2001). Effect of pore size and void fraction on cellular adhesion, proliferation, and matrix deposition. *Tissue Engineering*, *7*(5), 557–572. https://doi.org/10.1089/107632701753213183

Zepp, J. A., Morley, M. P., Loebel, C., Kremp, M. M., Chaudhry, F. N., Basil, M. C., Leach, J. P., Liberti, D. C., Niethamer, T. K., Ying, Y., Jayachandran, S., Babu, A., Zhou, S., Frank, D. B., Burdick, J. A., & Morrisey, E. E. (2021). Genomic, epigenomic, and biophysical cues controlling the emergence of the lung alveolus. *Science*, *371*(6534). https://doi.org/10.1126/science.abc3172

Zhang, B., Montgomery, M., Chamberlain, M. D., Ogawa, S., Korolj, A., Pahnke, A., Wells, L. A., Massé, S., Kim, J., Reis, L., Momen, A., Nunes, S. S., Wheeler, A. R., Nanthakumar, K., Keller, G., Sefton, M. V., & Radisic, M. (2016). Biodegradable scaffold with built-in vasculature for organ-on-a-chip engineering and direct surgical anastomosis. *Nature Materials*, *15*(6), 669–678. https://doi.org/10.1038/nmat4570

Zudaire, E., Gambardella, L., Kurcz, C., & Vermeren, S. (2011). A computational tool for quantitative analysis of vascular networks. *PLoS ONE*, *6*(11), e27385. https://doi.org/10.1371/journal.pone.0027385